Charles University

Faculty of Science

Study program: Organic Chemistry

Mgr. Jan Kretschmer

Syntéza chelátorů pro použití v diagnostických zobrazovacích metodách

Synthesis of chelators for use in diagnostic imaging

Doctoral thesis

Supervisor: RNDr. Miloslav Polášek, Ph.D.

Prague, 2022

Prohlášení:

Prohlašuji, že jsem závěrečnou práci zpracoval samostatně a že jsem uvedl všechny použité informační zdroje a literaturu. Tato práce ani její podstatná část nebyla předložena k získání jiného nebo stejného akademického titulu.

V Praze, 23.9.2022

Mgr. Jan Kretschmer

ACKNOWLEDGMENTS

First of all, I would like to thank my supervisor, Dr. Miloslav Polášek, for his time, patience, and everything he taught me. Dr. Polášek is not only a great chemist, but more importantly, a person who has the ability to look at things from a broader perspective and find connections that would otherwise remain hidden, and he is willing to share this skill and teach it. It has been a privilege to work with you for the past six years, and I am sure we will continue to collaborate in the future. This endeavor would not have been possible without the funding from the Czech Science Foundation (Project number: 17-22834Y), Charles University Grant Agency (Project number: 1608218), and the Erasmus Plus program. Not everybody is as fortunate as me to have such great lab colleagues, and I am very thankful for that. Dr. Tomáš David is person who was eager to help me anytime it was needed. He was trying to teach me to be an orderly and precise chemist, and he mostly succeeded. Thank you for that, Sandro. Our laboratory is running like clockwork thanks to Mgr. Miroslava Šedinová, who takes care of everything perfectly. Mirka was also a great support and helped me with analyses and purifications. Kelsea Jones was a great fellow to share an office with and was helpful, especially with my English language issues. Also, I would like to thank Dr. Milan Vrábel for providing space and facilities in my early years of research. David Hurný, Dr. Jan Klouda, Dr. Tomáš Jandušík, Róbert Reiberger, David Kodr and Martin Hadzima are wonderful friends who have been a support and source of inspiration for me over the years. I would also like to acknowledge Dr. Martin Dračínský for measurement and elucidation of NMR spectra, doc. Daniel Jirák and Martin Vít for MRI experiments, Ondřej Socha for the z-resolved ^{19}F NMR experiment, Dr. Jan Ráliš for help with pilot radiolabeling experiments, Mgr. Stanislava Matějková for ICP-MS analyses, and Dr. Ivana Císařová for X-ray crystallography. I am also extremely grateful for the opportunity to start a collaboration with Dr. André Ferreira Martins and his group at the Werner Siemens Imaging Center. Special thanks to Dr. Jonathan Meyer Cotton, Remy Chiaffarelli, Dr. Sabrina Hoffmann and Dr. Gregory Bowden. Words cannot express my gratitude to my family and my partner Karolina for their extraordinary support, without which I would not have been able to fully focus on the career I chose to pursue.

ABSTRACT

Metals play a crucial role in medicine as a part of therapeutic or diagnostic preparations. However, in the majority of cases, their properties cannot be utilized entirely in free ionic form. Organic molecules capable of chelation are used to open the full potential of the metal. The molecules are called chelators and are the core theme of this thesis. The most important function of these molecules is the chelation and coordination of the metal, but chelators can provide other important functionalities. This work, therefore, focuses on the design, synthesis, and application of such polyfunctional chelators and is divided into two parts:

DO3A-Hyp

This part of the thesis deals with chelators that can be used as amino acids to incorporate lanthanides into peptides. The developed chelators provide a short and rigid connection of the metal to the peptide chain. Tripeptides containing two units of such chelators with a central amino acid bearing a CF_3 group were synthesized to demonstrate the capability of DO3A-Hyp building blocks. Two paramagnetic metals were combined within this tripeptide, and it was shown that such a rigid and locked system could be used for combining their magnetic susceptibility tensors. These magnetic susceptibility tensors were used for manipulation of the ^{19}F NMR shift of the CF_3 reporter group. The combination of two different paramagnetic lanthanides resulted in four clearly distinguishable signals readable by ^{19}F NMR spectroscopy. A system constructed from such a platform and four paramagnetic metals (Dy, Ho, Tb, Tm) was used for 16-bit encoding and decoding of information. To further explore the potential, parallel reading of information by ^{19}F MRI was performed.

PET/MRI bimodal contrast agents

The second part of the thesis explores the area of under-investigated low molecular weight bimodal PET/MRI contrast agents. A suitable structural motif was designed, synthesized, and radiolabeled to prove the concept of a bimodal PET/MRI contrast agent. Cooperation with the Werner Siemens Imaging Center in Germany was set up to probe the properties and perspectives of prepared compounds. Within this cooperation, radiolabeling conditions were optimized and developed for radiolabeling on an automated radiosynthesis module. Two contrast agents were prepared. First, based on the DO3A motif, was prepared to serve as a perfusion agent. The second, structurally related to DO2A, was synthesized to serve as a lactate-responsive contrast agent. Properties such as kinetic inertness, relaxivity, and cytotoxicity were determined for these compounds *in vitro*. The perfusion PET/MRI contrast agent was synthesized, and phantoms thus prepared were measured simultaneously in a combined PET/MRI scanner to prove the capability for the intended use. As the last step, *in vivo* experiments were performed on mice, resulting in

data that confidently confirmed the suitability of this molecule as a perfusion bimodal PET/MRI contrast agent.

ABSTRAKT ČESKY

Sloučeniny kovů mají v medicíně zásadní roli jako součást léčebných nebo diagnostických přípravků. V naprosté většině případů však jejich vlastnosti nelze zcela využít v jejich volné iontové formě. K využití jejich plného potenciálu se používají organické molekuly schopné jejich zabudování. Tyto molekuly se nazývají chelátory a jsou hlavním tématem této disertační práce. Jejich nejdůležitější funkcí je samozřejmě chelatace, koordinace kovu, ale chelátory mohou poskytovat i další užitečné funkce. Z tohoto důvodu se práce zabývá návrhem, syntézou a použitím polyfunkčních chelátorů. Předkládaná práce se skládá ze dvou částí:

DO3A-Hyp

První část práce se zabývá chelátory, které lze použít jako aminokyseliny pro inkorporaci lanthanoidů do peptidů. Tyto chelátory zajišťují krátké a rigidní zabudování lanthanoidů do peptidového řetězce. Pro demonstraci schopností připravených stavebních bloků byly syntetizovány tripeptidy obsahující dva chelátory s centrální aminokyselinou nesoucí CF_3 skupinu. V tripeptidu byly následně kombinovány dva paramagnetické kovy a bylo ukázáno, že takovýto rigidní systém poskytující blízké připojení lze použít pro kombinaci tenzorů magnetické susceptibility přítomných paramagnetických kovů. Tenzory magnetické susceptibility byly následně použity pro manipulaci s ^{19}F NMR posunem reportérové CF_3 skupiny. Výsledkem kombinace dvou různých paramagnetických lanthanoidů byl vznik čtyři jasně rozlišitelných signálů, čitelných za použití ^{19}F NMR spektroskopie. Systém sestrojený na takovéto platformě v kombinaci se čtyřmi paramagnetickými kovy (Dy, Ho, Tb, Tm) byl použit pro kódování a dekódování informace. Pro další zkoumání potenciálu bylo provedeno paralelní čtení informace pomocí ^{19}F MRI.

Bimodální PET/MRI kontrastní látky

Druhá část práce zkoumá oblast málo prozkoumaných nízkomolekulárních bimodálních kontrastních látek pro PET/MRI. Byl navržen, syntetizován a radioaktivně značen vhodný strukturní motiv, který potvrdil funkčnost jakožto bimodální kontrastní látka pro PET/MRI. Byla navázána spolupráce s Werner Siemens Imaging Center v Německu za účelem prozkoumání vlastností a potenciálních použití připravených sloučenin. V rámci této spolupráce byly optimalizovány a vyvinuty podmínky pro radioaktivní značení. Podmínky byly také optimalizovány pro syntézu těchto látek za použití automatizovaného modulu pro radiosyntézu. Byly připraveny dvě kontrastní látky, z nichž jedna na bázi motivu DO3A byla připravena pro použití jako perfuzní kontrastní látka. Druhá, strukturně příbuzná s DO2A, byla syntetizována, aby sloužila jako kontrastní látka rozpoznávající laktát. U těchto sloučenin byly *in vitro* změřeny vlastnosti, jako jsou kinetická inertnost, relaxivita a cytotoxicita. Byla syntetizována perfuzní PET/MRI kontrastní

látka a z ní připravené fantomy byly zobrazeny v hybridním PET/MRI skeneru. V posledním kroku byly s touto látkou provedeny *in vivo* experimenty na myších, které potvrdili vhodnost použití této molekuly jako perfuzní bimodální kontrastní látky pro PET/MRI.

LIST OF PUBLICATIONS AND PATENTS

A part of the research presented in this dissertation has been published.

Publications

Kretschmer, J.; David, T.; Dračínský, M.; Socha, O.; Jirak, D.; Vít, M.; Jurok, R.; Kuchař, M.; Císařová, I.; Polasek, M. Paramagnetic encoding of molecules. *Nat. Commun.* **2022**, 13, 3179.

Patents

PCT/CZ2020/050032(2020, pending) – **Kretschmer, J.**; Polasek, M. Cyclen based compounds, coordination compounds, peptides, pharmaceutical preparation, and use thereof

Conferences

World molecular imaging congress 2019 (Montreal, Canada)–Poster

World molecular imaging congress 2018 (Seattle, USA)–Poster

Funding

CONCOORD: Controlled coordination for new radiopharmaceuticals - GAUK 1608218, principal investigator

Erasmus traineeship: Werner Siemens Imaging Center, Germany - Research collaboration with André F. Martins, June-July 2021 Development of PET/MRI bimodal probes

ABBREVIATIONS

AIBN	azobisisobutyronitrile
ASCII	American Standard Code for Information Interchange
Ar	aryl
Boc	*tert*-Butyloxycarbonyl
BPEN	*N*,*N*-bis(2-pyridyl-methyl)ethylenediamine
Bn	benzyl
BMS	bulk magnetic susceptibility
Bu	butyl
CA	contrast agent
CCDC	Cambridge Crystallographic Data Center
trans-CDTA	*trans*-1,2-Diaminocyclohexane-*N,N,N',N'*-tetraacetic acid
CSI	chemical shift imaging
CT	computed tomography
CuAAC	copper(I)-catalyzed alkyne-azide cycloaddition
DBU	1,8-Diazabicyclo[5.4.0]undec-7-ene
DCM	dichloromethane
DIAD	diisopropyl azodicarboxylate
DIPEA	*N,N*-diisopropylethylamine
DMF	*N*,*N*-dimethylformamide
DMAP	4-Dimethylaminopyridine
DMMTM	4-(4,6-Dimethoxy-1,3,5-triazin-2-yl)-4-methylmorpholinium chloride
DMSO	dimethylsulfoxide

DNA	deoxyribonucleic acid
DTPA	2-[bis({2-[bis(carboxymethyl)amino]ethyl})amino]acetic acid
EA	elemental analysis
EEDQ	*N*-Ethoxycarbonyl-2-ethoxy-1,2-dihydroquinoline
EIC	extracted ion chromatogram
Equiv	equivalent(s)
ESI	electrospray ionization
EtOAc	ethyl acetate
EtOH	ethanol
EWG	electron withdrawing group
FA	formic acid
FDA	U.S. Food and Drug Administration
Fmoc	fluorenylmethoxycarbonyl
GBCA	gadolinium based contrast agents
HATU	(1-[Bis(dimethylamino)methylene]-1*H*-1,2,3-triazolo[4,5-*b*]pyridinium 3-oxide hexafluorophosphate
HCTU	O-(1H-6-Chlorobenzotriazole-1-yl)-1,1,3,3-tetramethyluronium hexafluorophosphate
HMBC	heteronuclear multiple bond correlation spectroscopy
HPLC	high-performance liquid chromatography
ESI-HRMS	high-resolution mass spectrometry
HSQC	heteronuclear single quantum correlation spectroscopy
IOCB	Institute of Organic Chemistry and Biochemistry of the CAS
KOTf	potassium trifluoromethanesulfonate
K222	4,7,13,16,21,24-Hexaoxa-1,10-diazabicyclo[8.8.8]hexacosane

LD_{50}	median lethal dose
Me	methyl
MeOH	methanol
MeI	methyl iodide
MOPS	(*3*-(*N*-morpholino)propanesulfonic acid)
MRI	magnetic resonance imaging
Ms	mesyl
NAS	nucleophilic aromatic substitution
NBS	*N*-Bromosuccinimide
NMR	nuclear magnetic resonance
NPI	Nuclear Physics Institute of the CAS
PET	positron emission tomography
PEG	polyethylene glycol
Ph	phenyl
PSMA	prostate-specific membrane antigen
PTFE	polytetrafluoroethylene
PyAOP	((*7*-azabenzotriazol-*1*-yloxy)tripyrrolidinophosphonium hexafluorophosphate)
QMA	quaternary methyl ammonium
RT	room temperature
SPECT	single-photon emission computed tomography
SPIOs	superparamagnetic iron-oxide nanoparticles
TBAF	tetra-*n*-butylammonium fluoride
TBAOTf	tetrabutylammonium trifluoromethanesulfonate
t-BuOH	*tert*-Butyl alcohol

TCFH Chloro-*N*, *N*, *N*, *N*′-tetramethylformamidinium hexafluorophosphate

TEA triethylamine

TFA trifluoroacetic acid

TFAA trifluoroacetic anhydride

THF tetrahydrofuran

TLC thin layer chromatography

TRAP (3,3′,3"-((1,4,7-triazonane-1,4,7-triyl)tris(methylene))tris(hydroxyphosphoryl))-tripropanoic acid)

WSIC Werner Siemens Imaging Center

TABLE OF CONTENTS

1 INTRODUCTION

1.1 Metals in medicine

Forty-four years have passed since the registration of the first FDA-approved metal-based drug, cisplatin, an inorganic compound with antitumor activity.[1] Since then, a number of other preparations have been approved. We can divide them into two main categories: metal-based drugs for therapeutic applications and metal-based drugs for diagnostic purposes (Figure 1).

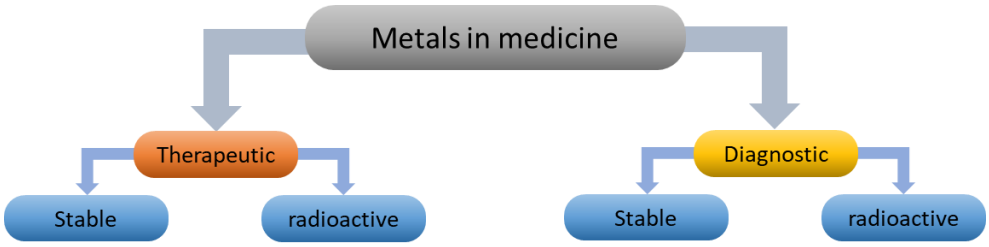

Figure 1: Different classes of clinically used metal-based drugs.

The above-mentioned cisplatin (Figure 2) represents the therapeutic group. Its antitumor activity is based on its ability to crosslink DNA bases and inhibit replication. In this category, we can also find other compounds based on platinum: Carboplatin and Oxaliplatin. Therapeutics based on antimony like meglumine antimoniate (Figure 2) are prescribed as the first choice for leishmaniasis (a parasitic disease). It is assumed that their therapeutic effect originates from the reaction between thiol-containing trypanothione, an unusual form of glutathione vital for parasites.[2] For vascular-targeted photodynamic (VTP) therapy in patients who have low-risk prostate cancer, palladium-based padeliporfin branded as TOOKAD is used. In this therapy, a low-power near-infrared laser is used to activate the photosensitizer (TOOKAD) that starts the production of oxygen radicals. These radicals destroy the blood vessels and cause necrosis in the tumor. [3] Sodium nitroprusside (Figure 2), branded as Nitropress, is used to lower blood pressure by releasing nitric oxide after reaction with thiol groups.[4] Auranofin, a gold salt of triethyl phosphine and (3,4,5-Triacetyloxy-6-sulfanyloxan-2-yl)methyl, branded as Ridaura, is used for the treatment of arthritis but is no longer a first-line treatment option due to the better medicines currently on the market. The way how auranofin acts is by the generation of reactive oxygen species and upregulation of the enzyme heme oxygenase-1.[5]

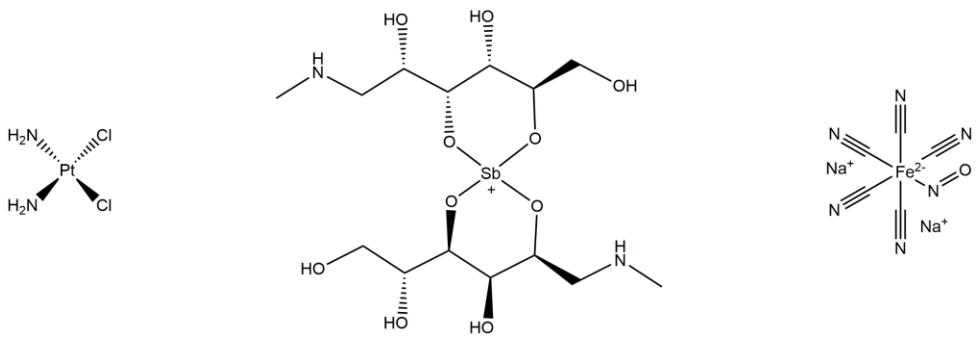

Figure 2: Selected examples of drugs based on stable metals. Cisplatin, meglumine antimoniate, and sodium nitroprusside.

Examples of metal-based therapeutics mentioned so far benefit from stable isotopes of the metals. However, radioactive isotopes of metals are tremendously important in therapeutic and diagnostic medicine. The radio-therapeutics utilize unstable metal isotopes that emit high-energy particles that damage the DNA molecules of cancer cells and efficiently kill them. Generally, in this type of therapy, the radionuclide is delivered to the tumor by targeted molecules (targeting vectors). A significant advantage of this approach is the precision of the treatment, where the negative effect on healthy tissue is minimized.[6] This precision attack is facilitated by the targeting vector selected against the specific type of cancer or by a physiological factor distinguishing the tumor from the healthy tissue. This type of treatment is called targeted radiotherapy.

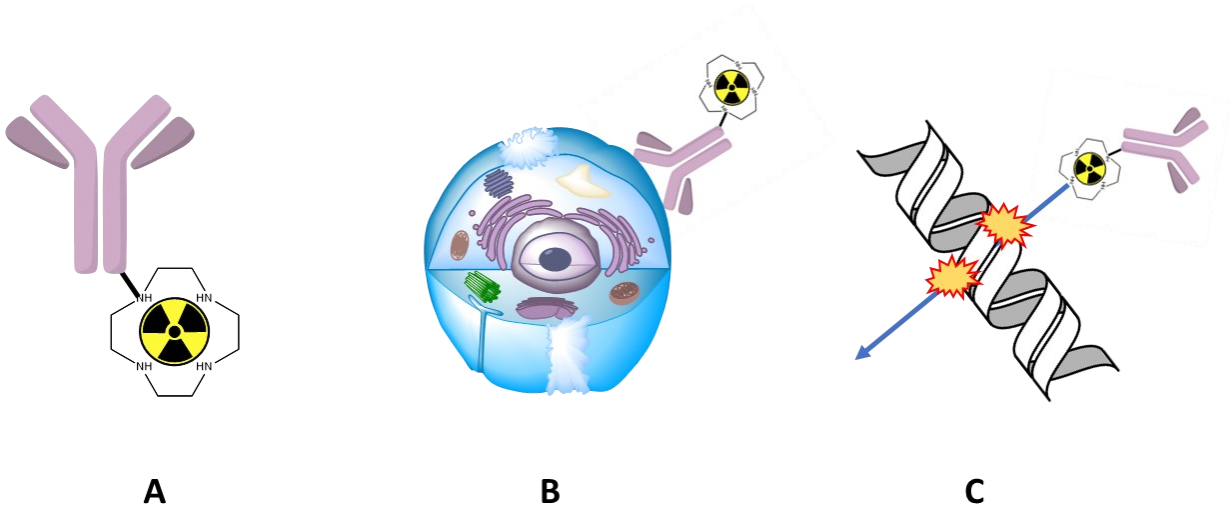

Figure 3: Targeted radiotherapy. The therapeutic radionuclide is connected to a targeting vector, in this case, an antibody. **B** Recognition of the target by the antibody radionuclide conjugate. **C** High energy particle emitted from the radionuclide damage the DNA of the cancer cell, leading to cell death and the destruction of the tumor.

The targeting vector is usually a biomolecule such as a peptide or an antibody, and the mechanism of action is depicted in Figure 3. FDA-approved metal-based radiopharmaceuticals for therapy are α or β^- emitters. In the case of β^- emitters, the particle which is emitted and does the damage is an electron. These radiopharmaceuticals are based on the radionuclides ^{90}Y and ^{177}Lu. Yttrium-90 is utilized as a conjugate with the rituximab antibody, available under the brand name Zevalin. Zevalin was the first antibody conjugate approved for radioimmunotherapy to treat blood cancer and non-Hodgkin's lymphoma.[7] Another case where the ^{90}Y is utilized is in the form of microspheres for the treatment of hepatocellular carcinoma that can't be surgically removed.[8] Lutetium-177 dotatate, Lutathera, the first FDA-approved radiopharmaceutical for peptide receptor radionuclide therapy, was approved in 2018. This radiopharmaceutical is composed of a targeting peptide and a chelate of the β^- emitter ^{177}Lu. This peptide specifically binds to somatostatin receptors of gastroenteropancreatic neuroendocrine tumors.[9] The most recent example of an approved radiopharmaceutical for therapy is Pluvicto, which is indicated for patients with PSMA-positive prostate cancer. It is a peptide-based bioconjugate that also carries ^{177}Lu (Figure 4).

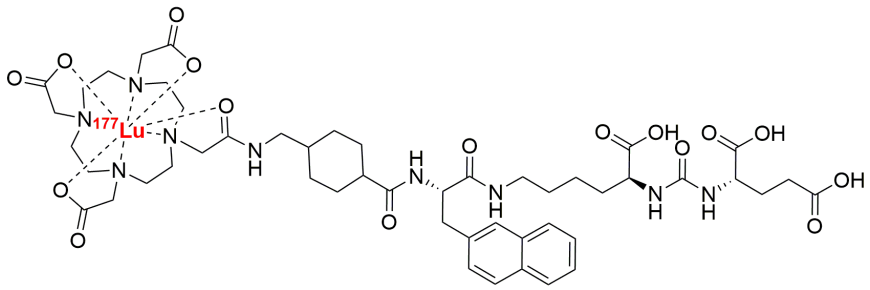

Figure 4: Structure of Pluvicto, a radiopharmaceutical for targeted radiotherapy that consists of ^{177}Lu chelate conjugated to the targeting peptide.

Precise diagnosis is crucial for the utilization of modern treatment approaches discussed above. This precise diagnosis can be achieved with the help of imaging techniques that rely on radiation sources. The source can be localized outside the patient's body, such as in the cases of X-ray and CT (computed tomography), or inside the patient. Positron emission tomography (PET) and single-photon emission computed tomography (SPECT) are techniques dependent on the latter. The radioactive sources that emit particles that are detected are called tracers. Because most of the periodic table of elements are metals, most appropriate radionuclides can also be found within metal elements. Metal radionuclides are essential as radiation sources in medical tracers. In SPECT imaging, the tracer must possess a radioactive metal that emits γ ray(s), while in PET imaging, the emitted particle is β^+ (positron). The most abundant group of FDA-approved diagnostic metal-based radiopharmaceuticals are drugs based on the γ-emitter ^{99m}Tc. This is mainly due to the development of the $^{99}Mo/^{99m}Tc$ generator in 1960, which accelerated research with this radionuclide by increasing its availability.[10] There are currently seventeen radiopharmaceuticals with ^{99m}Tc

approved by the FDA.[11] This radionuclide's use cases include ^{99m}Tc bicisate for stroke localization, ^{99m}Tc tilmanocept for localization lymph node drainage of primary tumors, ^{99m}Tc sestamibi as a cardiac perfusion agent, ^{99m}Tc pyrophosphate for bone imaging, and ^{99m}Tc Mertiatide for renal imaging. Another FDA-approved radiopharmaceutical for SPECT is gallium citrate. This drug contains the radioisotope ^{67}Ga and is used for imaging infection and inflammation.[12]

The other imaging technique using radioactive metals for imaging is positron emission tomography. Tracers for this technique emit a positron (β^+) which, after collision with an electron, annihilates and produces two photons that travel in opposite directions (180° apart). The metal radionuclide used for the preparation of the PET tracers is gallium-68 for imaging somatostatin receptor-positive neuroendocrine tumors as ^{68}Ga dotatate and ^{68}Ga dotatoc. The latest addition to FDA-approved ^{68}Ga radiopharmaceuticals with its application for imaging PSMA-positive cancers is ^{68}Ga gozetotide. The last metal radionuclide used in PET, approved by the FDA is copper-64. This radionuclide is utilized in ^{64}Cu dotatate for imaging of somatostatin receptor-positive neuroendocrine tumors. It is worth noting that other metal radionuclides are also in development.

As in the case of therapeutic drugs based on stable metal isotopes, we can also find a group of substances that use stable metal isotopes for diagnostic purposes. This type of metal-based pharmaceuticals is called contrast agents (CA). They are employed in MRI (magnetic resonance imaging), where they act as an indirect source of contrast by manipulating the MR signal of surrounding water molecules. The majority of the CAs used in MRI are built around gadolinium, a lanthanide with strongly paramagnetic properties. The paramagnetic element generates its own magnetic field when exposed to the external magnetic field because of its unpaired electrons. Due to the coordination of water molecules to gadolinium, the gadolinium chelate can interact with water molecules in its vicinity, resulting in an observable contrast. However, gadolinium in its free ionic form is toxic, therefore alternatives to gadolinium for MRI contrast enhancement are being sought. This resulted in the approval of the first (and so far, the only) manganese MRI CA, Mangafodipir, branded as Teslascan. However, it was withdrawn from the market in 2012. A final example of metal-based contrast agents used in MRI is iron oxide nanoparticles. Nevertheless, nanoparticles are not in the scope of this thesis, and further information about this topic can be found elsewhere.[13]

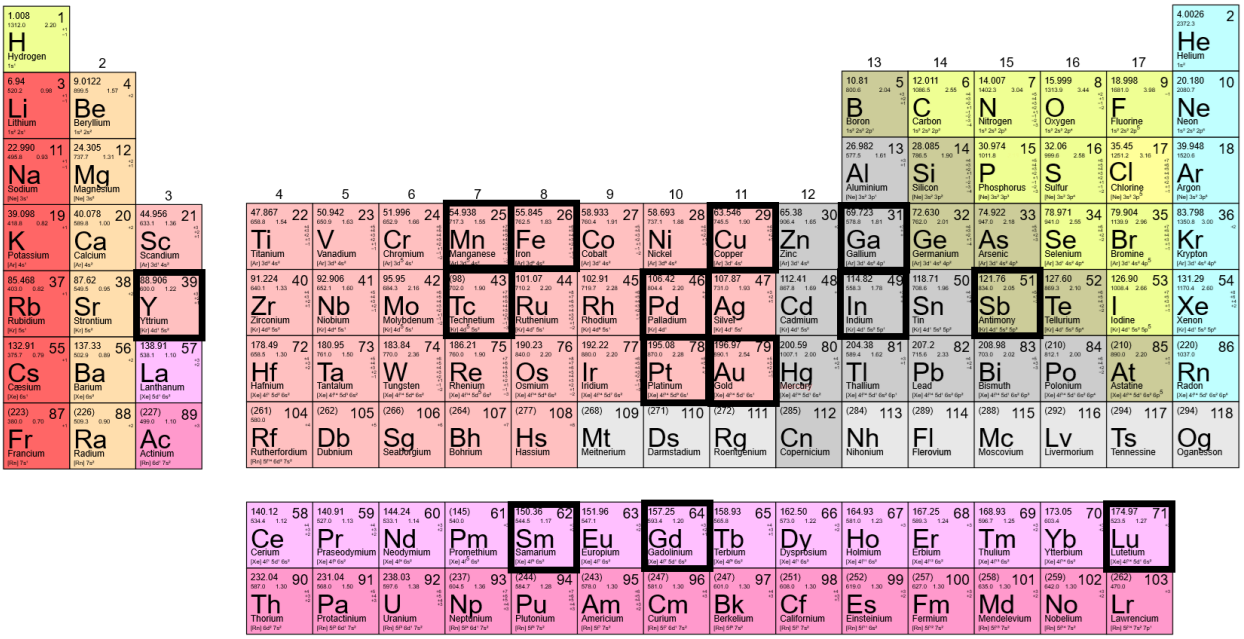

Figure 5: Metals used in FDA-approved pharmaceuticals are highlighted in the periodic table. The table highlights metals in complex compounds, not in a form of salts.

1.2 Lanthanides

The Lanthanides, fifteen elements from lanthanum to lutetium, are the largest subgroup of the periodic table. Together with Sc and Y, they are also called rare-earth elements. Lanthanide ions are most stable in an oxidation state of +3, but some exceptions can be found in oxidation states of +2 or +4. The lanthanides exhibit a large ionic radius, and this ionic radius is steadily decreasing across the series from the lanthanum to the lutetium. This phenomenon is called lanthanide contraction.[14] The difference in the size of the Ln^{3+} ionic radii between La (121.6 pm) and Lu (103.2 pm) is just ≈ 18 %, considering that there are thirteen elements between them.[15] The electronic configuration of the most stable +3 oxidation state is $[Xe]4f^n$ (n = 0–14). The 4f shell is concealed inside the ion, so the f electrons are not participating in the bonding. The coordination number tells us how many atoms, ions, or molecules are bound to the central atom in the coordination compound. For lanthanides, the coordination numbers are between 3 and 12, with 8 being the most common. [16] Lanthanide ions prefer to form coordination compounds with O, N, and S donors in the order O>N>S, and the most prevalent donor in aqueous solutions is the oxygen atom.[17] The hard character of the lanthanide ion drives the preference for oxygen donors with a high electrostatic component. The chemical similarity of lanthanides lies in their charge, ionic radii, and the inaccessibility of the f-orbital electrons for chemical bonding. These similarities make the separation of the lanthanides difficult and laborious. From the lanthanide series, only La^{3+} and Lu^{3+} are diamagnetic due to their electronic

configuration, $4f^0$ and $4f^{14}$, respectively, and $^1S_0$ ground levels. Other lanthanide ions possess magnetic moments whose strength is not only dependent on the number of unpaired electrons but also on the orbital contribution.

The unique properties of the lanthanides are utilized in many areas, such as in electronics, in magnets, and in displays. The lanthanides are also used in organic chemistry, especially for the reduction of functional groups and the formation of carbon-carbon bonds.[18, 19] Based on the low solubility of the lanthanides, it has been assumed that their functional presence in living organisms is unlikely. However, in an Italian volcanic mud pot, an acidophilic methanotrophic microbe was found. This bacterium, *Methylacidiphilum fumariolicum*, gets its energy by the oxidation of methane to methanol with a methanol dehydrogenase enzyme. Remarkably, this enzyme utilizes the lanthanides as the cofactor. Therefore, this bacterium is highly dependent on the presence of rare earth metals.[20] In the case of higher organisms, e.g., humans, the biogenic utilization of the lanthanides is unknown. More importantly, due to their comparable ionic radii with Ca^{2+}, trivalent lanthanides can bind to the same sites as Ca^{2+} on biological molecules, which is likely the cause of their toxicity.

1.3 Chelators

The majority of the metals in medicine are used not in their free ionic form but as coordination compounds or as chelates. A chelate is a coordination compound formed from a central metal ion and a ligand containing multiple donor atoms. For a chelate to form, the ligand must be bound to the metal ion at two or more points. In the case of lanthanides, the formation of a coordination compound is driven mainly by entropy. In the aqueous solution, the lanthanide cation and the ligand are solvated by the molecules of water. When the ligand is present, its donor atoms start to create the bonds with the lanthanide ion and, for this reason, the water molecules are dissociated. This process will cause the entropy of the system to rise. Due to the rise of entropy, complexation is preferred.[15]

A fruitful interplay between inorganic and organic chemistry can be seen in the case of contrast agents for magnetic resonance imaging. The gadolinium provides the enhancement of the contrast by shortening the relaxation time of neighboring water protons. However, the properties of gadolinium cannot be utilized in its unchelated form due to its toxicity. *In vivo*, unchelated gadolinium forms complexes with endogenous species like amino acids, phospholipids, and others. For example, the LD_{50} of chelated Gd^{3+} is 100 times lower than that of free Gd^{3+} when injected into rodents.[21] The metal has to be complexed for safe *in vivo* use by the organic chelator. Interestingly, the molecule of the chelator without the metal is almost as toxic as the unchelated metal itself, since it possesses approximately the same values of LD_{50}.[22] At this point, the

combination of the two provides an important benefit. The resulting metal chelate has very low toxicity and makes a useful MRI contrast agent.

A chelator is an organic molecule that consists of electron-donating atoms and functional groups that form coordinating bonds with an electron-accepting metal to form a chelate. The number of directly bound atoms to the metal ion of the chelate is called the coordination number. Importantly, chelators not only provide thermodynamic stability and kinetic inertness to suppress the leaching of free gadolinium, but also facilitate chelate biodistribution and renal excretion.[23] Various measurements can be made to assess the stability of the chelate. Thermodynamic stability describes the equilibrium state of the chelate, which is the ratio between the chelated and unchelated gadolinium. However, this constant does not tell us anything about the rate of the process. Thermodynamic stability is measured at a high pH (11) because there are no competing protons that could protonate the ligand and therefore destabilize the chelate. The conditional stability constant can be measured at a selected pH value. However, it is often measured at pH 7.4, where it provides relevant information on the stability of the chelate under physiological conditions. Both thermodynamic stability constants are predictive of the affinity of gadolinium for its ligand. The kinetic inertness provides information about the rate of dissociation, or the half-life of the chelate dissociation. Information about the value of kinetic inertness is relevant in situations where the system is far from reaching equilibrium, which is exactly the case of the *in vivo* environment. [24] The higher the values of the stability constant and kinetic inertness are, the less susceptible the gadolinium chelate is to leaching. Chelators that are clinically used for gadolinium chelation can be divided into two main types, linear and macrocyclic amino polycarboxylates. These types differ greatly in their *in vivo* stability, with macrocyclic chelators being superior to linear.[25] Based on this, only macrocyclic chelators with a cyclen (1,4,7,10-tetra-azacyclododecane) motif were prepared and investigated in this work.

1.3.1 Synthesis of chelators

The general procedure for the preparation of the macrocyclic chelators starts with the synthesis of the polyaza macrocycle. For example, the cyclen can be synthesized by cyclisation[26] or by the tetramerization of *N*-benzyl aziridine, which is used in the industrial scale synthesis [27] as depicted in Figure 6.

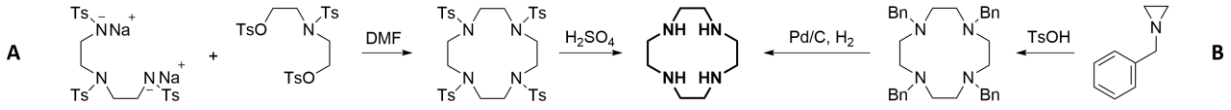

Figure 6: Schemes of cyclen synthesis. **A** Synthesis of cyclen by cyclisation. **B** Tetramerization synthesis used for industrial scale synthesis.

This work deals solely with lanthanide macrocyclic chelates. Complexes of lanthanides prefer coordination number 8 and donors with oxygen as discussed in Chapter 1.2. The macrocycle structure must be extended to provide enough donor atoms and to keep the molecule sufficiently kinetically inert. This is done by the addition of the pendant arms. The pendant arms are side chains that possess donor atoms that coordinate to the metal ion. Selected examples of ways the pendant arms can be incorporated in the macrocycle are shown in Figure 7. The pendant arm can be introduced by Mannich reaction (Figure 7A), epoxide opening (Figure 7B), nucleophilic substitution of the leaving group (LG) by the cyclen nitrogen. Commonly used leaving groups are halogens (Cl, Br, I) or sulfonic esters (OMs, OTs, OTf) (Figure 7C). A pendant arm can also be added by Michael addition to an unsaturated acceptor (Figure 7D).

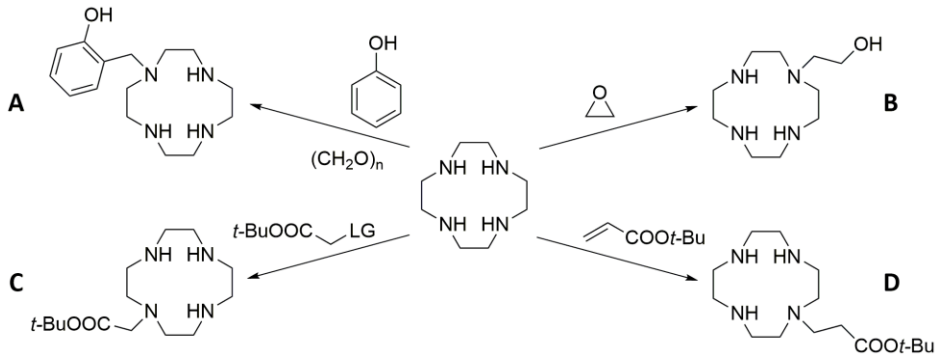

Figure 7: An illustration of different approaches for the connection of pendant arms to cyclen. **A** The addition of an aromatic pendant arm by the reaction of cyclen with phenol in paraformaldehyde. **B** Epoxide opening by cyclen furnishes a hydroxy product. **C** Nucleophilic substitution of LG (leaving group) by cyclen nitrogen. **D** Michaels' addition to unsaturated compounds.

Acetate is the most significant pendant arm in chelators designed for lanthanides. Several methods have been developed for the synthesis of chelators possessing protected acetate pendant arms in specific positions (Figure 8A). A chelator with three protected acetates, *t*Bu$_3$-DO3A, can be prepared by adding 3.3 equivalents of *tert*-butyl bromoacetate in dimethylacetamide to a suspension of 1 equivalent of cyclen and 3.3 equivalents of sodium acetate in dimethylacetamide, while maintaining a reaction temperature of -20 °C. The selectivity of the alkylation in this case is determined by the choice of solvent, with the product precipitating out of the reaction mixture as the HBr salt. [28] Variant of *t*Bu$_2$-DO2A where *tert*-butyl protected acetates are on opposite nitrogens of the cyclen is synthesized in a multistep process (Figure 8B). In the first step, Cbz (benzyl carbamate) protection of two opposite nitrogens is done by the addition of 2 equivalents of Cbz-Cl (benzyl chloroformate) in chloroform without base. Selectivity is caused by the protonation of two opposite macrocyclic nitrogens, leading to their electrostatic repulsion. In the second step, *tert*-butyl acetates are introduced on the vacant nitrogens of cyclen. The last step is the deprotection of the Cbz group by catalytic hydrogenation.[29] The cyclen can be selectively alkylated into 1,4 position with *tert*-butyl acetates by reaction with 2 equivalents of *tert*-butyl bromoacetate in chloroform while using

10 equivalents of triethylamine as a base (Figure 8C). The regioselectivity is provided by selective protonation of the macrocycle that prevents further alkylation.[30]

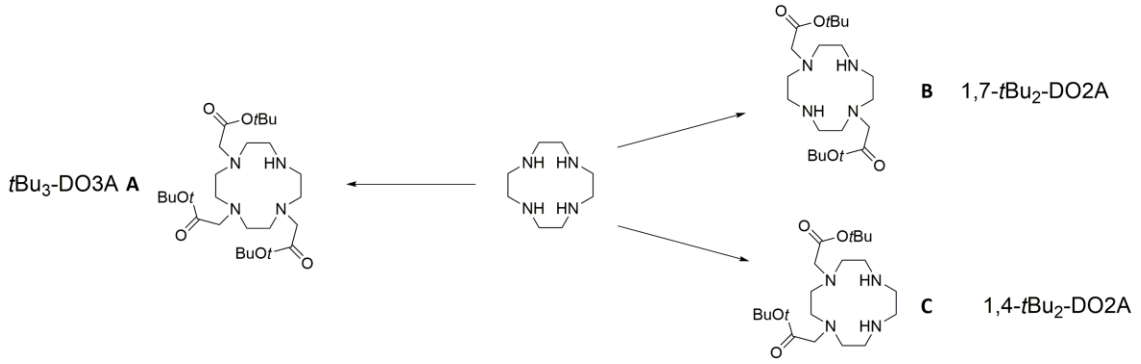

Figure 8: An illustration of synthetic pathways leading to alkylated cyclen in selected positions. **A** Preparation of *t*Bu$_3$-DO3A.[28] **B** Preparation of 1,7-*t*Bu$_2$-DO2A.[29] **C** Preparation of 1,4-*t*Bu$_2$-DO2A.[30]

An illustrative example of further steps from the protected chelator (*t*Bu$_3$-DO3A) that lead to the final complex is shown in Figure 9. The free nitrogen of cyclen can be alkylated by the selected pendant arm due to the fact that the carboxylates are protected by *tert*-butyls. The next step is the deprotection of *tert*-butyls from acetates to furnish chelator. The last step is the complexation of the metal ion while maintaining the pH.

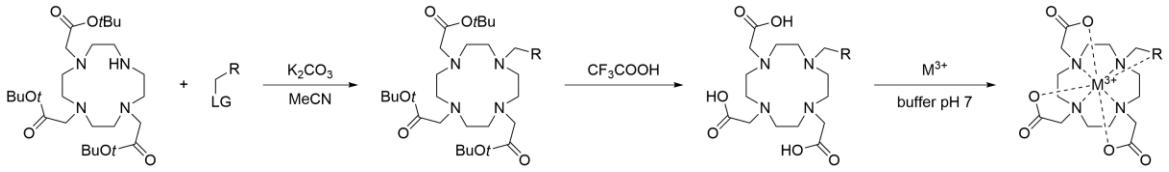

Figure 9: An example of a simple synthesis of a complex. In the first step, the free nitrogen of the macrocycle is alkylated, the other nitrogens carry acetates protected by tert-butyls. In the next step, TFA is used to deprotect the acetates to give the deprotected chelator. The last step is the complexation of metal by chelator in the buffer.

1.4 Imaging in medicine

In the introduction, it was described how important the place of metal-based drugs in medicine is. The two main application areas for these classes of pharmaceuticals are therapy and diagnostics. Based on the scope of this thesis, only diagnostic pharmaceuticals and related imaging techniques will be discussed. The undisputable benefits of imaging techniques have been mainly in helping with prevention, diagnosis, and monitoring treatment progress of human injuries and diseases through non-invasive approach. Currently, there are a variety of imaging techniques to choose from. The most clinically used techniques are X-ray, CT (computed tomography), ultrasound, MRI, and PET. For each one of them, the signal acquisition originates from different phenomena and therefore is suitable for different purposes. The oldest technique, X-ray, uses high energy electromagnetic radiation (20 keV to 150 keV) from an external radiation source, a cathode-ray tube. This radiation penetrates objects and is absorbed in varying degree, depending on their composition. CT, which uses the same source and type of radiation as X-ray, is widely available technique. In this case, the radiation is delivered and analyzed from multiple angles to rapidly obtain a 3D image after computer processing.[31] Ultrasound is used medicinally mainly as diagnostic sonography that uses sound waves with very high frequencies (3 to 10 MHz) to create images of the internal body structures.[32] Magnetic resonance imaging (MRI) uses magnetic field (most commonly 1.5 or 3T) and radiofrequency pulse to direct the spins of hydrogen atoms in water molecules. The return of the spins to their base state is recognized as the MRI signal. This technique is a 3D non-invasive, non-ionizing technique that provides deep tissue penetration with great resolution as small as 1 mm. This technique is particularly useful for the soft tissue because of its high water content. PET, on the other hand, needs an unnatural source of signal in the form of a tracer with an incorporated radionuclide that emits positrons.

For all the imaging techniques mentioned, contrast agents are available. However, only contrast agents for MRI and PET will be discussed within the scope of this thesis. A contrast agent, by its name, is a substance that causes contrast between the areas of tissue being examined. This contrast can be observed as differences in the intensity of the observed image of tissue. However, contrast agents for PET and MRI provide this effect on a very different basis. In the case of PET, the contrast agent (tracer) is essential to obtain an image because a positron emitting source is not naturally present in human body. In MRI, the image is the result of a water molecule signal. It can therefore be obtained without a contrast agent. However, the contrast agent helps to improve the contrast. Additionally, in comparison between MRI and PET, there is a remarkable difference in the required dose of contrast agent for each technique. Based on the PET's excellent sensitivity, just nano to picomolar[33] concentrations of PET tracers are required to obtain the image. A very low amount of a substance means a safe (non-toxic) concentration even for substances that would be dangerous in higher concentrations. As a result, they can be used as tracers after proper labelling with a

suitable radionuclide.[34] For MRI image enhancement, the dose ranges from 0.1 to 0.3 mmol kg^{-1}.[35] This implies that 10^5 to 10^8 more contrast agent is needed for MRI than for PET.

1.4.1 Positron emission tomography

In positron emission tomography, the signal is provided by the radioactive contrast agent. This contrast agent possesses a radionuclide that emits positron, and when this positron collides with an electron, an annihilation event occurs. The annihilation produces two photons in direction of exactly 180 ° to each other. These photons are later nearly simultaneously detected in the circular detector ring. There is a difference in time of detection of these photons, and from this difference it is possible to determine information about the location of the annihilation event (Figure 10).[36] The advantages of PET are the great sensitivity of detection and the possibility to quantify the contrast agent by detection of individual decay events.

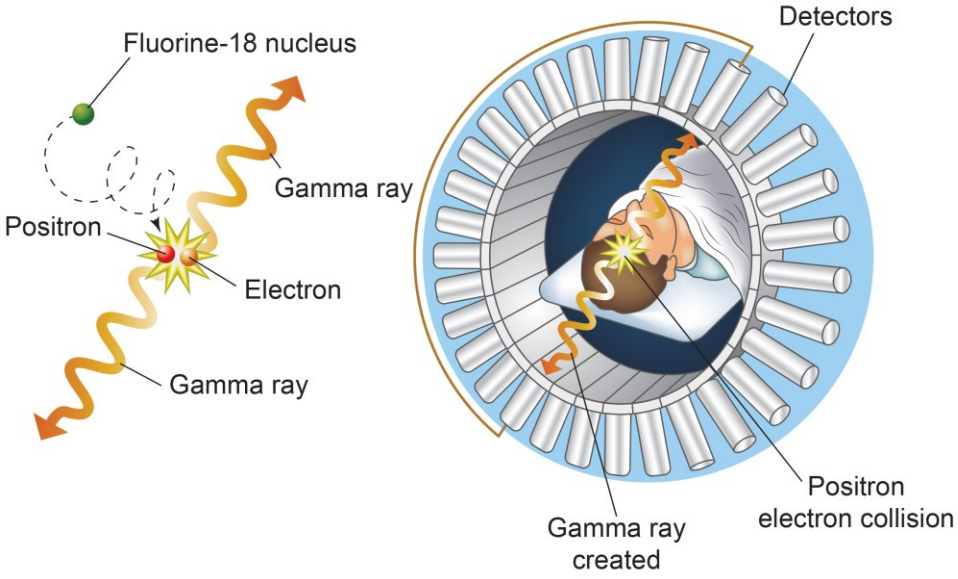

Figure 10: The principle of image acquisition from positron emission tomography. First, the positron is emitted by a positron-emitting nucleus. Upon collision with an electron, two photons are released and detected. Illustration re-drawn from Huettel et al. 2009.[37]

Unlike techniques such as CT or MRI, PET can be used to predict the development of pathologies due to its functional imaging capability. For example, tracers in immuno-PET can alert us to the onset of a pathological event before it manifests on the structural and anatomical level.[38]

We can divide the radionuclides used in the PET tracers into two groups. Light organic radionuclides and heavier metal radionuclides. Both groups require a different approach for their incorporation into the PET tracers. For the first group of lighter elements, the radionuclide is usually incorporated covalently into the

structure of the final tracer. We can find in this group the most commonly used PET radioisotopes: ^{18}F, ^{11}C, ^{13}N, and ^{15}O (Table 1). These isotopes are produced in cyclotrons.

Table 1: Selected clinically used PET radionuclides and their characteristics.

Nuclide	Half-life	Decay mode (%)	$E_{\beta+,max}$ [keV]
^{18}F	109.6 min	β+ (97) EC (3)	635
^{11}C	20.4 min	β+ (99.8) EC (0.2)	960
^{13}N	9.96 min	β+ (100)	1190
^{15}O	2.03 min	β+ (99.9) EC (0.1)	1720

The most clinically used radionuclide is ^{18}F in the form of [^{18}F] FDG (fluorodeoxyglucose) shown in Figure 11A. [^{18}F] FDG is the best known and most widely utilized tracer for PET as oncology diagnostic.[39] [^{18}F] FDG provides information about targeted tissue energy metabolism. This information is especially important in oncology because energy consumption of cancerous tissue is higher than the healthy one (Figure 11B, C). [^{18}F] FDG was first synthesized in 1968 by Dr. Josef Pacák *et al*. at the Department of Organic Chemistry, Charles University, in Czechoslovakia.[40] [^{18}F] F-DOPA is another important tracer used to study the dopaminergic system, which is especially important in the context of Parkinson's disease.[41] Tracers with ^{11}C radionuclide are utilized in the visualization of benzodiazepine receptors[42], to image D2/D3 receptors[43] and to discriminate between low and high grade gliomas.[44] [^{13}N] ammonia is used for the evaluation of coronary artery disease[45] and [^{15}O]H_2O is used for quantification of the ischemic burden after traumatic brain injury.[46]

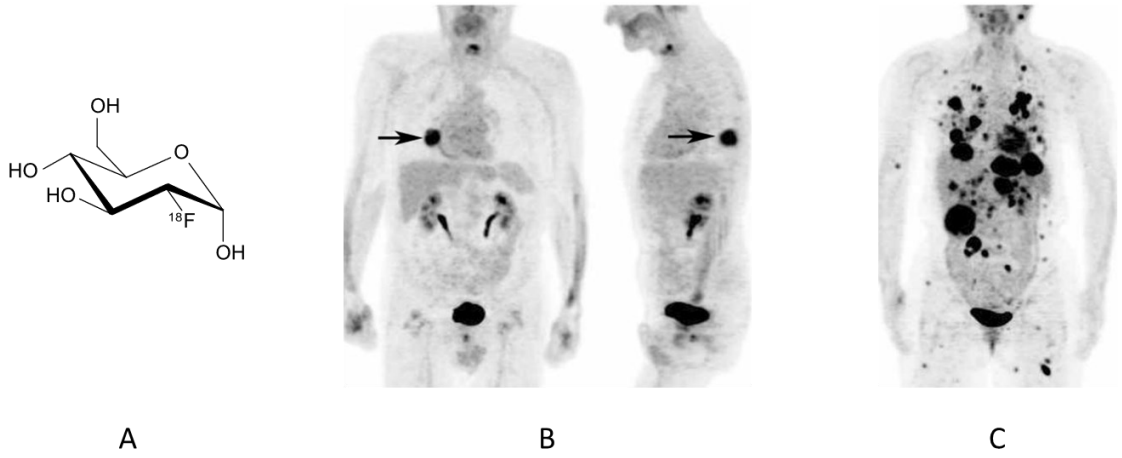

Figure 11: **A** Structure of [^{18}F] FDG. **B** PET scan utilizing [^{18}F] FDG in a patient diagnosed with lung cancer. Arrows indicate the newly discovered tumor in lower lung lobe. **C** PET scan using [^{18}F] FDG in a patient diagnosed with malignant melanoma. Numerous metastases are seen. PET images taken from. [47]

The second group consists of the metal-based PET tracers. Selected radionuclides used in these tracers and their properties are listed in Table 2.[48] For this group of tracers, the incorporation of radionuclide is done by complexation of the metal ion as a last step of the synthesis. Generally, this approach is more convenient, especially when tracers are composed of targeting biomolecules, e.g., antibodies. Of these radionuclides, only ^{68}Ga and ^{64}Cu are employed in FDA-approved radiopharmaceuticals. ^{68}Ga became a recent favorite choice for labelling in the case of ^{68}Ga-PSMA for prostate cancer diagnosis.[49] Production of ^{68}Ga is performed by the ^{68}Ge/^{68}Ga generator. This generator permits straightforward production of this isotope, thereby increasing the availability of ^{68}Ga.[50] Other ^{68}Ga-based radiopharmaceuticals used in current clinical practice are ^{68}Ga-DOTA-TOC for visualizing tumors that possess somatostatin receptors[51] or ^{68}Ga-DOTA-TATE for assessment of neuroendocrine tumours.[52]

Table 2: Metal-based radionuclides used in PET tracers.

Nuclide	Half-life	Decay mode (%)	$E_{\beta+,max}$ [keV]
^{68}Ga	67.8 min	β+ (88.9) EC (11.1)	1899
^{64}Cu	12.7 hours	β+ (17.5) EC (43.5) β- (38.5)	653
^{89}Zr	78.4 hours	β+ (22.7) EC (76.2)	902
^{86}Y	14.7 hours	β+ (31.9) EC (68.1)	1221

1.4.2 Magnetic resonance imaging

In Figure 12 an illustration of MRI scanner is shown. The scanner consists of a magnet that delivers the external magnetic field B_0. The strength of the field for clinically used scanners is typically 1.5 or 3T. Radiofrequency coils are used to deliver energy to the protons and also to receive their signals. MRI scanners have three opposite pairs of gradient coils in the x, y, and z-axis. These coils are used to encode the MRI signal in 3D space for its localization.

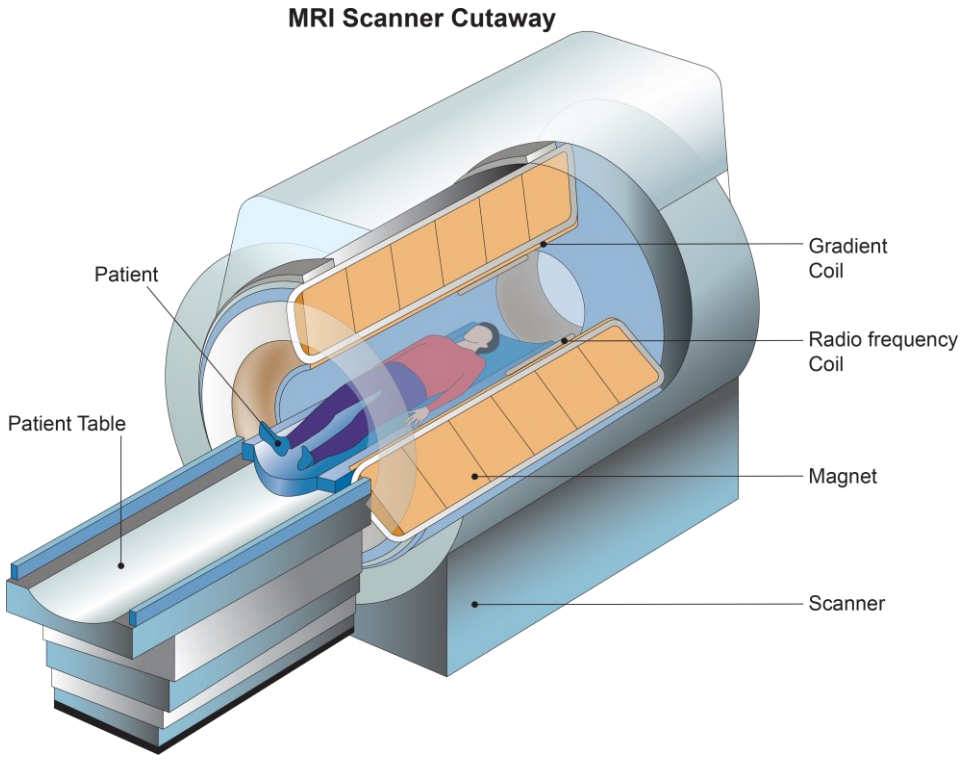

Figure 12: Scheme of an MRI scanner with descriptions of the individual parts. Illustration adapted from ref.[53]

MRI uses the nuclear magnetic resonance technique. Hydrogens belong to the group of atoms whose nuclei have non-zero nuclear spin (Figure 13A). The advantage of protons for the MRI technique is not based only on their magnetic properties but also on their high abundance in the human body. Without a magnetic field applied, these nuclear spins have a random arrangement, and the net magnetic moment is zero (Figure 13B). After an external magnetic field (B_0) is applied, these spins align with the direction of the applied magnetic field. These spins then rotate around their z-axis at a frequency called Larmor frequency (Figure 13C). The Larmor frequency $\omega=\gamma*B_0$ is directly proportional to the strength of the applied magnetic field and γ (gyromagnetic ratio). The Larmor frequency of the protons is 42.58 MHz per tesla. When an external magnetic field is applied, these spins align with this external magnetic field in two directions. The two directions have different energy levels. Spins aligned with the external magnetic field have lower energy, while spins oriented in the opposite direction have higher energy. Both energy levels are almost equally

populated, but slightly higher number of proton spins is aligned with the external magnetic field in the lower energy level (Figure 13C, D). The population ratio between the two levels is approximately 100,000 to 100,006. When the magnetization of all the protons in a magnetic field is combined, we get an overall magnetization vector (shown as the green arrow in Figure 13E). This magnetization has the same direction as the external magnetic field because of the small excess of spins that are oriented in the same direction. This magnetization is called longitudinal. Unfortunately, this magnetization can't be detected due to its same orientation as the external magnetic field B_0.

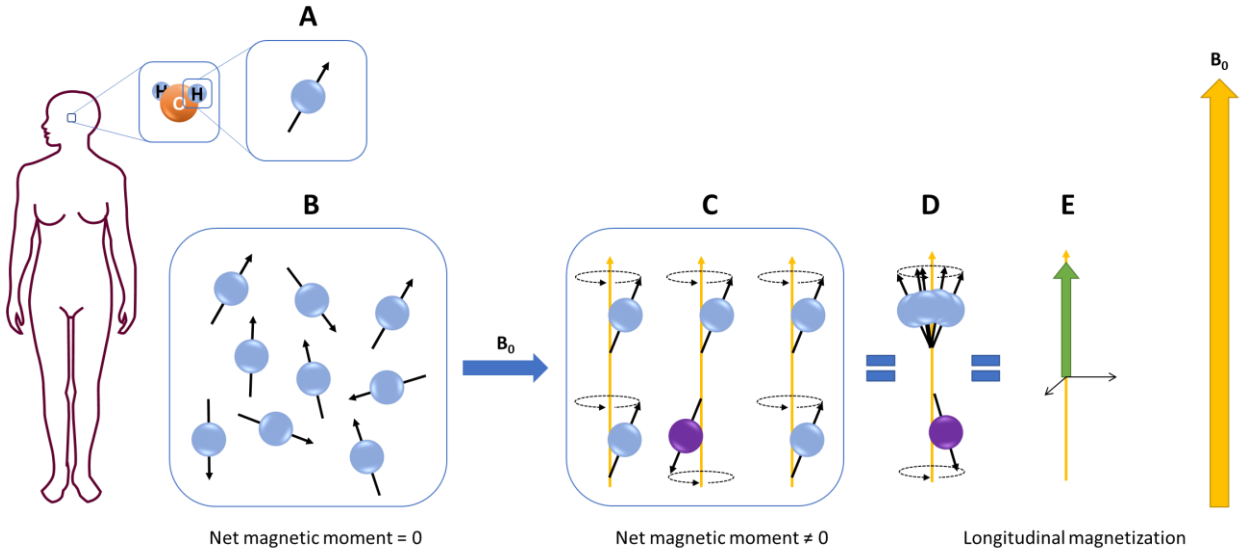

Figure 13: **A** MRI technique utilizes spins of water protons. **B** Without an external magnetic field, the spins are randomly oriented, and the net magnetic moment is zero. **C** When an external magnetic field B_0 is applied, the spins align parallel and antiparallel to it. However, a small excess of parallel spins aligns with the direction of B_0. **D** For easier visualization of the magnetization, the spins are grouped and the large excess of their population at both energy levels is not shown for simplicity. **E** Due to the small excess of spins aligned in direction with the external magnetic field, longitudinal magnetization is produced (green arrow).

Now, when the spins are aligned with the magnetic field (with a tiny excess of spins oriented in its direction), it is necessary to deliver energy in a form of radiofrequency pulse (Figure 14A). For this purpose, a radiofrequency coil is used, and the frequency value corresponds to the Larmor frequency of the protons. This radiofrequency pulse tips the vector of net magnetization from the longitudinal orientation to the transversal plane (Figure 14B). We call this vector of magnetization transverse magnetization. Transverse magnetization rotates perpendicular to the external magnetic field B_0 and therefore induces voltage in radiofrequency coils that is detected as FID (free induction decay).

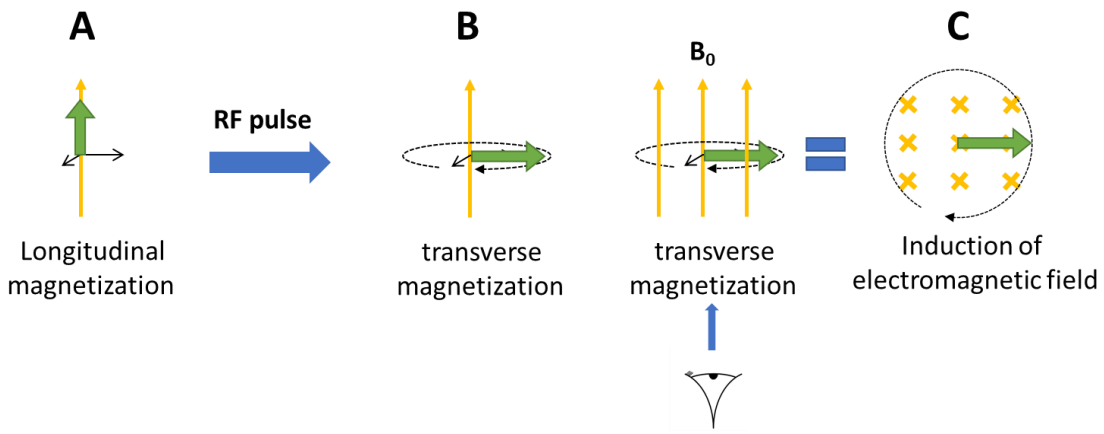

Figure 14: **A** Longitudinal magnetization is produced by the excess small fraction of spins that precess in the external magnetic field. **B** A radiofrequency pulse (RFP) is applied to tip the net magnetization vector from the longitudinal plane to the transversal plane. **C** The precessing transverse magnetization induces a voltage in radiofrequency coil.

After the end of the radiofrequency pulse energy input, the spins phase out. They do not continue to precess with the same phase. This phenomenon is called spin-spin or T_2 relaxation (Figure 15A). When higher-energy spins return to a lower-energy state, we call this event spin-lattice or T_1 relaxation. During this event, the previously absorbed energy is transferred to the surrounding tissue in the form of heat, and the original longitudinal magnetization is restored (Figure 15B). Fast T_1 relaxation allows faster scan repetition and thus faster signal accumulation, which results in a brighter image. The maximum signal intensity of tissue is determined by the density of protons in the tissue. Endogenous molecules, peptides, lipids, and sugars affect the T_1 and T_2 relaxation times of surrounding water molecules. Due to the differences in T_1 and T_2 relaxation rates across the tissue types, they can be distinguished. This is why MRI has excellent resolution according to tissue type. To localize the imaged area, a gradient coil is used to select a slice in the z plane. The x and y axis gradient coils are later used to uniquely encode each voxel of the x and y plane in this slice z. Each of the signals possesses a unique phase and frequency that can be localized in 3D space. T_1 and T_2 values can be modulated with exogenous agents such as MRI contrast agents. These agents modulate the relaxation times of surrounding water molecules. This modulation can later be observed as a brighter image for T_1 contrast agents or a darker image for T_2 contrast agents.

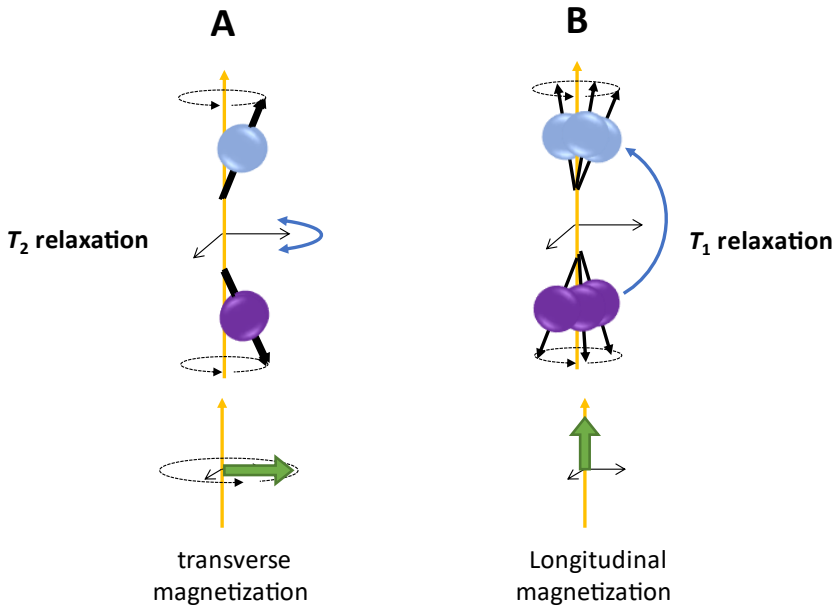

Figure 15: **A** When the RFP is no longer applied, the proton spins start to precess out of phase. This process is called T_2 relaxation. During this process, transverse magnetization is lost. **B** T_1 relaxation occurs when the spins on the higher energy level return to the lower energy level. During this process, longitudinal magnetization is restored. Both the T_1 and T_2 relaxation processes occur simultaneously.

1.4.2.1 Advanced MRI techniques

Functional MRI is used to image neuronal activity. Neuronal activity is associated with the consumption of energy. During this process, sugar and oxygen are used. Oxygen is delivered in the form of oxyhemoglobin that is transformed to the deoxyhemoglobin. Oxyhemoglobin is diamagnetic, while deoxyhemoglobin is slightly paramagnetic. Due to this, different regions with increased brain activity can be distinguished.[54]

Diffusion-weighted MRI is used to distinguish between the types of tissue by their different water diffusivity. Transport of water at the cellular level is done by diffusion. If water molecules are inside cells or other restricted spaces, their random diffusion is altered. This alteration is specific to every tissue. For example, in some tissues, the diffusion is isotropic. That means without any preferred direction. We can observe this phenomenon in the case of the cerebral spinal fluid. On the other hand, if the tissue has an ordered structure, as in the case of the white matter, the diffusion of the water molecules is anisotropic. Based on these differences, we can distinguish not only healthy tissue, but also changes resulting from pathological events can be observed. In the case of neurodegeneration and demyelination, increased diffusivity can be observed due to changes in the morphology of the affected tissue.[55]

Perfusion-weighted MRI measures the volume of blood perfusing a mass of tissue over a unit of time. It is utilized to determine cerebral perfusion and potential pathologies. Perfusion-weighted MRI is used in patients suffering from the stroke for differentiation between normal tissue, under-perfused tissue, and the stroke core.[56] Dynamic contrast enhancement (DCE-MRI) is type a of perfusion-weighted MRI technique. During this technique, T_1 contrast agent is injected. This contrast agent is distributed by the blood stream to the tissues where it changes the T_1 longitudinal relaxation time. This process is measured with the dynamic T_1-weighted imaging technique. After the measurement, the data can be analyzed quantitatively or semi-quantitatively. Quantitative analysis provides information about the dynamics of blood flow through tissue.[57]

Chemical exchange saturation transfer (CEST) MRI uses radiofrequency pulse to saturate exchangeable protons on endogenous or exogenous agents. This saturation is afterwards transferred to nearby water protons by chemical exchange and results in a decrease of the MRI water signal. By the application of saturation at a specific frequency, agents with exchangeable protons are detected. [58]

1.4.2.2 MRI contrast agents

An overview of the MRI contrast agents with the way their signal is detected is shown in Figure 16. Signal can be detected directly or indirectly. Direct detection means that the MRI signal of the contrast agent's atoms is measured directly. This group includes contrast agents that contain ^{19}F fluorine atoms, hyperpolarized ^{129}Xenon gas, or molecules with hyperpolarized ^{13}C carbon. Hyperpolarization is a technique by which the population of spins occupying the lower energy level can be increased. This can be performed in a high magnetic field and at a low temperature. This process of hyperpolarization increases the MRI signal of the contrast agent.[59] Contrast agents that contain ^{13}C can be spectroscopically detected without being hyperpolarized, but the intensity of the signal is low. Also, ^{1}H spectroscopy can be employed to directly detect metabolites or other particular molecules. In the case of indirect detection, the signal of water protons is measured. Contrast agents in this group change the relaxation times T_1 and T_2 of water protons in their proximity. We can observe this change as a change in the shade of the image. The T_1 contrast agents brighten the contrast area. This effect is produced by gadolinium, manganese, and iron (II) complexes. T_2 contrast agents darken the contrasted area, a representative of this class are SPIOs (Superparamagnetic iron oxides). The types of contrast agents that are addressed in this thesis are highlighted in Figure 16 in green.

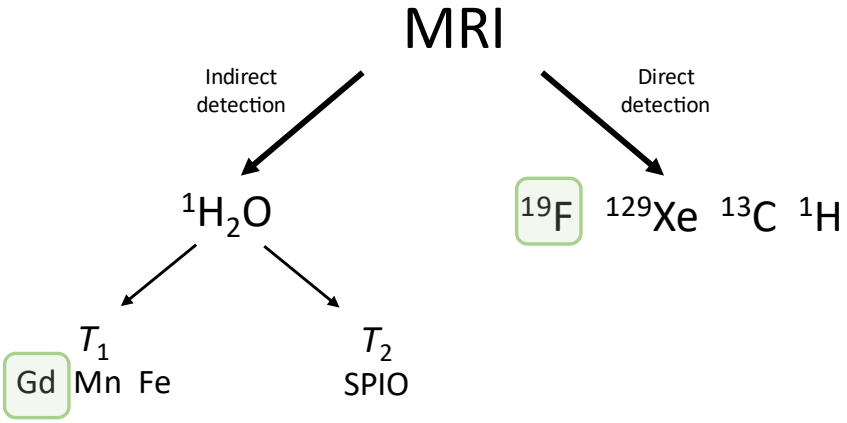

Figure 16: The schematic overview of contrast agents used in MRI with highlighted topics that are addressed in this thesis. Contrast enhancement can be obtained directly by detecting the contrast agent or indirectly by detecting the water proton signal that has been modified by the contrast agent. The fluorine isotope ^{19}F is measured directly from contrast agents carrying these nuclei. ^{129}Xe gas and ^{13}C can also be detected directly. However, it is advantageous to use them in hyperpolarized form to increase the signal. Metabolites or other molecules can also be detected by ^{1}H spectroscopy.

In MRI, gadolinium chelate-based contrast agents are used to provide contrast enhancement. Gadolinium-based contrast agents (GBCA) are widely used in MRI examinations. They are used in more than 30% of cases. Figure 17 shows the chemical structure of the "gold standard" GBCA, Gd-DOTA (Gadolinium (III) 1,4,7,10-tetraazacyclodododecane-1,4,7,10-tetraacetate).

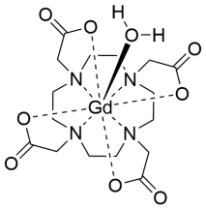

Figure 17: The chemical structure of Gd-DOTA, a macrocyclic gadolinium chelate with four acetate pendant arms.

1.4.2.3 Concept of relaxivity

All the commercially available T_1 MRI contrast agents are based on gadolinium. The most populated class of MRI contrast agents are the extracellular fluid (ECF) contrast agents. These agents are able to identify cases where an increase in blood flow, higher vascularization, or disrupted blood-brain barrier is present.[60] The importance of gadolinium for contrast enhancement in MRI arises from its electronic configuration with seven unpaired electrons. Seven unpaired electrons is the highest possible number, which gives the metal its powerful paramagnetic properties. This paramagnetic property allows these GBCAs to provide contrast enhancement by shortening the T_1 relaxation time of nearby water protons. Gadolinium in the chelate performs this process by relaxing the protons of bound water molecules. When a water molecule is

relaxed, it is replaced by another from the surroundings, and the process repeats. Since the human body is made up of 60% water, this approach is very effective.[61] More specifically, during T_1 relaxation, the higher energy proton spins return to a lower energy state, as described in Chapter 1.4.2. In this process the excess energy is transferred to its surroundings, especially to the water molecules. Gadolinium facilitates this energy transfer process by dipole-dipole interaction, thus shortening the relaxation time T_1.[62] The longitudinal magnetization is restored faster, more scans can be performed, and thus the image appears brighter. The capability of a contrast agent to affect the relaxation times of water protons is called relaxivity. Factors which affect the relaxivity are: the number of bound water molecules to the gadolinium ion (q), rotational motion of the chelate (τ_R) and exchange rate of the bound water molecule with the bulk water of the complex (k_{ex}), as is depicted in Chapter 1.4.2.3.[63] Relaxivity (r_i) can be determined from Equation 1, where ($1/T_i^0$) is the tissue's natural rate of relaxation, ($1/T_i$) is the relaxation when a contrast agent is present, and [CA] is the concentration of the contrast agent. Both longitudinal r_i (i = 1) and transversal r_i; (i = 2) can be determined by applying this equation.

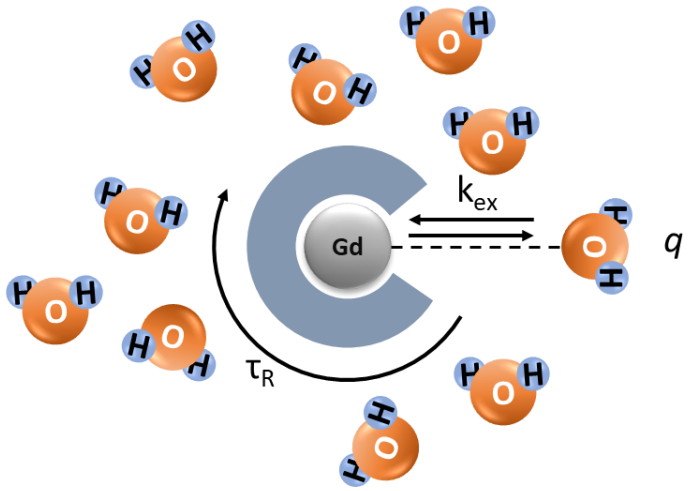

Figure 18: Schematic depiction of properties that affect relaxivity of T_1 gadolinium contrast agents, (k_{ex}) corresponds to water exchange rate, (q) is the number of bound water molecules to gadolinium, and (τ_R) is rotational motion correlation time.

$$\frac{1}{T_i} = \frac{1}{T_i^0} + r_i[\mathrm{CA}]; i = 1,2$$

Equation 1: Equation that can be used for the determination of relaxivity value.

Indirect enhancement of the MRI signal utilizes two types of contrast agents, T_1 and T_2. The T_1 contrast agents reduce the longitudinal T_1 relaxation rate, and the mechanism of this process is described above. An agent that reduces T_1 also reduces T_2, however, T_2 can be modulated in other ways as well. The T_2 relaxation can be changed by the creation of a local inhomogeneous magnetic field different to external B_0 by a T_2 contrast agent. The Larmor frequency in this local magnetic field created by the T_2 contrast agent is changed. If the Larmor frequency of the precession is different from the characteristic Larmor frequency for protons, the signal is suppressed, and the contrasted area appears dark. In Figure 19, examples of both types of contrast enhancement are shown. In the left picture (Figure 19A) a T_1-weighted MRI image of a patient with a brain tumor is shown. The tumor is brightened after injection of the T_1 contrast agent (Figure 19B). An example of how an increased concentration of a gadolinium based T_1 contrast agent increases the brightness of an image is shown in Figure 19C. Right image shows the effect of T_2 contrast agent, SPIOs. T_2 weighted image of mouse tumorous mammary glands (Figure 19D). After the introduction of the T_2 contrast agent the area with the tumor became dark (Figure 19E). Contrary to the example with the T_1 contrast agent (Figure 19C) in this case, with the increasing concentration of T_2 contrast agent, the image becomes darker (Figure 19F).

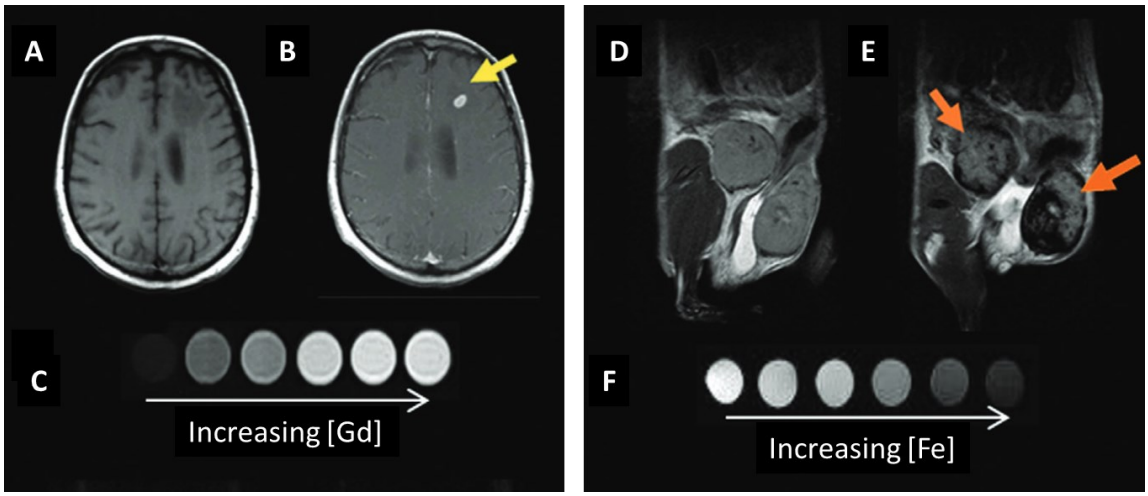

Figure 19: Examples of contrast provided by T_1 and T_2 contrast agents. **A** T_1 weighted MRI image of a brain tumor patient. **B** After the GBCA administration, the tumor is highlighted. **C** The image appears brighter with increasing T_1 contrast agent concentration. **D** T_2 weighted image of mammary glands tumors in mice. **E** After administration of the T_2 contrast agent, the area of accumulation appears darker. **F** By increasing the concentration of T_2 contrast agent, the T_2 weighted image appears darker. This figure was reproduced from ref.[62]

1.4.2.4 Responsive MRI contrast agents

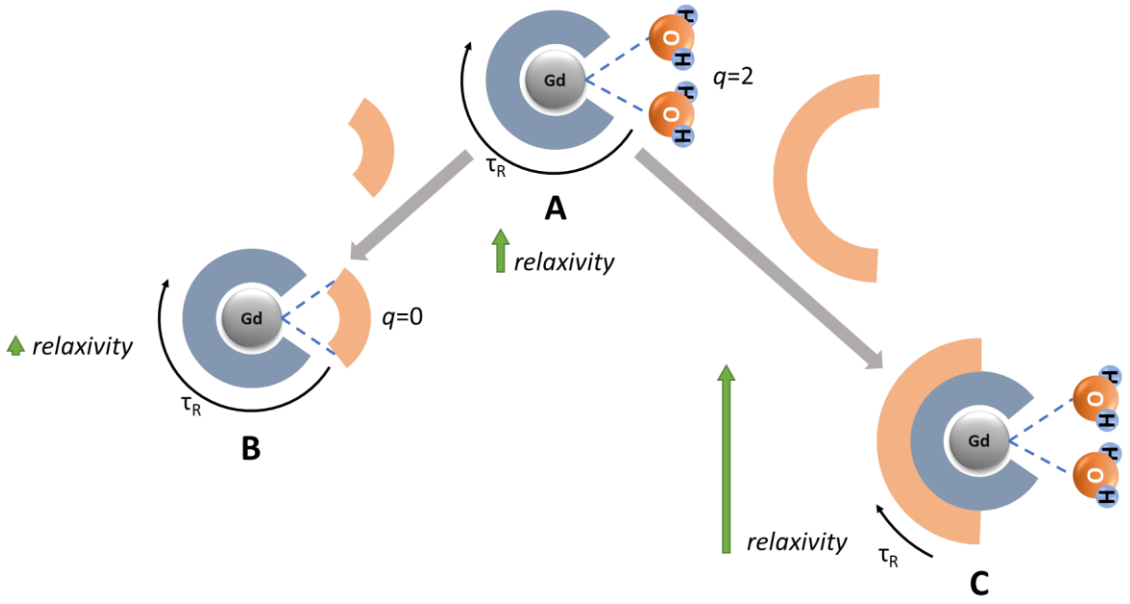

Figure 20: Schematic representations of two types of responsive contrast agents with a description of their responsiveness mechanisms. **A** The contrast agent starts with two coordinated water molecules (q = 2) and a certain value of the rotational motion correlation time (τ_R), which results in a moderate relaxivity value shown here by the green arrow. **B** Coordinated water molecules can be replaced by coordination of the analyte, resulting in a decrease in relaxivity. **C** The contrast agent may bind to a larger biomolecule, leading to slower rotational motion (higher τ_R) and, consequently, an increase in relaxivity.

Another class of MRI contrast agents are responsive contrast agents. These contrast agents are structurally tuned for the recognition of the selected stimuli (pH, small molecules, metals, redox events, etc.) by a change in relaxivity. As was described in Chapter 1.4.2.3, relaxivity is influenced by several parameters. These parameters include the number of coordinated water (q) molecules, rotational motion correlation time (τ_R), and the exchange rate between the coordinated water and the bulk (surrounding) water (k_{ex}). Any change to these parameters can affect the relaxivity and hence the intensity of the resulting MRI signal. Two basic principles of responsive contrast agents are shown in Figure 20. In this illustrative case, the contrast agent has two water molecules bound to the gadolinium ion (q = 2). The number of bound water molecules is directly proportional to the relaxivity of the contrast agent, here depicted as a green arrow (Figure 20A). Water molecules can be replaced by an analyte to which the contrast agent is responsive. This loss of water leads to a decrease in the relaxivity, observed in MRI image as a decrease in signal intensity (Figure 20B). Relaxivity also depends on the rotational correlation time of contrast agent (τ_R). This effect can be utilized when the contrast agent is tuned for binding to biomolecules. After the binding to the biomolecule, the rotational motion of the contrast agent slows significantly (τ_R increses). This leads to an increase in relaxivity and we can observe a stronger signal in MRI (Figure 20C). The responsiveness can

be tuned for metal ions[64–67], pH [68,69], enzymes [70,71], redox events[72,73], neurotransmitters[63], and other analytes. For example, in the presence of lactate, two water molecules bound to Gd-DO3A can be substituted by lactate.[74] This loss of water leads to a decrease in the relaxivity that can be detected as signal loss (Figure 21).

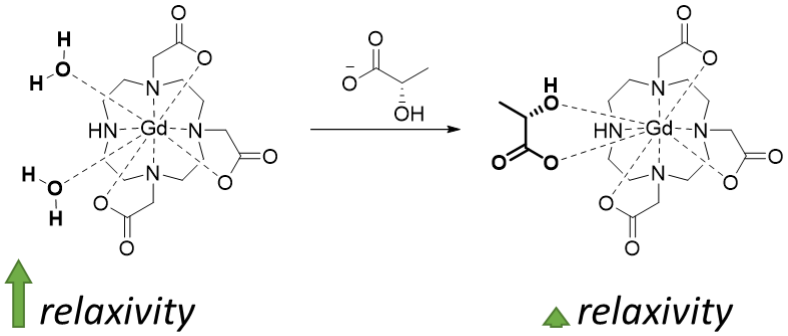

Figure 21: Two molecules of water bound to Gd-DO3A are replaced by the lactate anion. This loss of water molecules leads to a decrease in relaxivity.

Metals are involved in many essential biological processes, and around 300 enzymes require zinc for functioning. One of the current challenges in the development of responsive agents is therefore the design and preparation of zinc-responsive contrast agents. An interesting case of a zinc responsive contrast agent that combines two different responsivity principles is shown in Figure 22. Recognition of zinc is facilitated by another chelator selected specifically for this metal. In this case, the BPEN (*N,N*-bis-(2-pyridyl-methyl)ethylene diamine). After chelation of the Zn^{2+}, the relaxivity increases only slightly. However, the resulting molecule can bind to serum albumin. Due to this binding, rotational motion is slowed and relaxivity is significantly increased.[67] Recently, Gaoji Wang and Goran Angelovksi published work, where a Zn^{2+} responsive probe was developed with a remarkable 400% increase in relaxivity in the presence of Zn^{2+}.[75]

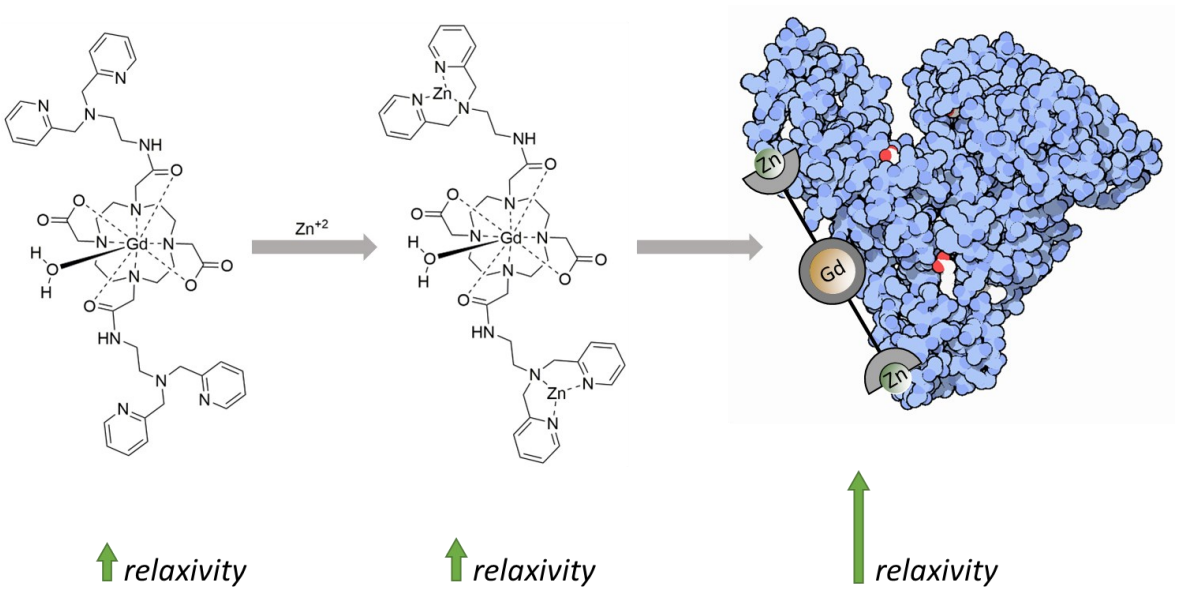

Figure 22: Demonstration of the function of the Zn(II) responsive MRI agent GdDOTA-diBPEN. Initially, BPEN moieties chelate the Zn(II) ions, leading to slightly increased relaxivity. However, this chelation allows binding to serum albumin. After binding, the relaxivity is increased substantially due to slowing of the rotational motion of the contrast agent.

1.4.3 Hybrid imaging technique PET/MRI

PET/MRI is hybrid imaging technique that combines positron emission tomography and magnetic resonance imaging. Combining both techniques into a single machine has several advantages. The patients don't have to undergo two separate examinations, which is time-saving and the stress associated with the examinations is reduced. Imaging in general causes a lot of stress and discomfort to pediatric patients due to the need to lie still and not move in the confined space of the scanner. For this reason, this hybrid technique presents an option, how pediatric patients can be spared multiple sedations or anaesthesia.[76] Another advantage of PET/MRI stems from the complementarity of both techniques. Information about tissue structure is obtained from MRI and quantitative and functional information is obtained from PET.

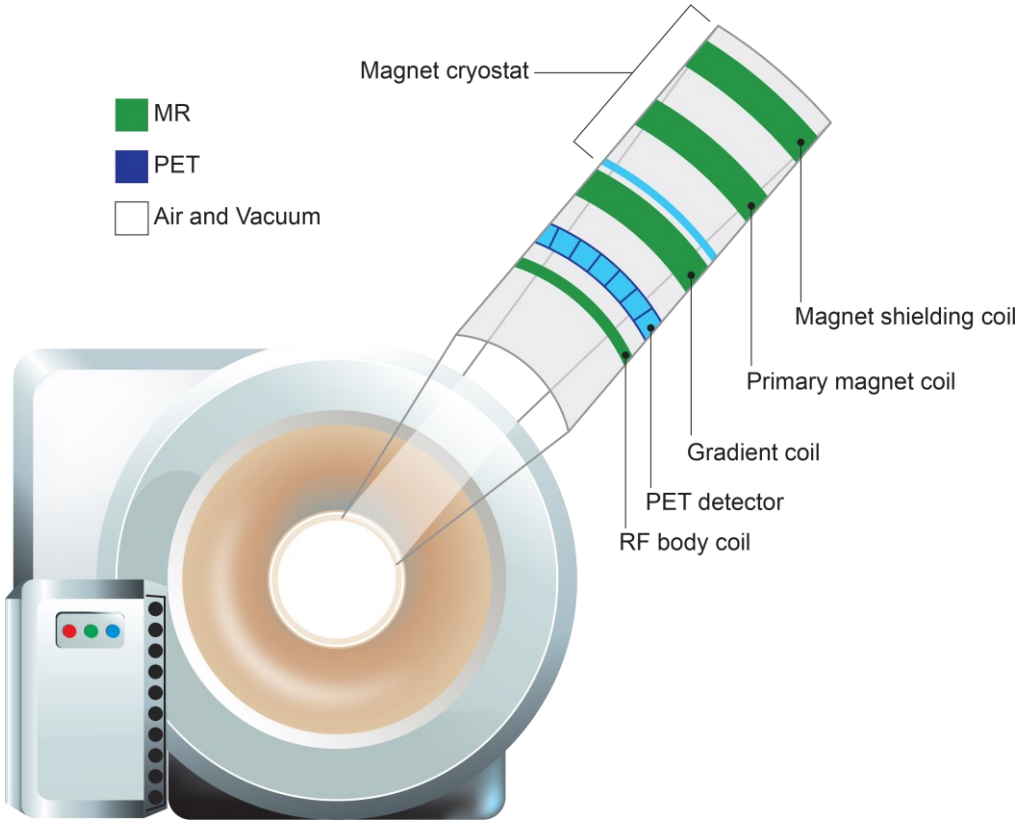

Figure 23: An illustration of a PET/MRI scanner with a description of its parts. The simultaneous acquisition of images from both modalities is enabled by the incorporation of the PET detector into the MRI scanner. Figure redrawn from ref. [77]

PET/MRI combines the excellent soft tissue resolution, the use of a wide range of MR techniques with the functional information of molecular imaging and the excellent sensitivity provided by PET. The PET/MRI system offers several advantages over the more commonly used hybrid PET/CT system. Most importantly, a lower radiation burden is being delivered to the patient, and higher information value from the examinations is gained. In a comparative study, it was discovered that using PET/MRI instead of PET/CT

reduced radiation dose by 79.6%. Additionally, PET/MRI provided additional information in 26.3% of cases.[78] There are multiple cases where PET/MRI use is advantageous to PET/CT.[79] In the staging of primary nasopharyngeal cancer, where [^{18}F]-FDG PET/MRI provides better information about lymph node metastases and in mapping of tumor extensions[80]. PET/MRI was superior to PET/CT in the detection of bone metastases of breast cancer patient[81] and for the determination of recurrence of prostate cancer.[82,83]

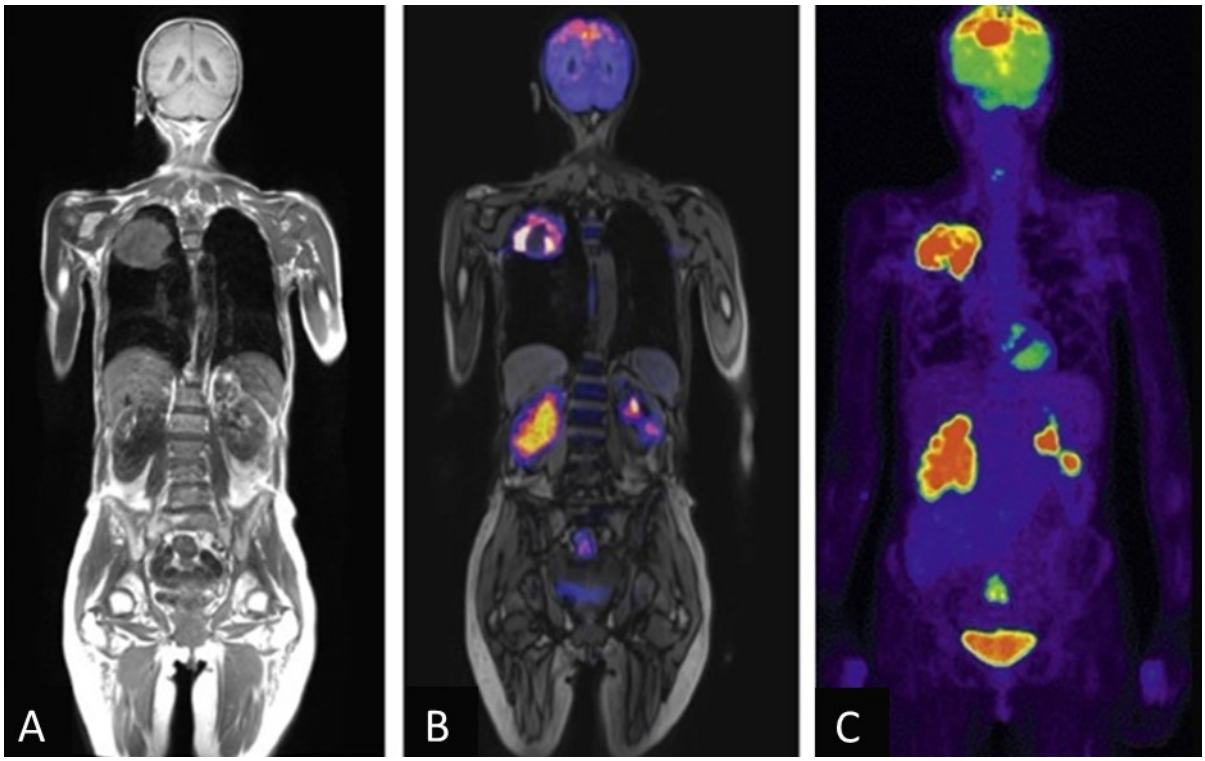

Figure 24: Whole body PET/MRI imaging in a patient with lung cancer. **A** Image from MRI with detailed morphological and tissue information. **B** MRI image superimposed with PET signal, combining the advantages of both modalities. **C** PET tracer signal obtained from tumors and metastases. Figure reproduced from ref.[84]

The hybrid PET/MRI technique offers new opportunities for contrast enhancement. This technique offers versatility in the choice of contrast agents. Based on the principle of PET, the tracer for this modality must always be present. However, contrast enhancement in the case of MRI is optional, so PET/MRI imaging can be performed without the use of an MRI contrast agent or using contrast agents for both MRI and PET. This is commonly done as PET/MRI examinations regularly utilize GBCAs for MRI contrast enhancement.[85, 81, 78] Although there are recent studies that try to avoid GBCAs use due to gadolinium toxicity, especially when PET/MRI scans are performed in pediatric patients.[86] Based on a 2016 survey for PET/MRI centers, the main areas of interest are oncology, cardiology, and neurology. For all of these areas, the most utilized tracer is [^{18}F] FDG. Other frequently used tracers with their areas of specialization are shown in

Table **3**. [87]

Table 3: The most frequently used PET tracers in PET/MRI examinations by the area of their specialization. Table reproduced from ref.[87]

Application of the tracer	Cardiology	Neurology	Oncology
1	[^{18}F] FDG	[^{18}F] FDG	[^{18}F] FDG
2	[^{13}N] NH_3	Other	Other
3	Other	[^{18}F] FET	PSMA ligands

The introduction of PET/MRI scanners into clinical practice has created the opportunity to create bimodal PET/MRI contrast agents. A probe of this type would be able to simultaneously provide contrast from both modalities and, for example, allow quantification of MRI relaxivity by PET, which is not possible from MRI signal alone. The higher temporal and spatial resolution that these probes offer could lead to new applications.[88] Dual PET/MRI contrast agents can be divided into two main groups, small molecule agents and nanoparticle-based agents.

1.4.3.1 Superparamagnetic iron oxides (SPIOs) PET/MRI bimodal contrast agents

For the purpose of this thesis, SPIO nanoparticles will be mentioned only briefly. Further information about SPIO based PET/MRI bimodal contrast agents can be found in reviews. [88, 89] Superparamagnetic iron oxides consist of iron oxide nanoparticles, which after exposure to an external magnetic field form their own magnetic field.[90] As already mentioned in Chapter 1.4.2.2, SPIOs mainly exhibit the T_2 effect, and therefore negative contrast is observed, resulting in a darkened area. These nanoparticles are coated with polymers for better dispersibility and use in PET/MRI (Figure 25A, B, C). Polymers suitable for the coating are for example, polyethylene glycol (PEG) [91,92] and dextran[93]. This coating is chemically modified in a way that radionuclides can be incorporated directly. For example, by radiometal complexation after ligand incorporation into to the SPIOs[91–93] (Figure 25) or alternatively by radiocation surface adsorption, which is done by heat induced radiolabelling.[94,95] The remarkable advantage of nanoparticles is that they can be easily prepared and modified. However, this type of contrast agent has several disadvantages that should be pointed out. One is less than ideal clearance from the bloodstream, as they are excreted through the liver into the intestine due to their size. Moreover, they also accumulate in the spleen and kidneys. The size and surface modification of SPIOs can't be precisely controlled. That means the preparation procedure is not likely to furnish similar well-defined species when repeated, in contrast to well-defined small molecular probes. Another disadvantage is the negative T_2 contrast in MRI provided by such nanoparticles.

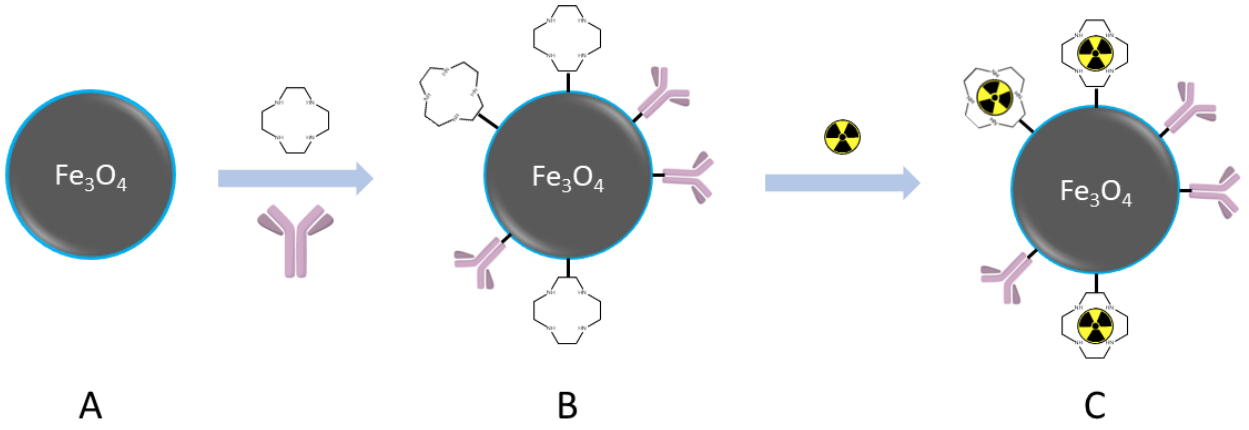

Figure 25: An illustration of how dual-modality SPIOs are prepared. **A** SPIO nanoparticles are coated (coating is shown as a blue layer). **B** These coated nanoparticles are modified with an aza-macrocylic ligand and a targeting vector such as a peptide or antibody. **C** Nanoparticles are radiolabeled with the radionuclide complexation in the last step.

1.4.3.2 Low molecular PET/MRI bimodal contrast agents

Currently, only a handful of low molecular bimodal PET/MRI CAs examples is available, mainly due to the challenges that must be met in the preparation of such bimodal contrast agents. The combination of PET and MRI modalities poses the challenge of how to prepare a contrast agent where the MRI component needs to be in 10^6–10^7 excess to the PET component. In the case of low molecular PET/MRI bimodal contrast agents, this dilemma is solved by the preparation of a mixture of a radioactive (hot) tracer with its non-radioactive (cold) equivalent in very large excess, as shown in Figure 26. The following examples illustrate the efforts that have been carried out so far.

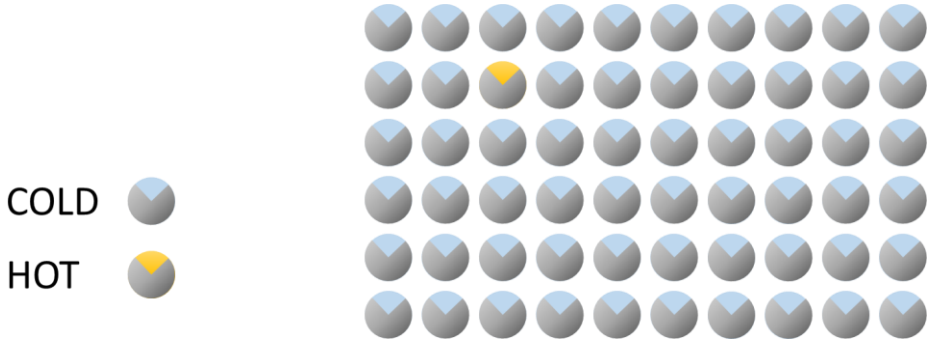

Figure 26: Simplified illustration of a mixture of the hot (radioactive) and the cold (non-radioactive) variants of PET/MRI bimodal tracer with a focus on the huge excess of the MRI part in comparison to the PET part. Chemically, they will both behave exactly the same way because they differ only in the choice of the isotope.

The earliest example was presented by Frullano *et al.* who synthesized a pH responsive PET/MRI contrast agent by decorating Gd-DOTA-4AmP with radiolabelled [^{18}F] Fluoroethylazide using CuAAC (copper(I)-catalyzed alkyne-azide cycloaddition (Figure 27). Due to the different levels of concentration needed for PET and MRI, a non-radioactive variant bearing ^{19}F instead of ^{18}F was also synthesized. Phantom measurements were performed and images from both modalities were obtained. Total radiosynthesis time, from radiolabeling of azido-fragment to click reaction, took 4 hours and radiochemical yield was 0.6% (product activity of 10.2 kBq starting from 1.80 GBq).[96] The total radiosynthesis time and radiochemical yield demonstrate how difficult it is to perform the task of preparation of the bimodal PET/MRI low molecular contrast agent.

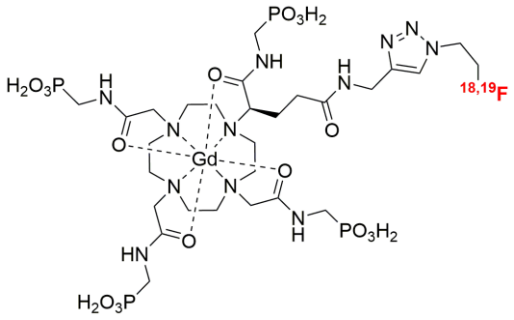

Figure 27: The structure of the bimodal PET/MRI contrast agent published in the pioneering work of Frullano *et al.* [96]

Another approach to achieving the bimodal PET/MRI contrast agent is by combining the radioactive metal as a PET signal source and paramagnetic metal for the MRI contrast. The first published case from Uppal *et al.* was realized by exchanging a fraction of gadolinium ions for ^{64}Cu in the fibrin targeted probe EP-2104R (Figure 28). A bimodal probe prepared in this way was used in the animal studies on the rats with a thrombus. These studies showed that the detection of the bimodal probe in the thrombus was possible.[97] This approach, although with positive results, has its limitations. The structural motif of DOTA chelator is not ideal for the chelation of the ^{64}Cu due to the low kinetic inertness of the Cu-DOTA chelate. This inadequacy can lead to *in vivo* ^{64}Cu leaching.[98] It happened in the case of this work, where the authors observed the deposition of ^{64}Cu in the liver, spleen, intestine, and stomach. In addition, their synthetic approach based on uncontrolled decomplexation followed by radiolabeling may lead to products with varying numbers of radiometals in varying positions, which may result in different pharmacokinetics of these products and thus different behavior.

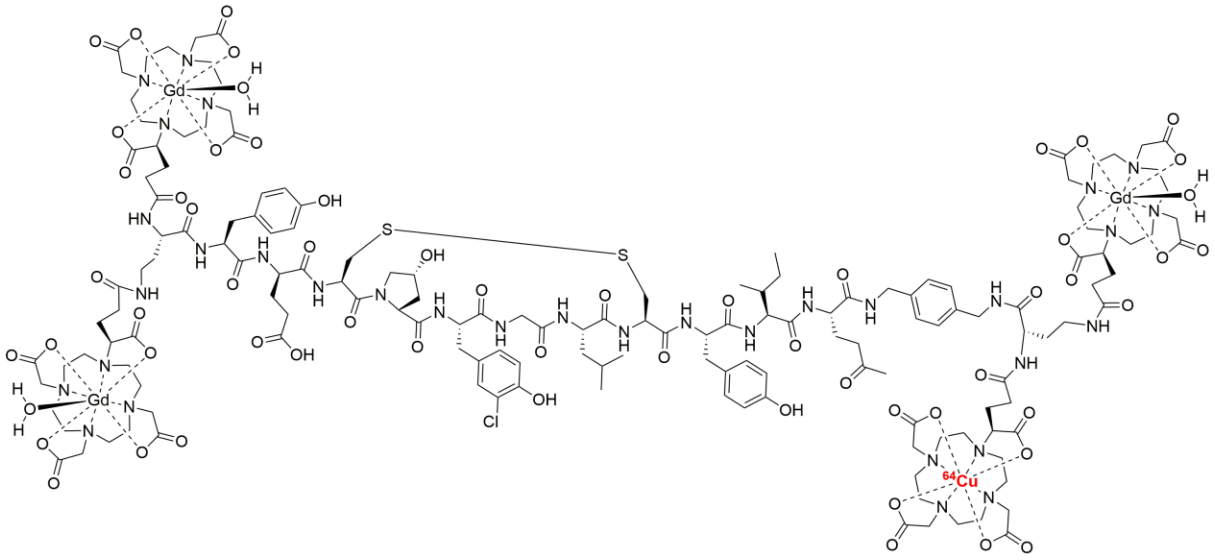

Figure 28: Fibrin targeted MRI probe EP2104R, which was used for PET/MRI probe preparation by fractional exchange of Gd for ^{64}Cu.

Notni *et al*. published work in which they prepared a bimodal PET/MRI probe using a gallium selective TRAP chelator (3,3′,3"-((1,4,7-triazonane-1,4,7-triyl)tris(methylene))tris(hydroxyphosphoryl))-tripropanoic acid) (Figure 29). The TRAP chelator served as a core for binding three DOTA units. Firstly, the chelator scaffold was fully complexed with gadolinium ions and then treated with DTPA (2-[bis({2-[bis(carboxymethyl)amino]ethyl})amino]acetic acid) to remove the gadolinium from the central TRAP chelator. The partially chelated product thus prepared was subsequently complexed with the ^{68}Ga and combined with the non-radioactive variant (containing natural non-radioactive Ga) of the probe in a 2.5×10^{7} excess of the cold probe to the hot one. This blend was later injected into mice, and the signals from MRI and PET were simultaneously acquired.[99] The combination of ^{68}Ga and Gd was utilized as well in the work of Kumar *et al.* where a dendrimeric bimodal PET/MRI probe was prepared.[100]

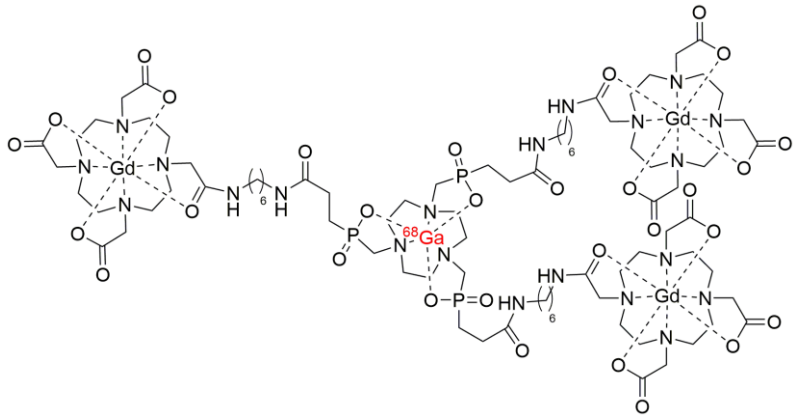

Figure 29: Structure of the bimodal PET/MRI contrast agent prepared by Notni *et al.* The contrast agent consists of a selective Ga(III) TRAP moiety with three gadolinium chelates connected by pendant arms.[99]

Due to the concerns about gadolinium deposition and toxicity, research has been intensified in the area of manganese-based MRI contrast agents. The most recent example of the low-molecular bimodal PET/MRI probe followed this trend by using a structure with multiple manganese chelation sites built around a benzene core (Figure 30). The core in this structure was functionalized by three *trans*-CDTA ligands (*trans*-1,2-Diaminocyclohexane-*N,N,N',N'*-tetraacetic acid) by the CuAAC reaction. These ligands were introduced to provide Mn(II) chelation. Three sites for manganese chelation were introduced to improve the relaxivity of the probe since the relaxivity of Mn(II) is lower than that of Gd(III). The final deprotected ligand with three *trans*-CDTA units was isotopically labelled by paramagnetic Mn spiked with positron emitting radionuclide ^{52g}Mn. By this way, a potential bimodal PET/MRI probe was prepared.[101] However, this approach has limitations in the stability of the [Mn(CDTA)] complexes. Authors describe the complex to have good serum stability, however in their previous work, [[^{52g}Mn]Mn(CDTA)]$^{2-}$ was prepared and incubated in human blood serum and subsequently analyzed. Intact radiocomplex analysis was then performed and a significant level of dechelation was found. [102]

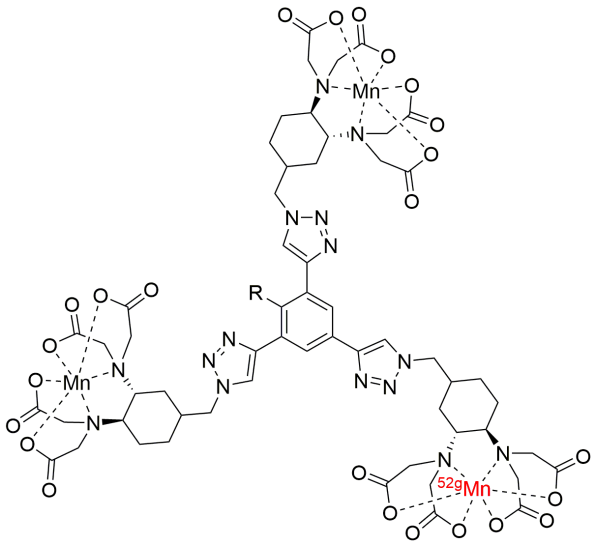

Figure 30: Structure of labelled ^{52g}Mn/55Mn PET/MRI bimodal probe synthesized by Brandt *et al.*[101]

The main features of PET/MRI bimodal contrast agents based on low molecular species or nanoparticles are summarized in Table 4.

Table 4: Comparison of low molecular and nanoparticle-based PET/MRI contrast agents. Table adapted from. [89]

	Low molecular complexes	**SPIO particles**
Visual effect in MRI	Brightening	Darkening
Preparation	Multistep synthesis	Rapid, can be chelator free
Size	< 1 nm	20–140 nm
Clearance	Kidney (if r<5.5 nm)	By liver into intestine
Targeting	Intercellular and intracellular	Intercellular, vascular system
Advantages	Precise control of contrast agent properties. Known pharmacokinetics, clearance, possible bio-responsive characteristics, more possibilities in targeting.	Easy preparation and modification. Great potential in parallel drug delivery and theragnostic functions.
Drawbacks	Limited control over the MRI/PET contrast source ratio desired for good performance of both modalities. Difficult synthetic accessibility.	Limited permeability due to the size. Low reproducibility of preparation. Non-ideal excretion from the system. Darkening effect may limit detection.

2 OBJECTIVES OF THIS WORK

The general objective of this thesis is to design, develop, and utilize novel multifunctional chelators. This thesis consists of two parts covering the following topics with specific objectives.

1) DO3A-Hyp building block:
    a) Preparation of building block based on a chelator and an amino acid, suitable for short and rigid incorporation of lanthanides into the peptide backbone.
    b) Synthesis of variously protected variants of the DO3A-Hyp building block that would allow metal chelates to be incorporated directly or via post-synthetic complexation.
    c) Exploring the properties of the DO3A-Hyp building block.
2) PET/MRI bimodal probe:
    a) Finding the right structural design for the preparation of low molecular bimodal PET/MRI probes.
    b) Design and optimization of radiolabeling conditions.
    c) Determination of physicochemical properties of designed molecules *in vitro*.
    d) Performance of *in vivo* experiments on mice.

3 RESULTS AND DISCUSSION

3.1 Building block DO3A-Hyp

3.1.1 Author contribution

The author synthesized and purified all the compounds that are the content of this part of the thesis. The author performed most of the spectroscopic measurements of the intermediates and their evaluation, however the final molecules were measured and evaluated by Dr. Martin Dračínský or Dr. Tomáš David. The crystallographic data were obtained thanks to the work of Dr. Ivana Císařová. ICP-MS analyses were performed by Mgr. Stanislava Matějková and HRMS by MS department of IOCB. ^{19}F MRI experiments were performed by Dr. Daniel Jirák and Martin Vít. Ondřej Socha performed the z-resolved ^{19}F NMR experiment. Illustrations reproduced from the article (Paramagnetic encoding of molecules)[103] are the work of Dr. Tomáš David.

3.1.2 Introduction

Pluvicto, a drug developed for the treatment of PSMA-positive prostate cancer, was approved by the FDA in 2022. This drug is used in targeted radiotherapy treatment for the delivery of the radioactive cargo into the cancer cells. Radioactive cargo refers to radionuclide that emits high energy beta particles that subsequently damage cancer cells' DNA, leading to their death. Pluvicto uses metal, beta emitter ^{177}Lu, as the radionuclide. However, the radioactive metal must be chelated with a chelator to utilize its properties. The chelating function is not the only function that the chelator must offer. As shown in Figure 31, such a chelator must possess a suitable functional group for connection to the targeting vector. In the case of Pluvicto, the connection is enabled by a simple amide bond, which is shown in green in the picture.

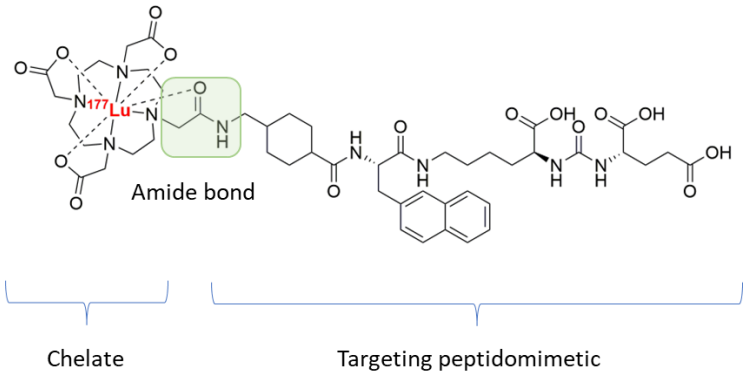

Figure 31: Pluvicto, a radiopharmaceutical used for targeted radiotherapy, consists of a radiometal chelate connected by an amide bond to a targeting peptidomimetic.

Lutathera is another FDA-approved drug used for targeted radiotherapy, which utilizes chelate connected to a targeting peptide. In the case of the mentioned radiopharmaceuticals, it is apparent that the current practice is to attach the chelate by a very simple amide bond to the N-end of the targeting molecule. This simple amide bond although sufficient for its purpose, limits the synthetic possibilities for the synthesis of more elaborate peptides bearing a metal chelate. Building blocks that would allow the chelate to be rigidly placed into any position in the peptide (for example, in the middle) would open the way to new types of compounds with unique properties. However, there is a limited number of building blocks that allow this, and those that are known suffer from disadvantages that limit their use. One example of such a building block that allows incorporation of a metal into the peptide is the DOTA-lysine (**DOTA-K**) motif shown in Figure 32, where the metal chelate is connected by a long and flexible lysine side chain to the peptide sequence. This attachment via lysine side chain, however, can lead to reduced rigidity and thus to the presence of several structural isomers, which is undesirable. Protected variants of DOTA-phenylalanine (**DOTA-F**, Figure 32) and **DOTA-K** were, for example, employed in the preparation of Gal-80 binding peptides by solid phase peptide synthesis.[104] Another amino acid/chelator is **DOTAla** (Figure 32), which bears an alanine arm that provides a rigid and close attachment of gadolinium to the peptide backbone. This chelator has been used in the synthesis of linear and cyclic peptide contrast agents, but it should be noted that the alanine pendant arm is prone to elimination, limiting the usability of this building block.[105] A successful example of the use of whole metal chelates as amino acids in the peptide synthesis is the work that dealt with the synthesis of short peptide tags based on **DOTA-K** terbium and lutetium chelates for mass spectroscopy.[106] The mentioned building blocks allow the incorporation of metals into the peptide chain with certain compromises, and in almost all cases, their use is limited to the incorporation of only one type of metal into the chain.

In an alternative approach to peptide synthesis, different types of metals have been successfully combined into a single molecule. Usually, several different reactions are used to assemble the individual metal-bearing blocks. For this reason, the combinatorial possibilities of these systems are limited, as ideally, one type of reaction should be sufficient to integrate the building blocks with the selected metal. One of the works reported the synthesis of a branched tetrapeptide ligand, which was sequentially metaled to furnish heterometallic lanthanide complexes that exhibited ratiometric luminescence.[107] Other examples include triheterometallic[108] and tetraheterometallic[109] lanthanide-containing architectures built from whole chelates. The construction of luminescent nanocoded compounds is an example of work, where functionalized lanthanide cryptates (**Cryptand-K**, Figure 32) were developed and used for the direct incorporation of metals using solid-phase peptide synthesis. [110]

The presented cases show that there is currently no synthetic tool that allows the incorporation of multiple types of metals into any position in the peptide chain without accepting compromises such as reduced rigidity or decreased chemical stability. A building block that would simultaneously provide increased rigidity and the ability to chain several metals into one spatially well-defined molecule is missing.

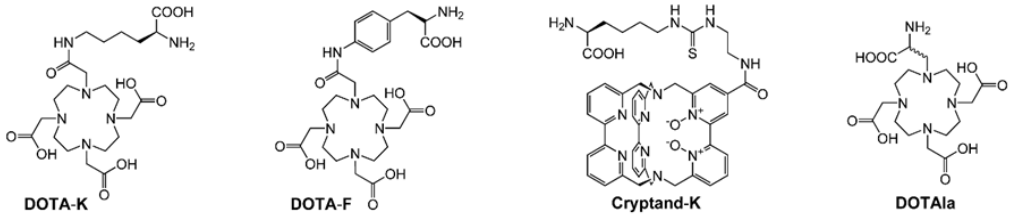

Figure 32: Chemical structures of chelators used for incorporation of the lanthanides into the peptides: **DOTA-K**, **DOTA-F**, **Cryptand-K**, and **DOTAla**. Figure reproduced from ref.[103]

3.1.3 Definition of a problem

The main aim of this part of the thesis is to design and synthesize the building blocks that would fulfill several requirements: a) The building block must provide rigid and close connection of the metal to the peptide backbone. b) It must allow the incorporation of multiple types of metals into a single molecule. c) It must limit the number of the possible structural isomers. d) It must be sufficiently kinetically inert. Currently used building blocks (**DOTA-K**, **DOTA-F**, **Cryptand-K,** and **DOTAla**) fulfil these requirements only partially. **DOTA-K**, **DOTA-F,** and **Cryptand-K** use long and flexible linker for connection to the peptide backbone. This results in low rigidity and leads to the existence of multiple structural conformations. In the case of **DOTAla**, the requirement for a short and rigid connection to the peptide backbone is met, but the pendant arm bearing the amino acid moiety is prone to elimination from the building block. Another disadvantage is that **DOTAla** cannot be incorporated into a peptide that already carries metal. Therefore, it is not possible to place multiple different metals in a single molecule in a controlled manner with this building block.

3.1.4 Molecular design

The DO3A-Hyp shown in Figure 33 was designed to meet the discussed requirements. This structure consists of two main parts. The first part serves as a chelator and the second part serves as an amino acid. For integration of the metal, the DO3A (1,4,7,10-tetraazacyclododecane-1,4,7-triacetic acid) motif was selected as a chelator part. As was discussed in the introductory Chapter 1.3, macrocyclic chelates are superior to linear, and acetates are pendant arms that form the strongest chelates with lanthanides. In order to give the desired building block more functions, a pendant arm fulfilling the function of an amino acid was added to the building block. It was decided that the introduction of proline was advantageous due to

its cyclic nature and the resulting rigidity. However, if only a proline pendant arm would be attached, the kinetic inertness requirement would not be met because this pendant arm could not coordinate to the metal center. For that reason, it was decided to include the hydroxyproline moiety. The hydroxyproline hydroxyl group could coordinate with the metal center of the chelate, thus helping to stabilize it. Also, *L*-hydroxyproline is a readily available natural amino acid possessing a chiral center. Incorporation of such a chiral center would introduce chirality to the final building block. This chirality would decrease the number of possible structural isomers. The hydroxyproline pendant arm would also introduce the desired rigidity to the building block. The hydroxyproline pendant arm allows several combinations of chiral centers, i.e., diastereomers or enantiomers. These we collectively refer to as the *DO3A-Hyp* family.

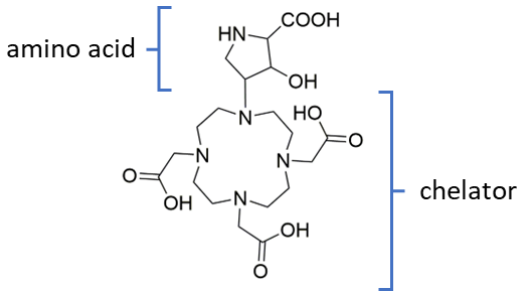

Figure 33: The structural design of the DO3A-Hyp building block presented in this work. This building block consists of an amino acid part and a chelator part. This was the initially planned structure, but the actual prepared molecule differs unexpectedly from this one for reasons that will be explained in Chapter 3.1.5.2.

A retrosynthetic analysis was done to plan the steps leading to the DO3A-Hyp building block (Figure 34A). It was planned to keep the acetate pendant arms of the macrocycle protected with protecting group (PG) until the last step. The same was planned for the amine and carboxylic acid moiety of the Hyp pendant arm (Figure 34B). Cleavage of the three C-N bonds leads to the formation of the key hydroxyamino precursor (Figure 34C). And finally, the cleavage of the C-N bond between the Hyp moiety and the macrocycle leads to key precursors, one of which is a commercially available cyclen and epoxide that had to be synthesized (Figure 34D).

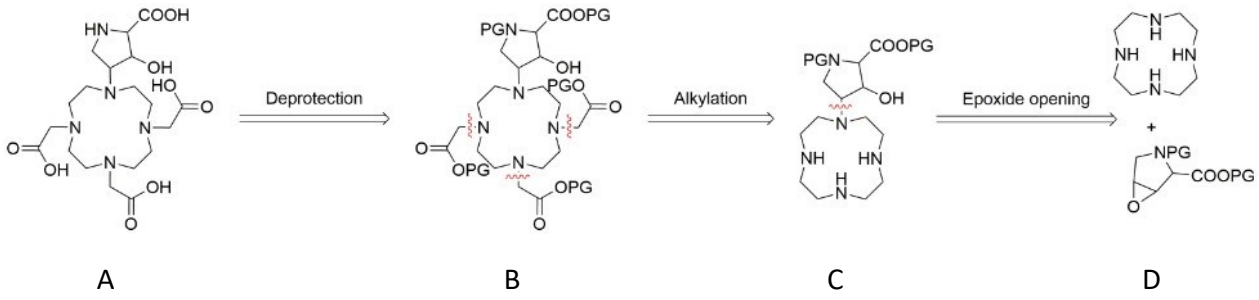

Figure 34: Retrosynthetic analysis of a building block from the DO3A-Hyp family, not yet considering stereochemistry. This was the initially planned structure, but the actual prepared molecule differs unexpectedly from this one for reasons that will be explained in Chapter 3.1.5.2. PG = protective group.

3.1.5 Synthesis

3.1.5.1 Synthesis of epoxide

Chirally pure, cheap and readily available *L*-hydroxyproline was selected as starting material for synthesis of desired epoxides (Figure 35). Firstly, the secondary amine of proline was protected by benzyl carbamate (Cbz) to furnish **Cbz-4-hydroxyroline.** The synthetic sequence continued with the protection of carboxylic acid by benzyl ester formation. The amine and carboxyl functional groups of proline had to be protected so that they would not participate in the next steps of the synthesis. e.g., the introduction of pendant arms to the aza-macrocycle by alkylation. Protection of amine with Cbz and the formation of benzyl ester from the carboxylic acid is advantageous for several reasons. Both protecting groups can be deprotected by catalytic hydrogenation in one step, and this type of protection is orthogonal to the acid-labile *t*Bu protection of acetates. The next step was the conversion of hydroxyl to a better leaving group. For this purpose, Mitsunobu conditions were employed to obtain iodide **2**. To obtain the olefin **4** , iodide **2** was transformed to selenide **3** and oxidative conditions were implemented to furnish exclusively one regioisomer of olefine **4**.[111] The one-pot, three-step synthetic sequence from **1** to **4** was optimized to deliver an overall yield of 84%. Oxidation with *m*-CPBA at elevated temperature provided final epoxides with yields of 53% for *trans* **5** (*1R*,*2S*,*5S*) and 21% for *cis* **5*** (*1S*,*2S*,*5R*) epoxide. These epoxides were easily separated by column chromatography thanks to their diastereomeric nature. The presented work deals only with epoxide **5** but it should be noted that epoxide **5*** can be used for the synthesis of other building block isomers from the DO3A-Hyp family.

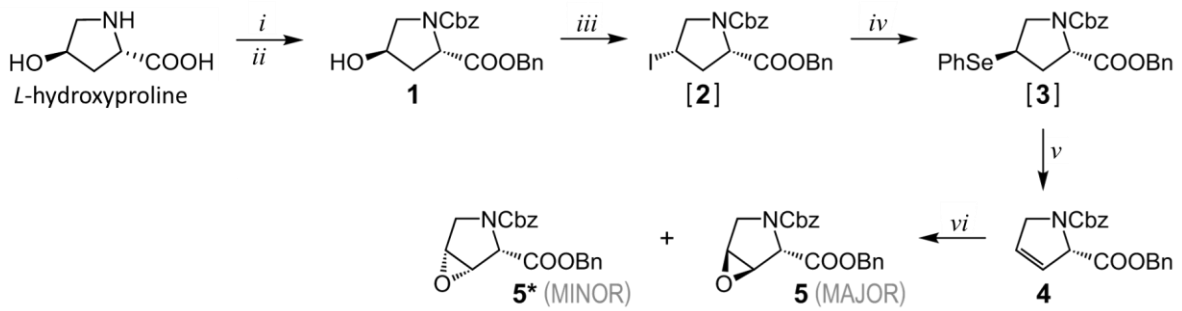

Figure 35: Synthesis of epoxide intermediates **5** and **5***. Conditions: (i) Cbz-Cl, $NaHCO_3$, H_2O/toluene, RT; (ii) BnBr, TEA, THF; (iii) PPh_3, THF, 0 °C followed by DIAD, MeI, 0 °C → RT; (iv) $(PhSe)_2$, EtOH, $NaBH_4$, 0 °C → RT; (vv) H_2O_2, THF, 0 °C → RT; (vi) mCPBA, $CHCl_3$, 85 °C. Intermediates in brackets were not isolated. Figure reproduced from ref.[103]

3.1.5.2 Epoxide opening

The epoxide opening was a crucial step for the synthesis of the final DO3A-Hyp building block since the epoxide brings the features of amino acid and rigidity. More importantly, this reaction allows the two parts of the molecule to be joined together (the macrocycle and the amino acid). A number of experiments were performed to find the right conditions for the reaction in order to proceed. Initially, epoxide **5** was attempted to be opened with cyclen in the presence of various Lewis acids: $Sc(OTf)_3$, $Zn(OTf)_2$, $Cu(OTf)_2$ and $Ca(OTf)_2$. The plan was to use the Lewis acid to polarize the C-O bond of the epoxide and thus facilitate the opening. However, none of the conditions tested provided the desired product. The next conditions that were tested were those utilizing microwave irradiation. Cyclen and **5** were mixed in dry ethanol and reacted using microwave irradiation. Finally, the desired product **6** was observed, but a side product resulting from benzyl carboxylate transesterification by ethyl was present as well. To suppress the formation of transesterification products, reactions using different solvents were tested. *Tert*-butanol proved to be the best choice as no transesterification products were observed when using this solvent. The synthesis utilizing microwave irradiation is not suitable for larger-scale synthesis. Therefore, the reaction conditions were optimized for conventional synthesis up to 12 grams of **5**. The yield was typically around 50% due to the side reaction where the **5** degrades to a byproduct, as is shown in Figure 36.

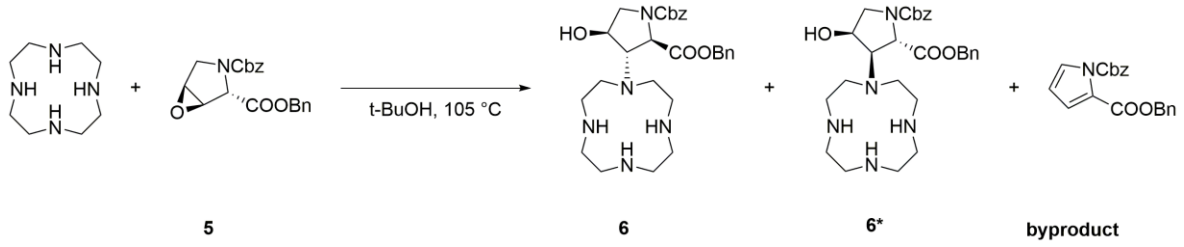

Figure 36: Opening of the epoxide **5** in tert-butanol at 105°C. The reaction provides intermediate **6** and a byproduct of elimination.

By opening the epoxide **5** with the free base of cyclen, the intermediates **6** and **6*** were obtained (Figure 36). Here, the actual synthesis started to differ from the originally planned retrosynthesis shown in the Figure 34. It should be noted that racemization occurred during this step, which gave the isomers **6** (*2R*,*3S*,*4S*) and **6*** (*2S*,*3R*,*4S*) in the 9:1 ratio in favor of the sterically less hindered **6** (*2R*,*3S*,*4S*). The proposed mechanism of the epoxide opening step is shown in Figure 37. The mechanism starts with deprotonation of the epoxide **5** at the alpha position of benzyl carboxylate. In the next step, the carbonyl group is restored, leading to the opening of epoxide and the formation of a double bond. This double bond is then attacked by cyclen, and a negative charge is stabilized on the oxygen leading to *TS* (transition state) and *TS**. The final step is the restoration of carbonyl group and protonation in alpha position. Of all the probable isomers of the products, only two, **6** and **6*** are sterically favored. However, this mechanism could not be proposed before the elucidation of crystal structures discussed in the following Chapter, 3.1.5.3, which revealed the true 3D structure of the molecules.

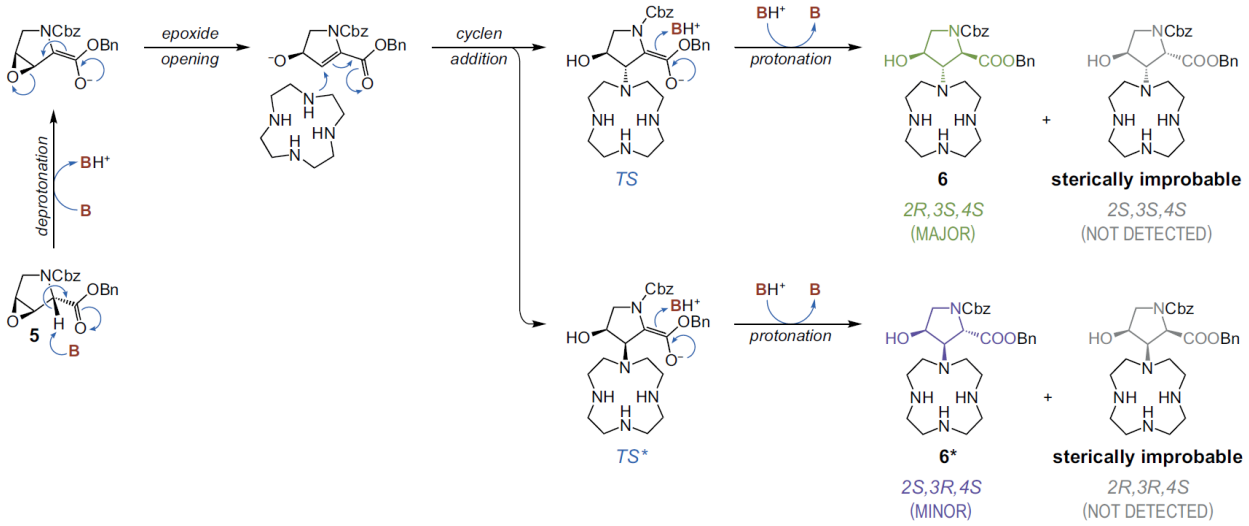

Figure 37: Proposed mechanism of epoxide opening. The crucial steps include deprotonation of epoxide in the benzyl carboxylate alpha position and Michael addition of cyclen to the resulting α, β unsaturated Michael acceptor. *2S*, *3S*, *4S* and *2R*, *3R*, *4S* isomers are not observed, probably due to steric hindrance between substituents on the proline ring. Figure reproduced from ref.[103]

3.1.5.3 Synthesis of DO3A-Hyp building blocks

After the successful epoxide opening step that furnished intermediates **6** and **6***, it was possible to proceed to the synthesis of the series of DO3A-Hyp building blocks. It was crucial to incorporate a variety of protective groups into specific positions in this series. In all cases, the carboxylate pendant arms of the macrocycle had to be protected from interfering during the amide coupling. For this protection, *tert*-butyl esters were selected as protective groups labile to TFA, while methyl esters were selected for basic deprotection. This complementarity of protective groups was necessary for the controlled synthesis of more

complex molecules. These molecules should consist of two DO3A-hyp building blocks, and the different protection strategies should enable the combination of different metals in specific positions within such molecules. The intermediates **6** and **6*** were modified in the desired manner to furnish the final chelators $\mathbf{L^1}$ and $\mathbf{L^2}$, $\mathbf{\textit{t}Bu_3L^1}$, $\mathbf{\textit{t}Bu_3L^2}$, **Fmoc-L^1**, and **Ac-Fmoc-Me$_3$L^1** (Figure 38). Synthesis of $\mathbf{L^1}$, $\mathbf{L^2}$, $\mathbf{\textit{t}Bu_3L^1}$, $\mathbf{\textit{t}Bu_3L^2}$, and **Fmoc-L^1** building block started with alkylation of **6** or **6*** with *tert*-butyl bromoacetate. The protection of acetate by the formation of *tert*-butyl esters was chosen because of the non-reactivity of this protecting group in subsequent synthetic steps, such as peptide bond formation. Catalytic hydrogenation using H_2, and Pd/C was used to deprotect the carboxyl and amino groups of the Hyp pendant arm in one step to yield the building blocks $\mathbf{\textit{t}Bu_3L^1}$ and $\mathbf{\textit{t}Bu_3L^2}$. These building blocks were used as a primary scaffold for the synthesis of tripeptides **TP1** and **TP2**, discussed in the following sections. Further deprotection of $\mathbf{\textit{t}Bu_3L^1}$ and $\mathbf{\textit{t}Bu_3L^2}$ with TFA yielded the building blocks $\mathbf{L^1}$ and $\mathbf{L^2}$. These fully deprotected building blocks can be used for the preparation of [M($\mathbf{L^1}$)] and [M($\mathbf{L^2}$)] chelates. In these chelates, the coordination of acetate pendant arms of the macrocycle to metal ions serves as a protective group. This results in their non-reactivity during the peptide coupling, so only the carboxylate from the Hyp pendant arm is activated during the synthetic step. Building block $\mathbf{\textit{t}Bu_3L^1}$ was also used for the synthesis of Fmoc protected building block **Fmoc-L^1**. To furnish this building block, $\mathbf{\textit{t}Bu_3L^1}$ was alkylated with Fmoc-Cl and subsequently deprotected with TFA. **Fmoc-L^1** was designed as a building block suitable for the preparation of [M(**Fmoc-L^1**)] chelates. The Fmoc protecting group is a well-established protecting group used regularly in peptide synthesis. The [M($\mathbf{L^1}$)], [M($\mathbf{L^2}$), and [M(**Fmoc-L^1**)] building blocks were synthesized to allow the incorporation of whole metal chelates into the peptide chain. **Ac-Fmoc-Me$_3$L^1** was employed when it was advantageous to incorporate the metal in later stages of synthesis. The synthesis of **Ac-Fmoc-Me$_3$L^1** began by alkylation of precursor **6** with methyl bromoacetate, which introduced methyl ester protected acetates into the building block. Methyl esters of carboxylic acids are labile to basic conditions and can thus be orthogonally deprotected in the presence of acid-labile protective groups of $\mathbf{\textit{t}Bu_3L^1}$, $\mathbf{\textit{t}Bu_3L^2}$ or they can survive the acidic conditions used for the deprotection of *tert*-butyl esters. Protection of hydroxyl on the proline ring was crucial because elimination of this moiety and the appearance of olefin was observed during peptide synthesis when the DO3A-Hyp building block was preactivated. The last two steps of **Ac-Fmoc-Me$_3$L^1** synthesis were catalytic hydrogenation and the introduction of the Fmoc protective group. The acetyl protection of the hydroxyl of **Ac-Fmoc-Me$_3$L^1** could be easily removed simultaneously with methyl ester and Fmoc protective groups in basic conditions.

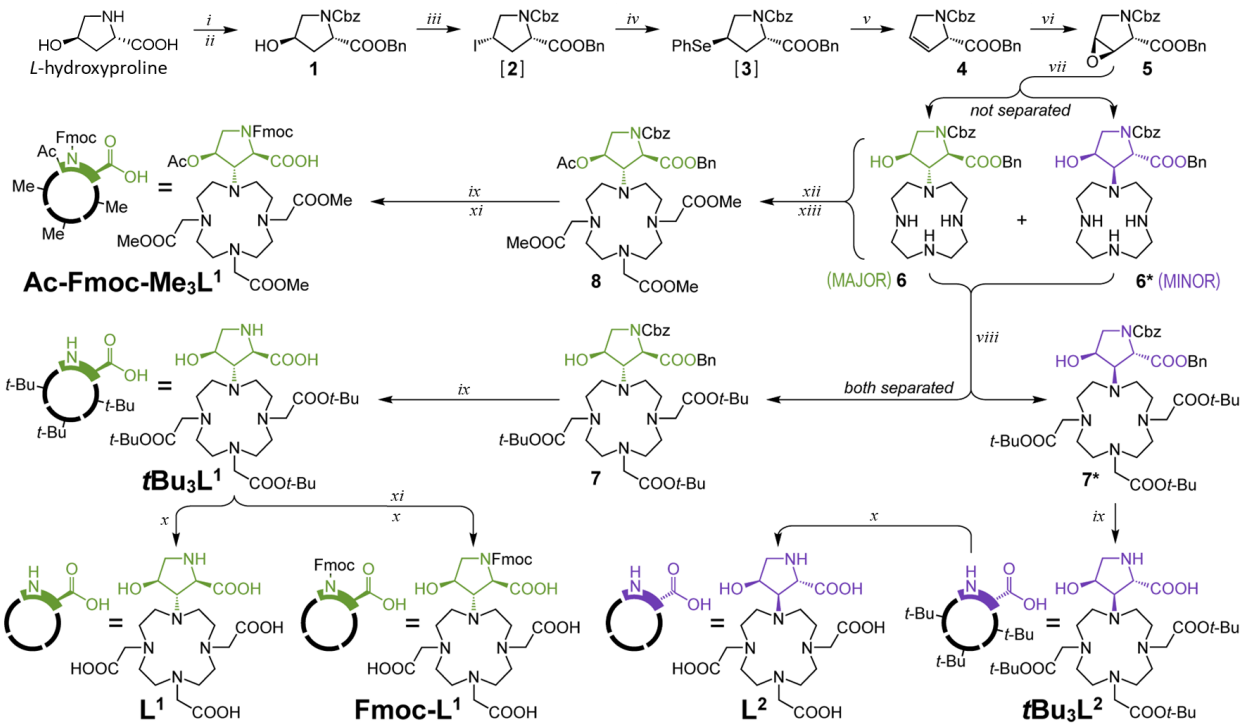

Figure 38: Synthetic scheme for building blocks $\mathbf{L^1}$, $\mathbf{L^2}$ and their protected variants. Conditions: (i) Cbz-Cl, $NaHCO_3$, H_2O/toluene, RT; (ii) BnBr, TEA, THF; (iii) PPh_3, THF, 0 °C followed by DIAD, MeI, 0 °C → RT; (iv) $(PhSe)_2$, EtOH, $NaBH_4$, 0 °C → RT; (vv) H_2O_2, THF, 0 °C → RT; (vi) mCPBA, $CHCl_3$, 85 °C; (vii) cyclen, t-BuOH, 105 °C; (viii) *t*-BuO_2CCH_2Br, K_2CO_3, MeCN; (ix) H_2, Pd@C, AcOH, MeOH; (x) TFA; (xi) FmocCl, aq. borate/NaOH buffer (pH 9.0), MeCN; (xii) MeO_2CCH_2Br, K_2CO_3, MeCN; (xiii) Ac_2O, TEA, DMAP, MeCN. Intermediates in brackets were not isolated. Figure reproduced from ref.[103]

The configuration of $\mathbf{L^1}$ and $\mathbf{L^2}$ stereocenters was examined with NMR at the beginning. However, conclusive results were not obtained from these measurements. Since X-ray crystallography is a robust and reliable method for the elucidation of molecular structures, it was decided to use it for the elucidation of configurations on $\mathbf{L^1}$ and $\mathbf{L^2}$ stereocenters. For this reason, crystals of [Dy($\mathbf{L^1}$)] and [Dy($\mathbf{L^2}$)] were prepared and subjected to X-ray crystallography. X-ray crystallography surprisingly revealed that the structures of [Dy($\mathbf{L^1}$)] and [Dy($\mathbf{L^2}$)] were different from what was originally expected from the retrosynthetic design in Figure 34. This discovery was followed by a subsequent search for a mechanism (discussed above in Figure 37) that would explain the obtained structures. Elucidated structures of [Dy($\mathbf{L^1}$)] and [Dy($\mathbf{L^2}$)] are shown in Figure 39. In both cases, the Hyp moiety is coordinated to dysprosium by carboxylate, and the hydroxyl of this moiety is uncoordinated.

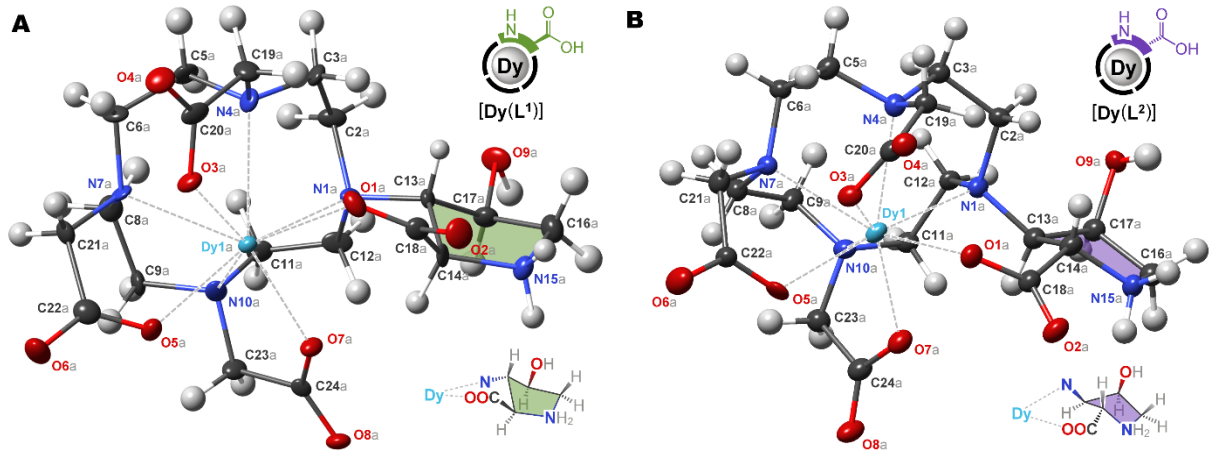

Figure 39: Crystal structures of [Dy(**L**^{1})] and [Dy(**L**^{2})]. In both structures, the proline ring is coordinated to metal center by carboxylate. **A** Stereo configuration on [Dy(**L**^{1})] proline ring is 2*R*,3*S*,4*S*. **B** Stereo configuration on [Dy(**L**^{2})] proline ring is 2*S*,3*R*,4*S*. [Dy(**L**^{1})] chelate occupies ΔλλλλSA square antiprismatic (SA) conformation while [Dy(**L**^{2})] occupies ΔδδδδTSA twisted square antiprismatic (TSA) conformation. Figure reproduced from ref.[103]

3.1.5.4 Tripeptides TP1, TP2

The building blocks presented in this work allow the preparation of compounds in which multiple different lanthanide ions can be placed at specific positions in the peptide chain in a controlled manner. Thanks to the amino acid nature of these building blocks, a modular approach to the synthesis can be implemented. It is possible to synthesize bimetallic tripeptides this way. To demonstrate the synthetic capabilities of the presented building blocks, **TP1** and **TP2** tripeptides were synthesized. The building blocks from the DO3A-Hyp family provide a short and rigid connection of metals **M**^{1} and **M**^{2} in **M**^{1}**M**^{2}**-TP1** and **M**^{1}**M**^{2}**-TP2** compounds. The main synthetic pathways to obtain these compounds are shown in Figure 40. Synthetic route **A** uses the ***t*Bu$_3$L**^{1} as a basic building block to synthesize intermediate **I**. For this reaction, the amino acid Fmoc-Phe{*p*-CF3}-OH was pre-activated with the coupling reagent PyAOP ((7-azabenzotriazol-1-yloxy)tripyrrolidinophosphonium hexafluorophosphate)) in DMSO and in the presence of DIPEA. The PyAOP coupling reagent was selected as the best performing from the screening of other coupling reagents, HATU, COMU, HCTU, DMMTM, EEDQ, and TCFH. Screening of coupling reagents was necessary because the DO3A-Hyp building blocks are proline-based and bulky, and therefore reactions do not proceed as readily as with commonly used building blocks. The PyAOP coupling reagent was successfully employed in all peptide couplings within this work. The intermediate **I** was provided after Fmoc was deprotected. At this stage, it was necessary to add a second building block that would allow incorporation of the second metal ion. For controlled synthesis of such bimetallic complexes, it was necessary to introduce building blocks that would be orthogonally protected to the ***t*Bu$_3$L**^{1}. For this purpose, the base-labile protected **Ac-Fmoc-Me$_3$L**^{1} building block was introduced. The reaction of intermediate **I** with the building

block **Ac-Fmoc-Me$_3$L^1**, followed by TFA deprotection, produced intermediate **II**. In this intermediate, one position was available for complexation of metal ion **M^2**. The metal ion was complexed and, following basic deprotection, furnished the mono-metalated intermediate **M^2-TP1**. This intermediate already has one position filled with metal ion **M^2**, but the other position is accessible for controlled incorporation of metal **M^1**. The route **A** was successfully used to synthesize a tripeptide consisting of two rigidly connected metals to the central amino acid **Phe{*p*-CF$_3$}**. Fully deprotected **TP1** with two vacant positions for complexation was synthesized by following the synthetic path described in route **B**. This route started similarly to route **A,** but instead of the first complexation step, the intermediate **II** was fully deprotected. Route **C,** leading to **M^{1}M^2-TP2** compounds, follows the same synthetic steps as route **A** with the difference that ***t*Bu$_3$L^2** is employed as a starting building block instead of ***t*Bu$_3$L^1**. This building block is streochemically distinct from ***t*Bu$_3$L^1** and was used to investigate how this structural change would affect properties in **M^{1}M^2-TP2** in comparison to **M^{1}M^2-TP1**.

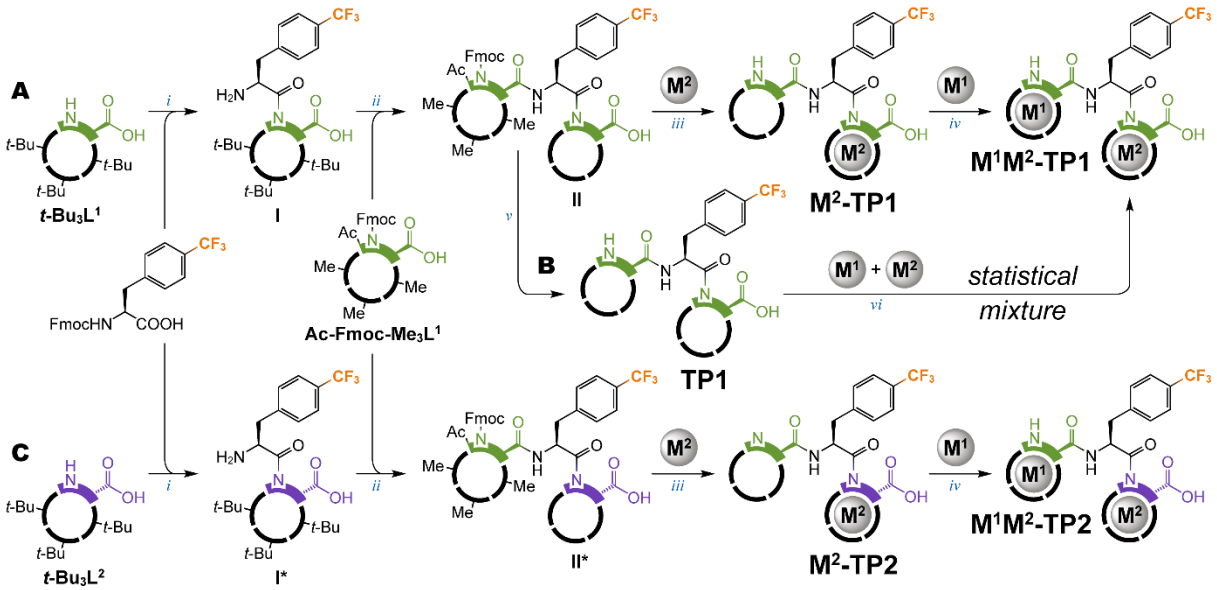

Figure 40: Main synthetic ways to **M^{1}M^2-TP1** and **M^{1}M^2-TP2** compounds. **A** Primary synthetic route to **M^{1}M^2-TP1** utilizing subsequential complexation steps. **B** The synthetic route for **TP1** used in the preparation of statistical mixtures. **C** Primary synthetic route to **M^{1}M^2-TP2** utilizing subsequential complexation steps. Conditions: (i) Fmoc-Phe{p-CF$_3$}-OH, PyAOP, DIPEA, DMSO followed by DBU, DMF; (ii) Ac-Fmoc-Me$_3$L^1, PyAOP, DIPEA, DMSO followed by TFA; (iii) M^{2}Cl$_3$, aq. MOPS/NaOH (pH 7.0) followed by LiOH, H$_2$O, MeOH; (iv) M^{1}Cl$_3$, aq. MOPS/NaOH (pH 7.0); (v) LiOH, H$_2$O, MeOH; (vi) M^{1}Cl$_3$, M^{2}Cl$_3$, aq. MOPS/NaOH (pH 7.0). Figure reproduced from ref.[103]

Building blocks [**M(L^1)**] and [**M(Fmoc-L^1)**] were designed and synthesized for direct incorporation of whole metal chelates into the peptide chain. To probe and demonstrate the capability of this approach, synthesis of **HoDy-TP1** and **DyHo-TP1** was performed (Figure 41). Dysprosium or holmium complexes of [M(**L^1**)] and [M(**Fmoc-L^1**)] were prepared and used to build the desired molecules with **Phe{p-CF$_3$}-**

OBn as a central amino acid. Firstly, the reaction between [M(**Fmoc-L^1**)] and **Phe{p-CF$_3$}-OBn** was done at an elevated temperature. This reaction provided intermediate **M^1-IV,** which, after deprotection of carboxylic acid by catalytic hydrogenation, furnished intermediate **M^1-V**. The intermediate was then reacted with another metal chelate building block [**M^2(L^1)**]. This reaction provided the Fmoc protected intermediate **Fmoc-M^{1}M^2-TP1**. After deprotection, the final **M^{1}M^2-TP1** compounds were obtained. To our best knowledge, this is the only example where whole chelates were used as an amino acid for the construction of such a rigid bimetallic system. Nevertheless, it should be noted that this synthetic route provided the desired products at a lower yield than the synthetic route **A** (Figure 40).

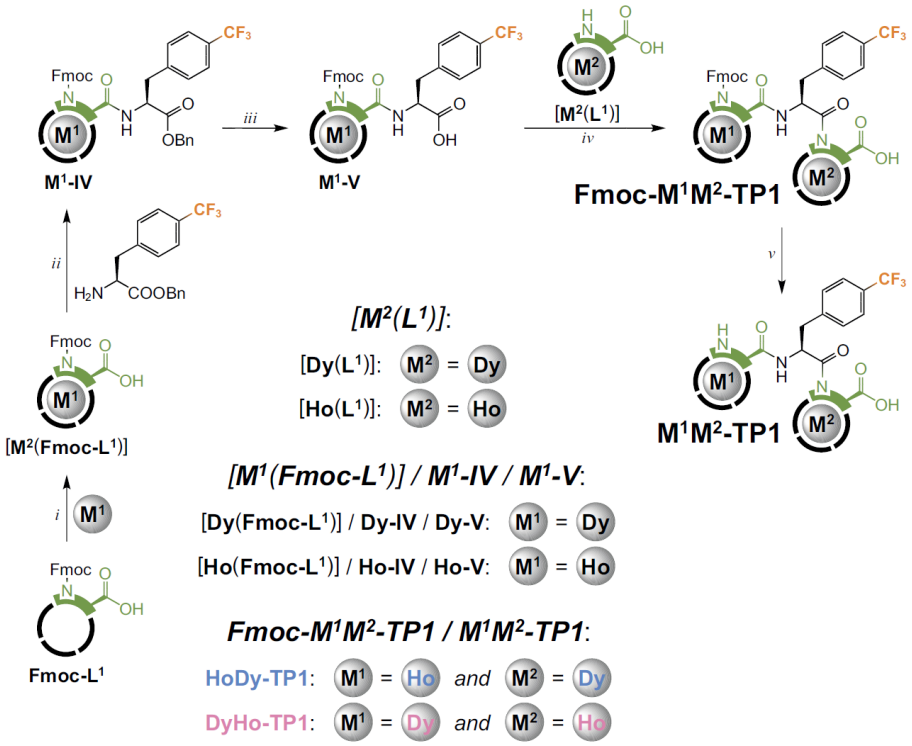

Figure 41: Synthesis of **DyHo-TP1** and **HoDy-TP1** using whole metal chelates. Conditions: (i) M^1Cl_3, aq. MOPS/NaOH (pH 7.0); (ii) H-Phe{p-CF_3}-OBn, PyAOP, DIPEA, DMSO, 80 °C; (iii) H_2, Pd@C, MeOH; (iv) [$M^2(L^1)$], PyAOP, DIPEA, DMSO; (v) DBU, DMF. Figure reproduced from ref.[103]

The explanation of the surprising reactivity of the metal chelates [**M(Fmoc-L^1)**] and [**M(L^1)**] during amide bond formation could be in the change of their coordination environment. The expected mechanism is described by the example [M(**L^1**)] (Figure 42). It is presumed that the chelate [M(**L^1**)] adopts in solution structure where the Hyp pendant arm is coordinated to the metal ion by carboxylate (Figure 42A). The coordination environment of the metal chelate has to change in order to let the amide coupling reaction proceed (Figure 42B). The amide bond formation is allowed because of the transient coordination of the

hydroxyl, which opens the way to the carboxylate modification. (Figure 42C). After the reaction, the coordination environment returns to a more thermodynamically stable state. (Figure 42D).

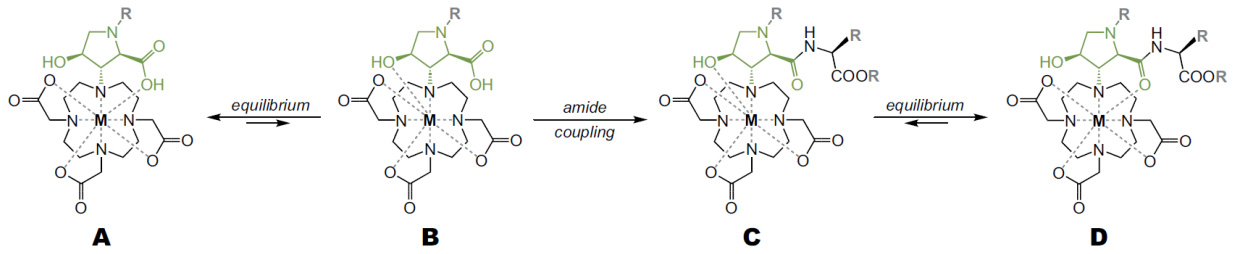

Figure 42: The proposed mechanism of [M(**L**[1])] coordination state change that allows peptide coupling. **A** In solution, the Hyp pendant arm is presumably coordinated by a carboxylic moiety. **B** In order for the peptide coupling to occur, the equilibrium must shift to favor coordination via the hydroxyl moiety. **C** Amide coupling is allowed in this state of coordination. **D** The equilibrium returns to coordination via the carbonyl moiety. Figure reproduced from ref.[103]

3.1.6 Control compounds

M[1]M[2]-TP3 tripeptides composed of two **DOTA-K** terminal units and Phe{p-CF_3} central amino acid were synthesized to verify the importance of rigidity in the design of the presented DO3A-Hyp building blocks. **DOTA-K** was selected as a suitable building block for this purpose as it contains a long flexible chain. This building block has very similar properties (kinetic inertness, possibility of connecting multiple units in the peptide sequence). **DOTA-K** is also a good example of the state of the art, as it has been previously used in multiple examples for the incorporation of lanthanides into peptides. The synthetic sequence leading to **M[1]M[2]-TP3** tripeptides is shown in Figure 43.

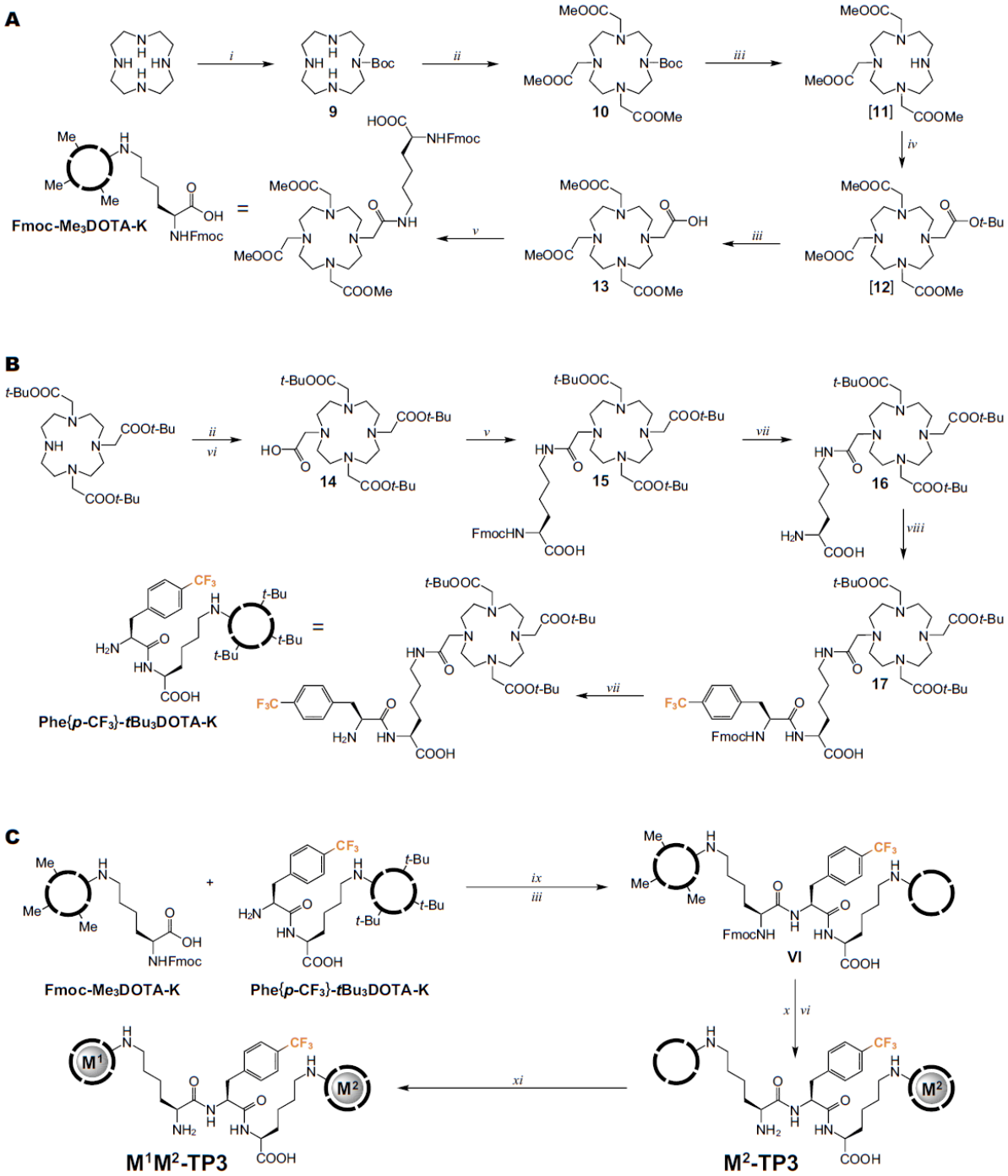

Figure 43: Synthesis of control tripeptides **M^{1}M^2-TP3** based on **DOTA-K**. **A** Synthesis of building block Fmoc-Me$_3$DOTA-K. **B** Synthesis of building block Phe{p-CF$_3$}-tBu$_3$DOTA-K. **C** Synthesis of M^{1}M^2-TP3 tripeptides. Conditions: (i) *tert*-butyl (4-nitrophenyl) carbonate, DCM; (ii) MeO_2CCH_2Br, K_2CO_3, MeCN; (iii) TFA; (iv) *t*-BuO_2CCH_2Br, K_2CO_3, MeCN; (v) H-Lys(Fmoc)-OH, PyAOP, DIPEA, DMSO; (vi) LiOH, MeOH, H_2O; (vii) DBU, DMF; (viii) Fmoc-Phe{p-CF$_3$}-OH, PyAOP, DIPEA, DMSO; (ix) PyAOP, DIPEA, DMSO; (x) M^2Cl_3, aq. MOPS/NaOH (pH 7.0); (xi) M^1Cl_3, aq. MOPS/NaOH (pH 7.0). Intermediates in brackets were not isolated. Figure reproduced from ref.[103]

3.1.7 Use case – Paramagnetically encoded molecules

A use case was investigated to demonstrate the unique properties of DO3A-Hyp building blocks. These building blocks allow the synthesis of complex molecules with closely and rigidly embedded metal chelates in the peptide backbone. A building block that would allow such precise control of the position of multiple metals in a single molecule has not yet been synthesized. And as it turns out, this feature can be advantageously used to create molecules, where the order of metals represents a form of information. Information that can be read spectroscopically. This attribute opens the possibility of using these molecules as molecular barcodes or probes for magnetic resonance imaging. Presented here are **TP1**, **TP2** systems based on $\mathbf{L^1}$ and $\mathbf{L^2}$ building blocks that allow the combination of two paramagnetic metals, $\mathbf{M^1}$ and $\mathbf{M^2}$. Because these metals are paramagnetic, they exhibit magnetic susceptibility tensors that can be combined due to the precise incorporation of the metals enabled by controlled synthesis. These magnetic susceptibility tensors can then be used to manipulate the ^{19}F NMR shift of the CF_3 reporter group, which is located on the middle amino acid so that it can sense the magnetic tensors from both metals (Figure 40). This approach can therefore yield a unique signal for each metal combination observable in ^{19}F NMR. Because of the mentioned properties, these molecules can be used to store information that can only be read by NMR. We have termed this information storage paramagnetic encoding. To investigate this idea of paramagnetic encoding, the previously synthesized tripeptides **TP1** and **TP2** were used. The main synthetic routes to obtain these paramagnetically encoded molecules were discussed in Section 3.1.5.4 Tripeptides TP1, TP2.

The possibilities of paramagnetic encoding of molecules were initially investigated on the $\mathbf{M^1M^2}$**-TP1** compound library. The **TP1** tripeptide was used for rapid and efficient screening of a large number of $\mathbf{M^1}$ and $\mathbf{M^2}$ combinations. This system allows the preparation of statistical mixtures of binuclear complexes by mixing **TP1** with an equimolar mixture of aqueous solutions of selected metals. Twenty-one statistical mixtures of these binuclear complexes were prepared and subsequently subjected to ^{19}F NMR spectroscopy. In all cases, four clearly distinguishable peaks in the ^{19}F NMR spectra were observed (Figure 44A and Figure 45). These results confirm that a system such as **TP1** provides a rigid, well-defined metal ion incorporation and thus even structural isomers such as **HoDy-TP1** and **DyHo-TP1** can be clearly distinguished (Figure 44A). All the **Dy/Ho-TP1** combinations were synthesized to assign each of the four individual combinations (Figure 44B). The combination of dysprosium and holmium was chosen due to their matching intensity and spacing of the individual peaks. Interestingly, the assignment of individual combinations revealed that the most distant peaks correspond to the structural isomers of **HoDy-TP1** and **DyHo-TP1**. While this combination would be illegible by other instruments such as MS or luminescence spectroscopy, paramagnetic encoding provides two clearly identifiable signals. To see whether the presence of stereochemically different $\mathbf{L^2}$ would result in distinct signals, Dy/Ho combinations of **TP2** were

synthesized. Indeed, ^{19}F NMR spectroscopy of **Dy/Ho-TP2** molecules revealed four unique signals that utterly differed from the signals of **Ho/Dy-TP1** (Figure 44C). The control experiment if paramagnetic encoding is possible with other building blocks such as **DOTA-K** has been investigated. Tripeptide **TP3** consisting of two terminal **DOTA-K** units bridged by Phe{*p*-CF_3} amino acid residue was synthesized. Dy/Ho combinations of this tripeptide were prepared in the same manner as previous examples. ^{19}F NMR spectroscopy of these control compounds revealed that signals are overlapping and split, possibly as a result of conformation averaging (Figure 44D). A high number of conformations is allowed by the excessively flexible lysine linker in the **DOTA-K** building block. This experiment proved that such flexible molecular scaffolds cannot be effectively used for the synthesis of paramagnetically encoded molecules.

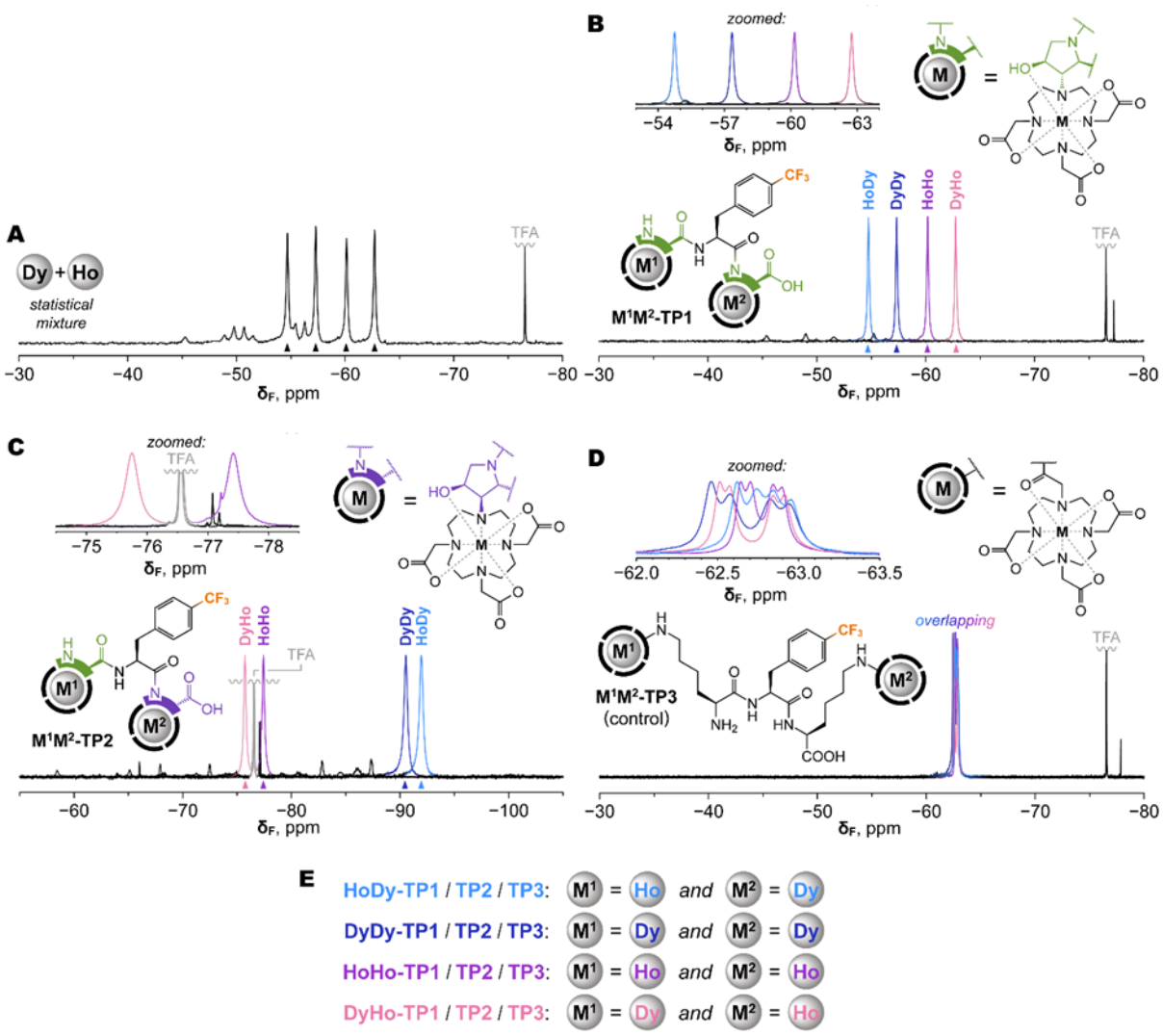

Figure 44: ^{19}F NMR spectroscopy of Dy^{+3}/Ho^{+3} **TP1**, **TP2**, **TP3** complexes. **A** ^{19}F NMR spectroscopy of Dy/Ho **TP1** statistical mixture prepared by uncontrolled complexation. Four major peaks can be observed in the ^{19}F NMR spectra, marked with black triangles. **B** overlaid ^{19}F NMR spectra of **Ho/Dy-TP1** combinations synthesized in a controlled manner, each of the peaks corresponds to the one in the statistical mixture. **C** Ho/Dy combinations of **TP2** provide four unique ^{19}F NMR signals to the **Ho/Dy-TP1**. **D** Ho/Dy combinations of control tripeptide **TP3** provide overlapping and split signals in ^{19}F NMR spectroscopy due to the flexible linker in the **DOTA-K** building block. **E** A summary of the prepared combinations. Figure reproduced from ref.[103]

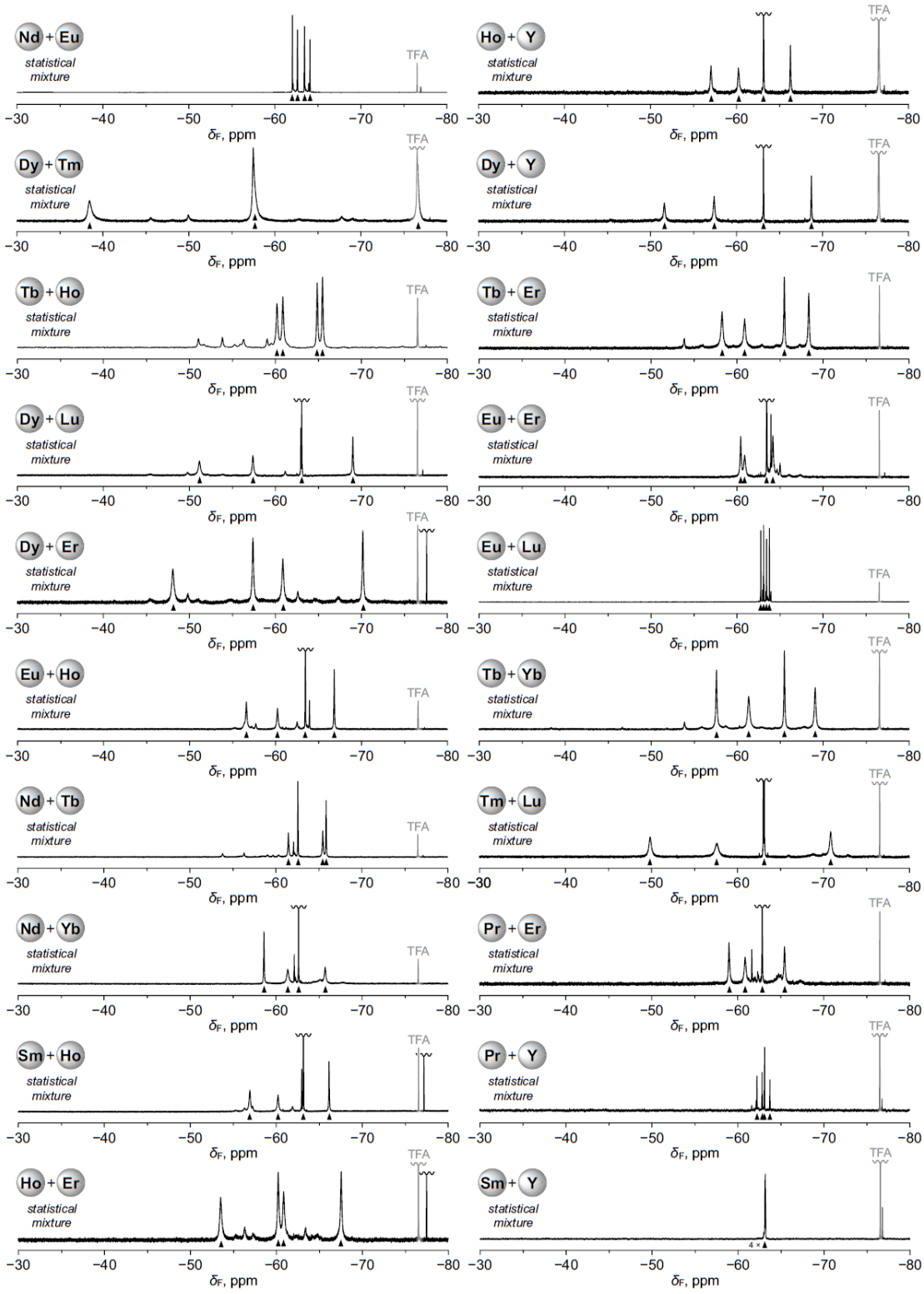

Figure 45: ^{19}F NMR spectroscopy of **TP1** statistical mixtures. Four clearly distinguishable signals, marked by black triangles, can be observed in all of the ^{19}F NMR spectra except the Dy/Tm example. Figure reproduced from ref.[103]

3.1.7.1 Paramagnetic encoding by multiplexing

Multiplexing is a method of information encoding by preparing mixtures that can be read as codes. These mixtures are prepared by the combination of elements. If two elements a and b are used, three unique codes are generated: a, b, and ab. This is the case of mass spectroscopy and luminescence, where the positions of elements cannot be distinguished (Figure 46A). A different situation occurs when the two elements are combined via paramagnetic encoding, where positional isomers are distinguishable. Therefore, from two elements a and b, four combinations ab, bb, aa, and ba can be prepared. These combinations will now be called codons and will be referred to with capital letters: A, B, C, and D. However, without controlled synthesis, it would be impossible to prepare the codons and the result would only be 3 codes: a, b, and ab. Controlled synthesis means control over the precise placement of those elements in the molecule. These codons can be further combined into unique codes where the presence of a codon corresponds to a value of 1 and its absence corresponds to a value of 0. Fifteen unique codes are produced by a combination of four A, B, C, and D codons (Figure 46B). This principle was demonstrated with Dy/Ho combinations in **TP1**. **TP1** acts, in this case, as a platform that is capable of recognizing permutations HoDy, DyDy, HoHo and DyHo. These four permutations can be later combined into 15 unique combinations readable by ^{19}F NMR spectroscopy (Figure 46C). Paramagnetic encoding brings the capability of combining two elements in a codon where their positions are crucial. Four elements in the same codon size (i.e. codon composed of two elements) result in 65535 unique combinations, which equals to 16-bit coding. In principle, the codon could be extended by one DO3A-Hyp unit. If this codon of size three would be used with four elements, 1.84×10^{19} unique codes could be theoretically generated (Figure 46D). The presented approach, multiplexing (mixing of molecules), was used as a technically convenient solution for the preparation of the codes. However, in theory, it would also be possible to connect individual codons into one single longer chain. This sequence of codons could be used for the creation of codes that would carry the same information as codes created by multiplexing, and thus the entire code could be contained in a single molecule. The DO3A-Hyp building blocks presented in this work make this synthetically feasible.

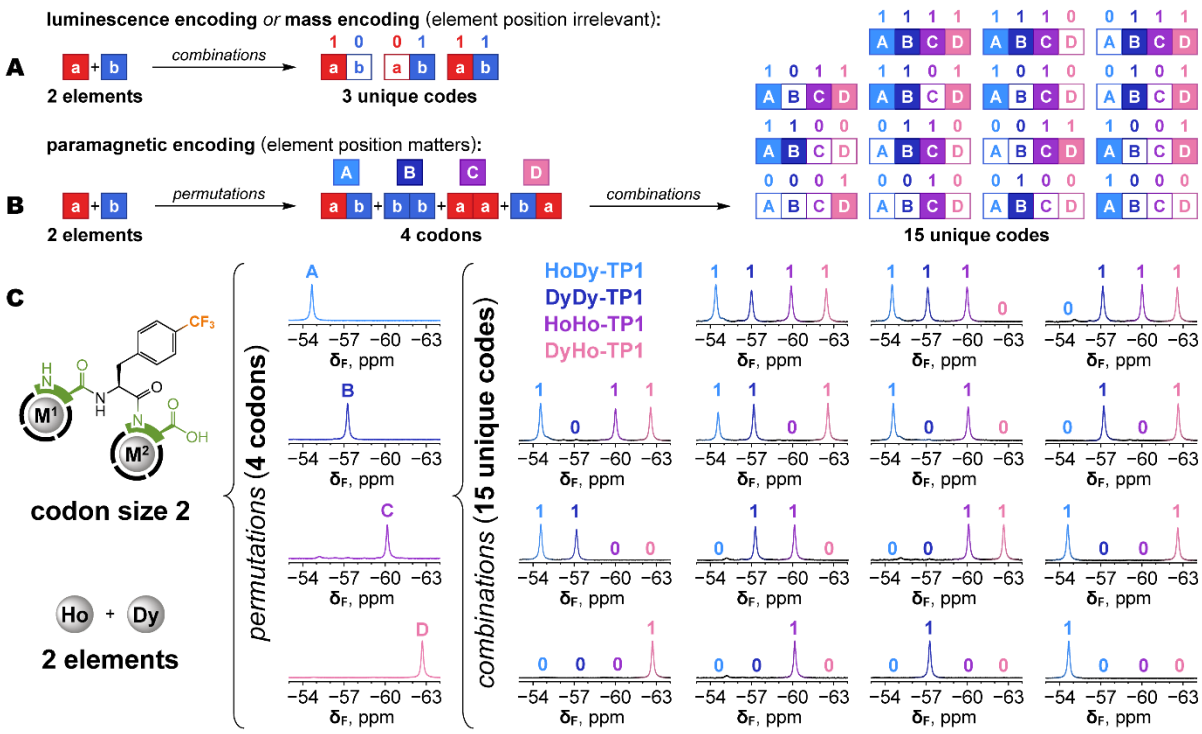

D

encoding principle	codon size	equation	number of possible unique codes for *N* elements		
luminescence *or* mass	—	$2^N - 1$	3 (**2 bits**; *N* = 2)	7 (**3 bits**; *N* = 3)	15 (**4 bits**; *N* = 4)
paramagnetic	2	$2^{N^2} - 1$	15 (**4 bits**; *N* = 2)	511 (**9 bits**; *N* = 3)	65535 (**16 bits**; *N* = 4)
	3	$2^{N^3} - 1$	255 (**8 bits**; *N* = 2)	1.34×10^8 (**27 bits**; *N* = 3)	1.84×10^{19} (**64 bits**; *N* = 4)

Figure 46: Encoding of information by multiplexing. **A** When read with mass spectroscopy or luminescence, the combination of two elements a and b yields only three codes. **B** Paramagnetic encoding allows two elements to be combined into four distinguishable codons. These four codons can be combined into 15 unique codes. **C** An example of multiplexing in the **TP1** platform using Ho/Dy permutations. Four codons are multiplexed to produce fifteen unique codes readable by ^{19}F NMR spectroscopy. **D** A comparison of paramagnetic encoding to other methods, as well as their capabilities. Figure reproduced from ref.[103]

3.1.7.2 Examples of practical information encoding and reading

To prove the capability of paramagnetic encoding in actual encoding and reading of information, Tb/Dy/Ho/Yb combinations in the **TP1** platform were prepared. All the sixteen combinations were individually synthesized by the route described in Figure 41A. Divergent combinatorial synthesis was used to prepare these combinations. First, four molecules **M^2-TP1** were synthesized, each with one different metal in the first position, and then four more from each by filling the second position, furnishing the **M^{1}M^2-TP1** combinations. Thus, a total of 16 compounds had to be synthesized, purified, and characterized. Both the preparative HPLC purification and the LC-MS analyses of these molecules showed that they behaved in a very similar way. This is interesting because it means that positional isomers are very difficult to distinguish by methods other than NMR. The combinations hence prepared were sufficient for the encoding of information in a 16-bit system, 16 combinations = 16 bits. The American Standard Code for Information

Interchange (ASCII) uses a 7-bit system to encode characters. Therefore, it was possible to encode two characters with the prepared 16 combinations. The encoding of two characters was, however, insufficient for practical use. Nevertheless, if a multilayer sample could be prepared, the practical usability of this approach would increase. For this purpose, a sample consisting of readable layers with encoded information separated by CCl_4 layers was prepared in a capillary. It should be pointed out that this step required extensive experimentation to achieve the desired effect. The glass capillary thus prepared was sealed with wax and inserted into the NMR tube containing D_2O for signal lock (Figure 47A). Two-dimensional Z-resolved ^{19}F NMR spectroscopy of five layers with encoded information separated by CCl_4 was performed. TFA was present in each one of the layers as a reference (Figure 47B). It was necessary to link the signals from the Z-resolved spectrum back to the original combinations of elements for decoding of the information. Firstly, it was necessary to reference all the signals due to the BMS (bulk magnetic susceptibility) effect for each layer separately. After this step, it was possible to assign all the signals to the corresponding combinations (Figure 47C). The presence or absence of a signal corresponded to a 0 or 1 value. All read values were plotted as shown in Figure 47D. A simplification was made since the **DyDy-TP1** and **YbTb-TP1** signals were close to each other and their assignment could be difficult. Each character written in the ASCII code starts with the value 0, so the **DyDy-TP1** combination was chosen as the start of the encoding to simplify the final decoding of the layers. This means that **DyDy-TP1** will never be used, thus eliminating the problem of proximity between **DyDy-TP1** and **YbTb-TP1** signals. Layers had to be divided into two sections, each consisting of 7 bits (Figure 47E). Final decoding of the values provided characters: L, a, n, t, h, a, n, i, d, and e (Figure 47F**,** G). This experiment proved that paramagnetic encoding is capable of information encoding that can be later read and decoded. The encoded word can be used, for example, as a password, which proves the practical applicability of the presented approach.

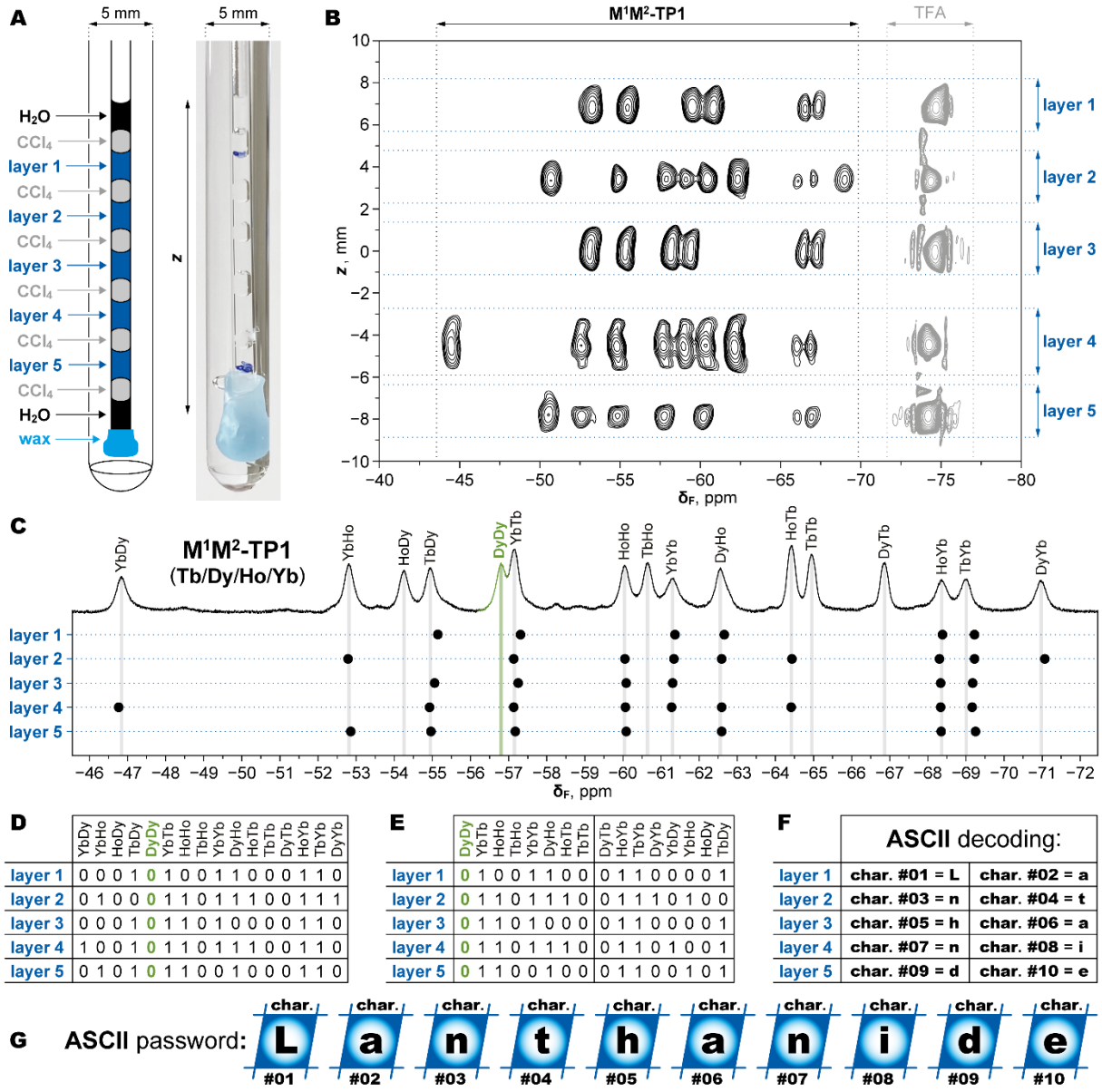

Figure 47: The use case of encoding and reading of information. **A** Multilayer NMR sample with encoded information in aqueous mixtures separated by CCl_4 layers prepared in capillary. This sample was sealed with wax and immersed in an NMR tube filled with D_2O. **B** 2D Z-resolved ^{19}F NMR spectroscopy revealed signals in all the five layers with TFA as a reference. **C** The signals had to be referenced due to the BMS effect. The referenced signals were then plotted to determine composition of each layer. **D** The presence or absence of each compound corresponds to a 0 or 1 value plotted in the table. **E** **DyDy-TP1** was selected as the beginning of the ASCII coding because of the close proximity of **DyDy-TP1** and **YbTb-TP1** signals. **F** Decoding of ASCII characters encoded in each layer. **G** The decoding provided the word Lanthanide. Figure reproduced from ref.[103]

The presented molecules **TP1**, **TP2** and **TP3** possess the trifluoromethyl reporter group and can therefore be visualized using ^{19}F MRI. MRI allows reading the signal in 3D space and can thus read multiple samples at once. To demonstrate the parallel reading of paramagnetically encoded information, a 5×7-well plate

sample was prepared. Selected wells of the plate were filled with solutions containing either one combination of Ho/Dy elements in the **TP1** molecule or a mixture of several of these molecules, while the rest of the wells were filled with H_2O. Each of the individual **Ho/Dy-TP1** combinations was prepared in MOPS buffer with a concentration of 0.36 mM in the well (Figure 48A). The overall ^{19}F MRI spectrum of the well plate sample shows four distinguishable peaks with intensities corresponding to the representation of each combination. All the Ho/Dy combinations of **TP1** can be clearly assigned (Figure 48B). Using a chemical shift imaging (CSI) pulse sequence, the selected **TP1** combination is visualized. The frequency of a particular molecule can be selected to display the image that has been drawn into the sample by that molecule. The letter "C" is read from the well plate when the frequency of **HoDy-TP1** is selectively displayed (Figure 48C). The other letters are read by following the frequency axis of the CSI spectrum, revealing the final word "CODE" (Figure 48C-F). This is another way paramagnetic encoding of molecules can be used to encode information. Furthermore, the presented molecular system provides a platform for the synthesis of fluorine contrast agents with tunable shift.

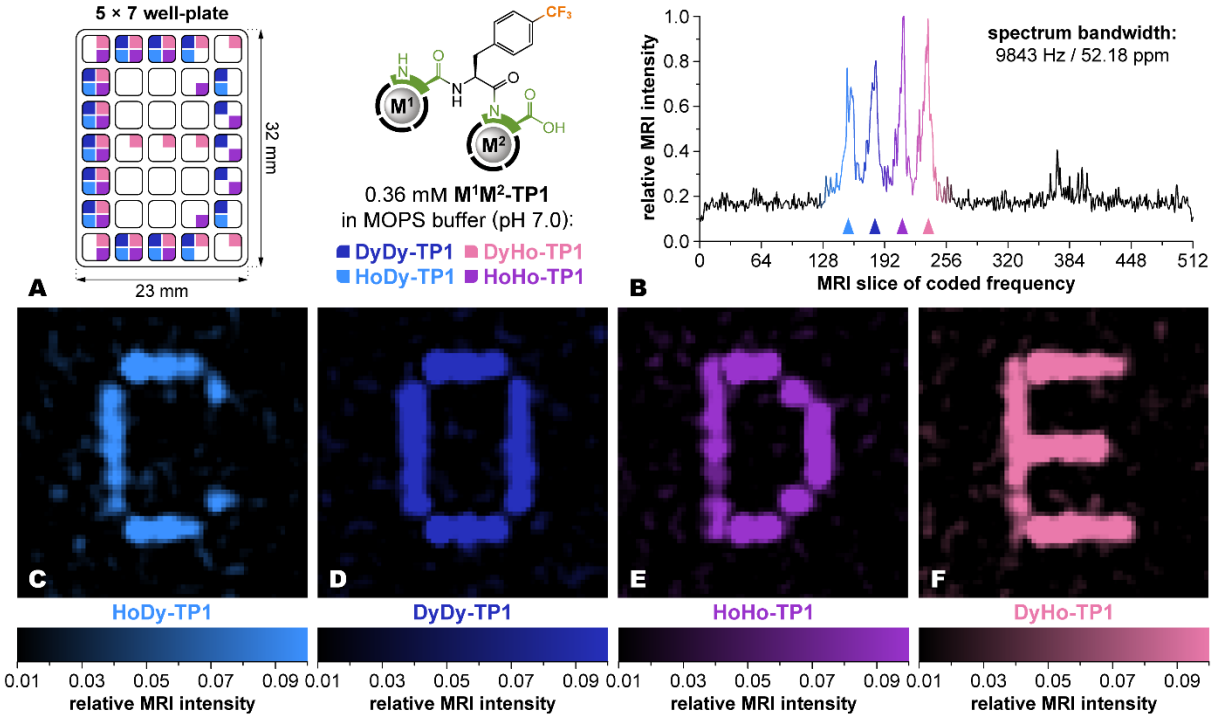

Figure 48: Parallel information reading by ^{19}F MRI. **A** Sample in the form of a 5×7 well plate with specific wells that contain Ho/Dy combinations in **TP1,** while the rest of the wells are filled with H_2O. **B** Full ^{19}F MRI spectrum of the whole well plate showing four signals with intesinty that corresponds to their representation. Each of the combinations is marked with a corresponding arrow. **C-F** CSI sequence pulse was used to read the encoded word “CODE”. Figure reproduced from ref.[103]

3.1.7.3 Conclusion

Within this project, a family of DO3A-Hyp building blocks was designed and synthesized. The reason for synthesizing these building blocks was the unavailability of molecules that would function as amino acids while providing a short and rigid metal attachment to the peptide chain. By appropriate choice of combinations of structural motifs, such properties were achieved in the building blocks presented here. These blocks combine the chelating properties of DO3A with connectivity brought by the pendant arm derived from the amino acid hydroxyproline. This amino acid moiety merges the versatility of peptide combinatorial synthesis with rigid attachment to the vicinity of the peptide chain. Because the controlled introduction of lanthanides into specific positions requires suitably protected building blocks, these building blocks had to be precisely decorated with suitable protective groups. The presented building blocks form a toolbox that offers incorporation of metals into the peptides in several possible ways. The building blocks were designed in a way that it is possible to incorporate the lanthanides by subsequential complexation or they can be directly incorporated as whole metal chelates. This diversity in approaches is a result of the orthogonality in protective groups that these building blocks possess. Tripeptides containing two such building blocks were synthesized to demonstrate the capabilities of the presented molecules and the need for their precise molecular design. The paramagnetic binuclear complexes of **M^1M^2-TP1** and **M^1M^2-TP2** were used to probe and demonstrate the potential of the presented system. It was demonstrated that the building blocks allow the combination of magnetic susceptibility tensors of paramagnetic metals in **M^1M^2-TP1/TP2** tripeptides. The combination of magnetic tensors would not be possible without full control over the position of the metal in the peptide sequence and without a short and rigid connection of the metal to the peptide backbone. The magnetic susceptibility tensors were used to manipulate the chemical shift of the CF_3 reporter group of these tripeptides, which was observed by ^{19}F NMR spectroscopy. It was shown that the different stereochemical environments between cases of **TP1** and **TP2** play a major role in how the magnetic tensors combine, leading to very diverse ^{19}F NMR signals. Control experiments were done with the **TP3** system, which is based on **DOTA-K**, to find out if this block produces the same effect. **DOTA-K** was found to be unsuitable because the individual signals were split and overlapping due to flexibility of this molecule. The **M^1M^2-TP1** system was also used in practical examples for the encoding and decoding of information. The information was encoded within a 16-bit system created from **Ho/Dy/Tb/Tm-TP1** compounds. To decode the information, 2D Z-resolved ^{19}F NMR spectroscopy was used to decipher the encoded word "Lanthanide". An experiment for parallel information reading was performed on an MRI scanner to add another practical example of encoding and decoding information using paramagnetic encoding. In this experiment, **Ho/Dy-TP1** combinations in the well plate were used to encode the information. A CSI pulse sequence was then used to read the encoded four-letter word "CODE". Tripeptide, **TP1**, is the first molecular prototype on which the new principle of information storage in molecules and

their mixtures has been demonstrated, including practical examples. However, the synthetic potential of DO3A-Hyp is much greater and, in principle, allows more complex molecular constructs to be developed. There are some limitations that still need to be overcome. For example, the fact that synthesis does not proceed well in the solid phase, and it would be beneficial to solve this issue. Other isomers that can be prepared but have not yet been explored could be a possible route to solving this problem. It is envisaged that the building blocks from the DO3A-Hyp family will find their applications in other fields as well, such as in the synthesis of therapeutics, diagnostics, and theragnostics.

3.2 PET/MRI

3.2.1 Author contribution

The author proposed the idea of dual modality PET/MRI bimodal contrast agent, which is presented in this thesis. The author designed, synthesized, and purified all the compounds that are the content of this part of the thesis. The author performed measurements for determination of kinetic inertness and relaxivity. The author performed most of the spectroscopic measurements of the intermediates and their evaluation, however, the final molecules were measured, and some evaluated by Dr. Martin Dračínský. ICP-MS analyses were performed by Mgr. Stanislava Matějková and HRMS by MS department of IOCB. The pilot radiolabeling experiments were done by Dr. Jan Ráliš. Radiolabeling experiments were conducted by the author at WSIC in collaboration with Dr. Jonathan Meyer Cotton. *In vitro* and *in vivo* PET/MRI experiments were done by Remy Chiaffarelli. Ramona Stremme performed radiosynthesis of a tracer for an *in vivo* PET/MRI experiment. Cytotoxicity studies were performed by Remy Chiaffarelli and Dr. Sabrina Hoffmann.

3.2.2 Introduction

The PET/MRI hybrid technique combines the benefits of both modalities, including MRI's excellent soft tissue resolution and PET's exceptional sensitivity. Both modalities can benefit from contrast enhancement provided by contrast agents, where in the case of MRI the enhancement is optional but in the case of PET it is indispensable. In PET/MRI clinical practice, contrast enhancement is acquired by co-administration of a mixture composed of GBCA for MRI enhancement and a PET tracer. A combination of MRI contrast agents that possess different mechanisms of action than PET tracer can provide beneficial information since two distinct processes can be monitored at the same time. However, there are currently no bimodal PET/MRI contrast agents in clinical use. Having both modalities in one molecule could be particularly beneficial for *in vivo* quantification of the MRI contrast agent. The quantification could play a major role in the case of responsive MRI contrast agents that can detect various molecular stimuli, but it is impossible to quantify the observed process because the precise concentration in the tissue is not known. This project aims at the design and development of a new family of bimodal PET/MRI contrast agents which could open the door for novel applications of the PET/MRI technique.

As already discussed in Chapter 1.4.3.2, one complication with the preparation of PET/MRI bimodal contrast agents is that MRI requires for contrast enhancement 10^6-10^9 higher molar amount of contrast agent than PET. According to this, the MRI contrast component has to be in large excess. This can be done by mixing a large excess of the non-radioactive (cold) version of the PET/MRI bimodal probe with a fraction of the hot PET/MRI bimodal probe. The molecules have to be the same, with the only difference in the

isotopes of nuclei. But the question is how to combine sources of contrast for both MRI and PET in one molecule while meeting the conditions described above. Several approaches have been tried, such as a combination of two different metals, gadolinium as an MRI component and a radiometal such as copper-64 (Figure 28) [97] or gallium-68 (Figure 29). [99] Another approach explored the concept of connecting a fragment bearing radionuclide by click reaction to the metal chelate (Figure 27).[96]

3.2.2.1 Definition of some terms

It is useful to explain a few terms that are commonly used in the radiochemical practice. Definition of the terms will be cited from the International Consensus Radiochemistry Nomenclature Guidelines.[112]

Radiochemical yield is the amount of activity in the product expressed as the percentage (%) of related starting activity utilized in the considered process (e.g., synthesis, separation, etc.). The quantity of both must relate to the same radionuclide and be decay corrected to the same point in time before the calculation is made.

Molar activity is the measured activity per mole of compound; measured in Bq/mol (GBq/μmol).

Specific activity is the measured activity per gram of compound; measured in Bq/g (GBq/μg).

3.2.3 Design considerations

The majority of the clinically used MRI contrast agents are based on gadolinium, and despite the concerns about toxicity, this type of contrast agents has stood the test of time. Therefore, it was decided that the bimodal PET/MRI contrast agent would consist of gadolinium chelate. Next, it was necessary to select a suitable PET radionuclide. Considering the advantages like broad clinical use, widespread production, and low cost, ^{18}F was selected. Because it is advantageous to incorporate the radionuclide in the last step of synthesis, it was decided to follow the most straightforward approach of direct radiolabeling of gadolinium chelate. On account of this, a chelator with suitable properties had to be designed. The chelator had to provide sufficiently high kinetic inertness of the chelate and it had to allow the incorporation of ^{18}F in the last step of synthesis. From our previous studies, it is known that the pyridine pendant arm provides comparable kinetic inertness to acetate with the advantage of possible pyridine ring functionalization.

Nucleophilic heteroaromatic substitution (NAS) on pyridine is facilitated by the presence of nitrogen in the aromatic system in comparison with a homoaromatic system consisting exclusively of carbon atoms (benzene). In the case of homoaromatic systems, the NAS has to be facilitated by a combination of a good leaving group and a strong electron withdrawing moiety. Nitrogen is more electronegative than carbon, and for that reason, the heteroaromatic system is more electron deficient, thus more electrophilic. This effect is increased with additional electron withdrawing groups on the pyridine ring. For example, the substituent

effect in NAS with 2-fluoropyridine was investigated, general scheme of reaction is shown in Figure 49. It was found that, except for fluorine in position 5 (Table 5, Entry 2) all the electron-withdrawing substituents increased the substitution rate. When the pyridine ring was substituted with a trifluoromethyl moiety, the reaction rate increased 3100 fold. [113]

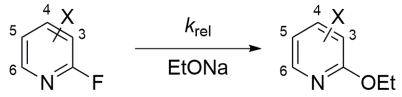

Figure 49: General reaction scheme of investigation of substituent effect on NAS with substituted 2-fluropyridines. [113]

Table 5: Substitution rates on 2-fluoropyridine with substituents in different positions. [113]

Entry	Substituent X	k_{rel}
1	6-EtO	0.078
2	5-F	0.67
3	H	1
4	6-F	56
5	4-F	86
6	3-F	50
7	4-Cl	69
8	3-Cl	75
9	5-CF_3	3100

The radio-fluorination on the pyridine ring has been investigated for the synthesis of several pyridine-based PET tracers, e.g. the nicotinic acetylcholine receptor ligand [^{18}F] F-A-85380.[114] The most common way to incorporate ^{18}F to pyridine ring is by nucleophilic aromatic substitution. Pyridine with a leaving group in position 2 was used for the investigation, which leaving group provides the highest radiochemical yield (Figure 50). Labelling was done by [^{18}F] KF/K_{222} in DMSO at varying temperatures and reaction times as shown in Table 6.[115] This study demonstrated that nitro and trimethylammonium leaving groups are superior to halides in radio-fluorination using ^{18}F.

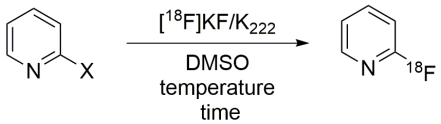

Figure 50: ^{18}F radio-labelling study on pyridine with different leaving groups (X) in position 2. [115]

Table 6: Study of the effect of a leaving group for the ^{18}F radiolabelling of pyridine at position 2. [115]

Temperature	Substituent	Radiochemical yield (%) Time of reaction (min)		
	X	5	10	20
120°C	Cl, Br, I	0	0	0
	NO_2	11	76	82
	N^+Me_3	81	87	91
150°C	Cl	1	3	23
	Br	1	16	25
	I	0	0	1
	NO_2	52	85	92
	N^+Me_3	89	89	90
180°C	Cl	11	28	57
	Br	56	60	87
	I	2	5	19
	NO_2	77	88	89
	N^+Me_3	88	91	92

Another study showed the importance of the position of the nitro leaving group on the pyridine in radiochemical labelling. It was demonstrated that the best results were delivered when the leaving group was in *ortho* or *para* position while *meta* position was almost non-reactive.[116]

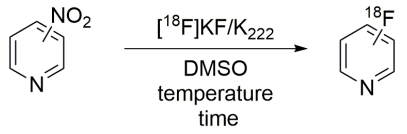

Figure 51: Investigation of the effect of nitro group position on radiochemical yield in ^{18}F labelling. [116]

Table 7: Investigation of the effect of nitro group position on radiochemical yield in ^{18}F labelling. [116]

	Heating 145°C				
Reaction time (min)	0.5	2	5	10	15
ortho	16	60	64	66	38
meta	0	0	0	1	1
para	15	47	52	60	43

Interestingly, in specific cases, the fluorine atom can undergo isotopic exchange between the isotopes ^{19}F and ^{18}F. This approach has been employed in the preparation of several PET tracers. Wagner *et al.* used fluorine isotopic exchange for the preparation of the 6-[^{18}F]fluoro-L-DOPA that is used in neurologic and oncologic PET. First, the protected precursor with an electro withdrawing group (formyl) in *para* position to fluorine was labelled by ^{18}F in isotopic exchange. The labelled precursor was then converted into 6-[^{18}F]fluoro-L-DOPA through Baeyer-Villiger oxidation with mCPBA followed by HBr hydrolysis (Figure 52).[117]

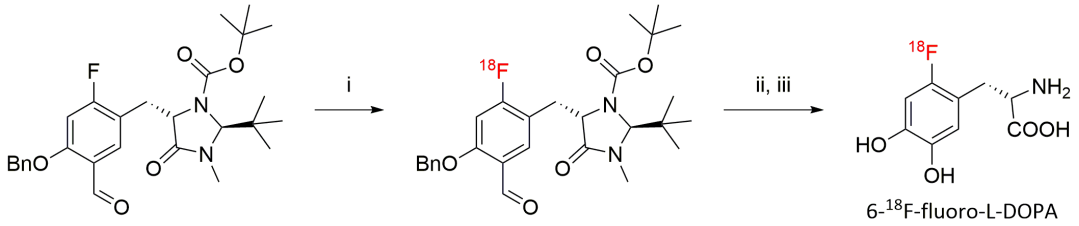

Figure 52: Radiosynthesis of 6-[^{18}F]fluoro-L-DOPA by fluorine isotopic exchange. i) TBA^{18}F/TBAHCO$_3$, DMF, 110°C, 8 minutes. ii) mCPBA, $CHCl_3$, 60°C, 20 min. iii) HBr (47%), 150°C, 30 min. [117]

Another example is the radiosynthesis of 4-[^{18}F]fluoro-L-tryptophan by Weiss *et al.* Similarly. As in case of 6-[^{18}F]fluoro-L-DOPA, an electron withdrawing formyl group was introduced to facilitate the radiolabeling. The ^{18}F <–> ^{19}F isotopic exchange was performed on the protected precursor, which subsequently underwent reductive decarbonylation and hydrolysis as shown in Figure 53.[118]

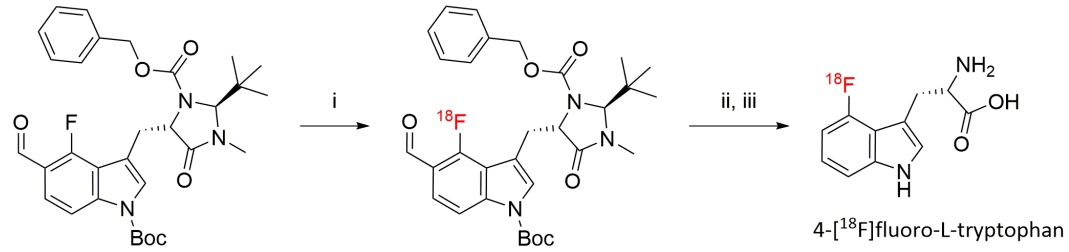

Figure 53: Radiosynthesis of 4-[^{18}F]fluoro-L-tryptophan by fluorine isotopic exchange. i) TBA^{18}F, DMF, 80°C, 15 minutes. ii) Wilkinson's catalyst, benzonitrile, microwave heating 100W, 2 min. iii) HCl, 150°C, 30 min. [118]

Interesting work was published by Brugarolas *et al.* [119] In this work, 3-[^{18}F]fluoro-4-aminopyridine was synthesized by direct radiolabeling of the pyridine-*N*-oxide precursor. This 3-[^{18}F]fluoro-4-aminopyridine is being investigated as a PET tracer for imaging of demyelination. During the labelling experiments, it was found that the tracer can be synthesized by ^{18}F <–> ^{19}F isotopic exchange. The isotopic exchange proceeded rapidly and at a moderate temperature (15 minutes at 25°C in DMSO). This result was achieved due to the presence of two electron withdrawing moieties on the pyridine core, a nitro group, and an *N*-oxide. By

oxidation of the pyridine nitrogen to *N*-oxide, the aromatic ring became electron deficient, which facilitated the reaction at position 3. After the labelling, the precursor was catalytically hydrogenated to give the desired PET tracer as shown in Figure 54.[119]

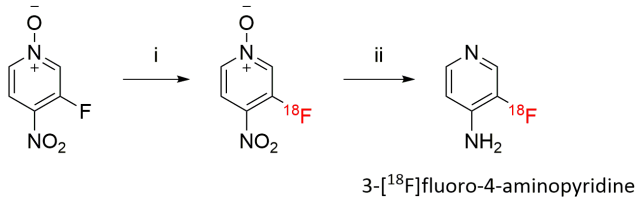

Figure 54: Radiosynthesis of 3-[^{18}F]fluoro-4-aminopyridine by fluorine isotopic exchange. i) TBA^{18}F, DMSO, 25°C, 15 minutes. ii) H_2 (1 atm) Pd/C, MeOH, 25°C, 15 min. [119]

Based on all the presented work, a design in which a cyclen-based macrocyclic chelator is provided with a single pyridine pendant arm and acetates was selected for the PET/MRI contrast agents family. This pyridine pendant arm contains a nitro group at *ortho* or at *para* position for nucleophilic substitution, where it is most reactive. To explore the possibility of introducing ^{18}F by isotopic exchange, another series of molecules carrying pyridine with fluorine in the *para* position were synthesized. The macrocycle was further substituted with two (1,7-DO2A-variant) or three acetates (DO3A variant). The DO3A variant was designed with the intention of serving as perfusion contrast agent, while the DO2A variant was designed to serve as lactate responsive contrast agent. The mechanism of responsiveness is described in Chapter 1.4.2.4. General structures of the designed chelators are depicted in Figure 55.

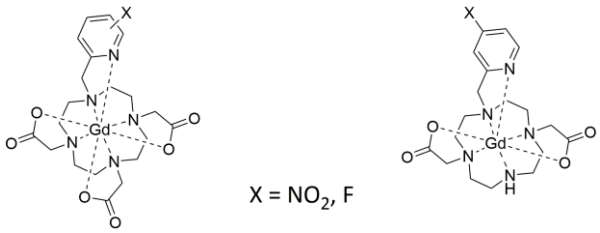

Figure 55: General structures of precursors for the synthesis of PET/MRI bimodal contrast agents.

3.2.4 Results and discussion

3.2.4.1 Synthesis of precursors

For the synthesis of designed chelators, the synthetic route starting from *t*Bu protected 1,7-DO2A and DO3A was selected. Precursors, 1,7-*t*Bu-DO2A and *t*Bu-DO3A, were synthesized according to the procedures described in Chapter 1.3. Suitable alkylating agents had to be prepared to incorporate the pyridine pendant arm into the macrocycle. Three ways were used for the synthesis of alkylation agents.

Conversion of substituted picolinic acid to methyl ester, followed by the reduction and transformation of the hydroxyl moiety to leaving group (Figure 56A). In most cases, the hydroxyl was transformed to chloride, but in cases where the boiling point of the alkylating agent was an issue, transformation to mesylate was done. The most straightforward approach, radical bromination, had the main disadvantage of generating a considerable amount of double brominated side product that lowered the final yield (Figure 56B). The Boekelheide reaction was used, in which oxygen from the *N*-oxide of pyridine is transferred to methyl in position 2 on pyridine during rearrangement (Figure 56C). This approach turned out to be very effective in the case of 2-hydroxymethyl-4-nitropyridine synthesis, where this reaction worked nicely even on a gram scale.

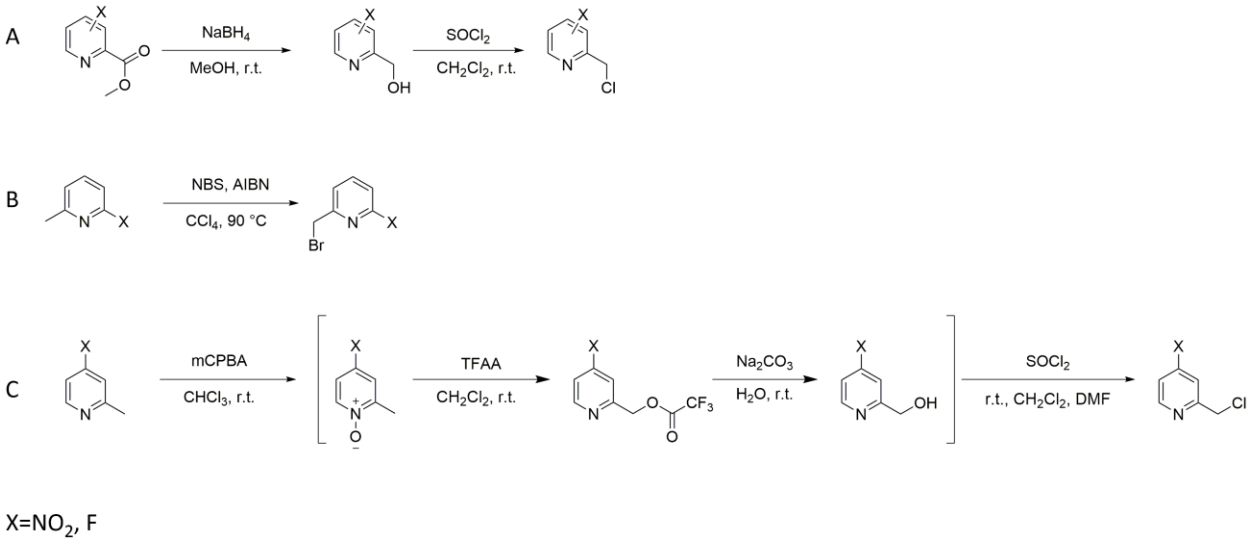

Figure 56: Synthetic routes used for the preparation of the alkylating agents. **A** Reduction of picolinic methyl ester to hydroxymethyl with subsequent transformation to chloride. **B** Radical bromination of methylpyridine. **C** The Boekelheide reaction.

After obtaining the alkylating reagents, these reagents were used to alkylate the *t*Bu-protected chelators. The TFA deprotection of *t*Bu protecting groups from acetates yielded the desired chelators, which were later complexed with gadolinium in buffered solution (Figure 57).

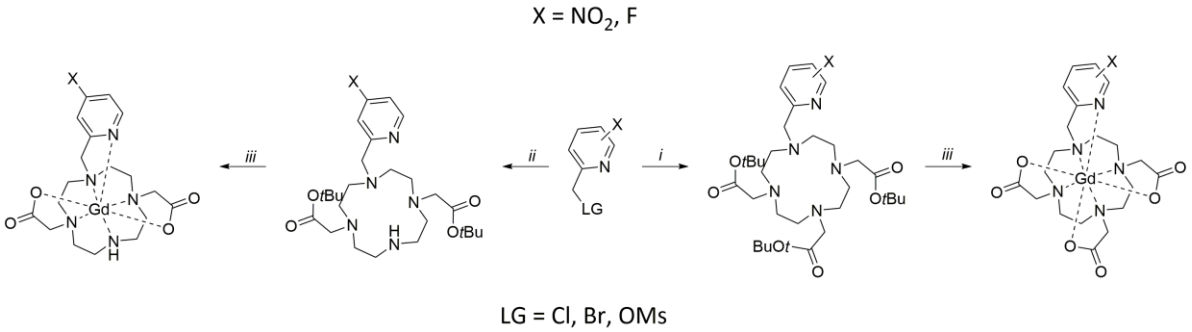

Figure 57: Synthetic routes leading to precursors of PET/MRI bimodal contrast agents. i) tBuDO3A*HBr, K_2CO_3, MeCN ii) 1,7-tBuDO2A, K_2CO_3, MeCN iii) 1) TFA 2) $GdCl_3$, MOPS buffer (0.5M, pH=7).

The substituents on the pyridine pendant arm were selected for specific reasons, which are discussed in the following text (Figure 58). Nitro derivatives were selected as precursors for nucleophilic aromatic substitution by $^{18}F^-$ to furnish the desired PET/MRI bimodal contrast agents **[Gd(^{18}FL^1)]** and **[Gd(^{18}FL^2)]** shown in Figure 58. The advantage of employing these precursors carrying the nitro leaving group on the pyridine pendant arm is an option to test the labelling conditions with cold $^{19}F^-$. As was discussed in the introduction, pyridines with a leaving group in *ortho* or *para* position are suitable substrates for nucleophilic aromatic substitution. A different case occurs with the pyridine pendant arms bearing fluorine atom. These molecules **[Gd(FL^1)]** and **[Gd(FL^2)]** were designed and synthesized to serve not only as cold standards for target radioactive ^{18}F counterparts, but to have two other important roles. The first role is as the source of the MRI signal. As was discussed in introduction, the MRI source must be in 10^6 to 10^9 molar excess to PET source in bimodal PET/MRI contrast agent. This requirement can be met by mixing of large excess of tracer´s cold variant with hot PET/MRI bimodal contrast agent, and **[Gd(FL^1)]** and **[Gd(FL^2)]** were designed and synthesized for exactly this purpose.

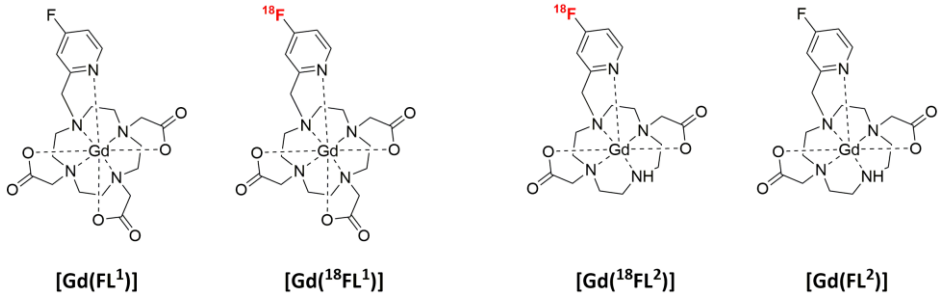

Figure 58: Structures of PET/MRI bimodal contrast agents **[Gd(^{18}FL^{1})]**, **[Gd(^{18}FL^{2})]** and their non-radioactive counterparts **[Gd(FL^{1})]**, **[Gd(FL^{2})]**

Second, **[Gd(FL^{1})]** and **[Gd(FL^{2})]** could be in principle used as substrates for ^{18}F <–> ^{19}F isotope exchange to obtain the PET/MRI contrast agents. This approach has been implemented in several syntheses of PET tracers, as was discussed in the introduction. However, this approach has never been tried in the case of metal chelates. If this approach succeeds, it will address several issues. Mainly, the preparation of the bimodal PET/MRI tracer would be simplified because the starting material for synthesis would be a chemically identical product, only with a different fluorine isotope. Another advantage would be the minimization of by-products resulting from substitution of the leaving group. However, the main drawback of this method is that the reaction conditions cannot be tested with non-radioactive material.

3.2.4.2 Finding suitable reaction conditions for the preparation of [(Gd)^{18}FL^{1}]

Initially, a series of gadolinium chelates with pyridine pendant arms substituted with a nitro group in the *ortho* or *para* position was prepared. Nucleophilic aromatic substitutions with non-radioactive ^{19}F^{-} on the pyridine ring were performed on this series, as shown in Figure 59 and Table 8. This series served as a platform that allowed testing of radiolabeling conditions without working with radioactivity for the selection of the best candidate for subsequent radiolabeling experiments. Tetrabutylammonium fluoride (TBAF) as a 1M solution in THF was used to introduce fluorine into the pyridine. The reactions were carried out in a nonpolar aprotic solvent, DMSO, to promote the nucleophilic aromatic substitution. Interestingly, only in the case of 4-nitropyridine, the reaction took place, and therefore this structural motif was selected for further experiments.

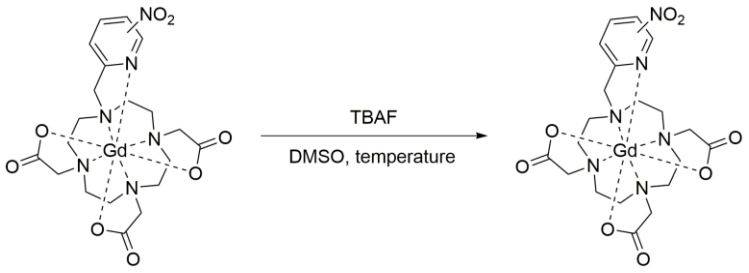

Figure 59: Screening for suitable structural design for nucleophilic aromatic substitution on the pyridine ring.

Table 8: Screening for suitable structural design for nucleophilic aromatic substitution on the pyridine ring.

X	Temperature (°C)	Conversion (%)
6-NO_2	50	0
4-NO_2	50	67
4-NO_2	75	99

In the next step, a series of lanthanide complexes of ligand **NO_2L^1** was prepared, namely: La, Pr, Eu, Tb, Ho, Tm, and Lu, as shown in Figure 60. These lanthanides were selected to partially cover the lanthanide series. The purpose was to determine whether there was any dependence between the rate of the fluorination reaction and its yield on the chelated metal. The series was purified by preparative HPLC using formic acid as an additive in the mobile phase. Purified complexes were subsequently subjected to fluorine introduction tests using TBAF in DMSO at 50°C and conversion was analyzed by LC-MS after 30 and 60 minutes as shown in Figure 61.

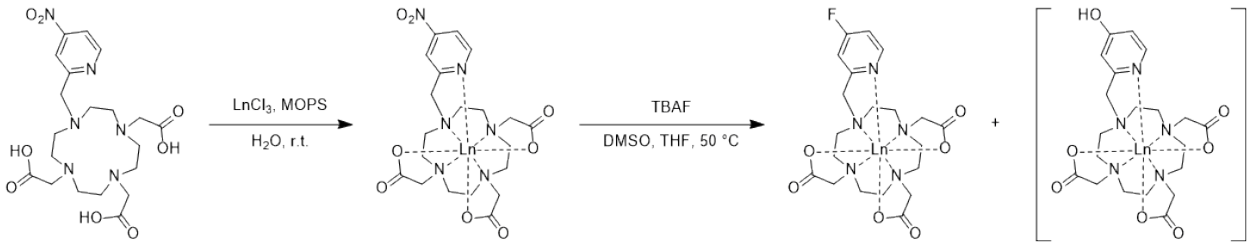

Figure 60: Preparation of a series of [Ln(**NO_2L^1**)] Ln=La, Pr, Eu, Gd, Tb, Ho, Tm, and Lu complexes to determine their effect on the fluorination reaction, with the structure of the main hydroxy by-product formed during the fluorination reaction shown in brackets.

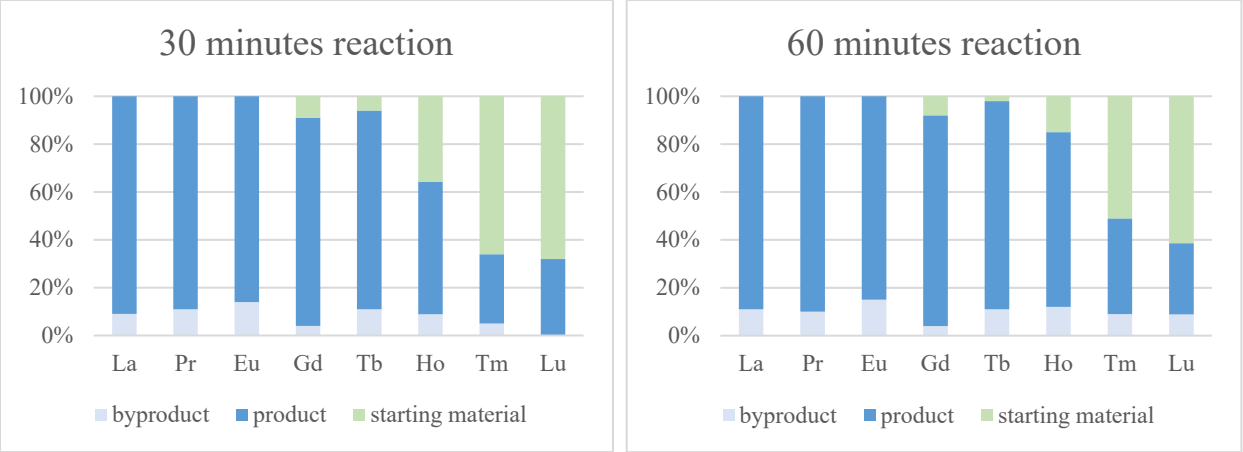

Figure 61: The graphs depict the percentual composition of reaction mixtures after fluorination with TBAF (3 eq., c = 45 nM) in DMSO at 50°C after 30 and 60 minutes on [Ln(NO_2L^1)] (1 eq., c = 15 mM), where Ln=La, Pr, Eu, Gd, Tb, Ho, Tm, Lu.

From the obtained data, it is apparent that the success of the fluorination reaction has a trend within the lanthanide series. The reaction proceeds most rapidly with metal complexes from the beginning of the lanthanide series, i.e., those with a larger ionic radius. In the cases of La, Pr, and Eu, the conversion took place quantitatively after 30 minutes. The changing ionic radius of the metal through the series is the probable cause of this effect. At the beginning of the lanthanide series, the radius is largest, and that can result in increased exposure of the nitro substituted pyridine pendant arm. However, isomerism of the complexes or loss of coordinated water could be reasons for the observed effect as well. It should be noted that in all cases, the reaction by-product that possessed the hydroxy pyridine pendant arm (Figure 60) was also present in a low percentage of the reaction mixture.

3.2.4.3 ^{18}F radiolabelling of [Gd(NO_2L^1)]

In cooperation with the Nuclear Physics Institute of the CAS (Dr. Jan Ráliš), pilot radiolabelling experiments of **[Gd(NO_2L^1)]** were performed. These pilot experiments confirmed that our proposed method of direct radiolabelling of gadolinium chelates with $^{18}F^-$ is feasible. Subsequently, a cooperation with WSIC (Werner Siemens Imaging Centre) was established to further develop this project, as WSIC is equipped with a PET/MRI scanner. After preliminary experiments, it was necessary to optimize the conditions with a focus on high radiochemical yield while maintaining the content of impurities as low as possible. These optimizations were initially carried out in collaboration with Dr. Jonathan Cotton of WSIC. Conditions that provided the purest reaction mixture with the highest conversion of 91% are listed in Table 9, entry 11. Most of the reactions were carried out in DMSO, but acetonitrile is also a suitable solvent, as shown in Table 9, entry 2. This proved to be important when radiosynthesis was performed on an automated radiosynthesis module (GE FX N), which is discussed later. Increased temperature gave a higher

radiochemical yield (compare entry 1 and entry 8, Table 9). Radiochemical yield was also better with longer reaction time (compare entry 1 and entry 3, Table 9). Reactions were carried out with an increased amount of precursor (Table 9, entries 4 and 14) with acceptable results.

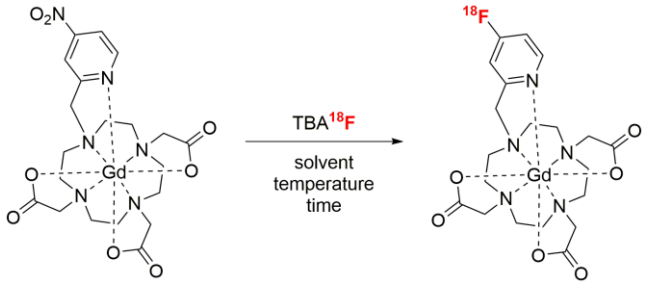

Figure 62: Schematic depiction of ^{18}F radio-labelling of **[Gd(NO$_2$L^1)]**.

Table 9: Optimization of radiolabeling conditions with the precursor **[Gd(NO$_2$L^1)]**. All reactions were carried out in dry solvents. The amount of precursor used was 1 mg unless otherwise stated. TBAF was used as a 1M solution in dry THF. Unless otherwise stated, QMA (quaternary methyl ammonium) stationary phase was used for $^{18}F^-$ absorption in all cases. A 1/1 MeCN/H_2O mixture was used as the solvent for the elution of $^{18}F^-$ with $TBAHCO_3$ to produce $TBA^{18}F$.

Reaction	[Gd(NO$_2$L^1)] ekv.(amount)	[Gd(NO$_2$L^1)] c (mmol)	TBAF ekv.	stationary phase/conditioning	Eluent	Solvents	Temperature °C	Time min	RCY %	conversion %
Entry 1	1	14.35	3	$NaHCO_3$	$TBAHCO_3$	DMSO	90	15	25	65
Entry 2	1	14.35	3	$NaHCO_3$	$TBAHCO_3$	MeCN	90	5	23	52
Entry 3	1	14.35	3	$NaHCO_3$	$TBAHCO_3$	DMSO	90	5	20	69
Entry 4	1 (6mg)	26.77	3	$NaHCO_3$	$TBAHCO_3$	DMSO	90	5	20	72
Entry 5	1 (1.9mg)	97.74	3	$NaHCO_3$	$TBAHCO_3$	DMSO	90	5	20	76
Entry 6	1	14.35	3	CB $PSHCO_3$	$TBAHCO_3$	DMSO	90	5	17	71
Entry 7	1	14.35	3	$NaHCO_3$	$K_{222}HCO_3$	DMSO	90	5	17	82
Entry 8	1	14.35	3	$NaHCO_3$	$TBAHCO_3$	DMSO	50	15	16	19
Entry 9	1	14.35	3	$NaHCO_3$	$TBAHCO_3$	DMSO	90	15	15	75
Entry 10	1	14.35	0	$NaHCO_3$	$K_{222}HCO_3$	DMSO	90	5	15	n/a
Entry 11	1(3.4mg)	36.70	3	KOTf	TBAOTf *	DMSO	90	5	15	91
Entry 12	1 (3mg)	14.35	3	$NaHCO_3$	$TBAHCO_3$	DMSO	90	5	11	74
Entry 13	1	14.35	3	$NaHCO_3$	$TBAHCO_3$	DMSO	50	15	10	65
Entry 14	1(10mg)	88.94	3	$NaHCO_3$	$TBAHCO_3$	Mixture	90	5	9	47
Entry 15	1 (3mg)	35.44	6	$NaHCO_3$	$TBAHCO_3$	DMSO	90	5	6	57
Entry 16	1	14.35	3	none **	$TBAHCO_3$	DMSO	90	5	5	62
Entry 17	1	14.35	3	CB $PSHCO_3$	$TBAHCO_3$	DMSO	90	5	5	61

Mixture of solvents in Entry 14 means MeCN/DMSO in ratio 5/1.

* In cases where the KOTf/TBAOTf system was used, methanol was used for the elution of $^{18}F^-$ to produce $TBA^{18}F$.

** The stationary phase was not reconditioned but was used as supplied in CO_3^{-2} cycle.

3.2.4.4 Optimization of [Gd(FL^1)] labelling

Table 9 shows that the nucleophilic aromatic substitutions with the precursor **[Gd(NO$_2$L^1)]** provided good radiochemical yields, but the purity of the resulting mixtures was not ideal because the by-products formed in the reaction had similar retention times to the product. Consequently, the possibility of isotopic fluorine substitution to **[Gd(FL^1)]** was investigated in a series of radiolabeling experiments. The results of these experiments are shown in Table 10. These experiments demonstrated that isotopic exchange of ^{18}F<–>^{19}F is possible. In addition, this approach lead to the similar conversion as the best result for **[Gd(NO$_2$L^1)]** and the by-products of the reaction had a significantly different retention time from the product which simplified the final purification. This is the case shown in Table 10, entry 1, where a combination of KOTf and TBAOTf was used. This optimized system was later used for the synthesis of high radioactivity samples that were used for *in vivo* experiments.

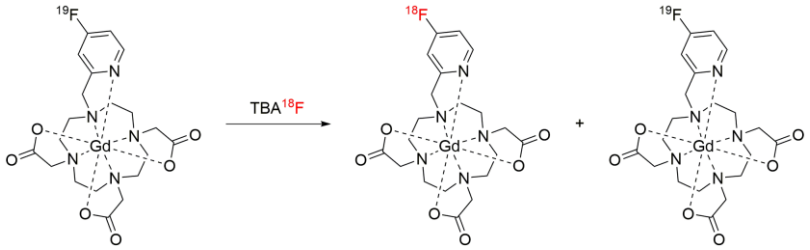

Figure 63: Schematic representation of the ^{18}F<–>^{19}F isotopic exchange reaction on the precursor **[Gd(FL^1)]**.

Table 10: Optimization of radiolabeling conditions with the precursor **[Gd(FL^1)]**. All reactions were carried out in dry solvents. The amount of precursor used was 1 mg unless otherwise stated. TBAF was used as a 1M solution in dry THF. Unless otherwise stated, QMA (quaternary methyl ammonium) stationary phase was used for ^{18}F$^-$ absorption in all cases. A 1/1 MeCN/H$_2$O mixture was used as the solvent for the elution of ^{18}F$^-$ with TBAHCO$_3$ to produce TBA^{18}F.

Reaction	[Gd(FL^1)] ekv.(amount)	[Gd(FL1)] c (mmol)	TBAF ekv.	stationary phase/conditioning	Eluent	Solvents	Temperature °C	Time min	RCY %	conversion %
Entry 1	1 (3.6mg)	40.82	2.5	KOTf	TBAOTf*	DMSO	90	5	15	90
Entry 2	1	14.35	3	$NaHCO_3$	$TBAHCO_3$	DMSO	90	5	15	84
Entry 3	1	14.35	3	CB PSHCO3	$TBAHCO_3$	DMSO	90	5	13	91
Entry 4	1	14.35	3	$NaHCO_3$	$TBAHCO_3$	DMSO	90	5	11	81
Entry 5	1	14.35	0	$NaHCO_3$	$TBAHCO_3$	DMSO	90	5	6	38

* In cases where the KOTf/TBAOTf system was used, methanol was used for the elution of ^{18}F$^-$ to produce TBA^{18}F.

3.2.4.5 Automated radiolabeling performed on radiosynthesis module

Initially, the labelling experiments were performed manually due to the ease of rapid testing of various reaction conditions. After finding the most suitable conditions, automated radio-synthesis was performed

using a programmable module. This module permits working with high doses of radioactivity and allows a subsequent purification. This whole process produces a purified, labelled product. The automated radiosynthesis module (GE FX N) consists of a lead cell (Figure 64A), where actual radiosynthesis and separation are done. Computer that allows the user to program the sequence (Figure 64B) and two-channel HPLC pump for chromatographic separation (Figure 64C) is part of the module. Several vials with a volume varying from 1 ml to 5 ml are present in the lead cell, as is depicted in Figure 65. Reaction volumes of the used solvents had to be upscaled due to the higher volumes of module vials. Following several rounds of optimization, it was discovered that a mixture of DMSO and acetonitrile produced the best results. Therefore, a mixture composed of 600 µL acetonitrile and 120 µL of DMSO was used for radiolabeling. The low content of DMSO is necessary for the rapid evaporation of the solvent after the reaction. Even a small volume of the residual DMSO can lead to a stretched-out peak of free $^{18}F^-$ which can interfere with the peak of the radiolabeled product during HPLC purification. Pilot radiosynthesis experiments using the module were performed with a QMA cartridge preconditioned with $NaHCO_3$. In this setup, $TBAHCO_3$ in a $MeCN/H_2O$ mixture was used for the $^{18}F^-$ elution. However, during further optimizations, it was found that the best results were achieved with QMA cartridges preconditioned with KOTf and TBAOTf $^{18}F^-$ elution in anhydrous MeOH.

Figure 64: Automated radiosynthesis module (GE FX N). **A** The chamber in which radiosynthesis is performed is shielded by a heavy lead door. **B** Radioactive labelling and purification is controlled by a software interface. **C** The reaction vessel of the module is connected to the HPLC system so that the radiolabeled product can be purified immediately after synthesis.

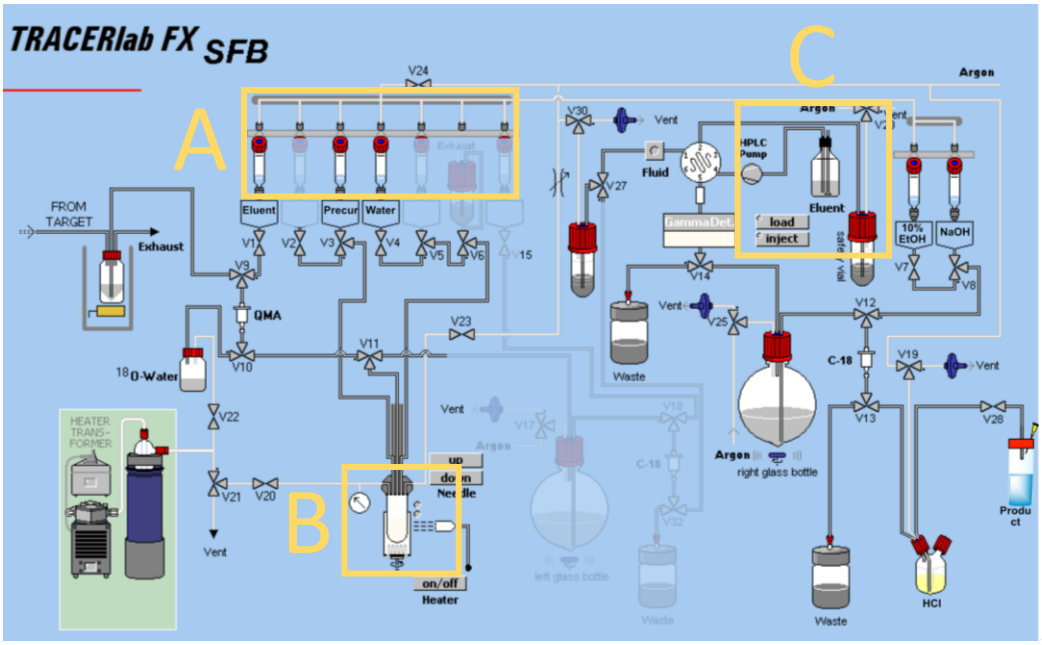

Figure 65: Demonstration of the program used for radiosynthesis and purification on the automated module. **A** As can be seen, vials of different volumes can be used to load the starting materials. **B** The reaction is carried out in the reactor under the selected conditions. **C** The radiolabeled product can then be purified on the HPLC.

The separation of radiolabeled product was carried out in 3% aqueous ethanol. Ethanol was selected as a less polar component of the eluent since it is less toxic to living organisms in comparison to other options such as methanol. The aluminum cartridge was incorporated into the system before the HPLC column for the removal of the free $^{18}F^-$. Fractions had to be collected manually and afterwards were measured in dose calibrator to determine activity of the product. After a series of optimizations, a product with an activity of 1340 MBq was obtained. This activity is equivalent to the usual imaging dose for more than 5 patients when ^{18}F-FDG is used. [120] A sample of the product was taken for HPLC analysis as well. It can be seen from the chromatogram in Figure 66 that only one radioactive product is present and the purity of the sample in the UV detector at 254 nm is very high (97%). These results show that the synthesis can be used for clinically relevant scales.

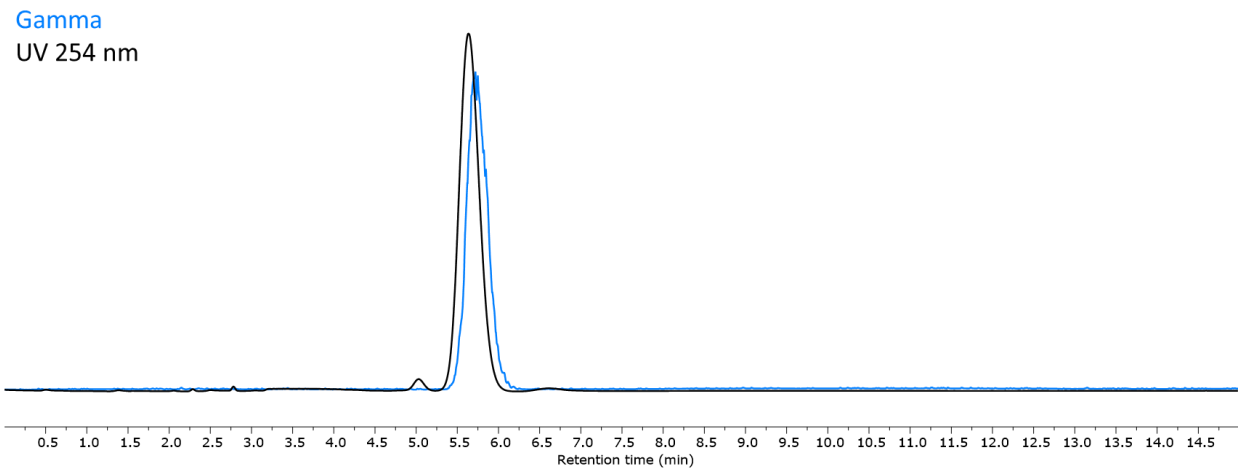

Figure 66: Chromatograms of the product consisting of labelled **[Gd(^{18}FL^{1})]** and non-radioactive **[Gd(FL^{1})]** after automated radiochemical synthesis on the module. The chromatogram (blue) from the gamma detector shows that the radioactivity is concentrated only in the product and that the free $^{18}F^-$ peak is not present. The chromatogram from the UV detection at 254 nm (black) shows the presence of a single product.

3.2.4.6 In vitro studies of physio-chemical properties

In addition to radiolabeling experiments to obtain **[Gd(^{18}FL^{1})]** and **[Gd(^{18}FL^{2})]**, physio-chemical properties of their non-radioactive counterparts **[Gd(FL^{1})]** and **[Gd(FL^{2})]** were determined. The results of these measurements are discussed in the following text.

Kinetic inertness

The kinetic inertness of **[Gd(FL^{1})]** and **[Gd(FL^{2})]** was tested using acid-assisted decomplexation with HCl (0.1M). As a reference, Magnevist®, gadolinium-DTPA (diethylenetriaminepentaacetic acid), a clinically used contrast agent, was used. All complexes were used as 1 mM solutions with a volume of 150 µL and incubated at 37 °C. Solution of $GdCl_3$ (1mM) in HCl (0.1M) was used as an example of fully released gadolinium from chelate. During decomplexation, the gadolinium ion leaves the complex and becomes fully solvated. The longitudinal relaxation time T_1 of the sample decreases during this process, since the solvated gadolinium shortens T_1 relaxation time to a greater degree than the chelated. The reaction reaches equilibrium when the complex is fully decomposed, and all the gadolinium is solvated. The relaxation time T_1 does not change in this equilibrium state. The T_1 relaxation time values were determined on a relaxometer (minispec mq20 NMR analyzer from Bruker) at 37°C and a field strength of 0.47 T. For comparison purposes, the stabilities were compared in paramagnetic relaxation rate: $R_{1p} = 1/T_1 - 1/T_{1d}$. The longitudinal relaxation time of the HCl (0.1M) corresponds to T_{1d}. A slow increase of R_{1p} values can be observed in the case of **[Gd(FL^{1})]** during the measurement, which suggests that the complex is slowly decomposed (Figure

67, top graph). Over a 259-minute period, the R_{1p} value of **[Gd(FL^1)]** increased by 12%. In the case of **[Gd(FL^2)]**, the R_{1p} value increased more rapidly, and the reaction reached equilibrium after 54 minutes. The results show that **[Gd(FL^2)]** is less kinetically inert than **[Gd(FL^1)]**, which is consistent with expectations. The decomposition of the chelate was fastest in the case of Magnevist, with no change in the R_{1p} value during the measurements, and therefore it can be assumed that the reaction reached equilibrium during the first 6 minutes of the measurement. It can be assumed that the complex completely decomposed, which correlates to the published half-life of Magnevist <5 s in 0.1M HCl.[25] The samples were remeasured after 24 hours (Figure 67, bottom graph), giving the same R_{1p} values for **[Gd(FL^2)]**, Magnevist and $GdCl_3$, while the R_{1p} value of **[Gd(FL^1)]** increased by 49%. Theoretically, the R_{1p} value should be the same for all measured complexes at the moment the system reaches equilibrium, however, as can be seen, there are slight differences between the equilibrium values of **[Gd(FL^2)]**, Magnevist and $GdCl_3$. This can be explained by an error in sample preparation, as analysis of the samples by ICP-MS revealed differences in gadolinium concentrations between the samples that reflect the R_{1p} values obtained. According to the findings, **[Gd(FL^1)]** and **[Gd(FL^2)]** are more stable than the clinically used Magnevist and thus suitable for *in vivo* applications.

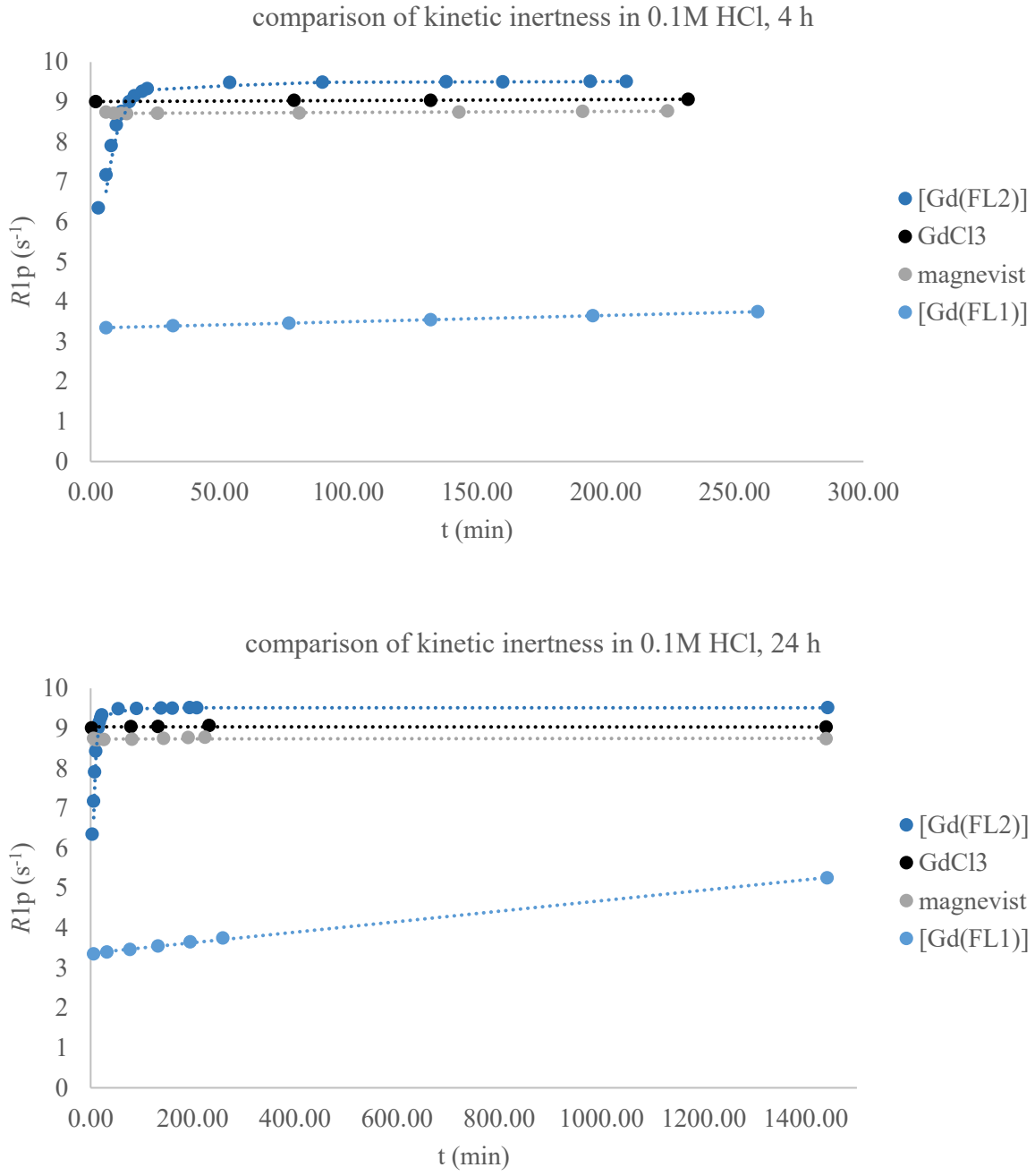

Figure 67: Comparison of kinetic inertness of **[Gd(FL^1)]**, **[Gd(FL^2)]** and Magnevist by acid-assisted decomplexation in 0.1M HCl at 37°C by measurement of relaxation rate on a relaxometer. The top graph shows data taken during the first 4 hours of the experiment and the bottom graph adds a data point after 24 hours. The R_{1p} value should be the same for all measured complexes at equilibrium but elemental analysis confirmed minor differences in concentrations of the samples (pipetting error) that explain the difference.

Relaxivity and number of coordinated water molecules

One of the most important properties of **[Gd(FL^1)]** and **[Gd(FL^2)]** as potential contrast agents for PET/MRI is relaxivity, which is the measure of effectiveness of a compound to act as an MRI contrast agent. For the relaxivity determination, samples of **[Gd(FL^1)]** and **[Gd(FL^2)]** were prepared at 0, 0.2, 0.5, 1, and 2 mM concentrations in a MOPS/NaOH buffer (50 mM, pH 7.0, 150 µL). The samples thus prepared were used for the determination of the longitudinal relaxation time T_1 values on the relaxometer (minispec mq20 NMR analyzer from Bruker) at 37°C and 0.47 T. Based on these results, it was possible to determine that the **[Gd(FL^1)]** has a relaxivity of 3.43 $mM^{-1}s^{-1}$ (Figure 68), which corresponds to the coordination of one water molecule to the metal. The value of **[Gd(FL^2)]** was determined to be 5.33 $mM^{-1}s^{-1}$, which indicates that more than one water molecule is coordinated to the chelate. Most likely, there is equilibrium between q = 1 and q = 2 species. For comparison, the relaxivity of most clinically used MRI contrast agents at comparable conditions is within the range 3 – 4 $mM^{-1}s^{-1}$.[121]

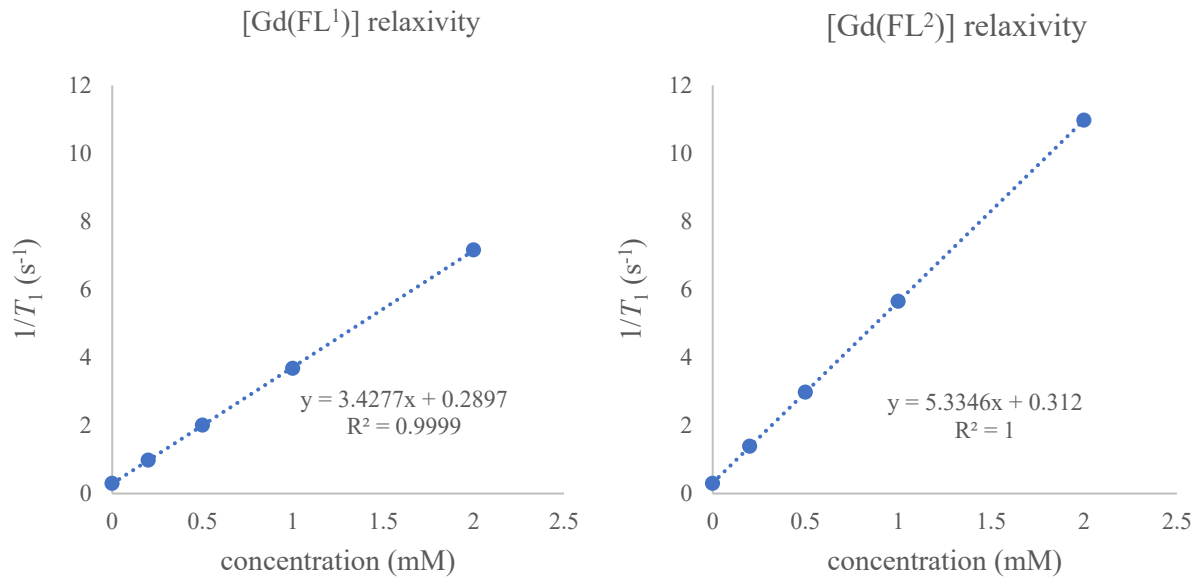

Figure 68: The relaxivities of **[Gd(FL^1)]** and **[Gd(FL^2)]** were determined by linear regression of their concentration versus longitudinal relaxation rate.

Cell viability assay of [Gd(FL^1)]

The basic premise of any drug or diagnostic substance is that it will not adversely affect healthy cells. An assay was performed to compare whether **[Gd(FL^1)]** of different concentrations would decrease cell viability. Cytotoxicity of examined substances is expressed as a percentage of viability compared to the viability of controls. The lower the viability value, the more toxic the substance is. Solutions of **[Gd(FL^1)]** at concentrations of 1 and 10 μM were prepared, and samples of the same concentration were also prepared from Magnevist. These Magnevist samples served as a standard for clinically used GBCA. The effect of the samples on cell viability after 6 hours of incubation is shown in Figure 69. Based on the results, it can be assumed that **[Gd(FL^1)]** does not have a significantly greater effect on cell viability than clinically used Magnevist.

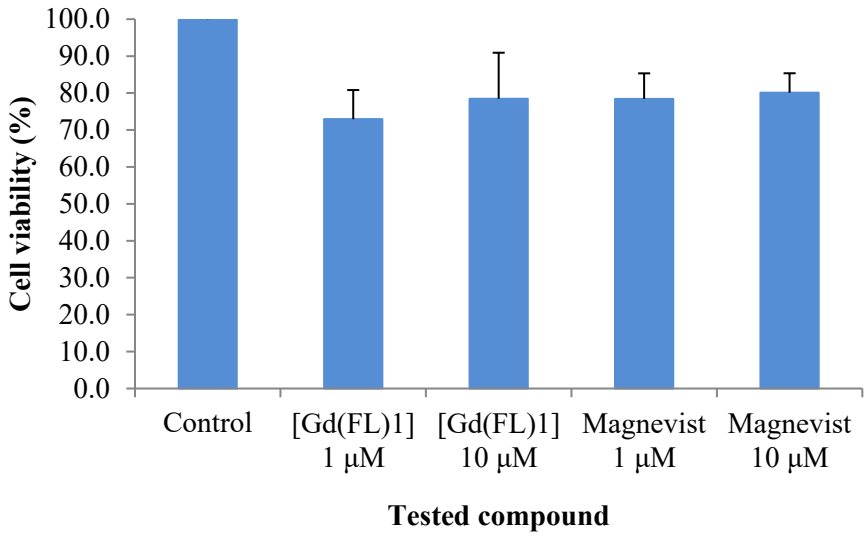

Figure 69: Measurement of cell viability as metabolic inhibition rate at various concentrations of **[Gd(FL^1)]** with Magnevist as a reference. For this experiment MC-38 cells were used, and the results are reported as mean viability ± SEM (standard error of the mean) of N = 3. More details are given in Chapter 5.2 of the experimental part.

3.2.4.7 Measurement of [Gd(^{18}FL^1)] PET/MRI phantoms

In Chapters 3.2.4.4 and 3.2.4.5, the reaction conditions were optimized for delivering a sufficiently pure sample with high activity. The relaxivity was determined in Chapter 3.2.4.6, where it was demonstrated that **[Gd(FL^1)]** has a suitable value to serve as a contrast agent for MRI. However, the compound must provide signal from both modalities simultaneously to meet the requirements of bimodal PET/MRI agent. The experiment to prove it was conducted. In this experiment, **[Gd(^{18}FL^1)]** was prepared on the automated radiosynthesis module (GE FX N) from the precursor **[Gd(FL^1)]**. Prepared sample was subsequently

combined with a larger amount of the non-radioactive **[Gd(FL^1)]** to provide sufficient MRI contrast. From mixture prepared this way, a series of samples possessing different concentrations (0.05-0.5 mM) were prepared. Five samples of 0.1 - 0.5 mM Magnevist concentrations were prepared to serve as a standard for the MRI modality. All the samples were then simultaneously measured on a PET/MRI scanner. Figure 70 shows a separate MRI image and an MRI image overlaid with PET. This experiment demonstrated that it is possible to observe the contrast signal from PET and MRI simultaneously. Thus, the concept of a dual PET/MRI contrast agent was confirmed.

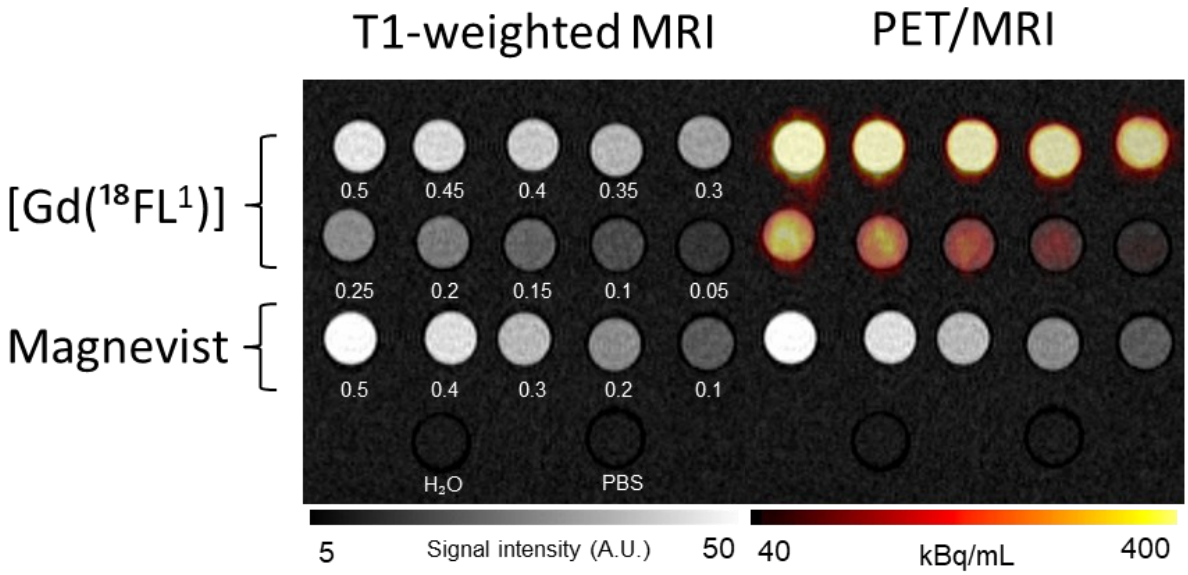

Figure 70: Validation of the dual contrast agent PET/MRI concept. In the T_1-weighted MRI image, decreasing signal enhancement can be observed in a series of **[Gd(**^{18}**FL**^{1}**)]** samples with concentrations ranging from 0.5 to 0.05 mM. In the **[Gd(**^{18}**FL**^{1}**)]** sample series, decreasing intensity can also be observed in the PET signal (color) in the PET/MRI image. The Magnevist samples provided an enhancement of the MRI signal, while no signal was observed in PET. Samples containing water and PBS buffer provide no signal in either modality.

3.2.4.8 Lactate-responsive bimodal PET/MRI probe [(Gd)^{18}FL^2]

The molecule **[Gd(**^{18}**FL**^{2}**)]** was designed as a PET/MRI responsive contrast agent. The design of its structure is altered in a way that this molecule lacks one acetate pendant arm compared to **[Gd(**^{18}**FL**^{1}**)]**. This structure alteration allows replacement of bound water molecules for lactate anion as depicted in Figure 71. This replacement leads to a decrease in the relaxivity of the complex and thus a reduction in the MRI signal. Lactate plays an important role in cancer metabolism, where its increased presence signals the transition of cancer cells to an anaerobic mode of energy acquisition.

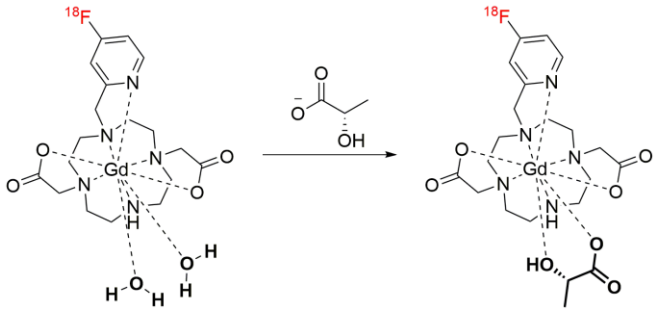

Figure 71: Responsive bimodal PET/MRI contrast agent **[Gd(^{18}FL^2)]** and schematic representation of the lactate anion binding. This binding causes a decrease in the hydration of the complex and thus a decrease in its relaxivity.

3.2.4.9 Optimization of [Gd(FL^2)] labelling

Initially, ^{18}F<–>^{19}F isotopic exchange was planned to perform on **[Gd(FL^2)]** (Figure 72). Same conditions for radiolabeling of **[Gd(FL^1)]** were used to label **[Gd(FL^2)]**. However, HPLC analysis revealed two radiolabeled compounds, but neither had a product retention time. The first peak was assigned to free $^{18}F^-$. Further analysis determined the identity of the second peak as the radiolabeled free ligand **^{18}FL^2** (Figure 73). The loss of metal and the resulting presence of free ligand was due to the lower kinetic inertness of **[Gd(FL^2)]**, which was discussed in Chapter 3.2.4.6. Fortunately, dechelatation can be suppressed by optimizing the reaction conditions. Initially, experiments were carried out using a combination of a QMA column pretreated with $NaHCO_3$ and $TBAHCO_3$ (in a H_2O/MeCN mixture) for the elution of $^{18}F^-$. It can be assumed that the leeching of gadolinium from chelate was a result of a combination of two factors. The first is the lower kinetic inertness of **[Gd(FL^2)]**, and the second is the formation of insoluble salts from the $TBAHCO_3$ elution solution between Gd(III) and bicarbonate. [22] When this precipitate forms, the gadolinium complex cannot be restored.

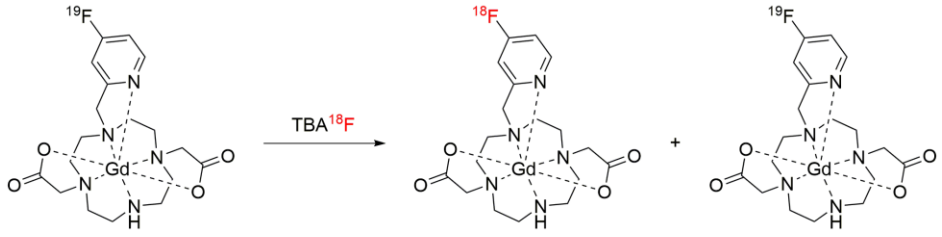

Figure 72: Scheme of the ^{18}F<–>^{19}F isotopic exchange reaction on the precursor **[Gd(FL^2)]**.

Table 11: Optimization of radiolabeling conditions with the precursor **[Gd(FL^2)]**. All reactions were carried out in dry solvents. The amount of precursor used was 1 mg unless otherwise stated. TBAF was used as a 1M solution in dry THF. Unless otherwise

stated, QMA (quaternary methyl ammonium) stationary phase was used for $^{18}F^-$ absorption in all cases. A 1/1 MeCN/H_2O mixture was used as the solvent for the elution of $^{18}F^-$ with $TBAHCO_3$ to produce $TBA^{18}F$.

Reaction	[Gd(FL^2)] ekv.(amount)	[Gd(FL^2)] c (mmol)	stationary phase/conditioning	Eluent	Temperature °C	RCY %	labeled ligand gamma %	conversion %	ligand conversion %
Entry 1	1(3mg)	33.06	$NaHCO_3$	$TBAHCO_3$	120	8	8	51	41
Entry 2	1	14.35	$NaHCO_3$	$TBAHCO_3$	120	0	8	25	75
Entry 3	1(3mg)	33.06	$NaHCO_3$	$TBAHCO_3$	150	0	6	21	71

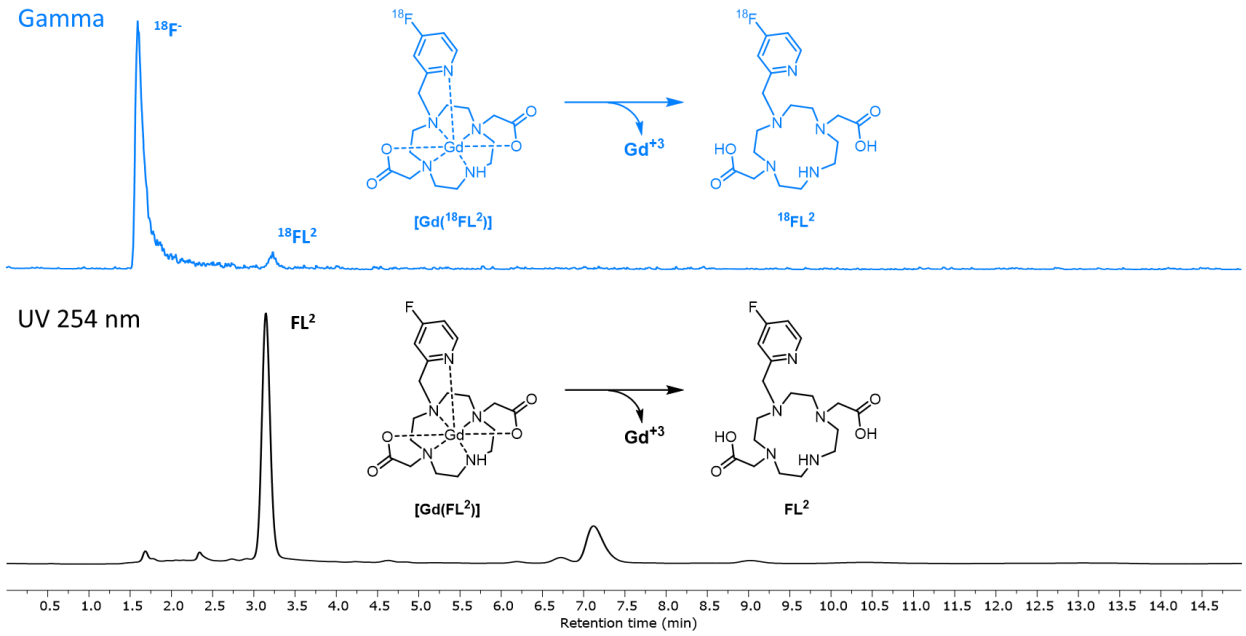

Figure 73: Chromatograms from the first attempts to prepare **[(Gd)$^{18}FL^2$]** by 18F<->19F isotopic exchange reactions on the precursor **[(Gd)FL^2]**. In the gamma detector, free $^{18}F^-$ and radiolabeled ligand **$^{18}FL_2$** are visible. In the UV detector at 254 nm, the free **FL^2** ligand is observed.

3.2.4.10 Optimization of [Gd(NO_2L^2)] labelling

Precursor **[(Gd)NO_2L^2]** was used in further experiments due to the gadolinium leaching previously discussed. This precursor proved to be superior to **[(Gd)FL^2]** in both radiochemical yield and suppression of gadolinium loss. The presence of radiolabeled **$^{18}FL^2$** or unlabeled **FL^2** in the reaction mixture indicated the decomposition of the gadolinium chelate, and interestingly, the amount of $TBAHCO_3$ in the final reaction mixture was related to the degree of dechelatation. In the reaction (Table 12, entry 7), 5 mg of $TBAHCO_3$ was used for elution of the $^{18}F^-$ from the QMA cartridge. In this case, 23% free ligand was present with 8% of RCY for the ligand, and the overall conversion was 36%. In another reaction (Table 12, entry 6), 2 mg of $TBAHCO_3$ were used instead. This resulted in a better conversion of 50% compared to

36% in the previous case (Table 12, entry 7). A lower decomplexation rate was also observed, 6% lower than in the reaction (Table 12, entry 7). Further improvement was observed in the case of (Table 12, entry 5), where just 1 mg of $TBAHCO_3$ was used for elution. This approach provided superior conversion of 69%, a radiochemical yield of 17%, and elimination of gadolinium loss, as the presence of free ligand was not observed. However, 1 mg was not sufficient to elute all $^{18}F^-$ from QMA cartridge, and therefore another method had to be implemented. The highest radiochemical yield without dechelatation was achieved using the KOTf/TBAOTf system (Table 12, entry 1 and 2). Gadolinium dechelatation was suppressed using this system. However, further experiments need to be carried out because the optimum separation conditions for complete removal of free $^{18}F^-$ from the reaction mixture, as seen in the chromatograms (Figure 75), have not yet been found.

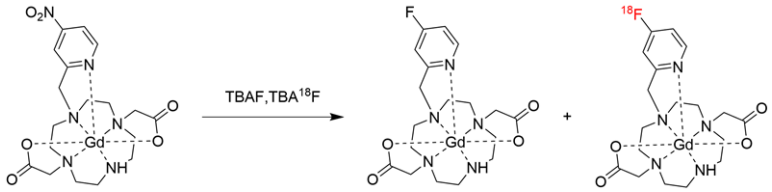

Figure 74: Scheme of radiochemical labelling of **[Gd(NO$_2$L^2)]** by nucleophilic aromatic substitution.

Table 12: Optimization of radiolabeling conditions with the precursor **[Gd(NO$_2$L^2)]**. All reactions were carried out in dry solvents. The amount of precursor used was 1 mg unless otherwise stated. TBAF was used as a 1M solution in dry THF. Unless otherwise stated, QMA (quaternary methyl ammonium) stationary phase was used for $^{18}F^-$ absorption in all cases. A 1/1 MeCN/H_2O mixture was used as the solvent for the elution of $^{18}F^-$ with $TBAHCO_3$ to produce TBA^{18}F. In cases where the KOTf/TBAOTf system was used, methanol was used for the elution of $^{18}F^-$ to produce TBA^{18}F.

Reaction	[Gd(NO$_2$L^2)] ekv.(amount)	[Gd(NO$_2$L^2)] c (mmol)	TBAF ekv.	stationary phase/conditioning	Eluent	Solvents	Temperature °C	Time min	RCY %	labelled ligand gamma %	conversion %	ligand conversion %
Entry 1	1(3mg)	35.21	3	KOTf	TBAOTf	DMSO	120	15	15	0	74	
Entry 2	1(3mg)	35.21	3	KOTf	TBAOTf	DMSO	120	15	15	0	72	
Entry 3	1(3mg)	35.21	3	KOTf	TBAOTf	DMSO	120	15	18	4	71	
Entry 4	1	14.35	3	KOTf	TBAOTf	DMSO	120	15	14	6	70	
Entry 5	1	14.35	3	NaHCO3	$TBAHCO_3$	DMSO	120	15	17	0	69	
Entry 6	1	14.35	3	NaHCO3	$TBAHCO_3$	DMSO	120	15	14	8	50	19
Entry 7	1	14.35	3	NaHCO3	$TBAHCO_3$	DMSO	120	15	11	8	36	23
Entry 8	1	14.35	3	NaHCO3	$TBAHCO_3$	DMSO	120	15	7	8	31	26
Entry 9	1	14.35	3	$NaHCO_3$	$TBAHCO_3$	DMSO	120	15	5	11	30	45
Entry 10	1	14.35	3	CB $PSHCO_3$	$TBAHCO_3$	DMSO	120	15	9	9	27	33
Entry 11	1(6mg)	62.7	3	$NaHCO_3$	$TBAHCO_3$	DMSO	120	15	6	9	11	40
Entry 12	1(2.9mg)	33.36	3	K2CO3	$TBAHCO_3$	DMSO	120	15	7	12	0	0
Entry 13	1(3.2mg)	36.66	3	$NaHCO_3$	$TBAHCO_3$	DMSO	120	15	0	9	0	54
Entry 14	1	14.35	3	NaHCO3	K222	DMSO	120	15	0	0	0	0

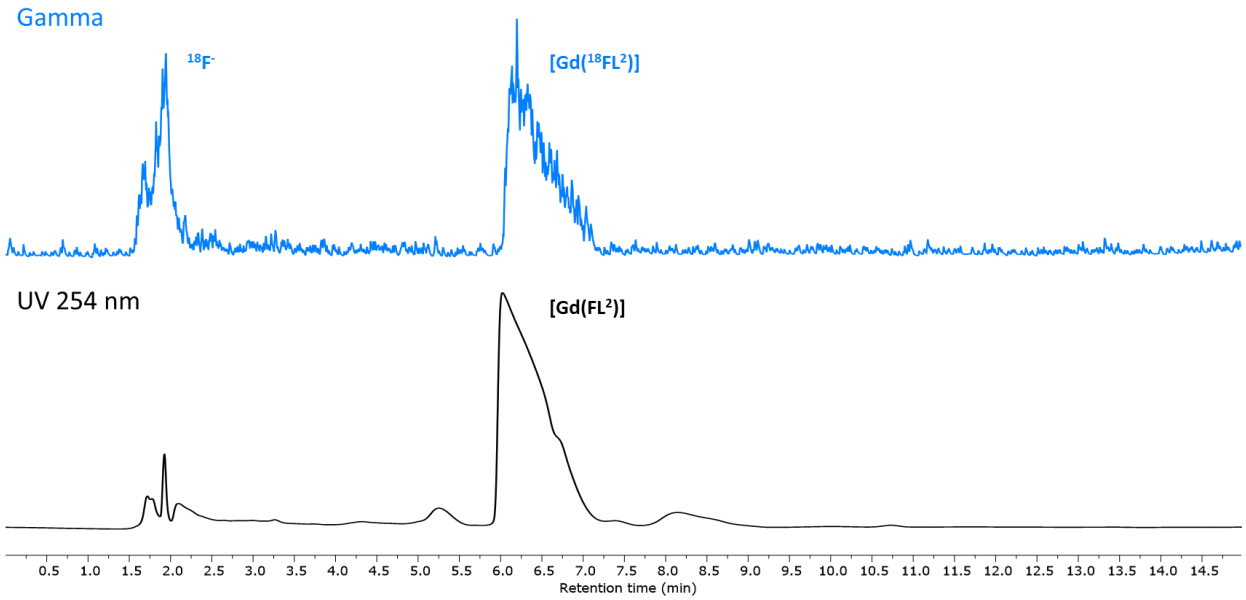

Figure 75: Chromatograms of a mixture of labelled **[Gd(^{18}FL^2)]** and unlabeled **[Gd(FL^2)]** after manual radiochemical synthesis from the precursor **[Gd(NO$_2$L^2)]**. Compared to the reaction using **[Gd(FL^2)]** as precursor (Figure 73), dechelation was suppressed and no free ligand is observed. However, free $^{18}F^-$ can be observed in the gamma chromatogram, and its removal yet needs to be optimized.

3.2.4.11 ***Lactate recognition with [(Gd)FL^2]***

In this experiment, the dependence of paramagnetic relaxation rate (R_{1p}) on lactate concentration (0.5 – 20 mM) was examined as shown in Figure 76. As a control experiment, a series of **[(Gd)FL^1]** samples were measured in parallel, where coordination is not possible due to the structural nature of this molecule. In the case of **[(Gd)FL^1]**, bidentate coordination of the lactate is not possible because the chelate contains eight donors and only one position is available for water or another ligand. As can be seen in the Figure 76, the relaxation rate of **[(Gd)FL^2]** indeed decreases with increasing lactate concentration (Figure 76, black dots), while the relaxation rate of **[(Gd)FL^1]** remains almost constant under the same conditions (Figure 76, blue dots). Data from this experiment suggest that the design of the **[(Gd)FL^2]** molecule allows lactate recognition.

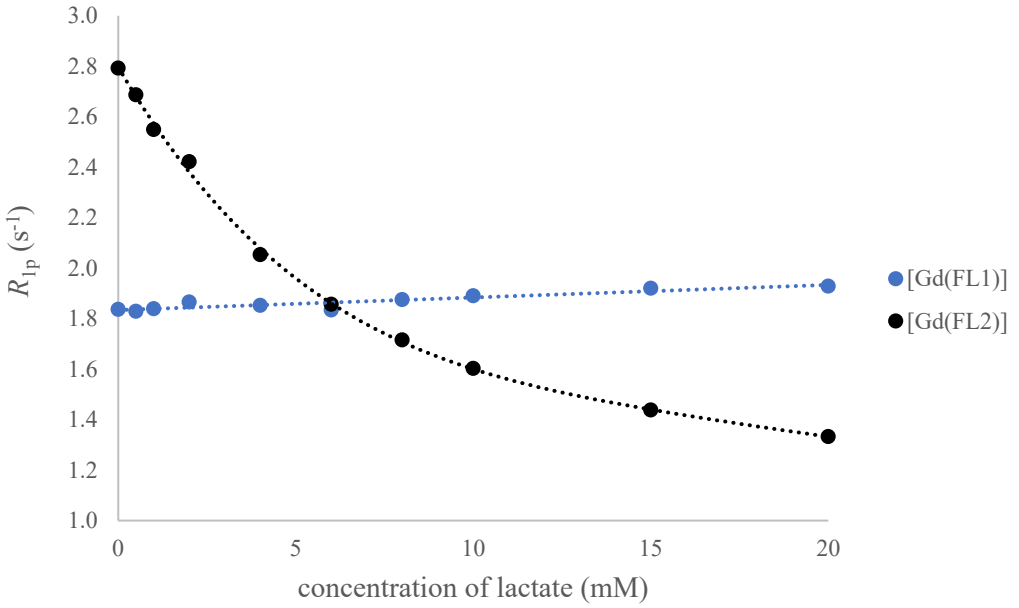

Figure 76: Dependence of paramagnetic relaxation rate of **[Gd(FL^2)]** on increasing lactate concentration. The experiment was performed at a temperature of 37 °C and a field strength of 0.47 T.

In vitro measurements of physio-chemical parameters of the chelates **[(Gd)FL^1]** and **[(Gd)FL^2]** provided the results summarized in Table 13.

Table 13: Summary of physio-chemical parameters of **[(Gd)FL^1]** and **[(Gd)FL^2]**

	[(Gd)FL^1]	**[(Gd)FL^2]**
Kinetic inertness	Kinetic inertness measurements under acidic conditions showed that **[(Gd)FL^1]** was significantly more stable than the clinically used Magnevist and **[(Gd)FL^2]**.	Kinetic inertness of **[(Gd)FL^2]** is more stable than the clinically used Magnevist.
Relaxivity and number of coordinated water molecules	The relaxivity for **[(Gd)FL^1]** was determined to be 3.43 $mM^{-1}s^{-1}$, this value corresponds to one coordinated water molecule.	The relaxivity of **[(Gd)FL^1]** is 5.33 $mM^{-1}s^{-1}$, this value corresponds to more than one coordinated water molecule. Most likely an equilibrium between q = 1 and q = 2 species.
Cytotoxicity test	The **[Gd(FL^1)]** has no greater effect on cell viability than clinically used Magnevist.	Data not available.
Responsiveness to lactate	The **[(Gd)FL^1]** doesn't respond to the presence of lactate.	The **[(Gd)FL^2]** recognizes presence of lactate.

3.2.4.12 In vivo [Gd(^{18}FL^1)] imaging

Optimized radiochemical synthesis and positive conclusions gained from physio-chemical measurements paved the way for *in vivo* imaging with **[Gd(^{18}FL^1)]**. Study to investigate the behavior of the PET/MRI bimodal contrast agent **[Gd(^{18}FL^1)]** in live mice was made possible thanks to the collaboration with WSIC. The MRI imaging was performed using the DCE-MRI technique, which is suitable for temporal and spatial observation of changing contrast agent concentration across the tissue. It is also very valuable in perfusion studies, where it is used to correlate the functionality of an organ with its anatomy. [122] In the first row of Figure 77, the DCE-MRI images show that the contrast agent is rapidly excreted by the kidneys. In the middle row of images, we can observe the PET signal, which also clearly shows that the contrast agent first accumulates in the kidneys, from where it is subsequently excreted into the bladder. This observation supports the assumption that the primary route of excretion is through the kidneys into the bladder. Simultaneous images from both modalities are shown in the bottom row.

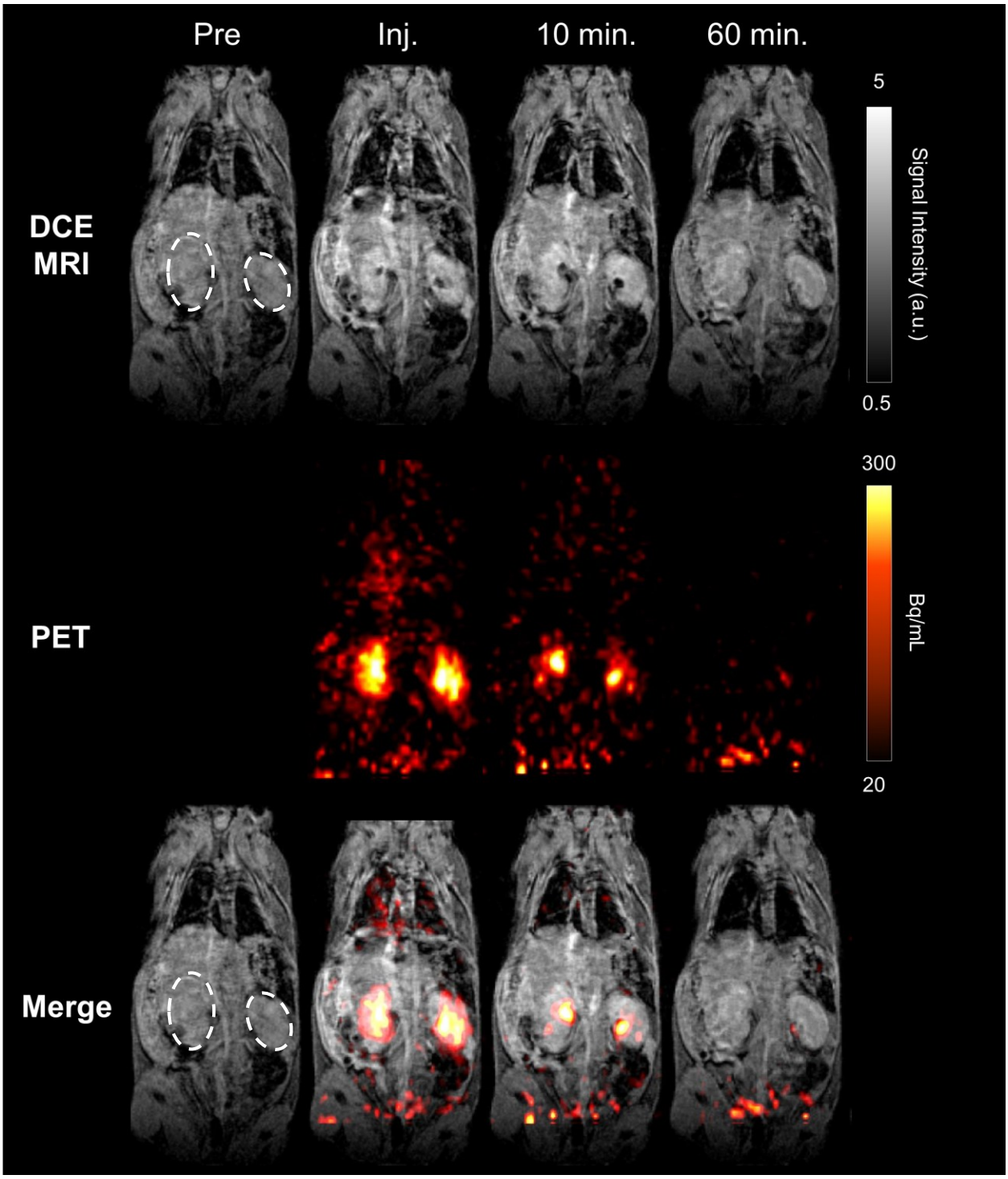

Figure 77: Images from *in vivo* application of **[Gd(**^{18}**FL**^{1}**)]** in mice. The top row of images shows (from left to right) MRI contrast before injection, during injection, 10 minutes after injection, and then 60 minutes after injection. The PET signal (color) is shown in the middle row of images at the same time points as the DCE-MRI. In the bottom row of images, the PET signal (color) is superimposed over the MRI signal (gray), also at the same time points. The contrast enhancement in the MRI and PET is delivered and acquired simultaneously. Kidneys are marked with dashed ovals.

3.2.5 PET/MRI: Conclusions

This part of the work focused on the design and synthesis of low-molecular weight bimodal contrast agents for PET/MRI, complexes **[Gd(^{18}FL^1)]** and **[Gd(^{18}FL^2)]**. Gadolinium complexes of DO2A and DO3A structural motifs with functionalized pyridine pendant arms were selected as precursors. In the search for a suitable pyridine leaving group that would allow direct incorporation of ^{18}F, the nitro group at the para position proved to be the most suitable. Based on these findings, the precursors **[Gd(NO$_2$L^1)]** and **[Gd(NO$_2$L^2)]** were synthesized. The compounds **[Gd(FL^1)]** and **[Gd(FL^2)]** were synthesized as cold standards and precursors for ^{19}F<−>^{18}F isotopic exchange. Preliminary radiolabeling experiments in collaboration with the Nuclear Physics Institute of the CAS have yielded encouraging results. Based on these results, a collaboration with the Werner Siemens Imaging Center was established to further explore the properties of the compounds on the PET/MRI scanner. In the course of this collaboration, the radiolabeling of **[Gd(NO$_2$L^1)]** was optimized and the procedure for ^{19}F<−>^{18}F isotope exchange on the precursor **[Gd(FL^1)]** was also developed. In the next step, the radiolabeling was further optimized on an automated radiosynthesis module to achieve sufficient radioactivity for *in vivo* experiments. This optimization delivered a sample with sufficient activity to theoretically carry out scans of five patients. Simultaneous acquisition of MRI and PET signals from *in vitro* experiment on a combined PET/MRI scanner confirmed the validity of the presented concept. Several physicochemical properties of **[Gd(FL^1)]** and **[Gd(FL^2)]** were measured before initiating *in vivo* experiments. Relaxivity, kinetic inertness, and cell viability assay yielded results validating the suitability for further *in vivo* experiments in mice, and therefore experiments with three mice were conducted. Dynamic contrast enhancement MRI and PET imaging on the PET/MRI scanner showed, how the dual contrast agent is first localized in the kidneys and then excreted into the bladder, which confirmed the initial assumption that this substance would be rapidly excreted primarily in the urine. By obtaining signals from both the MRI and PET modalities, the suitability of **[Gd(^{18}FL^1)]** as a bimodal perfusion PET/MRI contrast agent was confirmed. Radiolabeling experiments were also carried out with **[Gd(^{18}FL^2)]**, a lactate-responsive contrast agent. Experiments with **[Gd(^{18}FL^2)]** have provided very good aěconversion and reasonable radiochemical yields, however, complete removal of free ^{18}F$^-$ has not been achieved and the separation conditions yet need to be optimized. Measurements were carried out to demonstrate the ability of **[Gd(FL^2)]** as a lactate-responsive contrast agent. These measurements confirmed the responsiveness of the molecule, as it was observed that relaxivity decreased with increasing lactate concentration. In summary, two new bimodal contrast agents for PET/MRI were designed, synthesized, and their physicochemical properties were tested *in vitro*. One of these contrast agents, a perfusion agent **[Gd(^{18}FL^1)]**, was even tested *in vivo*. It can be expected that the results obtained in this project will pave the way for a new type of dual contrast agents for PET/MRI.

4 CONCLUSIONS

The presented work covers two topics: DO3A-Hyp building blocks and bimodal PET/MRI contrast agents. The unifying theme that runs through both parts could be described as an effort to develop chelators with additional beneficial functions. With this in mind, the DO3A-Hyp family of building blocks was developed, which allow incorporation of lanthanide chelates into peptide chains. Another important feature provided by these building blocks is the ability to controllably combine different lanthanides in peptide sequences. The exceptional property of these building blocks is their ability to provide a short and rigid connection to the peptide backbone. DO3A-Hyp building blocks were used to synthesize tripeptides consisting of two metal chelates in close proximity and one central amino acid bearing a CF_3 reporter group. Due to the rigidity and the possibility of close attachment to the peptide backbone, it was possible to combine the magnetic susceptibility tensors of the incorporated paramagnetic lanthanides and thus manipulate the paramagnetic shift of the CF_3 reporter group in the ^{19}F NMR. The fixation of two paramagnetic lanthanides in one peptide chain directs the magnetic susceptibility tensors such that the permutation of two elements leads to four unique signals. Based on this, a library of paramagnetically encoded molecules was synthesized and used to encode information in two settings. In the first setting, the information was encoded using mixtures of paramagnetically encoded molecules in layers of a single NMR sample, which were subsequently decoded using Z-resolved ^{19}F NMR. In the second setting, the information was also encoded by mixtures of paramagnetically encoded molecules, but these mixtures were organized in a well plate and decoded by ^{19}F MRI. The presented approach offers advantages over other currently used methods of encoding and decoding. For example, mass spectroscopy is a destructive method, and luminescence spectroscopy lacks the ability to recognize the order (positional isomers) of the units within an oligomer. In contrary, each of the codes prepared from paramagnetically encoded molecules can be read non-destructively by NMR.

The topic of multifunctional chelators was further investigated in the second part of this thesis. A method for direct radiolabeling of gadolinium chelates with $^{18}F^-$ was investigated with the prospect of creating a dual PET/MRI contrast agents. The pilot experiments with radiolabeling yielded positive results, which motivated us to establish a collaboration with the Werner Siemens Imaging Center. Within this collaboration, the radiolabeling procedures were optimized and further essential experiments were performed. The $^{19}F<\!\!-\!\!>^{18}F$ isotope exchange directly on gadolinium chelate was found to provide the most promising results. For *in vivo* imaging, it was essential to be able to produce a sample with sufficient activity. This was made possible by setting up radiochemical synthesis using an automated radiosynthesis module. With the sample thus prepared, phantoms were simultaneously measured on a PET/MRI scanner.

The measurements provided simultaneous images originating from both modalities, thus confirming the dual modality concept. The physiochemical parameters of these PET/MRI contrast agents, such as kinetic inertness and relaxivity, were also determined. In addition, the responsiveness of one of the contrast agents to lactate was evaluated and confirmed. All physicochemical measurements confirmed that both types of contrast agents are suitable for *in vivo* use. A small *in vivo* preclinical study was performed on three mice in order to further elucidate the behavior of the PET/MRI perfusion contrast agent. In these experiments, simultaneous PET and MRI images were obtained and showed contrast in animals from both techniques. Moreover, the *in vivo* study revealed that this perfusion contrast agent is rapidly excreted by the kidney into the bladder, which is preferred path of excretion. Further research is planned to identify the most promising diagnostic applications for the developed PET/MRI bimodal contrast agents.

5 EXPERIMENTAL PART

General: All chemicals were purchased from *Sigma-Aldrich* and *Fluorochem*. Dry solvents were purchased from *Acros Organics*. Deuterated solvents were purchased from *Eurisotop*. Throughout the text, all use of H_2O means Milli-Q water (18.2 mΩ·cm) and all use of M/Ln means M^{3+}/Ln^{3+}.

NMR spectroscopy: ^{1}H, ^{13}C and ^{19}F NMR spectra were recorded on Avance III™ HD 400 MHz spectrometer (*Bruker*, 400.1 MHz for ^{1}H, 100.6 MHz for ^{13}C) system equipped with either broad-band Prodigy cryo-probe with ATM module (5 mm CPBBO BB-^{1}H/^{19}F/D Z-GRD) or inversion broadband probe with ATM module (5 mm PA BBI ^{1}H/D-BB Z-GRD), Avance III™ HD 500 MHz spectrometer (*Bruker*, 500.0 MHz for ^{1}H, 125.7 MHz for ^{13}C, 470.4 MHz for ^{19}F) equipped with broad-band cryo-probe with ATM module (5 mm CPBBO BB-^{1}H/^{19}F/^{15}N/D Z-GRD) or Avance III™ HD 600 MHz spectrometer (*Bruker*, 600.1 MHz for ^{1}H, 150.9 MHz for ^{13}C) equipped with inverse triple resonance cryo-probe with ATM module (5 mm CPTCI ^{1}H/^{13}C/^{15}N/D Z-GRD). The temperature of the measurement is given for each experiment. Chemical shifts are in ppm, coupling constants in Hz. ^{19}F NMR spectra were referenced to TFA (δ_F = −76.55 ppm). Signals of cyclen macrocycle are abbreviated *mc*. Integrals in showcased NMR spectra were rounded to integers for clarity reasons (obscured signals that cannot be exactly integrated are colored grey). Signals arising from two rotamers (if resolved) are listed together, separated by semicolon.

Liquid chromatography: LC-MS experiments were performed on 1260 Infinity II (*Agilent*) equipped with Luna® Omega Polar column (5 µm, 100 Å, 150 × 4.6 mm) using H_2O–MeCN gradients (1 mL min^{-1} flow rate) with FA (0.1%) as an additive. Three methods were used: **Method 1** (0 min → 1 min 5% MeCN; 1 min → 10 min 5% → 100% MeCN); **Method 2** (0 min → 3 min 0% MeCN; 3 min → 10 min 0% → 50% MeCN); **Method 3** (0 min → 0.5 min 5% MeCN; 0.5 min → 5 min 5% → 100% MeCN; 5 min → 5.5 min 100% MeCN). **Method 4** (0 min → 3 min 5% MeCN; 3 min → 4 min 5% → 40% MeCN; 4 min → 10 min 40% → 75% MeCN). Preparative HPLC experiments were performed on 1260 Infinity II (*Agilent*) equipped with YMC-Actus Triart C18 column (5 µm, 100 Å, 250 × 20.0 mm) using H_2O–MeCN gradients (20 mL min^{-1} flow rate) with either FA (0.1%) or TFA (0.1%) as an additive. Normal phase flash chromatography (SiO_2, 40–60 µm, 60 Å) was performed on Combi*Flash*® NEXTGEN 300+ system from *Teledyne ISCO*. Reverse phase flash chromatography was performed with RediSep® R_f Gold C18 Aq column (*Teledyne ISCO*, 150 g) using H_2O–MeCN gradient system with TFA (0.1 %) as an additive.

High-resolution mass spectra: HRMS (with ESI ionization) were recorded on an *Agilent* 5975C MSD Quadrupol, Q-Tof micro from *Waters* or LTQ Orbitrap XL from *Thermo Fisher Scientific*.

Elemental analysis: CHN elemental analysis was performed on PE 2400 Series II CHN Analyzer from *Perkin Elmer*. Fluorine elemental analysis was performed by initial combustion of the sample in quartz vessel, followed by adsorption of resulting HF in H_2O and determining its concentration by potentiometry using fluoride ion selective electrode. Lanthanide content was determined by ICP-AES (SPECTRO Arcos from *SPECTRO Analytical Instruments*). All EA data are presented in calcd. (found) format.

5.1 DO3A-Hyp

^{19}F NMR spectroscopy: Measurements of all ^{19}F NMR spectra were done on Avance III^{TM} HD 500 MHz spectrometer (*Bruker*, 470.4 MHz for ^{19}F) equipped with broad-band cryo-probe with ATM module (5 mm CPBBO BB-^{1}H/^{19}F/^{15}N/D Z-GRD). Solutions of samples were prepared in MOPS/NaOH buffer (pH = 7) and placed into an insert capillary that was inserted into a 5 mm NMR tube containing D_2O (used for NMR frequency lock). The volume of solution in the insert observable by the spectrometer probe was approximately 50 µL. ^{19}F z-resolved NMR spectrum was acquired using a phase encoding pulse sequence with resolution 2048 x 64 points at 20 mm field of view, number of scans = 32K, acquisition time = 18 ms, relaxation delay = 100 µs (for technical reasons). The excitation pulse was approx. 31°, which was the result of optimization aiming to enhance the SNR of weaker (broader) signals, sacrificing the SNR of sharper peaks. This was possible due to the differences in T_1 relaxation times. Total experimental time was approx. 12 h. For subsequent processing only 700 x 64 raw points were used in order to reduce the noise. Data were apodized using QSINE window functions in both F2 (SSB = 10) and F1 (SSB = 1) dimensions and zero-filled to 8192 x 128 points. Processing was done in Bruker TopSpin 3.5 software. Spectra were visualized using the NumPy and Matplotlib Python libraries.

Magnetic resonance imaging: Stock solutions of individually synthesized **HoDy-TP1**, **DyDy-TP1**, **HoHo-TP1** and **DyHo-TP1** compounds in 0.5 M MOPS/NaOH buffer (pH = 7.0) were pipetted into a 7x5 well plate (cut out of standard 384 well plate) and the volume in each well was completed with water to 75 µL to reach compound concentrations ~0.36 mM each. The well plate was covered with plastic tape and imaged on 4.7 T scanner Bruker Biospec 47/20 (*Bruker BioSpin*, Ettlingen, Germany) with a custom-built dual ^{1}H/^{19}F RF surface coil. First, ^{1}H MRI was performed in all three planes (axial, coronal, and sagittal) for localization of the sample. Then, ^{19}F NMR spectra were acquired by 90° single pulse sequence to precisely determine resonance frequencies of the compounds. ^{19}F MRI images were obtained using a CSI sequence (120000 scans, repetition time = 700 ms, field of view = 50×50 mm; slice thickness = 10 mm, matrix of acquired image = 16×16×512, matrix of reconstructed image = 64×64×512, acquisition time = 23 hours 20 min, resonance frequency = 188630130 Hz, bandwidth = 9843 Hz/52.18 ppm). Images for display

were prepared in *Matlab*. First, the data in the Bruker format were imported to *Matlab* using *read_2dseq* function (by Cecil Yen (2021), https://www.mathworks.com/matlabcentral/fileexchange/69177-read_2dseq-quickly-reads-bruker-s-2dseq-mri-images). Maximum intensity projection along the frequency axis was used to find the peaks of the respective samples. Background signal (outside of main peaks) was calculated as an average of 41 slices (# 10–50 perpendicular to the frequency axis) and subtracted from each slice of the original data. Then, the intensity was normalized to 1 for the highest intensity. Final images displayed in Fig. 9 were obtained by averaging 15 slices (perpendicular to the frequency axis) around the maximum for each peak and mapping the image intensity to specific color maps.

X-Ray diffraction: The diffraction experiment for crystal structure determination was performed on D8 VENTURE Kappa Duo (Bruker) with PHOTONIII detector by IμS micro-focus sealed tube with MoKα (0.71073 Å) radiation at a temperature 120(2) K. The structure was solved by intrinsic phasing (XT)[123] and refined by full matrix least squares based on F^2 (SHELXL2018).[124] The hydrogen atoms on carbon were fixed into idealized positions (riding model) and assigned temperature factors $H_{iso}(H) = 1.2\ U_{eq}$ (pivot atom). In the case of [**Dy**(**L**^{1})]·3.5H_2O, the hydrogen atoms in –NH and –OH moieties were found on difference Fourier maps and refined under rigid body assumption with assigned temperature factors $H_{iso}(H) = 1.2\ U_{eq}$ (pivot atom). In the case of [**Dy**(**L**^{2})]·3H_2O, some hydrogen atoms in –NH and –OH moieties were found on difference Fourier maps and others were calculated into positions most suitable for the formation of hydrogen bonds. X-ray crystallographic data have been deposited with the Cambridge Crystallographic Data Centre (CCDC) under deposition number **2072548** for [**Dy**(**L**^{1})]·3.5H_2O and **2143481** for [**Dy**(**L**^{2})]·3H_2O. Both can be obtained free of charge from the Centre via its website (*www.ccdc.cam.ac.uk/getstructures*).

Figures are reproduced from the article (Paramagnetic encoding of molecules).[103]

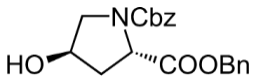

1

Synthesis of dibenzyl (*2S*,*4R*)-*4*-hydroxypyrrolidine-*1,2*-dicarboxylate (1): In a round-bottom glass flask (1 L), L-hydroxyproline (53.8 g, 0.41 mol, 1.00 equiv.) and $NaHCO_3$ (86.2 g, 1.03 mol, 2.5 equiv.) were dissolved in H_2O (370 mL). A solution of benzyl chloroformate (61.0 mL, 0.43 mol, 1.05 equiv.) in 90 ml of toluene was added dropwise to the reaction mixture. The reaction mixture was stirred at RT for 24 h. The organic phase containing toluene was separated and the water phase was extracted with ether (2 × 200 mL). The pH of remaining aqueous solution was adjusted to 2 with concentrated aq. HCl. The resulting

solid was extracted with ethyl acetate (3 × 150 mL). The organic layers were combined, washed with brine, and dried over anhydrous $MgSO_4$. Removal of the solvent provided a product as a colorless solid that was used without purification in the next step. In a round-bottom glass flask (2 L), (*2S*,*4R*)-*1*-((benzyloxy)carbonyl)-*4*-hydroxypyrrolidine-*2*-carboxylic acid (108 g, 0.41 mol, 1.00 equiv.) and BnBr (51.9 mL, 0.43 mol, 1.05 equiv.) were dissolved in THF (760 mL) followed by dropwise addition of TEA (43.3 g, 0.43 mol, 1.05 equiv.) at 0 °C. The solution was stirred at RT for 28 h The mixture was evaporated to dryness and the residue was re-dissolved in DCM (600 mL), washed subsequently with 1M HCl (2 × 300 mL), sat. aq. $NaHCO_3$ (2 × 250 mL), H_2O (300 mL) and brine (300 mL) and dried with anh. Na_2SO_4. Filtrate was evaporated to dryness and the colourless residue was re-dissolved in DCM and adsorbed onto SiO_2. The solid was transferred to sintered funnel and was washed with 5% EtOAc in Hexane (1.5 L) to wash away impurities followed by 50% EtOAc in Hexane (2 L) which yielded fractions containing product. Removal of the solvent afforded product as a colorless oil. Yield: 93 g (64%; 2 steps; based on (L-hydroxyproline). **NMR (CDCl$_3$, pair of rotamers): ^{1}H** (400.1 MHz, T = 300 K) δ_H 2.01–2.11 (C*H*$_2$–CH–CO, m, 1H); 2.21–2.40 (C*H*$_2$–CH–*C*O, m, 1H); 2.93 (O*H*, s, 1H); 3.49–3.73 (C*H*$_2$–N, m, 2H); 4.37–4.48 (C*H*–O, m, 1H); 4.55;4.59 (C*H*–CO, 2 × t, 1H, $^3J_{HH}$ = 7.9); 4.96–5.31 (C*H*$_2$–arom., m, 4H); 7.00–7.60 (arom., m, 10H). **^{13}C**{**^{1}H**} (100.6 MHz, T = 300 K) δ_C 38.31;39.11 (*C*H$_2$–CH–CO, 2 × s); 54.64;55.24 (*C*H$_2$–N, 2 × s); 57.90;58.14 (*C*H–CO, 2 × s); 66.85;66.98 (*C*H$_2$–arom., 2 × s); 67.28;67.31 (*C*H$_2$–arom., 2 × s); 69.16; 69.89 (*C*H–O, 2 × s); 127.50–128.79 (*arom.*, m); 135.36;135.57 (*arom.*, 2 × s); 136.19;136.40 (*arom.*, 2 × s); 154.71;155.18 (N–*C*O, 2 × s); 172.48;172.68 (*C*O, 2 × s). **ESI-HRMS:** 378.1315 $[M+Na]^+$ (theor. $[C_{20}H_{21}O_5N_1Na_1]^+$ = 378.1312).

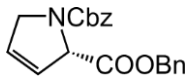

4

One-pot synthesis of dibenzyl (*S*)-2,5-dihydro-*1H*-pyrrole-1,2-dicarboxylate (4). ***Synthesis:*** In a round-bottom glass flask (500 mL), intermediate **1** (18.1 g, 51.0 mmol, 1.00 equiv.) and PPh_3 (14.1 g, 54.0 mmol, 1.05 equiv.) were dissolved in dry THF (120 mL) under Ar. Solution was cooled to 0 °C in an ice bath followed by dropwise addition of DIAD (98%, 10.6 mL, 53.8 mmol, 1.05 equiv.) and further followed by addition of MeI (3.36 mL, 54.0 mmol, 1.05 equiv.). The reaction mixture was then allowed to warm up to RT and it was further stirred at RT until disappearance of starting material that took approximately 3 h (controlled by TLC; SiO_2; Hexane–EtOAc 1:1). Reaction mixture containing intermediate **2** was then carefully evaporated to dryness (temperature of the bath was maintained at 30 °C). In a separate round-bottom glass flask (500 mL), $(PhSe)_2$ (7.96 g, 26.0 mmol, 0.5 equiv.) was suspended in dry EtOH (180 mL) and heated under condenser until dissolution under atmosphere of argon. Then, the reaction mixture was

put on an ice bath and $NaBH_4$ (2.00 g, 53.0 mmol, 1.04 equiv.) was added in four portions under Ar. The mixture was then stirred until colourless solution was produced followed by addition of solution of intermediate **2** in dry EtOH (80 mL) through condenser. Reaction mixture was then heated to 70 °C. After 60 mins, TLC confirmed consumption of starting material. Reaction mixture containing intermediate **3** was cooled to RT and diluted with THF (150 mL). Mixture was further cooled to 0 °C followed by dropwise addition of H_2O_2 (30% aq., 51.2 mL, 671 mmol, 13 equiv.). The reaction mixture was then allowed to warm up to RT and further stirred for 19 h. The solution was diluted with H_2O (400 mL) and extracted with 150 mL of Et_2O. Organic phase was washed with dil. aq. $NaHCO_3$ (2 × 150 mL), aq. Na_2SO_3 (10% aq., 2 × 150 mL), brine (2 × 150 mL) and evaporated to dryness. The residue was purified by column chromatography (SiO_2, 100 % Hexane to 15% EtOAc in Hexane). Fractions containing product were pooled and evaporated to dryness to yield the product as colourless oil. **Yield:** 14.5 g (84%; 3 steps; based on **1**). **NMR (CDCl$_3$):** **^{1}H** (400.1 MHz, *T* = 300 K) δ_H 4.22–4.45 (C*H*$_2$, m, 2H); 4.93–5.31 (C*H*–CO, C*H*$_2$–arom., m, 1H+4H); 5.69–5.81 (C*H*=CH, m, 1H); 5.89–6.07 (C*H*=CH, m, 1H); 7.04–7.60 (*arom.*, m, 10H). **^{13}C{^{1}H}** (100.6 MHz, *T* = 300 K) δ_C 53.56;54.06 (*C*H$_2$, 2 × s); 66.55;66.86 (C*H*–CO, 2 × s); 67.07;67.20;67.28;67.34 (*C*H$_2$–arom., 4 × s); 124.75;124.79 (*C*H=CH); 127.84–128.78 (*arom.*, m); 129.37;129.49 (*C*H=CH); 135.54;135.70 (*arom.*, 2 × s); 136.54;136.69 (*arom.*, 2 × s); 154.09;154.55 (N–*C*O, 2 × s); 169.89;170.19 (*C*O, 2 × s). **ESI-HRMS:** 338.1383 $[M+H]^+$ (theor. $[C_{20}H_{20}O_4N]^+$ = 338.1387).

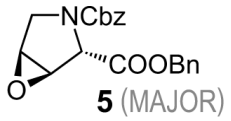

5 (MAJOR)

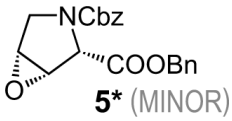

5* (MINOR)

Synthesis and of dibenzyl (*1R*,*2S*,*5S*)-*6*-oxa-*3*-azabicyclo[*3.1.0*]hexane-*2*,*3*-dicarboxylate (5) and dibenzyl (*1S*,*2S*,*5R*)-*6*-oxa-*3*-azabicyclo[*3.1.0*]hexane-*2*,*3*-dicarboxylate (5*): In a round-bottom glass flask (250 mL), intermediate **4** (11.83 g, 35.1 mmol, 1.0 equiv.) was dissolved in $CHCl_3$ (175 mL) followed by addition of MCPBA (77%, 14.2 g, 63.4 mmol, 1.8 equiv.). The solution was stirred at 85 ºC for 20 h. Mixture was concentrated followed by addition of DCM (70 mL) to produce precipitate. Reaction mixture was put into the freezer for 24 h. White precipitate was removed by filtration. Filtrate was evaporated and the residue was purified by column chromatography (SiO_2, 100% P.E. to 40% EtOAc in P.E.). Fractions containing pure compounds were evaporated, yielding **5** as transparent oil and **5*** as white solid. **Characterization of 5** (MAJOR)**: Yield:** 6.86 g (55%; 1 step; based on **4**). **NMR (CDCl$_3$, pair of rotamers): ^{1}H** (400.1 MHz, *T* = 300 K) δ_H 3.58;3.60 (C*H*$_2$–N, 2 × dd, 1H, $^2J_{HH}$ = 12.5, $^3J_{HH}$ = 1.4); 3.69;3.72 (CH$_2$–C*H*–O, 2 × dd, 1H, $^3J_{HH}$ = 2.9, $^3J_{HH}$ = 1.4); 3.80 (O–C*H*–CH–CO, d, 1H, $^3J_{HH}$ = 2.9); 3.95;4.00 (C*H*$_2$–N, 2 × d, 1H, $^2J_{HH}$ = 12.5); 4.71;4.81 (CH–CO, 2 × s, 1H); 5.05–5.32 (C*H*$_2$–arom., m, 4H); 7.03–7.62

(*arom.*, m, 10H). **^{13}C{^{1}H}** (100.6 MHz, T = 300 K) δ_C 47.27;47.52 (*C*H$_2$–N, 2 × s); 54.35;54.89 (CH$_2$–*C*H–O, 2 × s); 56.59;57.31 (O–*C*H–CH–CO, 2 × s); 60.74;60.89 (*C*H–CO, 2 × s); 67.44;67.54 (*C*H$_2$–arom., 2 × s); 67.56;67.63 (*C*H$_2$–arom., 2 × s); 127.83–128.95 (*arom.*, m); 135.21;135.08 (*arom.*, 2 × s); 136.25;136.31 (*arom.*, 2 × s); 154.76;155.28 (N–*C*O, 2 × s); 168.85;168.91 (*C*O, 2 × s). **ESI-HRMS:** 376.1152 [M+Na]$^+$ (theor. [$C_{20}H_{19}O_5N_1Na_1$]$^+$ = 376.1155). **EA** ($C_{20}H_{19}NO_5 \cdot 0.2H_2O$, M_R = 357.0): C 67.3 (67.4); H 5.5 (5.3); N 3.9 (3.8). **Characterization of 5*** (MINOR)**: Yield:** 2.67 g (22%; 1 step; based on **4**). **NMR (CDCl$_3$, pair of rotamers): ^{1}H** (400.1 MHz, T = 300 K) δ_H 3.58;3.63 (C*H*$_2$–N, 2 × dd, 1H, $^2J_{HH}$ = 12.5, $^3J_{HH}$ = 2.0); 3.78;3.80 (CH$_2$–C*H*–O, 2 × dd, 1H, $^3J_{HH}$ = 3.0, $^3J_{HH}$ = 2.0); 3.90;3.93 (C*H*$_2$–N, 2 × d, 1H, $^2J_{HH}$ = 12.5); 3.96–4.00 (O–C*H*–CH–CO, m, 1H); 4.46;4.52 (CH–CO, 2 × d, 1H, $^3J_{HH}$ = 2.4); 4.92–5.33 (C*H*$_2$–arom., m, 4H); 7.03–7.58 (*arom.*, m, 10H). **^{13}C{^{1}H}** (100.6 MHz, T = 300 K) δ_C 47.99;48.42 (*C*H$_2$–N, 2 × s); 55.78;56.23 (CH$_2$–*C*H–O, 2 × s); 57.37;58.21 (O–*C*H–CH–CO, 2 × s); 60.18;60.43 (*C*H–CO, 2 × s); 67.33;67.46 (*C*H$_2$–arom., 2 × s); 67.51;67.62 (*C*H$_2$–arom., 2 × s); 127.96–128.88 (*arom.*, m); 135.42;135.57 (*arom.*, 2 × s); 136.15;136.33 (*arom.*, 2 × s); 154.51;155.05 (N–*C*O, 2 × s); 167.15;167.65 (*C*O, 2 × s). **ESI-HRMS:** 376.1151 [M+Na]$^+$ (theor. [$C_{20}H_{19}O_5N_1Na_1$]$^+$ = 376.1155). **EA** ($C_{20}H_{19}NO_5 \cdot 0.2H_2O$, M_R = 357.0): C 67.3 (67.2); H 5.5 (5.2); N 3.9 (3.7).

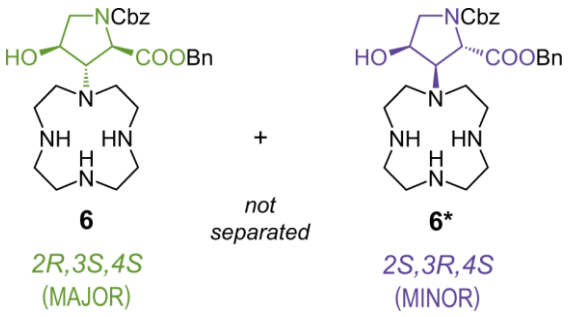

Synthesis of intermediate 6 and 6*: In a round-bottom glass flask (250 mL), intermediate **5** (2.0 g, 5.60 mmol, 1.0 equiv.) and cyclen (3.9 g, 22.6 mmol, 4.0 equiv.) were dissolved in dry *t*-BuOH (120 mL). The resulting solution was stirred at 105 °C for 24 h. After cooling to RT, reaction mixture was quenched with TFA (2.65 mL) and concentrated to dryness. Resulting oil was purified by flash chromatography (C18, H$_2$O/MeCN gradient with 0.1% TFA additive). Fractions with product were joined and lyophilized to give product (as a mixture of *2R,3S,4S–2S,3R,4S* regioisomers in ~9:1 ratio) in the form of TFA salt as faint brown solid (regioisomer separation was possible in the next steps – **7** and **8**). **Yield:** 2.30 g (54%; 1 step; based on **5**). **ESI-HRMS:** 526.3010 [M+H]$^+$ (theor. [$C_{28}H_{40}O_5N_5$]$^+$ = 526.3024). **EA** ($C_{28}H_{39}N_5O_5 \cdot 2.3TFA \cdot 0.3H_2O$, M_R = 793.3): C 49.4 (49.5); H 5.3 (5.1); N 8.8 (8.8); F 16.5 (16.3).

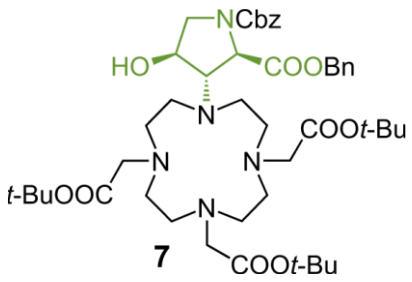

7

Synthesis of intermediate 7: In a pearl-shaped glass flask (50 mL), intermediate **6**·2.3TFA·0.3H_2O (mixture of *2R,3S,4S–2S,3R,4S* regioisomers in ~9:1 ratio, 788 mg, 0.99 mmol, 1.0 equiv.) and K_2CO_3 (863 mg, 6.24 mmol, 6.3 equiv.) were mixed in 20 mL of MeCN followed by addition of tert-butyl bromoacetate (630 µL, 4.23 mmol, 4.3 equiv.). The resulting suspension was stirred at RT for 16 h. Reaction mixture was filtered through syringe microfilter (PTFE), and the filtrate was evaporated to dryness. Residue was purified by preparative HPLC (C18, H_2O/MeCN gradient with 0.1% FA additive). Fractions with pure product (*2R,3S,4S*) were joined and lyophilized to give product in the form of mixed TFA/FA salt as white solid. **Yield:** 575 mg (62%; 1 step; based on **6**·2.3TFA·0.3H_2O). **NMR (CD$_3$CN, pair of rotamers):** ^{1}**H** (600.1 MHz, T = 298.1 K) δ_H 1.46–1.47 (CH_3, m, 27H); 2.58–3.23 (*mc*, CH_2, m, 16H+1H); 3.44–3.62 (CH_2–CO, CH–N, m, 2H+1H); 3.62–3.83 (CH_2–CO, m, 4H); 3.83–3.90 (CH_2, m, 1H); 4.06–4.24 (CH–O, m, 1H); 4.24–4.36 (CH–CO, m, 1H); 4.97–5.20 (CH_2–arom., m, 4H); 7.07–7.51 (*arom.*, m, 10H); **^{13}C{^{1}H}** (150.9 MHz, T = 298.1 K) δ_C 28.47 (*C*H$_3$, s); 28.50 (*C*H$_3$, s); 47.59 (*mc*, s); 50.58 (*mc*, s); 52.00 (*C*H$_2$, s); 53.10 (*mc*, s); 53.34 (*mc,* s); 56.05 (*C*H$_2$–CO, s); 56.44 (*C*H$_2$–CO, s); 58.21;58.67 (*C*H–CO, 2 × s); 68.00–68.22 (*C*H$_2$–arom., m); 70.54;71.13 (CH–O, 2 × s); 72.09;72.98 (*C*H–N, 2 × s); 83.5 (*C*–CH$_3$, s); 84.27 (*C*–CH$_3$, s); 128.77–129.80 (*arom.*, m); 136.64;136.84 (*arom.*, 2 × s); 137.80;138.06 (*arom.*, 2 × s); 155.01;155.65 (*C*O–N, 2 × s); 169.25 (*C*O–O, s); 170.54 (*C*O–O, s); 172.88;173.22 (*C*O–O, 2 × s). **ESI-HRMS:** 868.5063 $[M+H]^+$ (theor. $[C_{46}H_{70}O_{11}N_5]^+$ = 868.5066). **EA** ($C_{28}H_{39}N_5O_5$·0.3TFA·0.8FA, M_R = 939.1): C 60.6 (60.8); H 7.6 (7.5); N 7.5 (7.2); F 1.8 (2.0).

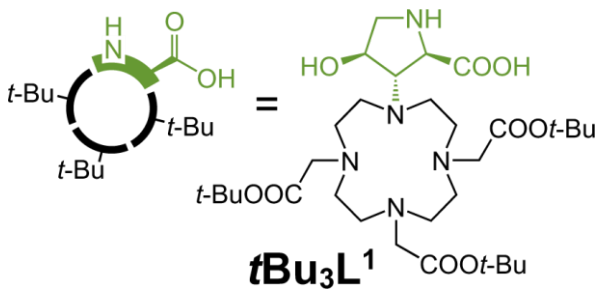

Synthesis of building block *t*Bu$_3$L^1: In a pear-shaped glass flask (50 mL), Pd@C (10%, 57 mg) was three-times secured with Ar followed by addition of solution of intermediate **7**·0.3TFA·0.8H$_2$O (522 mg, 556 µmol, 1.0 equiv.) in MeOH (20 mL) through septum. The mixture was then stirred at RT for 30 min with slow bubbling of H$_2$ (from balloon) through the mixture. Reaction mixture was filtered through syringe microfilter (PTFE) and the filtrate was evaporated to dryness. Residue was purified by flash chromatography (C18, H$_2$O/MeCN gradient with 0.1% TFA additive). Fractions with product were joined and lyophilized to give product in the form of TFA salt as white solid. **Yield:** 313 mg (56%; 1 step; based on **7**·0.3TFA·0.8H$_2$O). **NMR (CD$_3$CN): ^{1}H** (500.0 MHz, T = 330 K) δ_H 1.47 (C*H*$_3$, s, 9H); 1.49 (C*H*$_3$, s, 18H); 2.99–3.22 (*mc*, C*H*$_2$, m, 8H+1H); 3.22–3.46 (*mc*, m, 8H); 3.46–3.56 (C*H*$_2$, C*H*$_2$–CO, m, 1H+1H); 3.61 (C*H*$_2$–CO, d, 1H, $^2J_{HH}$ = 17.8); 3.84 (C*H*–N, dd, 1H, $^3J_{HH}$ = 8.2, $^3J_{HH}$ = 6.9); 3.87–4.00 (C*H*$_2$–CO, m, 4H); 4.13 (C*H*–CO, d, 1H, $^3J_{HH}$ = 8.2); 4.44 (C*H*–O, q, 1H, $^3J_{HH}$ = 7.0). **^{13}C{^{1}H}** (125.7 MHz, T = 330 K) δ_C 28.43 (*C*H$_3$, s); 28.57 (*C*H$_3$, s); 47.16 (*mc*, s); 50.21 (CH$_2$, s); 50.36 (*mc,* s); 52.95 (*mc,* s); 52.98 (*mc,* s); 55.73 (*C*H$_2$–CO, s); 55.92 (*C*H$_2$–CO, s); 58.32 (*C*H–CO, s); 69.26 (*C*H–N, s); 71.04 (*C*H–O, s); 83.80 (*C*–CH$_3$, s); 85.28 (*C*–CH$_3$, s); 168.26 (*C*O, s); 170.80 (*C*O, s); 171.44 (*C*O, s). **ESI-HRMS:** 644.4227 [M+H]$^+$ (theor. [C$_{31}$H$_{58}$O$_9$N$_5$]$^+$ = 644.4229). **EA** (C$_{31}$H$_{57}$N$_5$O$_9$·3.0TFA·0.9H$_2$O, M_R = 1002.0): C 44.4 (44.4); H 6.2 (6.3); N 7.0 (7.0); F 17.1 (17.0).

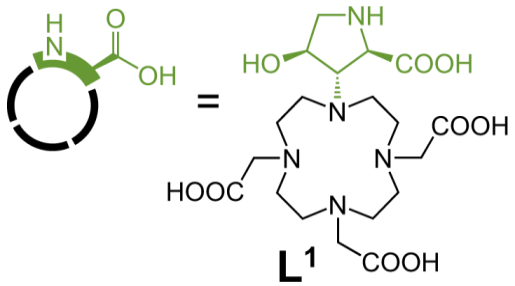

Synthesis of building block L^1: In a pear-shaped glass flask (25 mL), ***t*-Bu$_3$L^1**·3.0TFA·0.9H$_2$O (278 mg, 0.28 mmol) was dissolved in TFA (4 mL). The resulting solution was stirred at RT for 5 h. The mixture was evaporated to dryness and once co-evaporated with MeOH. Residue was purified by preparative HPLC

(C18, H_2O/MeCN gradient with 0.1% TFA additive). Fractions with product were joined and lyophilized to give product in the form of TFA salt as white solid. **Yield:** 156 mg (71%; 1 step; based on ***t*-Bu$_3$L^1**·3.0TFA·0.9H_2O). **NMR (DMSO-d$_6$): ^{1}H** (500.0 MHz, T = 330 K) δ_H 2.87–2.91 (*mc*, m, 4H); 3.00–3.05 (CH_2, *mc*, m, 1H+4H); 3.10–3.18 (*mc*, m, 8H); 3.38 (CH_2, dd, 1H, $^2J_{HH}$ = 11.7, $^3J_{HH}$ = 6.4); 3.57 (C*H*–N, dd, 1H, $^3J_{HH}$ = 7.1, $^3J_{HH}$ = 5.9); 3.63 (CH_2–CO, s, 2H); 3.77 (CH_2–CO, s, 4H); 4.09 (C*H*–CO, d, 1H, $^3J_{HH}$ = 7.1); 4.30 (C*H*–O, q, 1H, $^3J_{HH}$ = 6.3). **^{13}C{^{1}H}** (125.7 MHz, T = 330 K) δ_C 46.22 (*mc*, s); 49.08 (*mc*, s); 49.60 (*C*H–CO, s); 51.41 (*mc,* s); 51.88 (*mc*, s); 53.81 (*C*H$_2$–CO, s); 54.52 (*C*H$_2$–CO, s); 57.42 (CH_2, s); 69.08 (*C*H–O, s); 70.01 (*C*H–N, s); 169.92 (*C*O, s); 170.11 (*C*O, s); 171.08 (*C*O, s). **ESI-HRMS:** 474.2209 $[M-H]^-$ (theor. $[C_{19}H_{32}O_9N_5]^-$ = 474.2206). **EA** ($C_{19}H_{33}N_5O_9$·2.4TFA·2.5H_2O, M_R = 794.1): C 36.0 (36.0); H 5.1 (4.8); N 8.8 (8.7); F 17.2 (17.0).

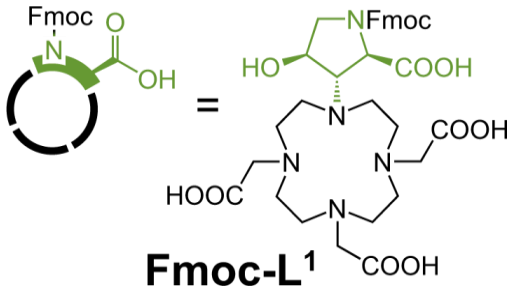

Fmoc-L^1

Synthesis of building block Fmoc-L^1: In a pear-shaped glass flask (25 mL), ***t*Bu$_3$L^1**·3.0TFA·0.9H_2O (69.0 mg, 68.9 µmol, 1.0 equiv.) was dissolved in a mixture of MeCN (4 mL) and aq. borate buffer (200 mM, pH 9.0, 3.45 mL, 690 µmol, 10 equiv.) followed by addition of FmocCl (17.8 mg, 68.8 µmol, 1.0 equiv.). The mixture was stirred at RT for 30 mins. Solution was purified by preparative HPLC (C18, H_2O/MeCN gradient with 0.1% TFA additive). Fractions with *tert*-butyl protected product were joined and evaporated to dryness. Residue was dissolved in TFA (2 mL) and stirred at RT for 5 h. The mixture was evaporated to dryness and once co-evaporated with MeOH. Residue was purified by preparative HPLC (C18, H_2O/MeCN gradient with 0.1% FA additive). Fractions with product were joined and lyophilized to give product in the form of mixed FA/TFA salt as white solid. **Yield:** 41 mg (60%; 2 steps; based on ***t*Bu$_3$L^1**·3.0TFA·0.9H_2O). **NMR (DMSO-d$_6$, pair of rotamers): ^{1}H** (500.0 MHz, T = 298.1 K) δ_H 2.67–3.29 (*mc*, CH_2, m, 16H+1H); 3.42–4.21 (CH_2, C*H*–N, C*H*–CO, C*H*–O, CH_2–CO, m, 1H+1H+1H+1H+6H, obscured by signal from H_2O); 4.21–4.33 (*Fmoc*, m, 3H); 7.29–7.37 (*Fmoc*, m, 2H); 7.40–7.45 (*Fmoc*, m, 2H); 7.62–7.67 (*Fmoc*, m, 2H); 7.87–7.92 (*Fmoc*, m, 2H). **^{13}C{^{1}H}** (125.7 MHz, T = 298.1 K) δ_C 45.68–54.03 (*mc*, *C*H$_2$–CO, m); 46.82;46.89 (*Fmoc*, 2 × s); 50.91;51.45 (CH_2, 2 × s); 55.84;57.01 (*C*H–CO, 2 × s); 66.89;67.33 (*Fmoc*, 2 × s); 69.13;69.24 (*C*H–O, 2 × s); 70.20;71.43 (*C*H–N, 2 × s); 120.33–120.44 (*Fmoc*, m);

125.30;125.38;125.45;125.54 (*Fmoc*, 4 × s); 127.35–127.43 (*Fmoc*, m); 127.86–128.08 (*Fmoc*, m); 140.86;140.92;140.99;141.02 (*Fmoc*, 4 × s); 143.85;143.88;143.95;143.99 (*Fmoc*, 4 × s); 153.84+154.05 (N–*C*O, 2 × s); 170.25 (*C*O, s); 172.11 (*C*O, s); 173.48;173.73 (*C*O, 2 × s). **ESI-HRMS:** 698.3033 $[M+H]^+$ (theor. $[C_{34}H_{44}O_{11}N_5]^+$ = 698.3032). **EA** ($C_{34}H_{43}N_5O_{11}$·2.0TFA·1.3FA M_R = 985.5): C 47.9 (47.8); H 4.9 (4.8); N 7.1 (7.0); F 11.6 (11.7).

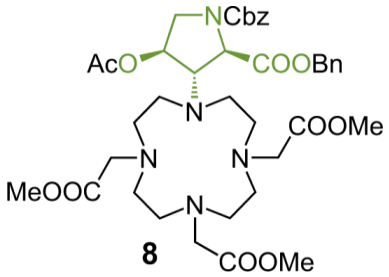

8

Synthesis of intermediate 8: In a pear-shaped glass flask (50 mL), intermediate **6**·2.3TFA·0.3H_2O (mixture of *2R,3S,4S–2S,3R,4S* regioisomers in ~9:1 ratio, 464 mg, 585 µmol, 1.0 equiv.) and K_2CO_3 (508 mg, 3.68 mmol, 6.3 equiv.) were mixed in 25 mL of MeCN followed by addition of methyl bromoacetate (209 µL, 2.21 mmol, 3.8 equiv.). The resulting suspension was stirred for at RT 16 h. Reaction mixture was filtered through syringe microfilter (PTFE), and the filtrate was evaporated to dryness. Residue was purified by preparative HPLC (C18, H_2O/MeCN gradient with 0.1% TFA additive). Fractions with fully alkylated intermediate were joined and lyophilized. The resulting white solid was dissolved in MeCN (8 mL) followed by addition of Ac_2O (102 µL, 1.08 mmol; 1.8 equiv.), TEA (362 µL, 2.60 mmol, 4.5 equiv.) and DMAP (3 mg, 22 µmol, ~4 mol %). The resulting solution was stirred at RT for 24 h. Reaction mixture was evaporated to dryness and the residue was purified by preparative HPLC (C18, H_2O/MeCN gradient with 0.1% TFA additive). Fractions with pure product (*2R,3S,4S*) were joined and lyophilized to give product in the form of TFA salt as white solid. **Yield:** 323 mg (54%; 2 steps; based on **6**·2.3TFA·0.3H_2O). **NMR (CD$_3$CN, pair of rotamers):** ^{1}**H** (500.0 MHz, T = 298.1 K) δ_H 1.95;1.96 (C*H*$_3$–C, 2 × s, 3H); 2.50–3.24 (*mc*, C*H*$_2$, m, 16H+1H); 3.32–3.79 (C*H*–N, C*H*$_2$–CO, C*H*$_3$–O, m, 1H+6H+9H); 3.93–4.07 (C*H*$_2$, m, 1H); 4.35–4.42 (C*H*–CO, m, 1H); 7.02–7.55 (*arom.*, m, 10H). ^{13}**C**{^{1}**H**} (125.7 MHz, T = 298.1 K) δ_C 21.16 (*C*H$_3$–C, s); 46.95;47.15 (*mc*, s); 50.13;50.37 (*C*H$_2$, 2 × s); 52.50–52.96 (*C*H$_3$–O, m); 51.69–55.35 (mc, *C*H$_2$–CO, m); 60.18;60.60 (*C*H–CO, 2 × s); 67.95–68.13 (*C*H$_2$–arom., m); 70.17;71.41 (*C*H–N, 2 × s); 73.40;74.11 (*C*H–O, 2 × s); 128.66–129.62 (*arom.*, m); 136.55;136.71 (*arom.*, 2 × s); 137.56;137.72 (*arom.*, 2 × s); 155.41;155.61 (*C*O–N, 2 × s); 170.32–171.43 (*C*O–O, m); 171.73;172.02 (*C*O–O, 2 × s). **ESI-HRMS:** 784.3757 $[M+H]^+$ (theor. $[C_{39}H_{54}O_{12}N_5]^+$ = 784.3764). **EA** ($C_{39}H_{53}N_5O_{12}$·1.9TFA·0.8H_2O, M_R = 1014.9): C 50.7 (50.9); H 5.6 (5.6); N 6.9 (6.6); F 10.7 (10.6).

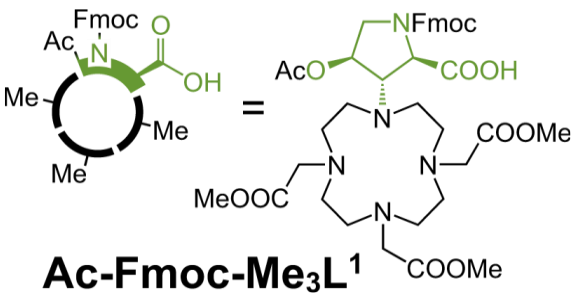

Ac-Fmoc-Me$_3$L^1

Synthesis of building block Ac-Fmoc-Me$_3$L^1: In a pear-shaped glass flask (50 mL), Pd@C (10%, 35 mg) was three-times secured with Ar followed by addition of solution of intermediate **8**·1.9TFA·0.8H$_2$O (346 mg, 341 μmol, 1.0 equiv.) in MeOH (30 mL) through septum. The mixture was then stirred at RT for 30 min with slow bubbling of H$_2$ (from balloon) through the mixture. Reaction mixture was filtered through syringe microfilter (PTFE) and the filtrate was evaporated to dryness. Residue was purified by preparative HPLC (C18, H$_2$O/MeCN gradient with 0.1% TFA additive). Fractions with partially deprotected intermediate were joined and lyophilized. The resulting white solid (153 mg, assuming M·TFA, M_R = 674, 0.23 mmol) was dissolved in a mixture of MeCN (12 mL) and aq. borate buffer (200 mM, pH 9.0, 11.3 mL, 2.26 mmol, 10 equiv.) followed by addition of FmocCl (58 mg, 0.23 mmol, 1.0 equiv.). The mixture was stirred for at RT for 30 mins. Solution was then concentrated and purified by preparative HPLC (C18, H$_2$O/MeCN gradient with 0.1% TFA additive). Fractions with product were joined and lyophilized to give product in the form of TFA salt as white solid. **Yield:** 184 mg (52%; 2 steps; based on **8**·1.9TFA·0.8H$_2$O). **NMR (CD$_3$CN, pair of rotamers):** ^{1}**H** (500.0 MHz, T = 323 K) δ_H 1.99;2.02 (C*H*$_3$–C, 2 × s, 3H); 2.66–4.22 (*mc*, C*H*$_2$, C*H*–N, C*H*$_3$–O, C*H*$_2$–CO, m, 16H+2H+1H+9H+6H); 4.21–4.55 (*Fmoc*, C*H*–CO, m, 3H+1H); 4.80–5.16 (C*H*–O, m, 1H); 7.33–7.44 (*Fmoc*, m, 4H); 7.61–7.67 (*Fmoc*, m, 2H); 7.82–7.86 (*Fmoc*, m, 2H). ^{13}**C**{^{1}**H**} (125.7 MHz, T = 323 K) δ_C 21.31 (*C*H$_3$–C, s); 48.24 (*Fmoc*, s); 52.99 (*C*H$_3$–O, s); 53.62 (*C*H$_3$–O, s); 46.89–55.14 (*mc*, C*H*$_2$–CO, *C*H$_2$, m); 58.77;59.93 (*C*H–CO, 2 × s); 68.43 (*Fmoc*, s); 69.05;70.43 (*C*H–N, 2 × s); 74.03 (*C*H–O, s); 121.12 (*Fmoc*, s); 126.22 (*Fmoc*, s); 128.30 (*Fmoc*, s); 128.90 (*Fmoc*, s); 142.25–142.41 (*Fmoc*, m); 145.06–145.28 (*Fmoc*, m); 154.69;155.47 (N–*C*O, 2 × s); 169.24–172.59 (*C*O, *C*O, m). **ESI-HRMS:** 782.3600 $[M+H]^+$ (theor. $[C_{39}H_{52}O_{12}N_5]^+$ = 782.3607). **EA** ($C_{39}H_{51}N_5O_{12}$·1.9TFA·1.3H$_2$O, M_R = 1035.7): C 50.3 (50.6); H 5.5 (5.4); N 6.9 (6.5); F 10.6 (10.7).

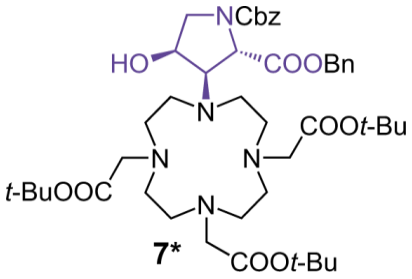

Synthesis and of intermediate 7*: Obtained as a side product during synthesis of **7.** Fractions with pure product (*2S,3R,4S*) were joined and lyophilized to give product as white solid. **Yield:** 47 mg (5%; 1 step; based on **6**·2.3TFA·0.3H_2O assuming **7***·0.3TFA·0.8FA, M_R = 939). **NMR (CD$_3$CN, pair of rotamers):** **^{1}H** (500.0 MHz, T = 298.1 K) δ_H 1.42 (CH_3, s, 27H); 2.34–2.56 (*mc*, m, 4H); 2.56–2.90 (*mc*, m, 12H); 3.02–3.33 (CH_2–CO, m, 6H); 3.33–3.43 (CH_2, m, 1H); 3.43–3.59 (CH_2, C*H*–N m, 1H+1H); 4.10–4.30 (C*H*–O, m, 1H); 4.30–4.47 (C*H*–CO, m, 1H); 4.79–5.31 (CH_2–arom., m, 4H); 7.07–7.51 (*arom.*, m, 10H). **^{13}C{^{1}H}** (125.7 MHz, T = 298.1 K) δ_C 28.39 (CH_3, s); 52.49;52.88 (*mc*, 2 × s); 53.39;53.50 (CH_2, 2 × s); 53.84;53.88 (*mc*, 2 × s); 54.41;54.44 (*mc*, 2 × s); 56.64 (CH_2–CO, s); 57.51;57.54 (CH_2–CO, 2 × s); 57.77;58.39 (C*H*–CO, 2 × s); 67.50;67.55 (CH_2–arom., 2 × s); 67.64;67.71 (CH_2–arom., 2 × s); 68.29;69.34 (C*H*–N, 2 × s); 72.45;72.96 (C*H*–O, 2 × s); 81.16 (*C*–CH_3, s); 81.47 (*C*–CH_3, s); 128.44–129.79 (*arom.*, m); 136.70;136.90 (*arom.*, 2 × s); 137.83;138.08 (*arom.*, 2 × s); 155.36;155.73 (*C*O–N, 2 × s); 171.31 (*C*O–O, s); 171.81 (*C*O–O, s); 172.88;173.22 (*C*O–O, 2 × s). **ESI-HRMS:** 868.5068 $[M+H]^+$ (theor. $[C_{46}H_{70}O_{11}N_5]^+$ = 868.5066).

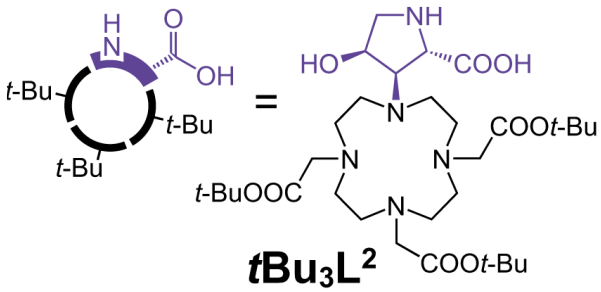

Synthesis of building block *t*Bu$_3$L^2: In a glass flask (4 mL), Pd@C (10%, 4 mg) was three-times secured with Ar followed by addition of solution of intermediate **7***·0.3TFA·0.8FA (47 mg, 50 µmol, 1.0 equiv.) in MeOH (2 mL) through septum. The mixture was then stirred at RT for 30 min with slow bubbling of H_2 (from balloon) through the mixture. Reaction mixture was filtered through syringe microfilter (PTFE) and the filtrate was evaporated to dryness. Residue was purified by preparative HPLC (C18, H_2O/MeCN gradient with 0.1% TFA additive). Fractions with product were joined and lyophilized to give product in the form of TFA salt as white solid. **Yield:** 27 mg (56%; 1 step; based on **7***·0.3TFA·0.8FA). **NMR (DMSO-d$_6$):** **^{1}H** (600.1 MHz, T = 345 K) δ_H 1.46 (CH_3, s, 9H); 1.47 (CH_3, s, 18H); 2.87–3.01 (*mc*, m, 6H);

3.05–3.23 (*mc*, CH_2, m, 10H+1H); 3.34 (CH_2, dd, 1H, $^2J_{HH}$ = 12.2, $^3J_{HH}$ = 3.6); 3.50 (CH_2–CO, d, 1H, $^2J_{HH}$ = 17.3); 3.53 (CH_2–CO, d, 1H, $^2J_{HH}$ = 17.3); 3.67 (CH–N, dd, 1H, $^3J_{HH}$ = 9.7, $^3J_{HH}$ = 4.4); 3.80 (CH_2–CO, d, 2H, $^2J_{HH}$ = 17.1); 3.89 (CH_2–CO, d, 2H, $^2J_{HH}$ = 17.1); 4.30 (CH–CO, d, 1H, $^3J_{HH}$ = 9.7); 4.41–4.47 (CH–O, m, 1H). **^{13}C{^{1}H}** (150.9 MHz, T = 345 K) δ_C 27.67 (*C*H$_3$, s); 27.70 (*C*H$_3$, s); 47.24 (*mc*, s); 48.59 (*mc*, s); 51.37 (*C*H$_2$, s); 52.19 (*mc,* s); 52.88 (*mc,* s); 54.07 (*C*H$_2$–CO, s); 58.32 (*C*H–CO, s); 55.68 (*C*H$_2$–CO, s); 65.68 (*C*H–N, s); 70.43 (*C*H–O, s); 81.12 (*C*–CH$_3$, s); 82.10 (*C*–CH$_3$, s); 167.60 (*C*O, s); 169.53 (*C*O, s); 169.86 (*C*O, s). **ESI-HRMS:** 644.4227 $[M+H]^+$ (theor. $[C_{31}H_{58}O_9N_5]^+$ = 644.4229). **EA** ($C_{31}H_{57}N_5O_9$·3.0TFA·3.1H_2O, M_R = 1041.6): C 42.7 (42.2); H 6.4 (5.9); N 6.7 (6.3); F 16.4 (16.0).

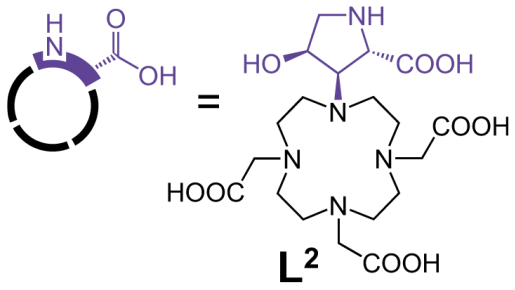

Synthesis of building block L^2: In a pear-shaped glass flask (25 mL), ***t*-Bu$_3$L^2**·3.0TFA·3.1H_2O (88 mg, 84 µmol) was dissolved in TFA (2 mL). The resulting solution was stirred at RT for 4 h. The mixture was evaporated to dryness and once co-evaporated with MeOH. Residue was purified by preparative HPLC (C18, H_2O/MeCN gradient with 0.1% TFA additive). Fractions with product were joined and lyophilized to give product in the form of TFA salt as white solid. **Yield:** 48 mg (72%; 1 step; based on ***t*-Bu$_3$L^2**·3.0TFA·3.1H_2O). **NMR (DMSO-d$_6$): ^{1}H** (500.0 MHz, T = 330 K) δ_H 2.84–3.07 (*mc*, m, 6H); 3.07–3.22 (CH_2, *mc*, m, 1H+6H); 3.22–3.40 (CH_2, *mc*, m, 1H+4H); 3.43–3.61 (CH_2–CO, m, 2H); 3.77 (CH–N, dd, 1H, $^3J_{HH}$ = 9.6, $^3J_{HH}$ = 4.4); 3.92 (CH_2–CO, s, 4H); 4.28 (CH–CO, d, 1H, $^3J_{HH}$ = 9.6); 4.39–4.48 (CH–O, m, 1H). **^{13}C{^{1}H}** (125.7 MHz, T = 330 K) δ_C 46.73 (*mc*, s); 48.17 (*mc*, s); 51.15 (*C*H$_2$, s); 51.95 (*mc*, s); 52.27 (*mc*, s); 53.51 (*C*H$_2$–CO, s); 54.29 (*C*H$_2$–CO, s); 54.90 (*C*H–CO, s); 64.42 (*C*H–N, s); 70.15 (*C*H–O, s); 169.15 (*C*O, s); 169.94 (*C*O, s); 171.79 (*C*O, s). **ESI-HRMS:** 476.2350 $[M+H]^+$ (theor. $[C_{19}H_{34}O_9N_5]^+$ = 476.2351). **EA** ($C_{19}H_{33}N_5O_9$·2.4TFA·2.5H_2O, M_R = 794.1): C 36.0 (36.7); H 5.1 (4.6); N 8.8 (8.1); F 17.2 (16.8).

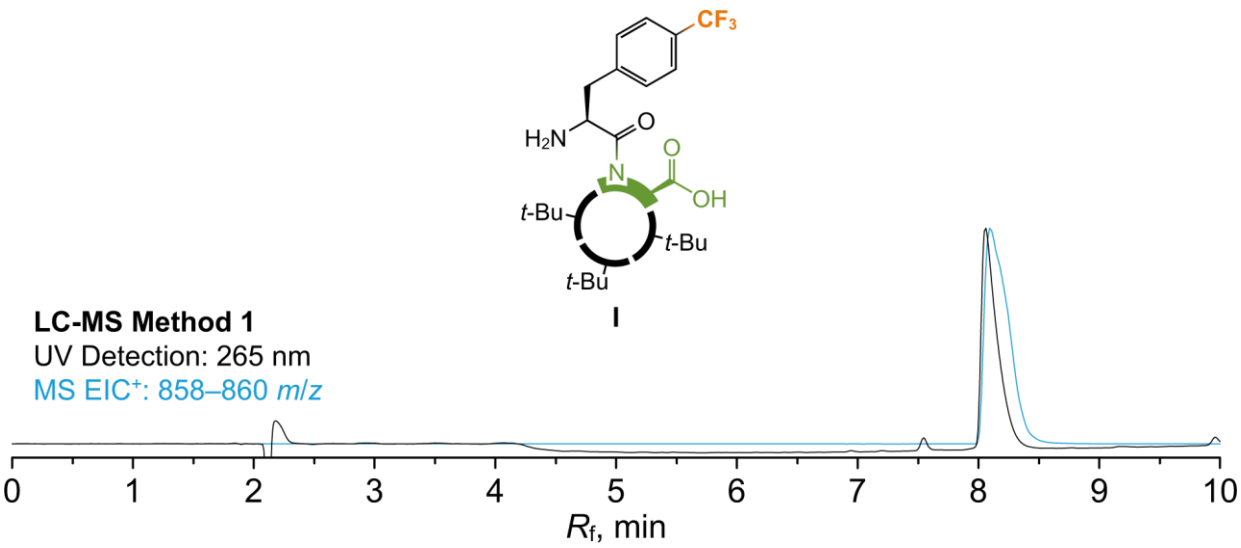

Synthesis and LC-MS chromatogram of intermediate I: In a glass vial (4 mL), Fmoc-Phe{p-CF_3}-OH (29 mg, 63.4 µmol, 1.1 equiv.), PyAOP (33 mg, 63.4 µmol, 1.1 equiv.) and DIPEA (55 µL, 314 µmol, 5.5 equiv.) were dissolved in dry DMSO (1.2 mL). After 2 mins, ***t*Bu$_3$L^1**·3.0TFA·0.9H_2O (57.4 mg, 57.3 µmol, 1.0 equiv.) was added and solution was stirred at RT for 30 mins. Solution was purified by preparative HPLC (C18, H_2O/MeCN gradient with 0.1% FA additive). Fractions with Fmoc protected product were joined and lyophilized. The resulting white solid was dissolved in dry DMF (2.4 mL) followed by addition of DBU (48 µL, 322 µmol, 5.6 equiv.). After 5 mins, the reaction was quenched with TFA (25 µL, 327 µmol, 5.7 equiv.) and diluted with H_2O (1 mL). Solution was then purified by preparative HPLC (C18, H_2O/MeCN gradient with 0.1% FA additive). Fractions with product were joined and lyophilized to give product as white solid. **Yield:** 26 mg (53%; 2 steps; based on ***t*Bu$_3$L^1**·3.0TFA·0.9H_2O assuming zwitterionic form of **I**, M_R = 859.0). **ESI-HRMS:** 859.4789 $[M+H]^+$ (theor. $[C_{41}H_{66}F_3O_{10}N_6]^+$ = 859.4787).

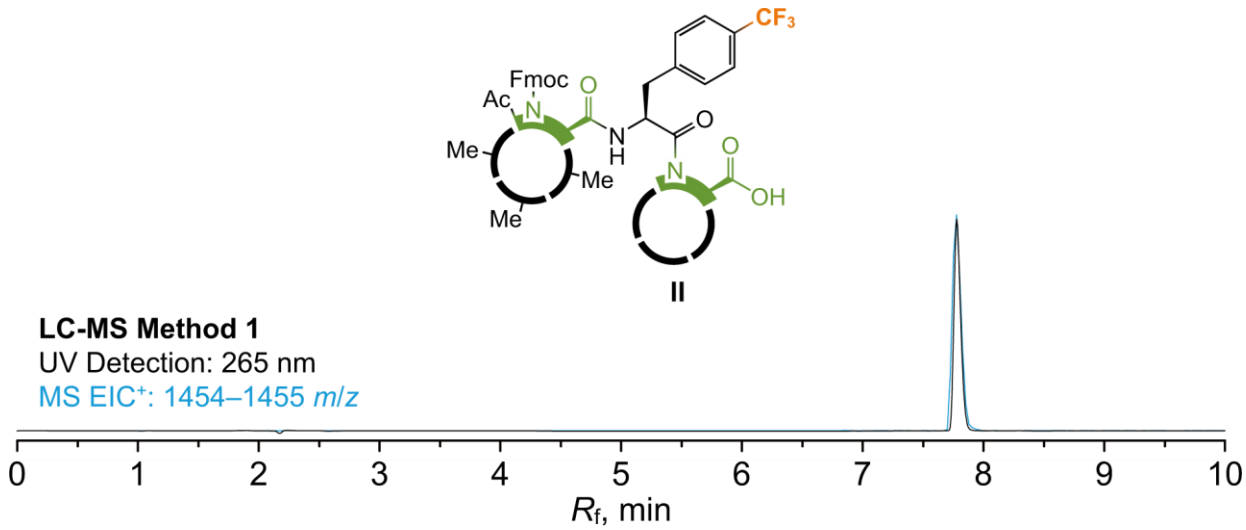

Synthesis and LC-MS chromatogram of intermediate II: In a glass vial (4 mL), **Ac-Fmoc-Me$_3$L^1**·1.9TFA·1.3H_2O (17.8 mg, 17.4 µmol, 1.0 equiv.) was dissolved in dry DMSO (850 µL) followed by addition of freshly prepared solution of PyOAP (100 mM in dry DMSO, 174 µL, 17.4 µmol, 1.0 equiv.) and of DIPEA (25 µL, 143 µmol, 8.2 equiv.). The resulting mixture was stirred at RT for 2 mins followed by addition of solution of **I** (22.9 mg, 26.7 µmol assuming zwitterionic form, 1.5 equiv.) in dry DMSO (1 mL) and the mixture was further stirred at RT for 30 mins. Solution was then purified by preparative HPLC (C18, H_2O/MeCN gradient with 0.1% FA additive). Fractions with *tert*-butyl product were joined and lyophilized. The resulting solid was dissolved in TFA (3 mL) and the resulting solution was stirred at RT for 16 h. Reaction mixture was evaporated to dryness and twice co-evaporated with MeOH. Residue was purified by preparative HPLC (C18, H_2O/MeCN gradient with 0.1% TFA additive). Fractions with product were joined and lyophilized. **Yield:** 19.0 mg (66%; 2 steps; based on **Ac-Fmoc-Me$_3$L^1**·1.9TFA·1.3H_2O assuming **II**·2TFA, M_R = 1682). **ESI-HRMS:** 1454.6357 $[M+H]^+$ (theor. $[C_{68}H_{91}F_3O_{21}N_{11}]^+$ = 1454.6338).

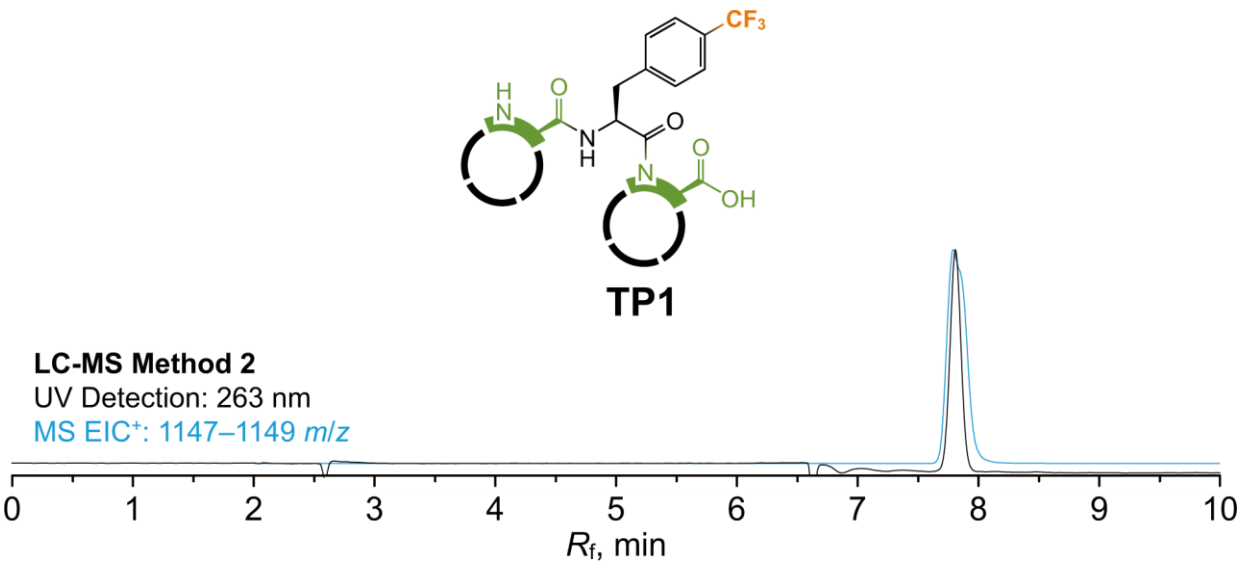

Synthesis and LC-MS chromatogram of TP1: In a glass vial (20 mL), **II** (19 mg, 11.3 µmol assuming **II**·2TFA, 1.0 equiv (.was dissolved in MeOH (3.6 mL) and H_2O (0.4 mL) followed by addition of aq. LiOH (1.0 M, 325 µL, 325 µmol, 29 equiv.). The resulting solution was stirred at RT for 2 d. The mixture was then purified by preparative HPLC (C18, H_2O/MeCN gradient with 0.1% TFA additive). Fractions with product were joined and lyophilized to give product as white solid. **Yield:** 9.7 mg (62%; 2 steps; based on **II**·2TFA assuming **TP1**·2TFA, M_R = 1376). **ESI-HRMS:** 1148.5084 $[M+H]^+$ (theor. $[C_{48}H_{73}F_3O_{18}N_{11}]^+$ = 1148.5082.

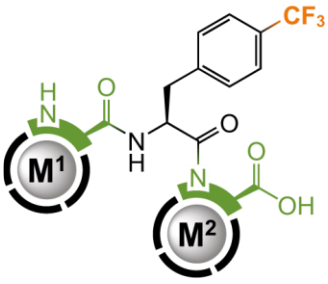

M¹M²-TP1

***M¹M²-TP1** statistical mixture combinations:*

Nd + Eu	Dy + Er	Eu + Lu
Dy + Ho	Eu + Ho	Tb + Yb
Ho + Y	Nd + Tb	Tm + Lu
Dy + Y	Nd + Yb	Pr + Er
Dy + Tm	Sm + Ho	Ho + Er
Tb + Ho	Tb + Er	Sm + Y
Dy + Lu	Eu + Er	Pr + Y

Post-synthesis of M¹M²-TP1 statistical mixtures: Solid **TP1** (assuming **TP1**·2TFA, M_R = 1376) was dissolved in aq. MOPS/NaOH buffer (pH 7.0) to a final concentration of 2.5 mM **TP1** in 500 mM MOPS/NaOH buffer. In a plastic Eppendorf tube (0.5 mL), buffered stock solution of **TP1** (95 µL, 240 nmol, 1.0 equiv.) was added to a mixture of aq. M^1Cl_3 (100 mM, 2.5 µL, 250 nmol, 1.05 equiv.) and of aq. M^2Cl_3 (100 mM, 2.5 µL, 250 nmol, 1.05 equiv.). The resulting mixture was briefly vortexed and transferred into an NMR insert tube, which was then put into 5 mm NMR tube filled with D_2O and directly used for ^{19}F NMR measurements (21 combinations of M^{3+} cations are listed below; charges were omitted for clarity reasons).

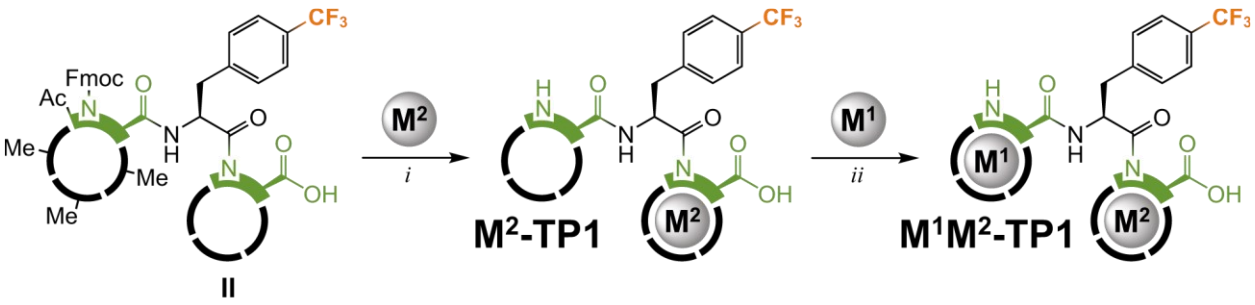

M²-TP1:

Tb-TP1: M² = Tb

Dy-TP1: M² = Dy

Ho-TP1: M² = Ho

Yb-TP1: M² = Yb

M¹M²-TP1:

TbTb-TP1: M¹ = Tb *and* M² = Tb

DyTb-TP1: M¹ = Dy *and* M² = Tb

HoTb-TP1: M¹ = Ho *and* M² = Tb

YbTb-TP1: M¹ = Yb *and* M² = Tb

TbDy-TP1: M¹ = Tb *and* M² = Dy

DyDy-TP1: M¹ = Dy *and* M² = Dy

HoDy-TP1: M¹ = Ho *and* M² = Dy

YbDy-TP1: M¹ = Yb *and* M² = Dy

TbHo-TP1: M¹ = Tb *and* M² = Ho

DyHo-TP1: M¹ = Dy *and* M² = Ho

HoHo-TP1: M¹ = Ho *and* M² = Ho

YbHo-TP1: M¹ = Yb *and* M² = Ho

TbYb-TP1: M¹ = Tb *and* M² = Yb

DyYb-TP1: M¹ = Dy *and* M² = Yb

HoYb-TP1: M¹ = Ho *and* M² = Yb

YbYb-TP1: M¹ = Yb *and* M² = Yb

Synthesis of M^1M^2-TP1 tripeptides with Tb^{3+}, Dy^{3+}, Ho^{3+} and Yb^{3+} cations. Charges were omitted for clarity reason. ***Conditions:*** (*i*) M^2Cl_3, aq. MOPS/NaOH buffer (pH 7.0) *followed by* LiOH, H_2O, MeOH; (*ii*) M^1Cl_3, aq. MOPS/NaOH buffer (pH 7.0).

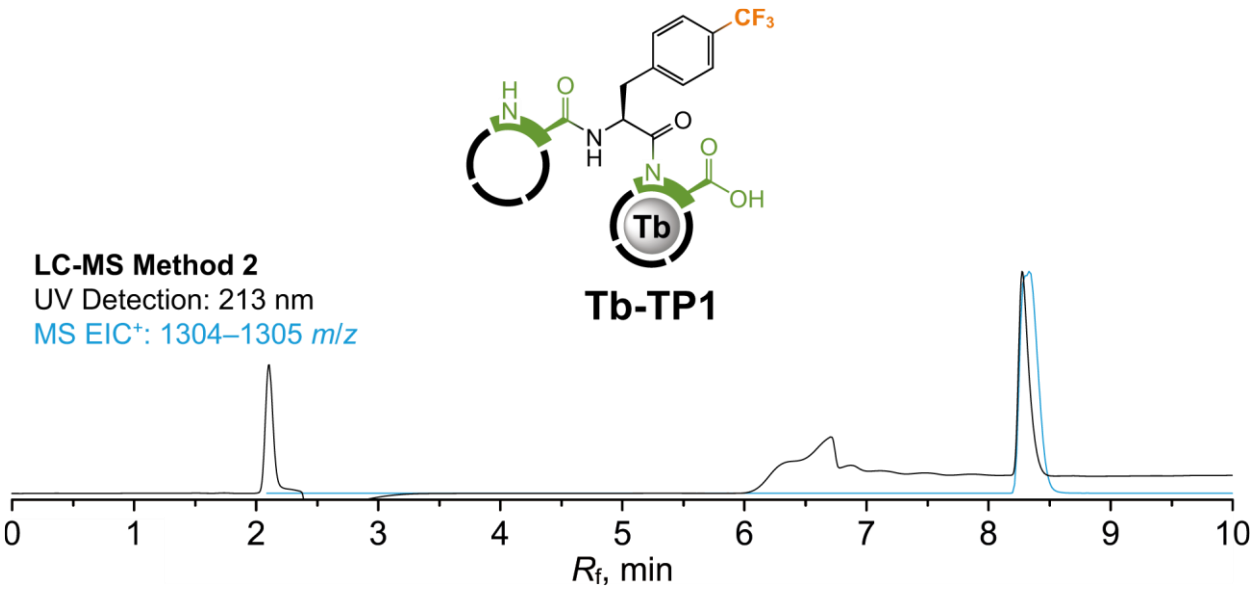

Synthesis and LC-MS chromatogram of intermediate Tb-TP1: In a glass vial (4 mL), **II** (2.9 mg, 1.7 µmol assuming **II**·2TFA, 1.0 equiv.) was dissolved in aq. MOPS/NaOH buffer (500 mM, pH 7.0, 580 µL, 290 µmol, 170 equiv) followed by addition of aq. $TbCl_3$ (100 mM, 24 µL, 2.4 µmol, 1.4 equiv.). The resulting solution was stirred at RT for 15 mins. The mixture was then purified by preparative HPLC (C18, H_2O/MeCN gradient with 0.1% FA additive). Fractions with product were joined and lyophilized to give product as white solid. The resulting white solid was dissolved in a mixture of MeOH (2.0 mL) and H_2O (150 µL) followed by addition of aq. *LiOH* (1 M, 106 µL, 106 µmol, 62 equiv.) and the mixture was stirred at RT for 5 d. Reaction was then quenched by FA (5.0 µL, 110 µmol, 65 equiv.) and the mixture was evaporated to dryness. The residue was purified by preparative HPLC (C18, H_2O/MeCN gradient with 0.1% FA additive). Fractions with product were joined and lyophilized to give product as white solid. **Yield:** 2.2 mg (90%; 2 steps; based on **II**·2TFA assuming **Tb-TP1**·2.5FA, M_R = 1419). **ESI-HRMS:** 1304.4091 $[M+H]^+$ (theor. $[C_{48}H_{70}O_{18}N_{11}F_3Tb_1]^+$ = 1304.4100).

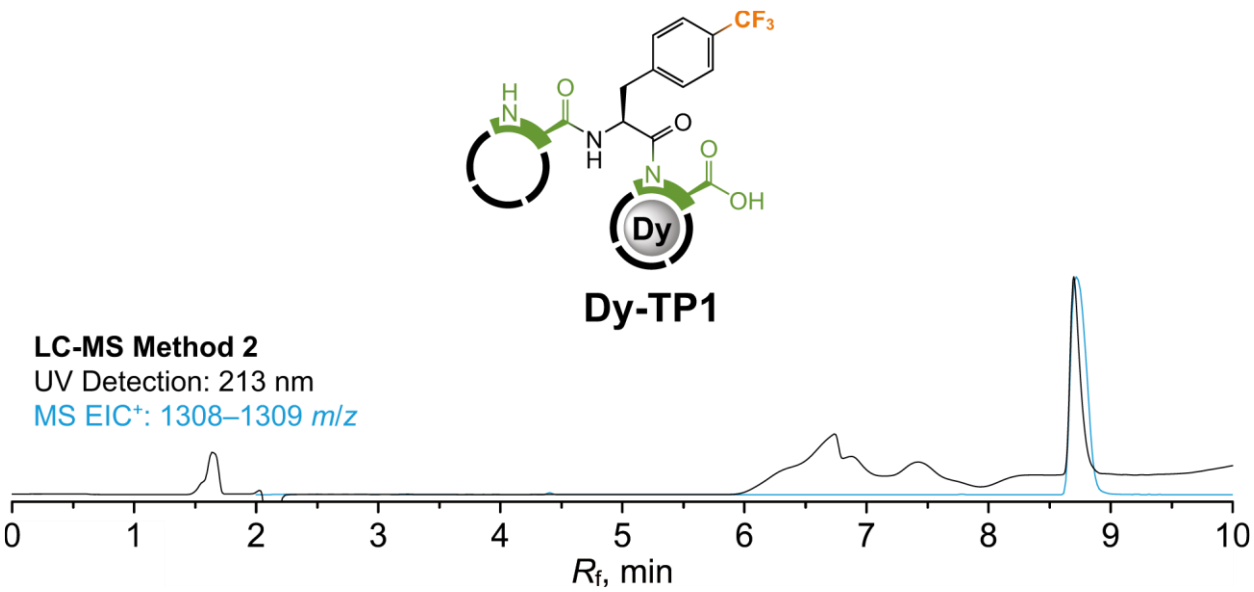

Synthesis and LC-MS chromatogram of intermediate Dy-TP1: In a glass vial (4 mL), **II** (5.0 mg, 3.0 µmol assuming **II**·2.0TFA, 1.0 equiv.) was dissolved in aq. MOPS/NaOH buffer (500 mM, pH 7.0, 1.0 mL, 500 µmol, 170 equiv) followed by addition of aq. $DyCl_3$ (100 mM, 41 µL, 4.1 µmol, 1.4 equiv.). The resulting solution was stirred at RT for 15 mins. The mixture was then purified by preparative HPLC (C18, H_2O/MeCN gradient with 0.1% FA additive). Fractions with product were joined and lyophilized to give product as white solid. The resulting white solid was dissolved in a mixture of MeOH (2.4 mL) and H_2O (180 µL) followed by addition of aq. LiOH (1 M, 113 µL, 113 µmol, 38 equiv.) and the mixture was stirred at RT for 5 d. Reaction was then quenched by FA (5.0 µL, 110 µmol, 37 equiv.) and the mixture was evaporated to dryness. The residue was purified by preparative HPLC (C18, H_2O/MeCN gradient with 0.1% FA additive). Fractions with product were joined and lyophilized to give product as white solid. **Yield:** 2.7 mg (64%; 2 steps; based on **II**·2.0TFA assuming **Dy-TP1**·2.5FA, M_R = 1423). **ESI-HRMS:** 1309.4130 $[M+H]^+$ (theor. $[C_{48}H_{70}O_{18}N_{11}F_3Dy_1]^+$ = 1309.4139).

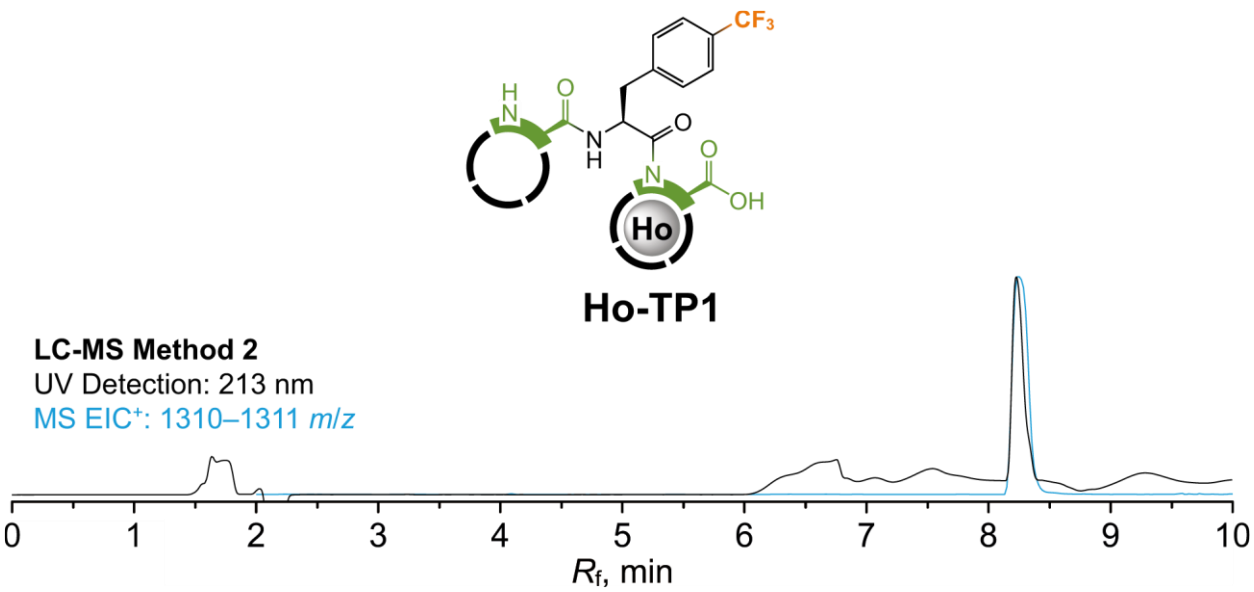

Synthesis and LC-MS chromatogram of intermediate Ho-TP1: In a glass vial (4 mL), **II** (4.0 mg, 2.4 µmol assuming **II**·2.0TFA, 1.0 equiv.) was dissolved in aq. MOPS/NaOH buffer (500 mM, pH 7.0, 0.8 mL, 430 µmol, 170 equiv) followed by addition of aq. $HoCl_3$ (100 mM, 33 µL, 3.3 µmol, 1.4 equiv.). The resulting solution was stirred at RT for 15 mins. The mixture was then purified by preparative HPLC (C18, H_2O/MeCN gradient with 0.1% FA additive). Fractions with product were joined and lyophilized to give product as white solid. The resulting white solid was dissolved in a mixture of MeOH (2.0 mL) and H_2O (150 µL) followed by addition of aq. LiOH (1 M, 102 µL, 102 µmol, 43 equiv.) and the mixture was stirred at RT for 5 d. Reaction was then quenched by FA (5.0 µL, 110 µmol, 46 equiv.) and the mixture was evaporated to dryness. The residue was purified by preparative HPLC (C18, H_2O/MeCN gradient with 0.1% FA additive). Fractions with product were joined and lyophilized to give product as white solid. **Yield:** 2.1 mg (61%; 2 steps; based on **II**·2.0TFA assuming **Ho-TP1**·2.5FA M_R = 1425). **ESI-HRMS:** 1310.4146 $[M+H]^+$ (theor. $[C_{48}H_{70}O_{18}N_{11}F_3Ho_1]^+$ = 1310.4150).

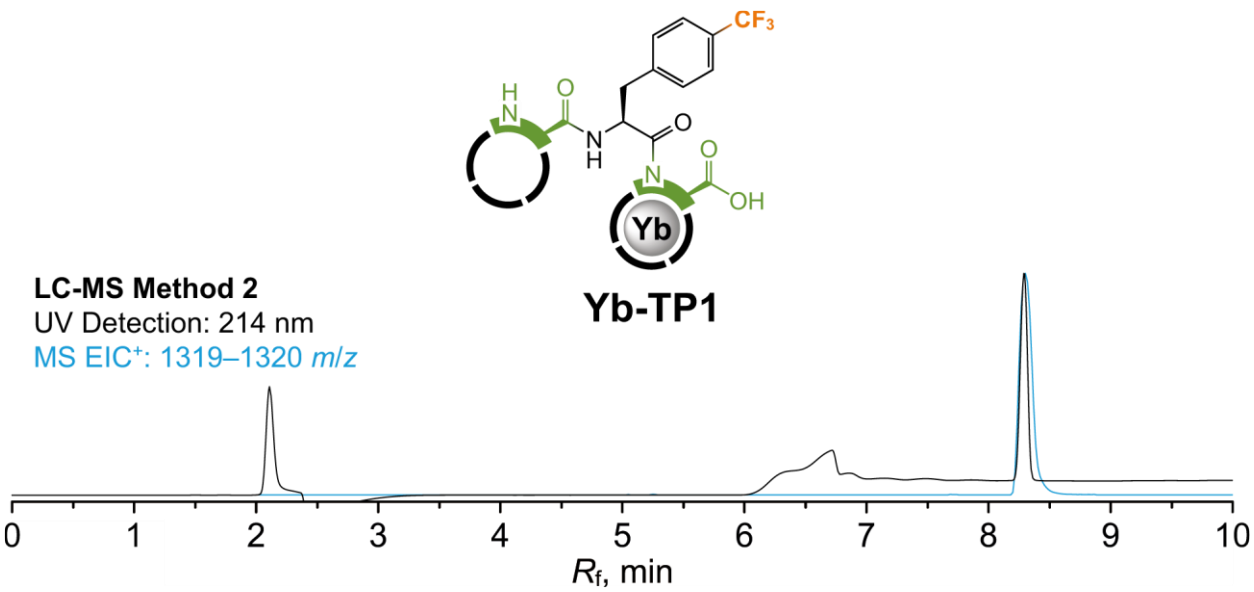

Synthesis and LC-MS chromatogram of intermediate Yb-TP1: In a glass vial (4 mL), **II** (2.9 mg, 1.7 µmol assuming **II**·2.0TFA, 1.0 equiv.) was dissolved in aq. MOPS/NaOH buffer (500 mM, pH 7.0, 580 µL, 500 µmol, 170 equiv) followed by addition of aq. $YbCl_3$ (100 mM, 24 µL, 2.4 µmol, 1.4 equiv.). The resulting solution was stirred at RT for 15 mins. The mixture was then purified by preparative HPLC (C18, H_2O/MeCN gradient with 0.1% FA additive). Fractions with product were joined and lyophilized to give product as white solid. The resulting white solid was dissolved in a mixture of MeOH (2.0 mL) and H_2O (150 µL) followed by addition of aq. LiOH (1 M, 104 µL, 104 µmol, 61 equiv.) and the mixture was stirred at RT for 5 d. Reaction was then quenched by FA (5.0 µL, 110 µmol, 65 equiv.) and the mixture was evaporated to dryness. The residue was purified by preparative HPLC (C18, H_2O/MeCN gradient with 0.1% FA additive). Fractions with product were joined and lyophilized to give product as white solid. **Yield:** 1.6 mg (65%; 2 steps; based on **II**·2.0TFA assuming **Yb-TP1**·2.5FA, M_R = 1433). **ESI-HRMS:** 1319.4240 $[M+H]^+$ (theor. $[C_{48}H_{70}O_{18}N_{11}F_3Yb_1]^+$ = 1319.4236).

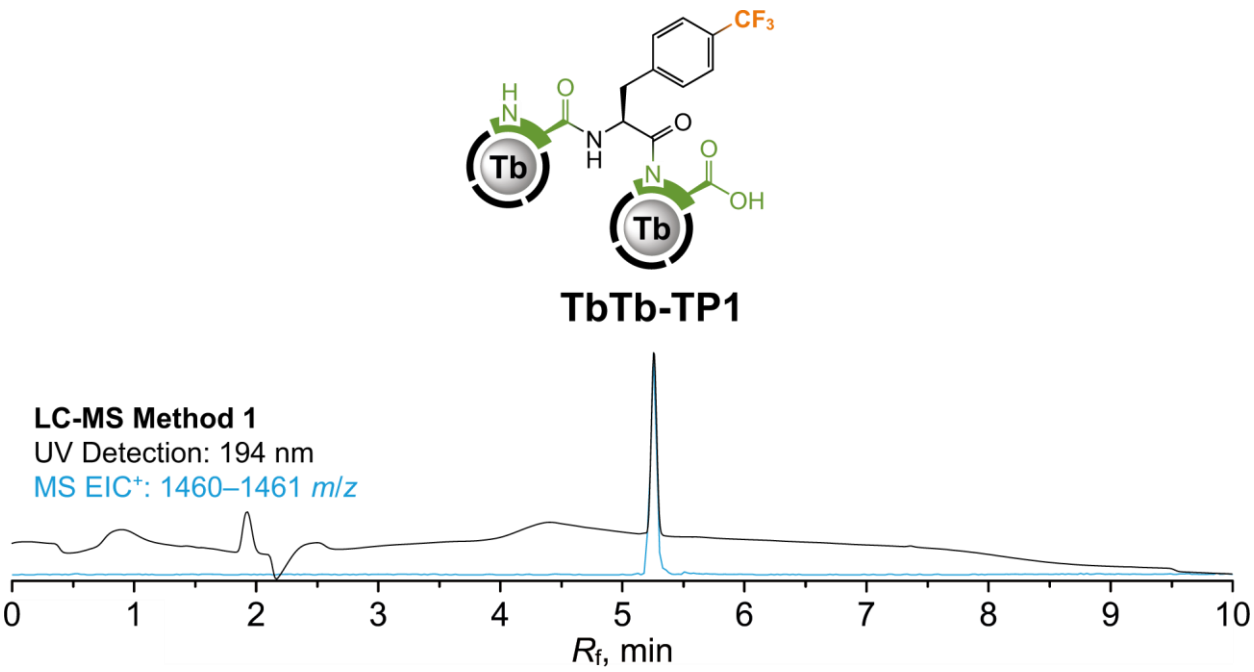

Synthesis and LC-MS chromatogram of TbTb-TP1: In a glass vial (4 mL), **Tb-TP1** (0.6 mg, ~0.4 µmol assuming **Tb-TP1**·2.5FA, 1.0 equiv.) was dissolved in aq. MOPS/NaOH buffer (500 mM, pH 7.0, 500 µL, 250 µmol, ~600 equiv.) followed by addition of aq. $TbCl_3$ (100 mM, 5 µL, 0.5 µmol, ~1.2 equiv.) and the resulting solution was stirred at RT for 15 mins. The mixture was then purified by preparative HPLC (C18, H_2O/MeCN gradient with 0.1% TFA additive). Fractions with product were joined and lyophilized to give product as white solid. **Yield:** ~0.3 mg. **NMR (aq. MOPS pH = 7.0, external D_2O):** ^{19}**F** (470.4 MHz, T = 298.2 K) δ_F –55.76 (CF_3, s). **ESI-HRMS:** 730.6594 $[M+2H]^{2+}$ (theor. $[C_{48}H_{68}O_{18}N_{11}F_3Tb_2]^{2+}$ = 730.6596).

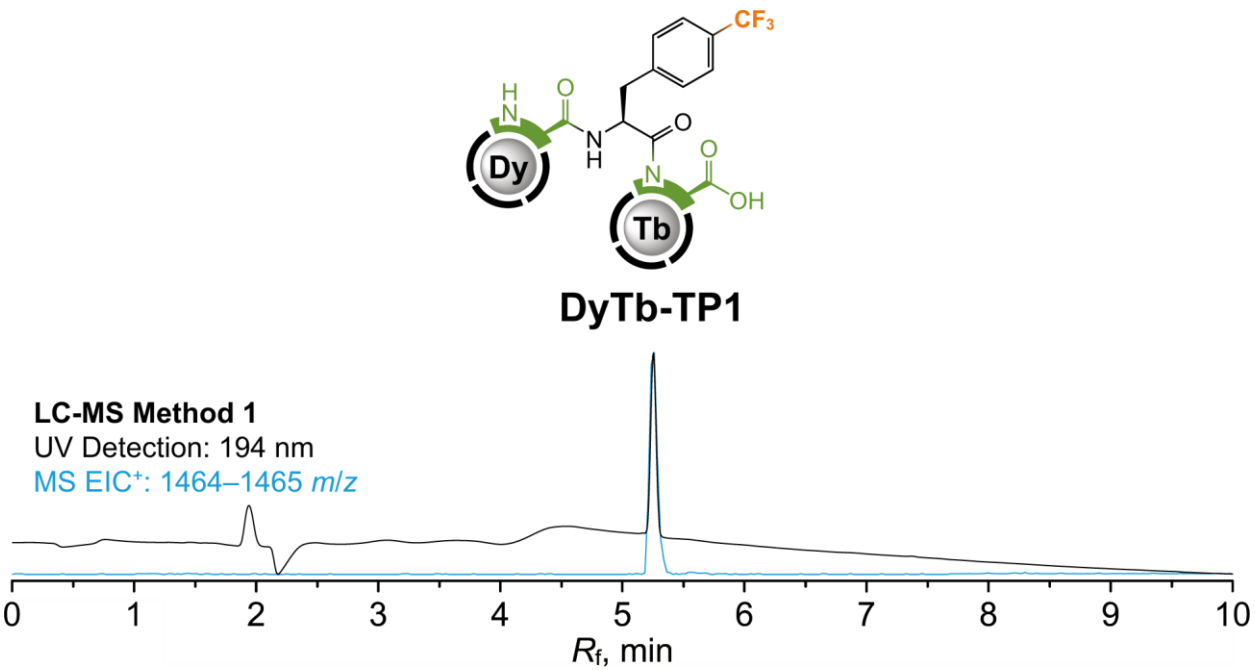

Synthesis and LC-MS chromatogram of DyTb-TP1: In a glass vial (4 mL), **Tb-TP1** (0.6 mg, ~0.4 µmol assuming **Tb-TP1**·2.5FA, 1.0 equiv.) was dissolved in aq. MOPS/NaOH buffer (500 mM, pH 7.0, 500 µL, 250 µmol, ~600 equiv.) followed by addition of aq. $DyCl_3$ (100 mM, 5 µL, 0.5 µmol, ~1.2 equiv.) and the resulting solution was stirred at RT for 15 mins. The mixture was then purified by preparative HPLC (C18, H_2O/MeCN gradient with 0.1% TFA additive). Fractions with product were joined and lyophilized to give product as white solid. **Yield:** ~0.3 mg. **NMR (aq. MOPS pH = 7.0, external D_2O): ^{19}F** (470.4 MHz, T = 298.2 K) δ_F –67.29 (CF_3, s). **ESI-HRMS:** 731.6605 $[M+2H]^{2+}$ (theor. $[C_{48}H_{68}O_{18}N_{11}F_3Dy_1Tb_1]^{2+}$ = 731.6604).

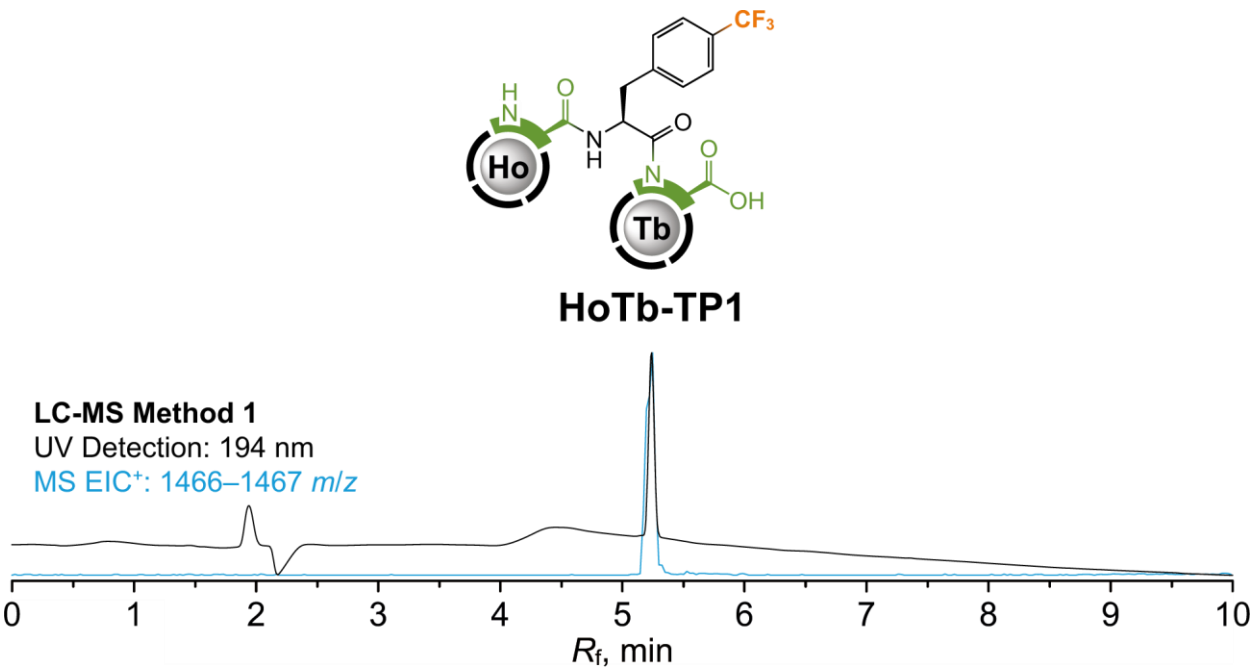

Synthesis and LC-MS chromatogram of HoTb-TP1: In a glass vial (4 mL), **Tb-TP1** (0.5 mg, ~0.4 µmol assuming **Tb-TP1**·2.5FA, 1.0 equiv.) was dissolved in aq. MOPS/NaOH buffer (500 mM, pH 7.0, 500 µL, 250 µmol, ~700 equiv.) followed by addition of aq. $HoCl_3$ (100 mM, 5 µL, 0.5 µmol, ~1.4 equiv.) and the resulting solution was stirred at RT for 15 mins. The mixture was then purified by preparative HPLC (C18, H_2O/MeCN gradient with 0.1% TFA additive). Fractions with product were joined and lyophilized to give product as white solid. **Yield:** ~0.3 mg. **NMR (aq. MOPS pH = 7.0, external D_2O):** ^{19}**F** (470.4 MHz, T = 298.2 K) δ_F –64.81 (CF_3, s). **ESI-HRMS:** 733.6620 $[M+2H]^{2+}$ (theor. $[C_{48}H_{68}O_{18}N_{11}F_3Ho_1Tb_1]^{2+}$ = 733.6621).

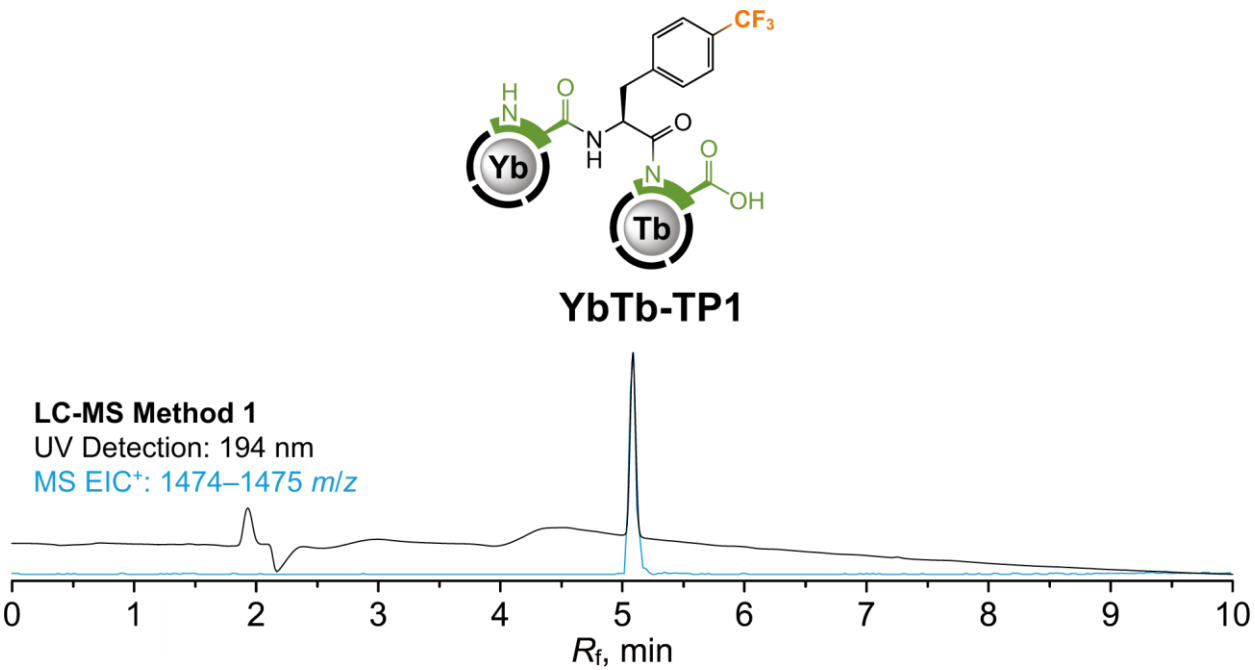

Synthesis and LC-MS chromatogram of YbTb-TP1: In a glass vial (4 mL), **Tb-TP1** (0.5 mg, ~0.4 µmol assuming **Tb-TP1**·2.5FA, 1.0 equiv.) was dissolved in aq. MOPS/NaOH buffer (500 mM, pH 7.0, 500 µL, 250 µmol, ~700 equiv.) followed by addition of aq. $YbCl_3$ (100 mM, 5 µL, 0.5 µmol, ~1.4 equiv.) and the resulting solution was stirred at RT for 15 mins. The mixture was then purified by preparative HPLC (C18, H_2O/MeCN gradient with 0.1% TFA additive). Fractions with product were joined and lyophilized to give product as white solid. **Yield:** ~0.3 mg. **NMR (aq. MOPS pH = 7.0, external D_2O):** ^{19}**F** (470.4 MHz, T = 298.2 K) δ_F –57.56 (CF_3, s). **ESI-HRMS:** 738.1665 $[M+2H]^{2+}$ (theor. $[C_{48}H_{68}O_{18}N_{11}F_3Yb_1Tb_1]^{2+}$ = 738.1664).

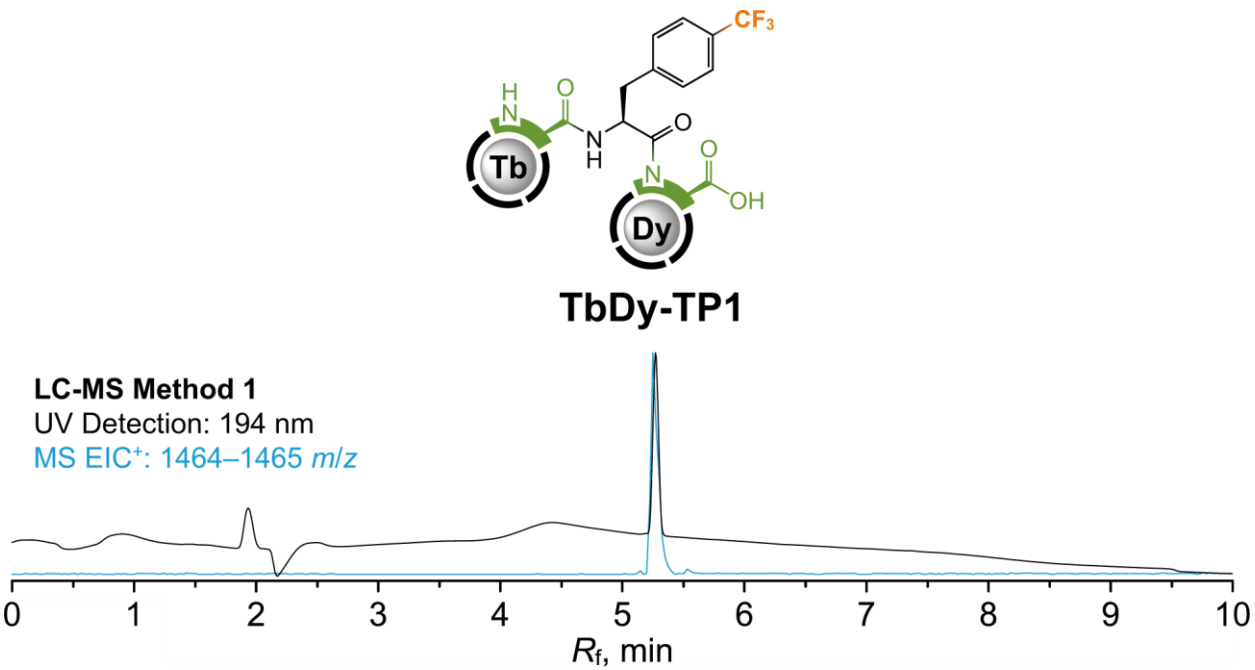

Synthesis and LC-MS chromatogram of TbDy-TP1: In a glass vial (4 mL), **Dy-TP1** (0.5 mg, ~0.4 µmol assuming **Dy-TP1**·2.5FA, 1.0 equiv.) was dissolved in aq. MOPS/NaOH buffer (500 mM, pH 7.0, 250 µL, 125 µmol, ~350 equiv.) followed by addition of aq. $TbCl_3$ (100 mM, 5 µL, 0.5 µmol, ~1.4 equiv.) and the resulting solution was stirred at RT for 15 mins. The mixture was then purified by preparative HPLC (C18, H_2O/MeCN gradient with 0.1% TFA additive). Fractions with product were joined and lyophilized to give product as white solid. **Yield:** ~0.4 mg. **NMR (aq. MOPS pH = 7.0, external D_2O): ^{19}F** (470.4 MHz, T = 298.2 K) δ_F –55.55 (CF_3, s). **ESI-HRMS:** 733.1610 $[M+2H]^{2+}$ (theor. $[C_{48}H_{68}O_{18}N_{11}F_3Tb_1Dy_1]^{2+}$ = 733.1615).

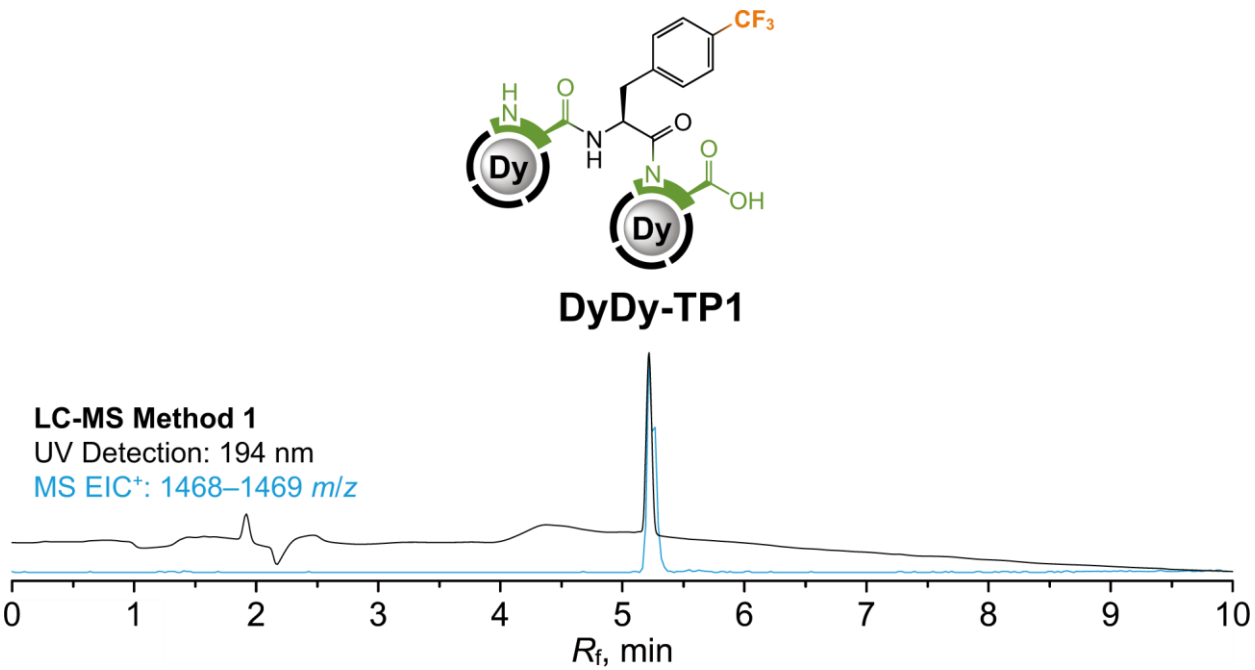

Synthesis and LC-MS chromatogram of DyDy-TP1: In a glass vial (4 mL), **Dy-TP1** (1.0 mg, ~0.7 µmol assuming **Dy-TP1**·2.5FA, 1.0 equiv.) was dissolved in aq. MOPS/NaOH buffer (500 mM, pH 7.0, 500 µL, 250 µmol, ~350 equiv.) followed by addition of aq. $DyCl_3$ (100 mM, 9 µL, 0.9 µmol, ~1.3 equiv.) and the resulting solution was stirred at RT for 15 mins. The mixture was then purified by preparative HPLC (C18, H_2O/MeCN gradient with 0.1% TFA additive). Fractions with product were joined and lyophilized to give product as white solid. **Yield:** ~1.0 mg. **NMR (aq. MOPS pH = 7.0, external D_2O):** ^{19}**F** (470.4 MHz, T = 298.2 K) δ_F –57.02 (CF_3, s). **ESI-HRMS:** 735.6632 $[M+2H]^{2+}$ (theor. $[C_{48}H_{68}O_{18}N_{11}F_3Dy_2]^{2+}$ = 735.6634).

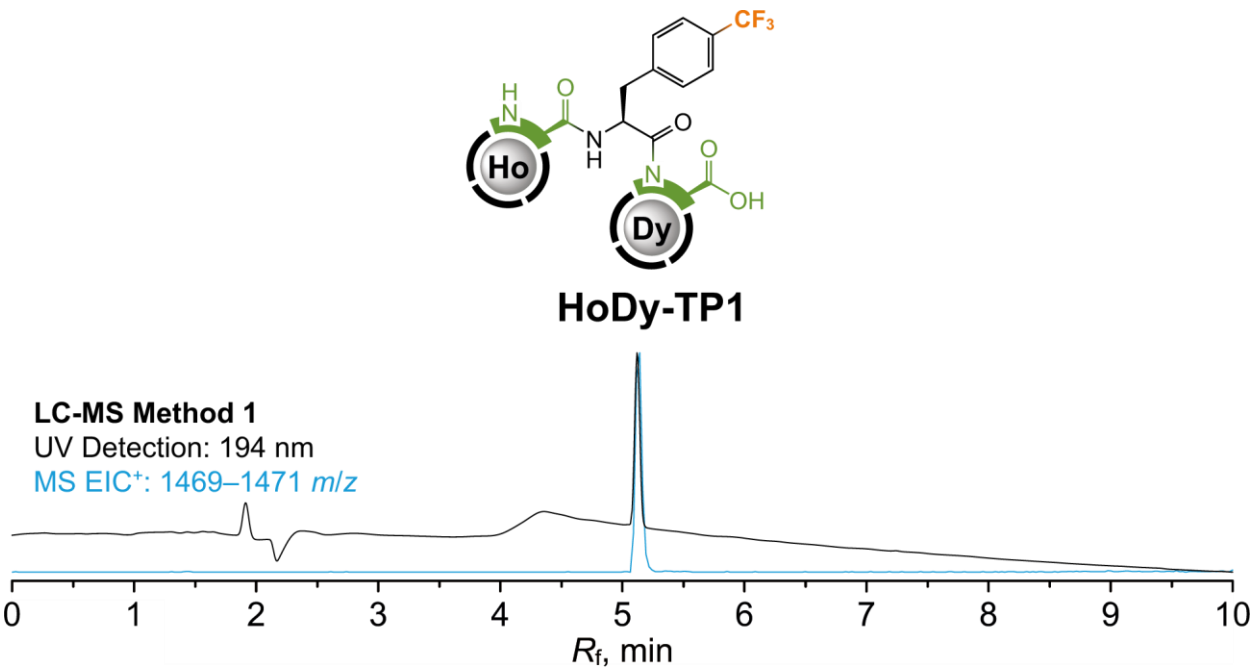

Synthesis and LC-MS chromatogram of HoDy-TP1: In a glass vial (4 mL), **Dy-TP1** (0.5 mg, ~0.4 µmol assuming **Dy-TP1**·2.5FA, 1.0 equiv.) was dissolved in aq. MOPS/NaOH buffer (500 mM, pH 7.0, 250 µL, 125 µmol, ~350 equiv.) followed by addition of aq. $HoCl_3$ (100 mM, 5 µL, 0.5 µmol, ~1.4 equiv.) and the resulting solution was stirred at RT for 15 mins. The mixture was then purified by preparative HPLC (C18, H_2O/MeCN gradient with 0.1% TFA additive). Fractions with product were joined and lyophilized to give product as white solid. **Yield:** ~0.5 mg. **NMR (aq. MOPS pH = 7.0, external D_2O):** ^{19}**F** (470.4 MHz, T = 298.2 K) δ_F –54.61 (CF_3, s). **ESI-HRMS:** 736.1641 $[M+2H]^{2+}$ (theor. $[C_{48}H_{68}O_{18}N_{11}F_3Ho_1Dy_1]^{2+}$ = 736.1640).

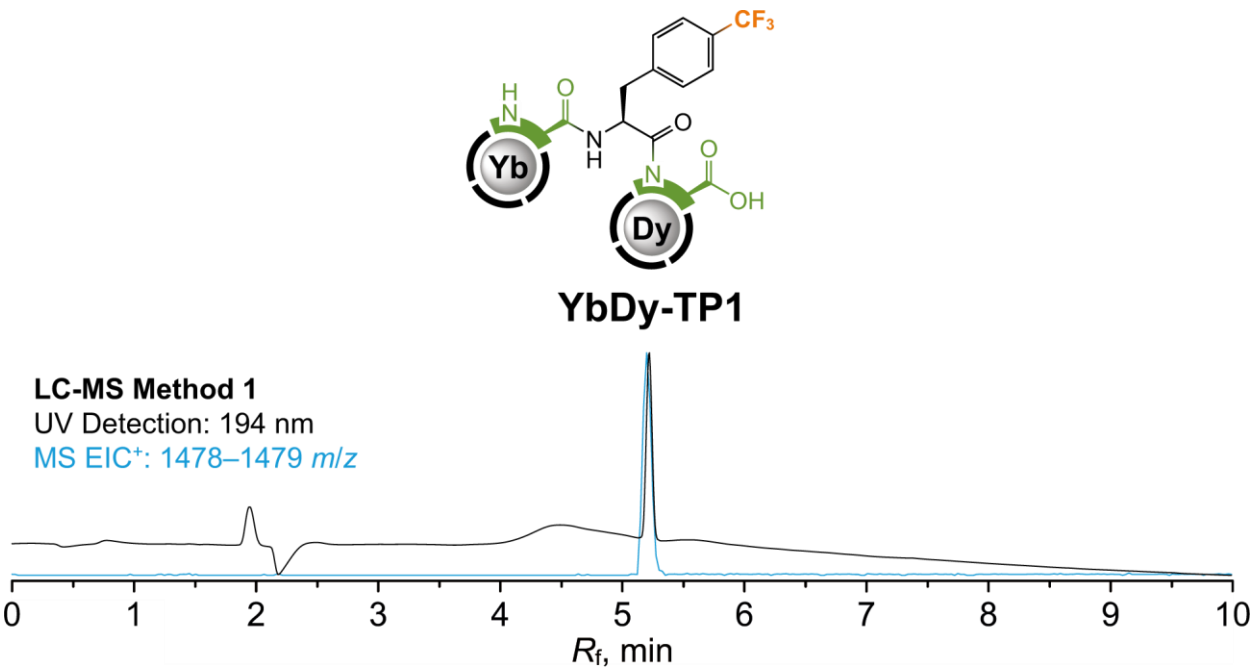

Synthesis and LC-MS chromatogram of YbDy-TP1: In a glass vial (4 mL), **Dy-TP1** (0.5 mg, ~0.4 µmol assuming **Dy-TP1**·2.5FA, 1.0 equiv.) was dissolved in aq. MOPS/NaOH buffer (500 mM, pH 7.0, 250 µL, 125 µmol, ~350 equiv.) followed by addition of aq. $YbCl_3$ (100 mM, 5 µL, 0.5 µmol, ~1.4 equiv.) and the resulting solution was stirred at RT for 15 mins. The mixture was then purified by preparative HPLC (C18, H_2O/MeCN gradient with 0.1% TFA additive). Fractions with product were joined and lyophilized to give product as white solid. **Yield:** ~0.4 mg. **NMR (aq. MOPS pH = 7.0, external D_2O):** ^{19}**F** (470.4 MHz, T = 298.2 K) δ_F –47.38 (CF_3, s). **ESI-HRMS:** 740.6698 $[M+2H]^{2+}$ (theor. $[C_{48}H_{68}O_{18}N_{11}F_3Yb_1Dy_1]^{2+}$ = 740.6683).

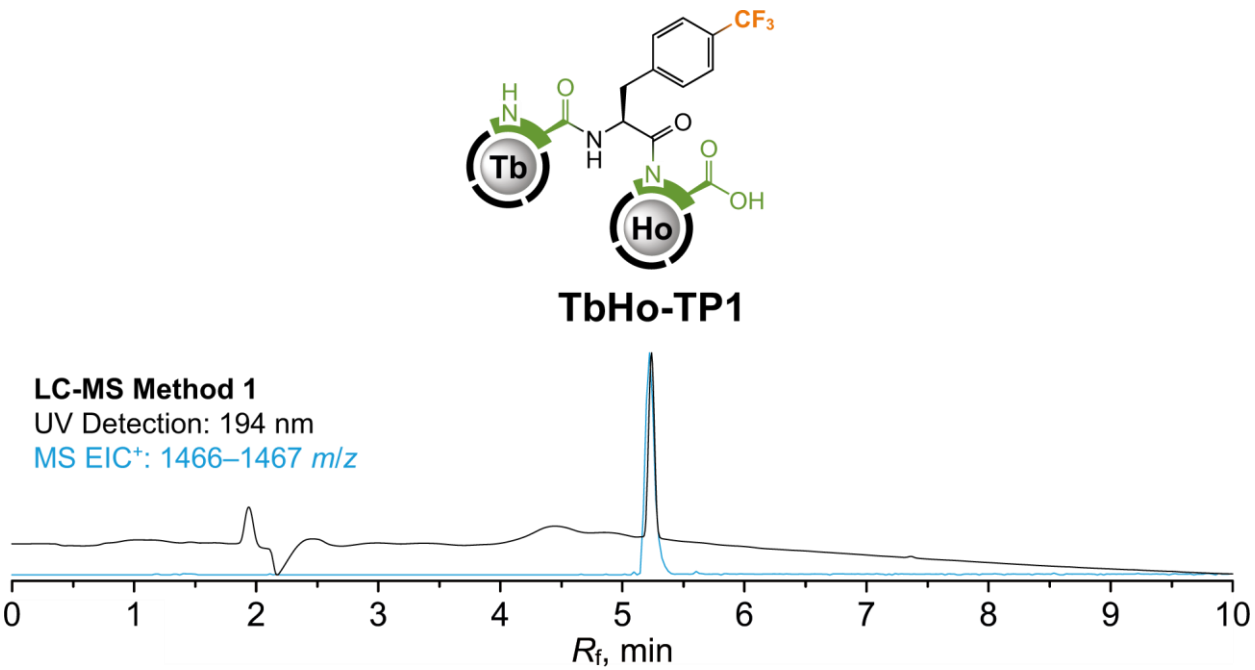

Synthesis and LC-MS chromatogram of TbHo-TP1: In a glass vial (4 mL), **Ho-TP1** (0.5 mg, ~0.4 µmol assuming **Ho-TP1**·2.5FA, 1.0 equiv.) was dissolved in aq. MOPS/NaOH buffer (500 mM, pH 7.0, 250 µL, 125 µmol, ~350 equiv.) followed by addition of aq. $TbCl_3$ (100 mM, 5 µL, 0.5 µmol, ~1.4 equiv.) and the resulting solution was stirred at RT for 15 mins. The mixture was then purified by preparative HPLC (C18, H_2O/MeCN gradient with 0.1% TFA additive). Fractions with product were joined and lyophilized to give product as white solid. **Yield:** ~0.4 mg. **NMR (aq. MOPS pH = 7.0, external D_2O):** ^{19}**F** (470.4 MHz, T = 298.2 K) δ_F –60.91 (CF_3, s). **ESI-HRMS:** 744.6528 $[M+2H]^{2+}$ (theor. $[C_{48}H_{68}O_{18}N_{11}F_3Tb_1Ho_1]^{2+}$ = 744.6531).

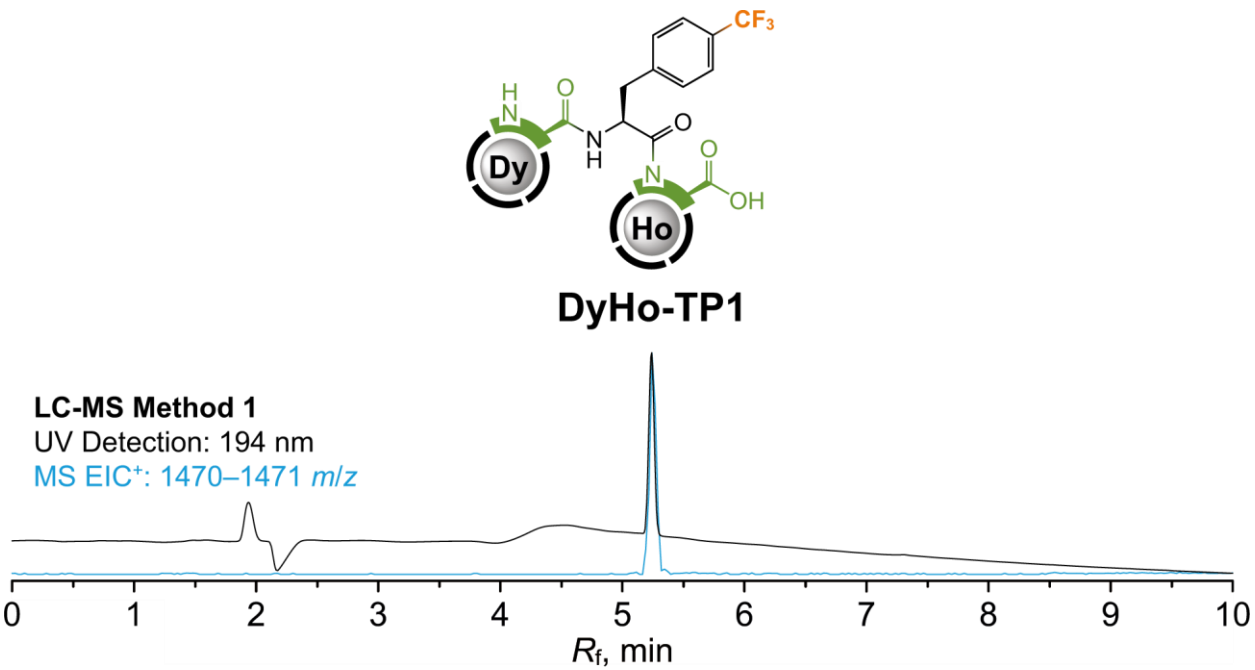

Synthesis and LC-MS chromatogram of DyHo-TP1: In a glass vial (4 mL), **Ho-TP1** (0.4 mg, ~0.3 µmol assuming **Ho-TP1**·2.5FA, 1.0 equiv.) was dissolved in aq. MOPS/NaOH buffer (500 mM, pH 7.0, 250 µL, 125 µmol, ~900 equiv.) followed by addition of aq. $DyCl_3$ (100 mM, 3 µL, 0.3 µmol, ~1.1 equiv.) and the resulting solution was stirred at RT for 15 mins. The mixture was then purified by preparative HPLC (C18, H_2O/MeCN gradient with 0.1% TFA additive). Fractions with product were joined and lyophilized to give product as white solid. **Yield:** ~0.4 mg. **NMR (aq. MOPS pH = 7.0, external D_2O):** ^{19}**F** (470.4 MHz, T = 298.2 K) δ_F –62.75 (CF_3, s). **ESI-HRMS:** 736.1643 $[M+2H]^{2+}$ (theor. $[C_{48}H_{68}O_{18}N_{11}F_3Dy_1Ho_1]^{2+}$ = 736.1640).

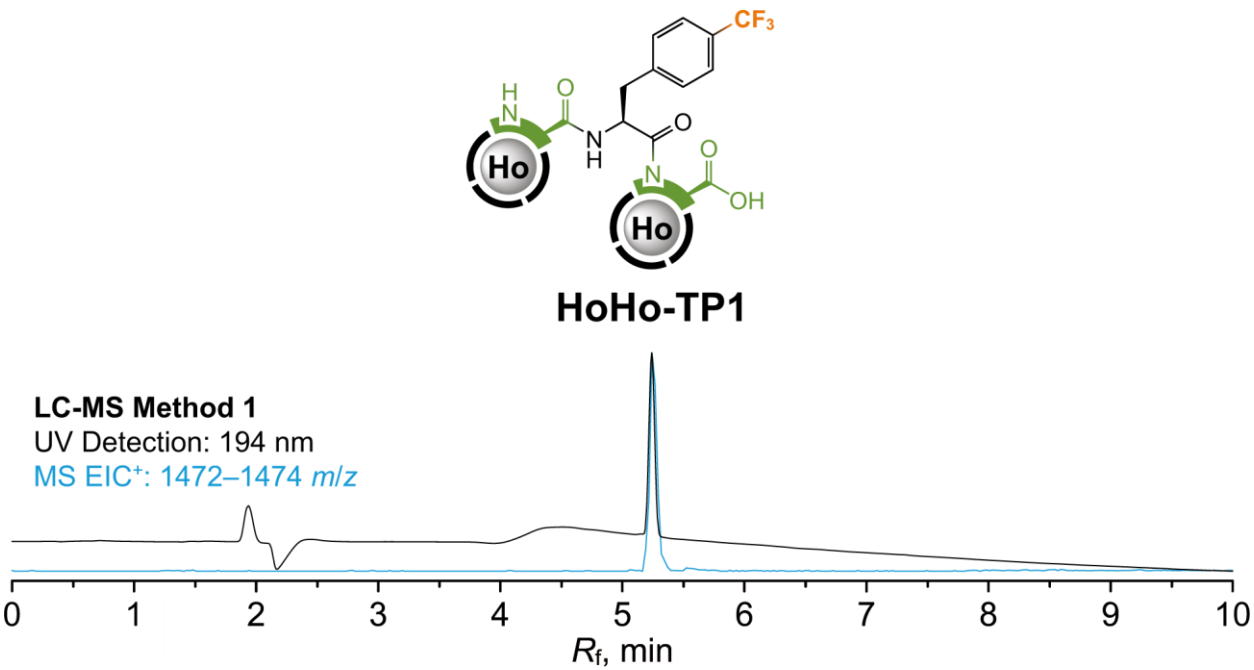

Synthesis and LC-MS chromatogram of HoHo-TP1: In a glass vial (4 mL), **Ho-TP1** (0.4 mg, ~0.3 µmol assuming **Ho-TP1**·2.5FA, 1.0 equiv.) was dissolved in aq. MOPS/NaOH buffer (500 mM, pH 7.0, 250 µL, 125 µmol, ~900 equiv.) followed by addition of aq. $HoCl_3$ (100 mM, 3 µL, 0.3 µmol, ~1.1 equiv.) and the resulting solution was stirred at RT for 15 mins. The mixture was then purified by preparative HPLC (C18, H_2O/MeCN gradient with 0.1% TFA additive). Fractions with product were joined and lyophilized to give product as white solid. **Yield:** ~0.4 mg. **NMR (aq. MOPS pH = 7.0, external D_2O):** ^{19}**F** (470.4 MHz, T = 298.2 K) δ_F –60.20 (CF_3, s). **ESI-HRMS:** 736.6644 $[M+2H]^{2+}$ (theor. $[C_{48}H_{68}O_{18}N_{11}F_3Ho_2]^{2+}$ = 736.6646).

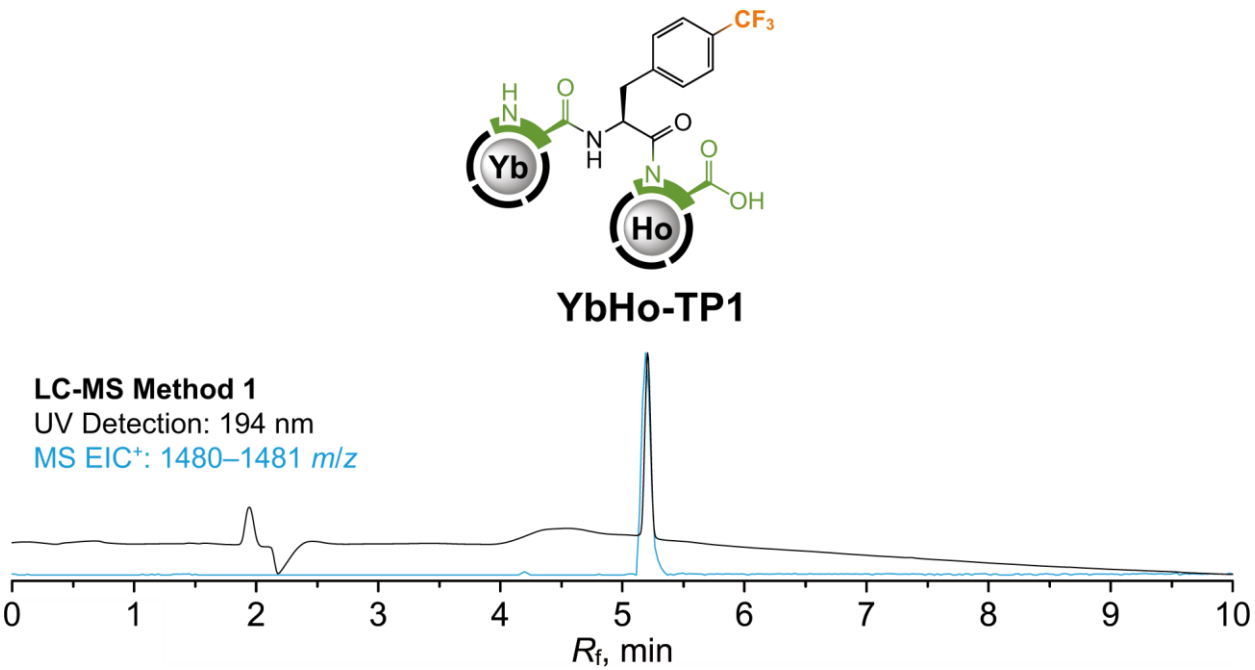

Synthesis and LC-MS chromatogram of YbHo-TP1: In a glass vial (4 mL), **Ho-TP1** (0.5 mg, ~0.4 µmol assuming **Ho-TP1**·2.5FA, 1.0 equiv.) was dissolved in aq. MOPS/NaOH buffer (500 mM, pH 7.0, 250 µL, 125 µmol, ~350 equiv.) followed by addition of aq. $YbCl_3$ (100 mM, 5 µL, 0.5 µmol, ~1.4 equiv.) and the resulting solution was stirred at RT for 15 mins. The mixture was then purified by preparative HPLC (C18, H_2O/MeCN gradient with 0.1% TFA additive). Fractions with product were joined and lyophilized to give product as white solid. **Yield:** ~0.3 mg. **NMR (aq. MOPS pH = 7.0, external D_2O):** ^{19}**F** (470.4 MHz, T = 298.2 K) δ_F –53.02 (CF_3, s). **ESI-HRMS:** 741.1700 $[M+2H]^{2+}$ (theor. $[C_{48}H_{68}O_{18}N_{11}F_3Yb_1Ho_1]^{2+}$ = 741.1688).

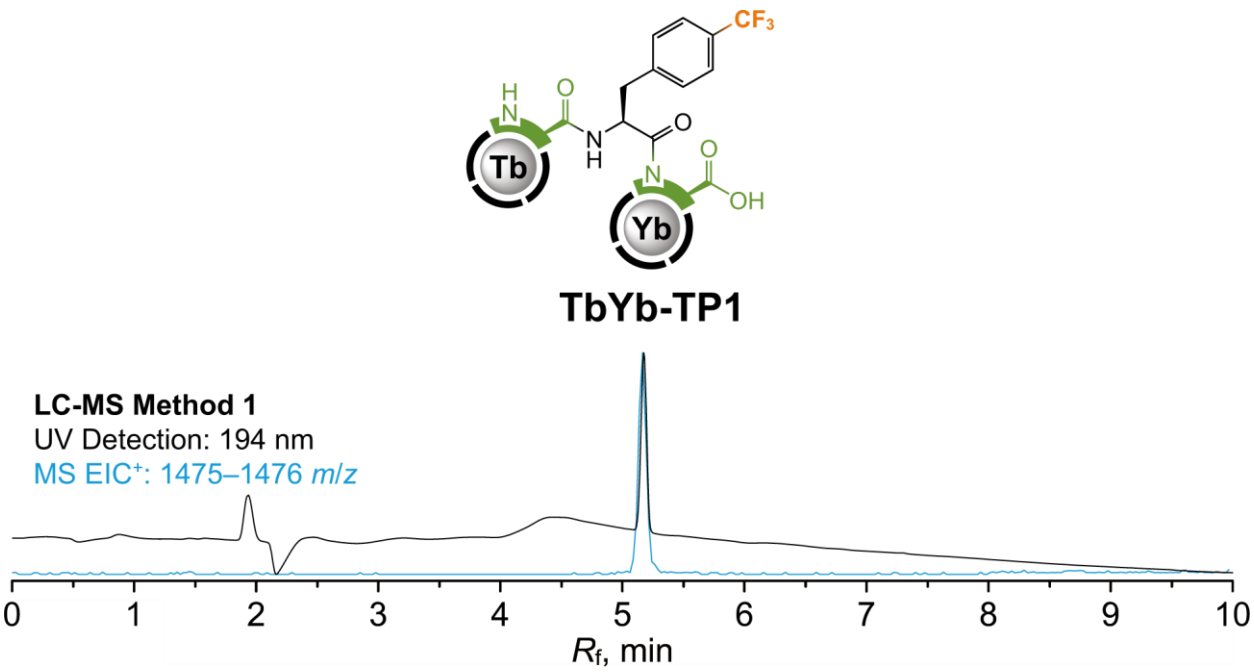

Synthesis and LC-MS chromatogram of TbYb-TP1: In a glass vial (4 mL), **Yb-TP1** (0.4 mg, ~0.3 µmol assuming **Yb-TP1**·2.5FA, 1.0 equiv.) was dissolved in aq. MOPS/NaOH buffer (500 mM, pH 7.0, 250 µL, 125 µmol, ~900 equiv.) followed by addition of aq. $TbCl_3$ (100 mM, 4 µL, 0.4 µmol, ~1.4 equiv.) and the resulting solution was stirred at RT for 15 mins. The mixture was then purified by preparative HPLC (C18, H_2O/MeCN gradient with 0.1% TFA additive). Fractions with product were joined and lyophilized to give product as white solid. **Yield:** ~0.3 mg. **NMR (aq. MOPS pH = 7.0, external D_2O):** ^{19}**F** (470.4 MHz, T = 298.2 K) δ_F –69.10 (CF_3, s). **ESI-HRMS:** 738.1662 $[M+2H]^{2+}$ (theor. $[C_{48}H_{68}O_{18}N_{11}F_3Tb_1Yb_1]^{2+}$ = 738.1664).

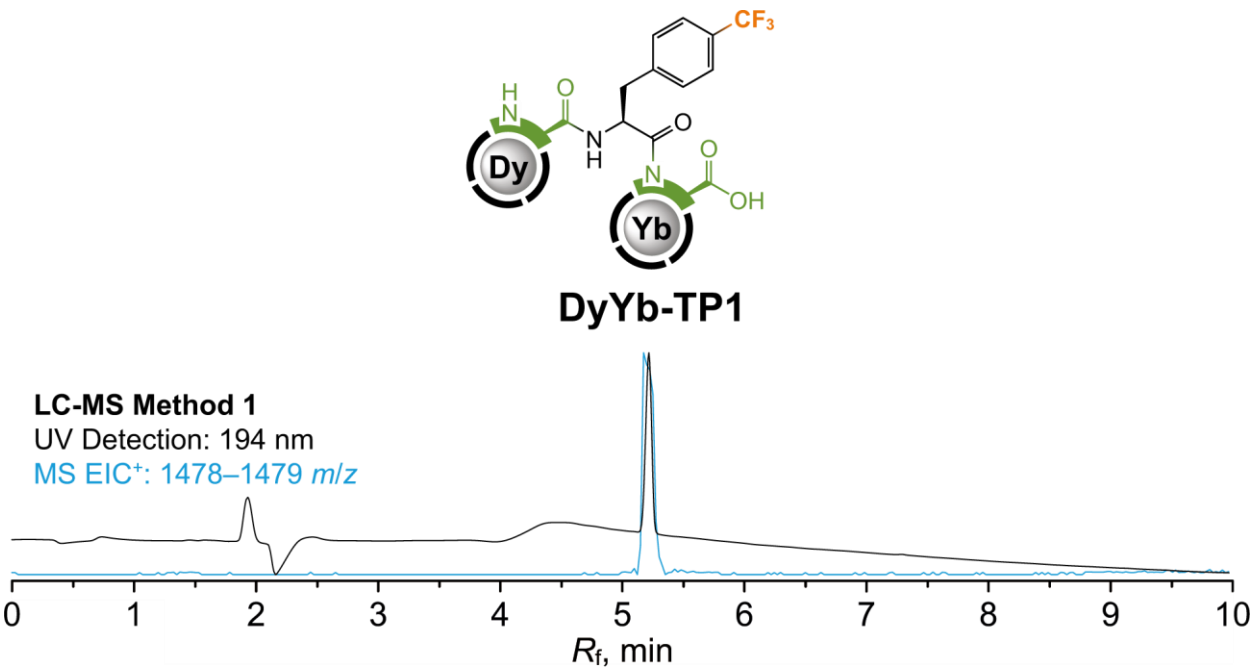

Synthesis and LC-MS chromatogram of DyYb-TP1: In a glass vial (4 mL), **Yb-TP1** (0.4 mg, ~0.3 µmol assuming **Yb-TP1**·2.5FA, 1.0 equiv.) was dissolved in aq. MOPS/NaOH buffer (500 mM, pH 7.0, 250 µL, 125 µmol, ~900 equiv.) followed by addition of aq. $DyCl_3$ (100 mM, 4 µL, 0.4 µmol, ~1.4 equiv.) and the resulting solution was stirred at RT for 15 mins. The mixture was then purified by preparative HPLC (C18, H_2O/MeCN gradient with 0.1% TFA additive). Fractions with product were joined and lyophilized to give product as white solid. **Yield:** ~0.4 mg. **NMR (aq. MOPS pH = 7.0, external D_2O):** ^{19}**F** (470.4 MHz, T = 298.2 K) δ_F –71.04 (CF_3, s). **ESI-HRMS:** 740.6689 $[M+2H]^{2+}$ (theor. $[C_{48}H_{68}O_{18}N_{11}F_3Dy_1Yb_1]^{2+}$ = 740.6683).

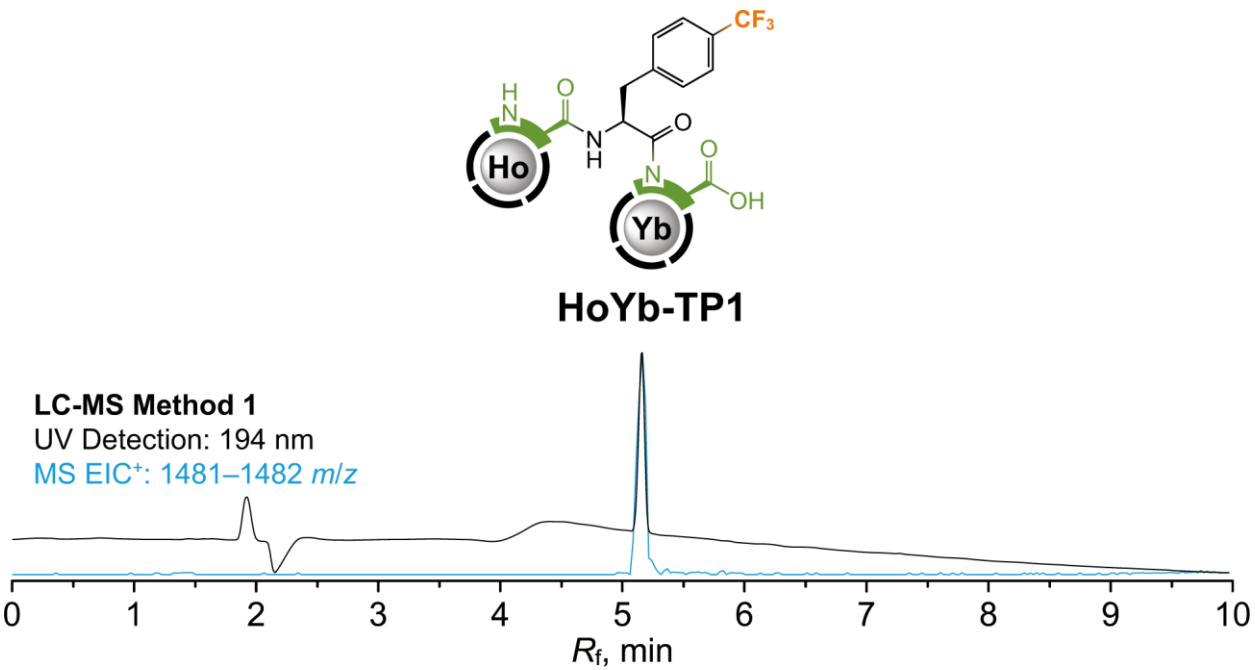

Synthesis and LC-MS chromatogram of HoYb-TP1: In a glass vial (4 mL), **Yb-TP1** (0.4 mg, ~0.3 µmol assuming **Yb-TP1**·2.5FA, 1.0 equiv.) was dissolved in aq. MOPS/NaOH buffer (500 mM, pH 7.0, 250 µL, 125 µmol, ~900 equiv.) followed by addition of aq. $HoCl_3$ (100 mM, 4 µL, 0.4 µmol, ~1.4 equiv.) and the resulting solution was stirred at RT for 15 mins. The mixture was then purified by preparative HPLC (C18, H_2O/MeCN gradient with 0.1% TFA additive). Fractions with product were joined and lyophilized to give product as white solid. **Yield:** ~0.3 mg. **NMR (aq. MOPS pH = 7.0, external D_2O): ^{19}F** (470.4 MHz, T = 298.2 K) δ_F –68.39 (CF_3, s). **ESI-HRMS:** 741.1687 $[M+2H]^{2+}$ (theor. $[C_{48}H_{68}O_{18}N_{11}F_3Ho_1Yb_1]^{2+}$ = 741.1688).

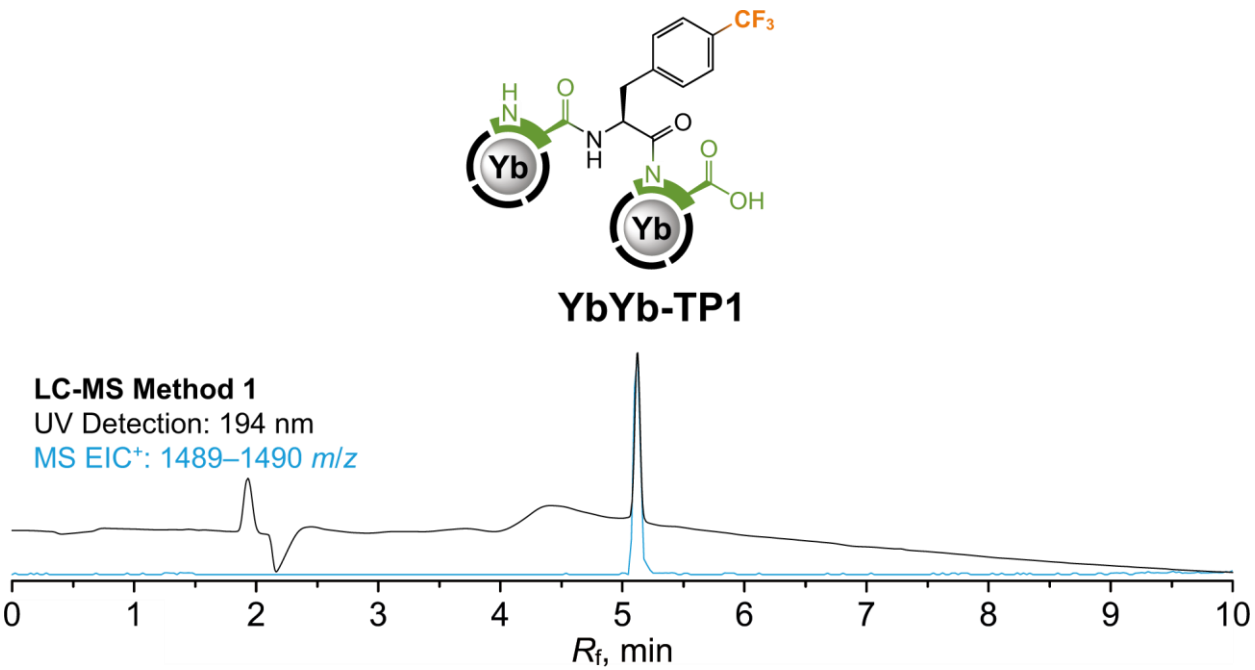

Synthesis and LC-MS chromatogram of YbYb-TP1: In a glass vial (4 mL), **Yb-TP1** (0.4 mg, ~0.3 µmol assuming **Yb-TP1**·2.5FA, 1.0 equiv.) was dissolved in aq. MOPS/NaOH buffer (500 mM, pH 7.0, 250 µL, 125 µmol, ~900 equiv.) followed by addition of aq. $YbCl_3$ (100 mM, 4 µL, 0.4 µmol, ~1.4 equiv.) and the resulting solution was stirred at RT for 15 mins. The mixture was then purified by preparative HPLC (C18, H_2O/MeCN gradient with 0.1% TFA additive). Fractions with product were joined and lyophilized to give product as white solid. **Yield:** ~0.4 mg. **NMR (aq. MOPS pH = 7.0, external D_2O): ^{19}F** (470.4 MHz, T = 298.2 K) δ_F –61.37 (CF_3, s). **ESI-HRMS:** 745.6728 $[M+2H]^{2+}$ (theor. $[C_{48}H_{68}O_{18}N_{11}F_3Yb_2]^{2+}$ = 745.6731).

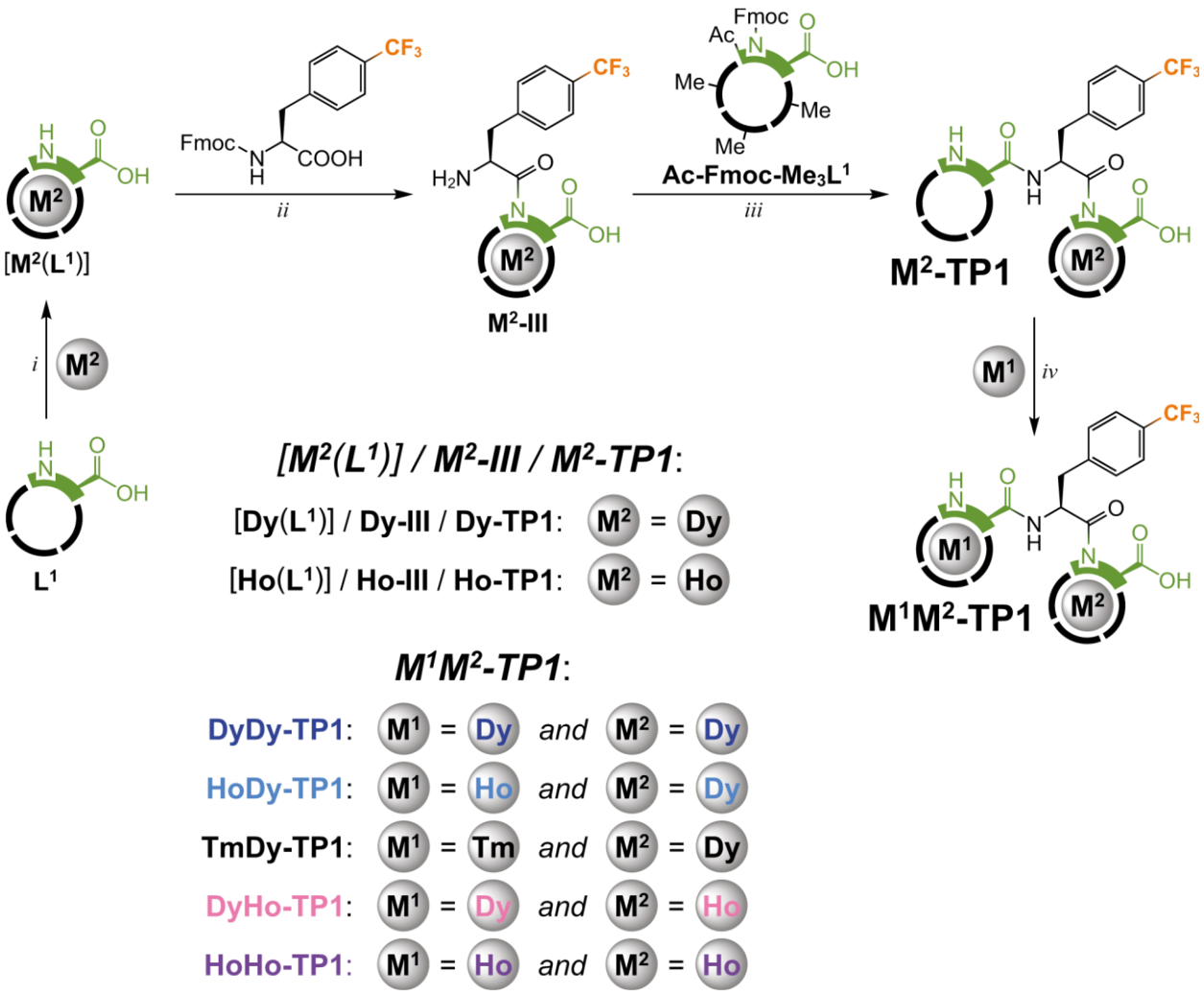

Alternative synthesis of M^1M^2-TP1 tripeptides with Dy^{3+}, Ho^{3+} and Tm^{3+} cations. Charges were omitted for clarity reason. ***Conditions:*** (*i*) M^2Cl_3, aq. MOPS/NaOH buffer (pH 7.0); (*ii*) Fmoc-Phe{*p*-CF_3}-OH, PyAOP, DIPEA, DMSO *followed by* DBU, DMF; (*iii*) **Ac-Fmoc-Me_3L^1**, PyAOP, DIPEA, DMSO *followed by* LiOH, H_2O, MeOH; (*vi*) M^1Cl_3, aq. MOPS/NaOH buffer (pH 7.0).

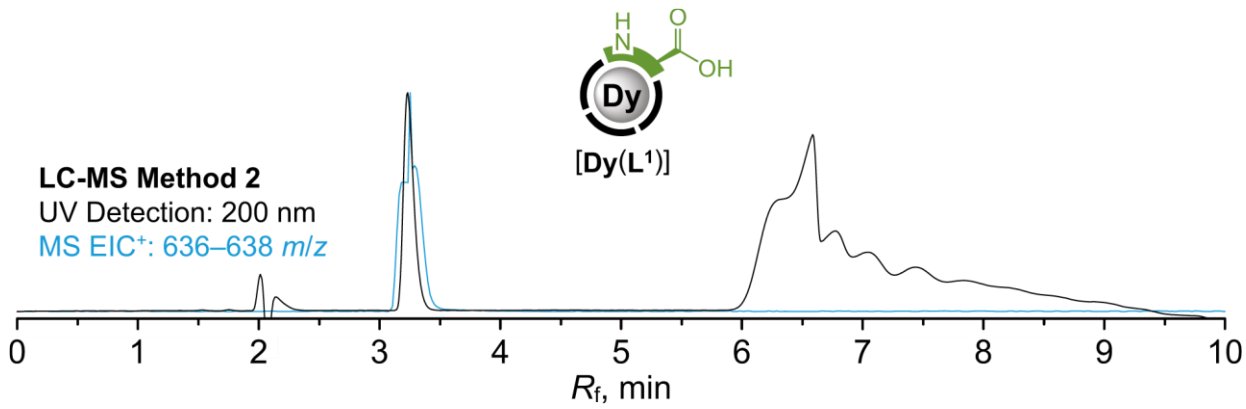

Synthesis and LC-MS chromatogram of building block [Dy(L^1)]: In a glass vial (4 mL), **L^1**·2.4TFA·2.5H_2O (76.8 mg, 96.8 µmol, 1.0 equiv.) was dissolved in aq. MOPS/NaOH buffer (3.0 M, pH 7.0, 1.30 mL, 3.90 mmol, 40 equiv.) followed by addition of aq. $DyCl_3$ (100 mM, 1.03 mL, 103 µmol, 1.1 equiv.) and the resulting solution was stirred at RT for 15 mins. The mixture was then purified by preparative HPLC (C18, H_2O/MeCN gradient with 0.1% TFA additive). Fractions with product were joined and lyophilized to give product as white solid. **Yield:** 61.0 mg (76%; 1 step; based on **L^1**·2.4TFA·2.5H_2O). **ESI-HRMS:** 637.1413 $[M+H]^+$ (theor. $[C_{19}H_{31}O_9N_5Dy_1]^+$ = 637.1408). **EA** ($C_{19}H_{30}N_5O_9Dy_1$·1.2TFA·3.0H_2O, M_R = 825.8): C 31.1 (31.3); H 4.5 (4.3); N 8.5 (8.4); F 8.3 (8.1); Dy 19.7 (19.3). ***Preparation of single crystals:*** In a glass vial (4 mL), aq. solution of [**Dy**(**L^1**)] (repurified on HPLC with 0.1% FA additive – assuming zwitterionic form; ~20 mM, 62 µL, ~1.24 µmol, 1.0 equiv.; filtered through syringe microfilter) was mixed with aq. solution of HBr (~1.0 M, 1.24 µL, 1.24 µmol, ~1.0 equiv.) and the resulting solution was briefly vortexed. Then, *1,4*-dioxane (~160 µL) was slowly added dropwise until opalescence occurred. The mixture was then sealed with a cap and gently heated using heat gun until clear solution was produced. The mixture was then left standing at RT for 3 weeks, producing single crystals of [**Dy**(**L^1**)]·3.5H_2O suitable for X-Ray analysis. Similar crystallization experiment with $HClO_4$ instead of HBr yielded identical crystals.

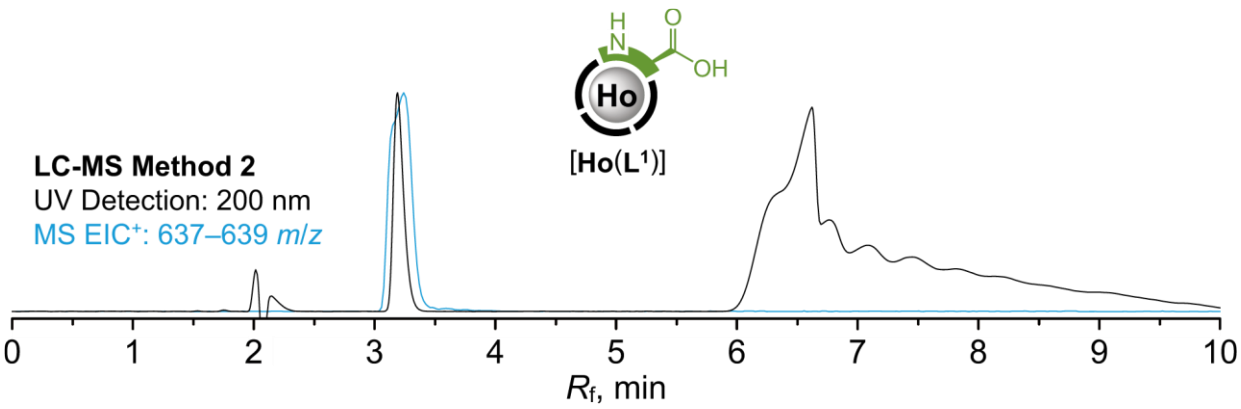

Synthesis and LC-MS chromatogram of building block [Ho(L¹)]: In a glass vial (4 mL), **L¹**·2.4TFA·2.5H_2O (76.8 mg, 96.8 µmol, 1.0 equiv.) was dissolved in aq. MOPS/NaOH buffer (3.0 M, pH 7.0, 1.30 mL, 3.90 mmol, 40 equiv.) followed by addition of aq. $HoCl_3$ (100 mM, 1.03 mL, 103 µmol, 1.1 equiv.) and the resulting solution was stirred at RT for 15 mins. The mixture was then purified by preparative HPLC (C18, H_2O/MeCN gradient with 0.1% TFA additive). Fractions with product were joined and lyophilized to give product as pinkish solid. **Yield:** 61.7 mg (78%; 1 step; based on **L¹**·2.4TFA·2.5H_2O). **ESI-HRMS:** 638.1424 $[M+H]^+$ (theor. $[C_{19}H_{31}O_9N_5Ho_1]^+$ = 638.1420). **EA** ($C_{19}H_{30}N_5O_9Ho_1$·1.1TFA·3.0H_2O, M_R = 816.8): C 31.2 (31.4); H 4.6 (4.3); N 8.6 (8.3); F 7.7 (7.8); Ho 20.2 (19.8).

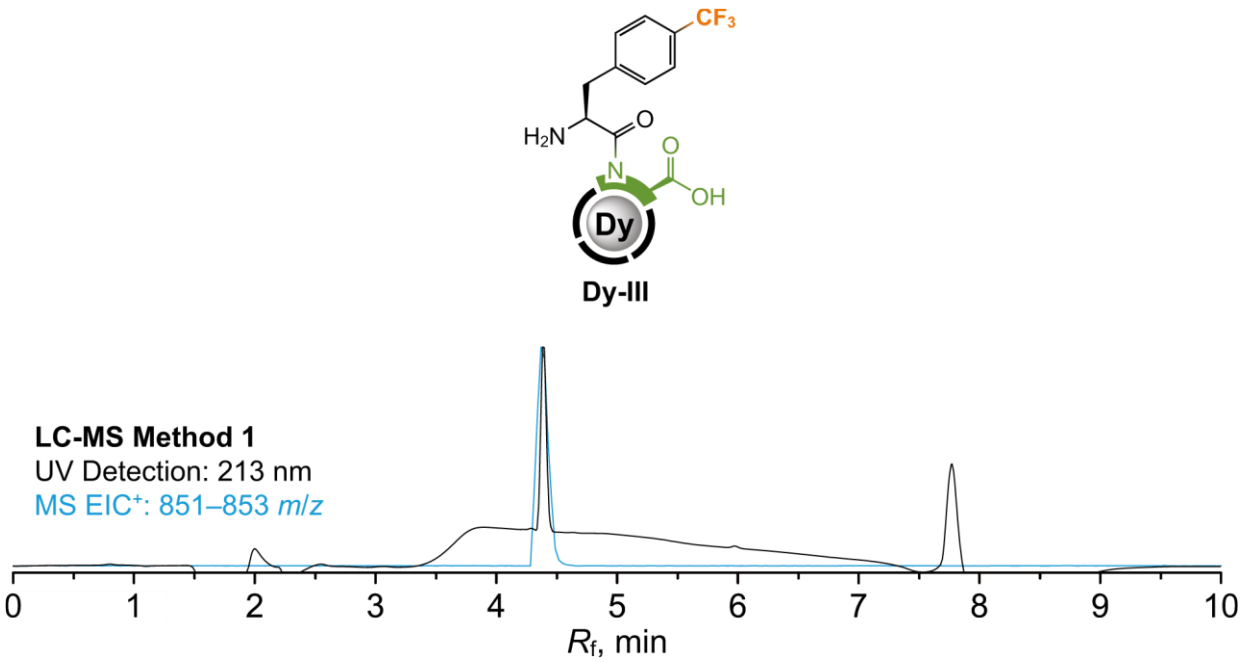

Synthesis and LC-MS chromatogram of intermediate Dy-III: In a glass vial (4 mL), [**Dy**(**L**^{1})] ·1.2TFA·3.0H_2O (12.8 mg, 15.5 µmol, 1.0 equiv.) was dissolved in dry DMSO (764 µL), followed by addition of Fmoc-Phe{*p*-CF_3}-OH (100 mM in dry DMSO, 389 µL, 38.9 µmol, 2.5 equiv.), PyAOP (100 mM in dry DMSO, 389 µL, 38.9 µmol, 2.5 equiv.) and DIPEA (13.5 µL, 77.1 µmol, 5.0 equiv.). The resulting solution was sonicated at RT for 2 mins and then further stirred at RT for 30 mins. The mixture was then purified by preparative HPLC (C18, H_2O/MeCN gradient with 0.1% FA additive). Fractions with Fmoc protected product were joined and lyophilized. The resulting white solid was dissolved in 2% DBU in DMF (891 µL, 119 µmol, 7.7 equiv.) and the solution was stirred at RT for 5 mins. Reaction was quenched with TFA (8 µL, 105 µmol, 6.8 equiv.) followed by addition of H_2O (100 µL). The mixture was then purified by preparative HPLC (C18, H_2O/MeCN gradient with 0.1% TFA additive). Fractions with product were joined and lyophilized to give product as white solid. **Yield:** 8.5 mg (51%; 2 steps; based on [**Dy**(**L**^{1})] ·1.2TFA·3.0H_2O). **ESI-HRMS:** 852.1981 $[M+H]^+$ (theor. $[C_{29}H_{39}O_{10}N_6F_3Dy_1]^+$ = 852.1966). **EA** ($C_{29}H_{38}N_6O_{10}F_3Dy_1$·1.1TFA·5.0$H_2O$, M_R = 1065.6): C 35.2 (34.8); H 4.6 (4.4); N 7.9 (7.7); F 11.2 (10.9).

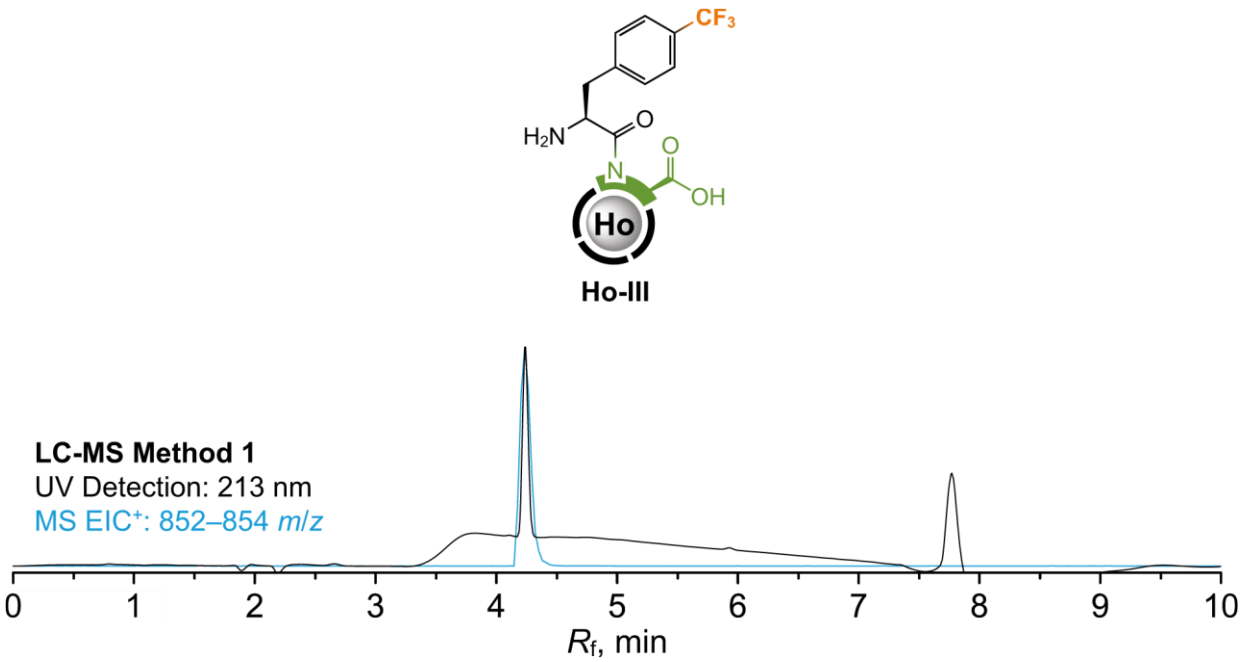

Synthesis and LC-MS chromatogram of intermediate Ho-III: In a glass vial (4 mL), [**Ho**(**L**^{1})]·1.1TFA·3.0H_2O (13.8 mg, 16.9 µmol, 1.0 equiv.) was dissolved in dry DMSO (826 µL), followed by addition of Fmoc-Phe{*p*-CF_3}-OH (100 mM in dry DMSO, 420 µL, 42.0 µmol, 2.5 equiv.), PyAOP (100 mM in dry DMSO, 420 µL, 42.0 µmol, 2.5 equiv.) and DIPEA (14.6 µL, 84.0 µmol, 5.0 equiv.). The resulting solution was sonicated at RT for 2 mins and then further stirred at RT for 30 mins. The mixture was then purified by preparative HPLC (C18, H_2O/MeCN gradient with 0.1% FA additive). Fractions with Fmoc protected product were joined and lyophilized. The resulting pinkish solid was dissolved in 2% DBU in DMF (906 µL, 121 µmol, 7.2 equiv.) and the solution was stirred at RT for 5 mins. Reaction was quenched with TFA (9 µL, 118 µmol, 7.0 equiv.) followed by addition of H_2O (100 µL). The mixture was then purified by preparative HPLC (C18, H_2O/MeCN gradient with 0.1% TFA additive). Fractions with product were joined and lyophilized to give product as pinkish solid. **Yield:** 8.7 mg (49%; 2 steps; based on [**Ho**(**L**^{1})]·1.1TFA·3.0H_2O assuming **Ho-III**·1.0TFA·5.0H_2O according to **Dy-IV** analogy, M_R = 1057). **ESI-HRMS:** 853.1985 $[M+H]^+$ (theor. $[C_{29}H_{39}O_{10}N_6F_3Ho_1]^+$ = 853.1978).

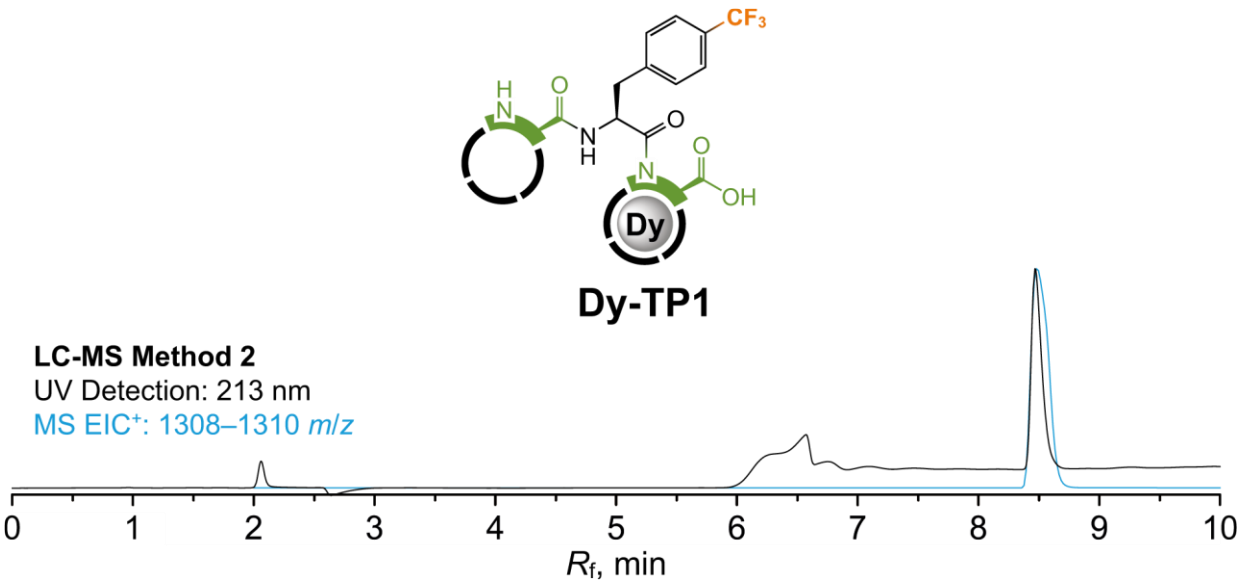

Synthesis and LC-MS chromatogram of intermediate Dy-TP1: In a glass vial (4 mL), **Dy-III**·1.1TFA·5.0H_2O (25.4 mg, 23.8 µmol, 1.0 equiv.) was dissolved in dry DMSO (1.28 mL), followed by addition of **Ac-Fmoc-Me$_3$L^1**·1.9TFA·1.3H_2O (100 mM in dry DMSO, 238 µL, 23.8 µmol, 1.0 equiv.), PyAOP (100 mM in dry DMSO, 596 µL, 59.6 µmol, 2.5 equiv.) and DIPEA (29.0 µL, 166 µmol, 7.0 equiv.). The resulting solution was stirred at RT for 30 mins. The mixture was then purified by preparative HPLC (C18, H_2O/MeCN gradient with 0.1% FA additive). Fractions with protected product were joined and lyophilized. The resulting white solid was dissolved in a mixture of MeOH (3.68 mL) and H_2O (0.41 mL) followed by addition of aq. LiOH (100 mM, 364 µL, 364 µmol, 15 equiv.) and the mixture was stirred at RT for 43 h. Reaction was then quenched by FA (12.5 µL, 331 µmol, 14 equiv.) and the mixture was evaporated to dryness. The residue was purified by preparative HPLC (C18, H_2O/MeCN gradient with 0.1% FA additive). Fractions with product were joined and lyophilized to give product as white solid. **Yield:** 15.5 mg (46%; 2 steps; based on **Dy-III**·1.1TFA·5.0H_2O assuming **Dy-TP1**·2.5FA, M_R = 1423). **ESI-HRMS:** 1309.4130 $[M+H]^+$ (theor. $[C_{48}H_{70}O_{18}N_{11}F_3Dy_1]^+$ = 1309.4139).

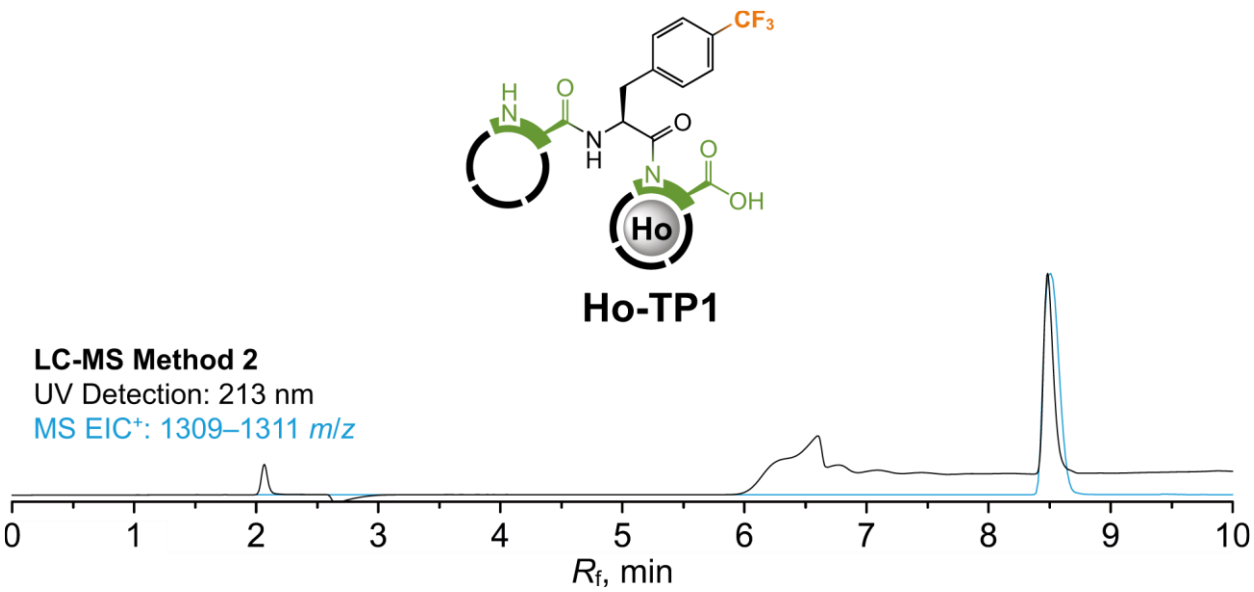

Synthesis and LC-MS chromatogram of intermediate Ho-TP1: In a glass vial (4 mL), **Ho-III** (26.3 mg, 24.9 µmol assuming **Ho-III**·1.0TFA·5.0H_2O, 1.0 equiv.) was dissolved in dry DMSO (1.33 mL), followed by addition of **Ac-Fmoc-Me$_3$L^1**·1.9TFA·1.3H_2O (100 mM in dry DMSO, 247 µL, 24.7 µmol, 1.0 equiv.), PyAOP (100 mM in dry DMSO, 617 µL, 61.7 µmol, 2.5 equiv.) and DIPEA (30.0 µL, 171 µmol, 6.9 equiv.). The resulting solution was stirred at RT for 30 mins. The mixture was then purified by preparative HPLC (C18, H_2O/MeCN gradient with 0.1% FA additive). Fractions with protected product were joined and lyophilized. The resulting pinkish solid was dissolved in a mixture of MeOH (4.11 mL) and H_2O (0.46 mL) followed by addition of aq. LiOH (100 mM, 373 µL, 373 µmol, 15 equiv.) and the mixture was stirred at RT for 43 h. Reaction was then quenched by FA (14.1 µL, 374 µmol, 15 equiv.) and the mixture was evaporated to dryness. The residue was purified by preparative HPLC (C18, H_2O/MeCN gradient with 0.1% FA additive). Fractions with product were joined and lyophilized to give product as pinkish solid. **Yield:** 19.1 mg (54%; 2 steps; based on **Ho-III**·1.0TFA·5.0H_2O assuming **Ho-TP1**·2.5FA, M_R = 1425). **ESI-HRMS:** 1310.4146 $[M+H]^+$ (theor. $[C_{48}H_{70}O_{18}N_{11}F_3Ho_1]^+$ = 1310.4150).

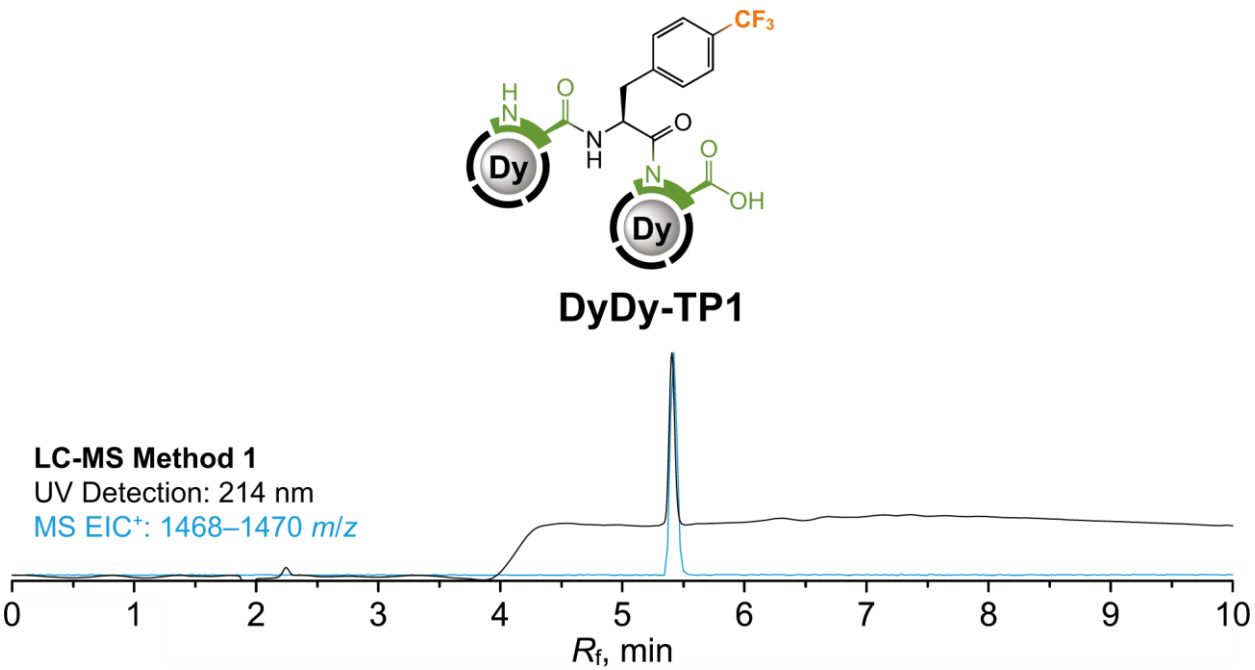

Synthesis and LC-MS chromatogram of DyDy-TP1: In a glass vial (4 mL), **Dy-TP1** (7.0 mg, 4.9 µmol assuming **Dy-TP1**·2.5FA, 1.0 equiv.) was dissolved in aq. MOPS/NaOH buffer (500 mM, pH 7.0, 2.0 mL, 1.0 mmol, 200 equiv.) followed by addition of aq. $DyCl_3$ (100 mM, 59 µL, 5.9 µmol, 1.2 equiv.) and the resulting solution was stirred at RT for 15 mins. The mixture was then purified by preparative HPLC (C18, H_2O/MeCN gradient with 0.1% TFA additive). Fractions with product were joined and lyophilized to give product as white solid. **Yield:** 7.3 mg (94%; 1 step; based on **Dy-TP1**·2.5FA assuming **DyDy-TP1**·1.0TFA, M_R = 1581). **NMR (aq. MOPS pH = 7.0, external D_2O): ^{19}F** (470.4 MHz, T = 298.2 K) δ_F –57.33 (CF_3, s). **ESI-HRMS:** 735.6657 $[M+2H]^{2+}$ (theor. $[C_{48}H_{68}O_{18}N_{11}F_3Dy_2]^{2+}$ = 735.6634).

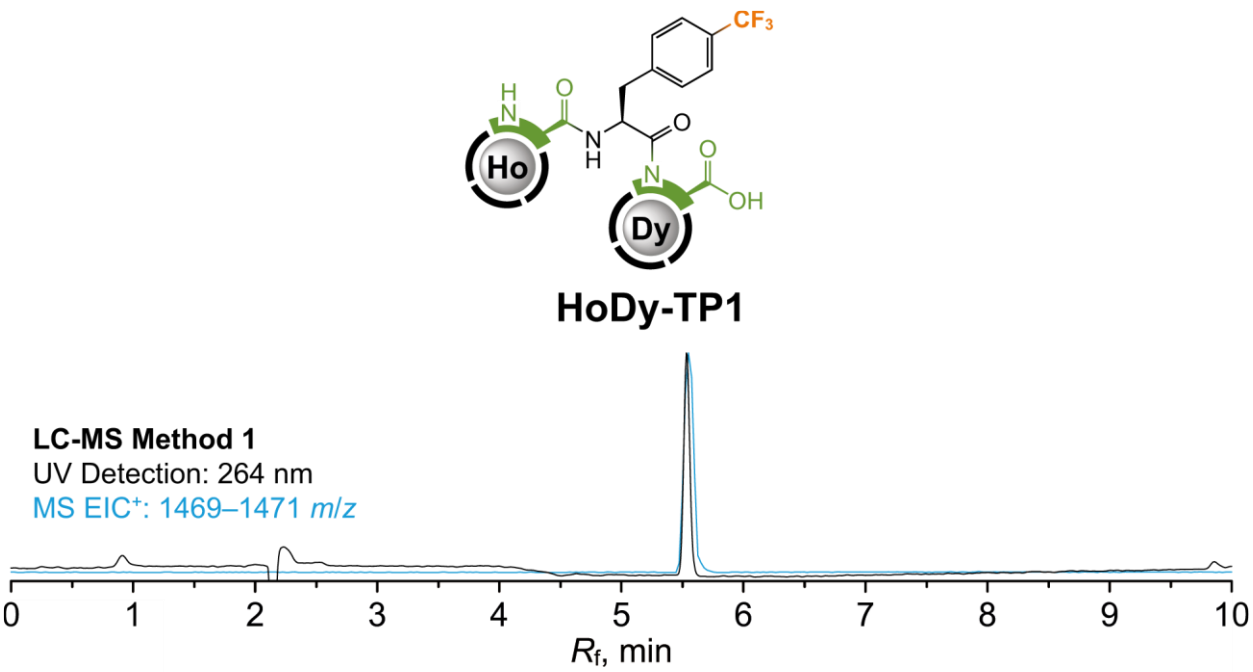

Synthesis and LC-MS chromatogram of HoDy-TP1: In a glass vial (4 mL), **Dy-TP1** (7.0 mg, 4.9 µmol assuming **Dy-TP1**·2.5FA, 1.0 equiv.) was dissolved in aq. MOPS/NaOH buffer (500 mM, pH 7.0, 2.0 mL, 1.0 mmol, 200 equiv.) followed by addition of aq. $HoCl_3$ (100 mM, 59 µL, 5.9 µmol, 1.2 equiv.) and the resulting solution was stirred at RT for 15 mins. The mixture was then purified by preparative HPLC (C18, H_2O/MeCN gradient with 0.1% TFA additive). Fractions with product were joined and lyophilized to give product as pinkish solid. **Yield:** 7.4 mg (95%; 1 step; based on **Dy-TP1**·2.5FA assuming **HoDy-TP1**·1.0TFA, M_R = 1584). **NMR (aq. MOPS pH = 7.0, external D_2O):** ^{19}**F** (470.4 MHz, T = 298.2 K) δ_F –54.75 (CF_3, s). **ESI-HRMS:** 736.1659 $[M+2H]^{2+}$ (theor. $[C_{48}H_{68}O_{18}N_{11}F_3Dy_1Ho_1]^{2+}$ = 736.1640).

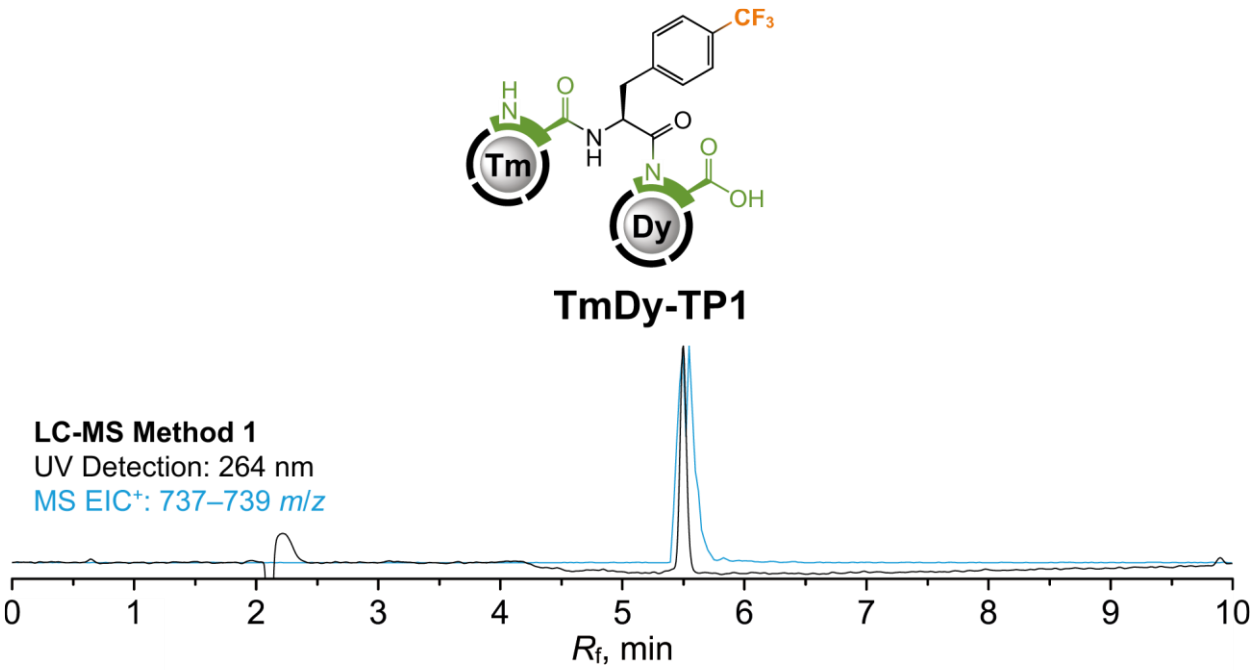

Synthesis and LC-MS chromatogram of TmDy-TP1: In a glass vial (2 mL), **Dy-TP1** (0.8 mg, 0.56 µmol assuming **Dy-TP1**·2.5FA, 1.0 equiv.) was dissolved in aq. MOPS/NaOH buffer (500 mM, pH 7.0, 100 µL, 50 µmol, 90 equiv.) followed by addition of aq. $TmCl_3$ (100 mM, 12 µL, 1.2 µmol, 2.1 equiv.) and the resulting solution was stirred at RT for 15 mins. The mixture was then purified by preparative HPLC (C18, H_2O/MeCN gradient with 0.1% TFA additive). Fractions with product were joined and lyophilized to give product as white solid. **Yield:** 0.7 mg (79%; 1 step; based on **Dy-TP1**·2.5FA assuming **TmDy-TP1**·1.0TFA, M_R = 1588). **NMR (aq. MOPS pH = 7.0, external D_2O): ^{19}F** (470.4 MHz, T = 298.2 K) δ_F –38.16 (CF_3, s). **ESI-HRMS:** 738.1666 $[M+2H]^{2+}$ (theor. $[C_{48}H_{68}O_{18}N_{11}F_3Dy_1Tm_1]^{2+}$ = 738.1659).

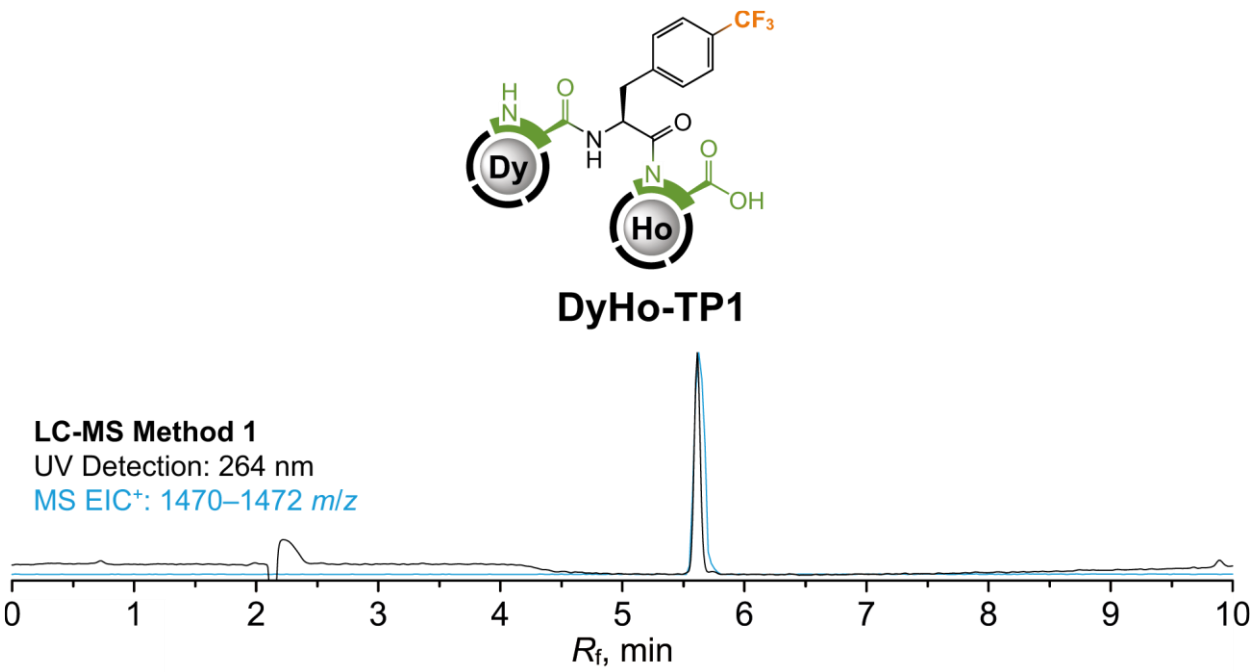

Synthesis and LC-MS chromatogram of DyHo-TP1: In a glass vial (4 mL), **Ho-TP1** (9.0 mg, 6.3 µmol assuming **Ho-TP1**·2.5FA, 1.0 equiv.) was dissolved in aq. MOPS/NaOH buffer (500 mM, pH 7.0, 2.0 mL, 1.0 mmol, 160 equiv.) followed by addition of aq. $DyCl_3$ (100 mM, 76 µL, 7.6 µmol, 1.2 equiv.) and the resulting solution was stirred at RT for 15 mins. The mixture was then purified by preparative HPLC (C18, H_2O/MeCN gradient with 0.1% TFA additive). Fractions with product were joined and lyophilized to give product as pinkish solid. **Yield:** 8.1 mg (81%; 1 step; based on **Ho-TP1**·2.5FA assuming **DyHo-TP1**·1.0TFA, M_R = 1584). **NMR (aq. MOPS pH = 7.0, external D_2O):** ^{19}**F** (470.4 MHz, T = 298.2 K) δ_F –62.75 (CF_3, s). **ESI-HRMS:** 736.1651 $[M+2H]^{2+}$ (theor. $[C_{48}H_{68}O_{18}N_{11}F_3Ho_1Dy_1]^{2+}$ =736.1640).

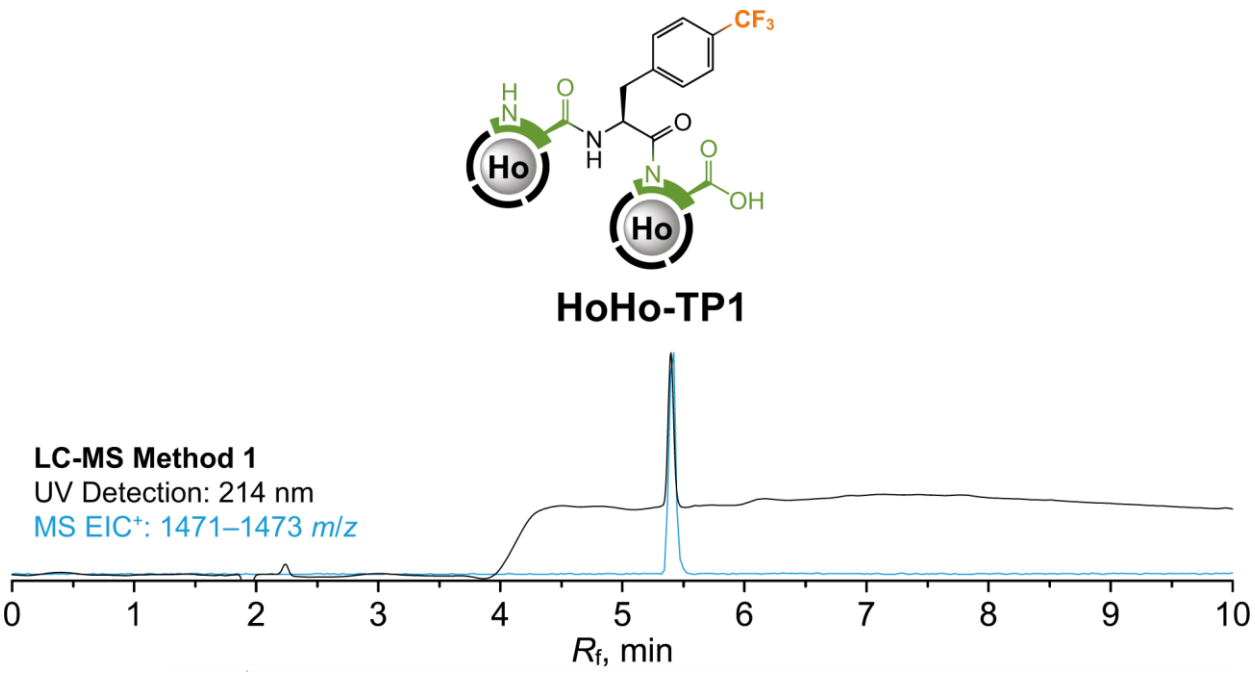

Synthesis and LC-MS chromatogram of HoHo-TP1: In a glass vial (4 mL), **Ho-TP1** (9.0 mg, 6.3 µmol assuming **Ho-TP1**·2.5FA, 1.0 equiv.) was dissolved in aq. MOPS/NaOH buffer (500 mM, pH 7.0, 2.0 mL, 1.0 mmol, 160 equiv.) followed by addition of aq. $HoCl_3$ (100 mM, 76 µL, 7.6 µmol, 1.2 equiv.) and the resulting solution was stirred at RT for 15 mins. The mixture was then purified by preparative HPLC (C18, H_2O/MeCN gradient with 0.1% TFA additive). Fractions with product were joined and lyophilized to give product as pinkish solid. **Yield:** 8.7 mg (87%; 1 step; based on **Ho-TP1**·2.5FA assuming **HoHo-TP1**·1.0TFA, M_R = 1586). **NMR (aq. MOPS pH = 7.0, external D_2O): ^{19}F** (470.4 MHz, T = 298.2 K) δ_F –60.19 (CF_3, s). **ESI-HRMS:** 1472.3229 $[M+H]^+$ (theor. $[C_{48}H_{67}O_{18}N_{11}F_3Ho_2]^+$ =1472.3219).

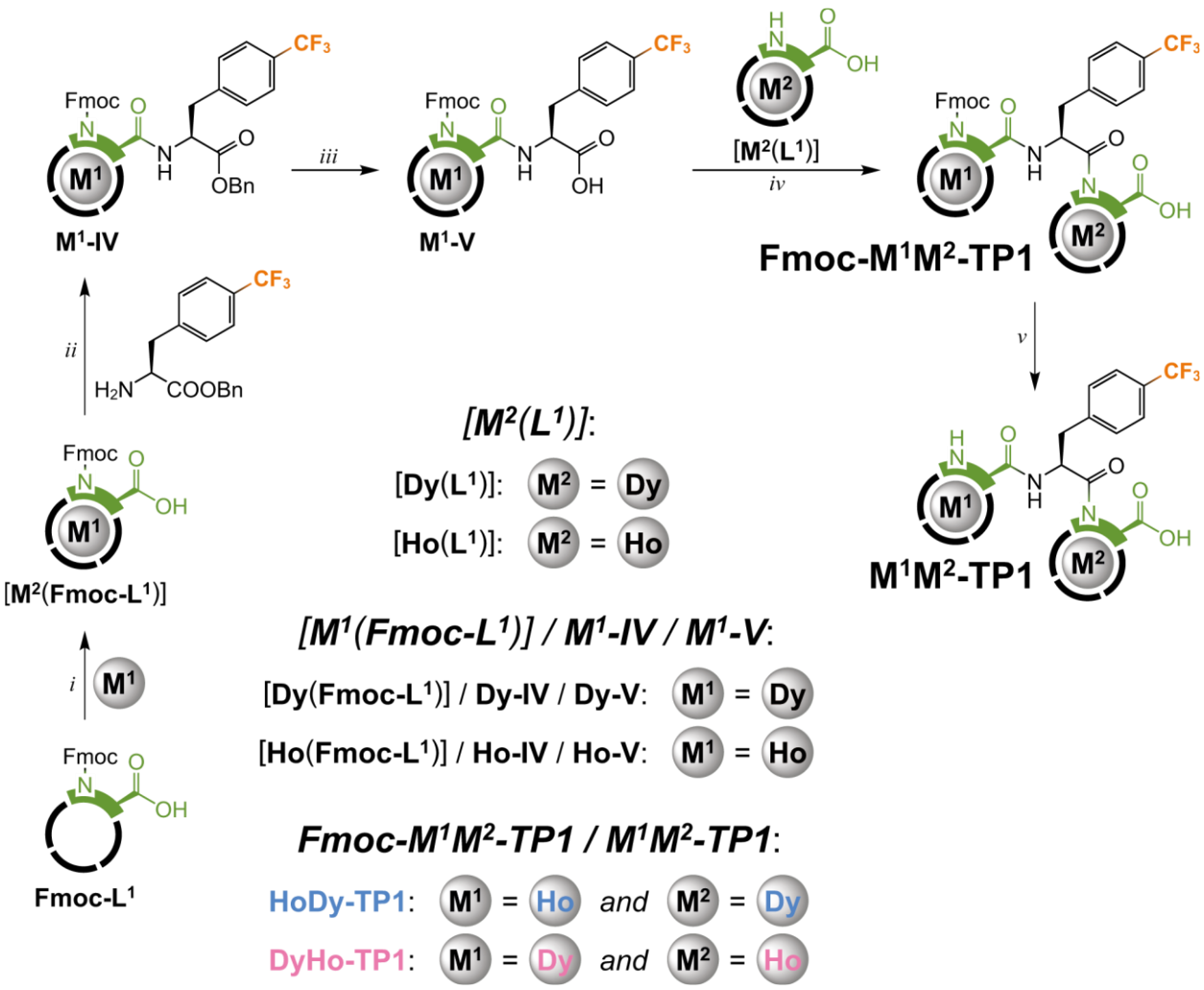

Direct synthesis of DyHo-TP1 and HoDy-TP1. ***Conditions:*** (*i*) M^1Cl_3, aq. MOPS/NaOH (pH 7.0); (*ii*) H-Phe{*p*-CF_3}-OBn, PyAOP, DIPEA, DMSO, 80 °C; (*iii*) H_2, Pd@C, MeOH; (*iv*) [$\mathbf{M^2(L^1)}$], PyAOP, DIPEA, DMSO; (*v*) DBU, DMF.

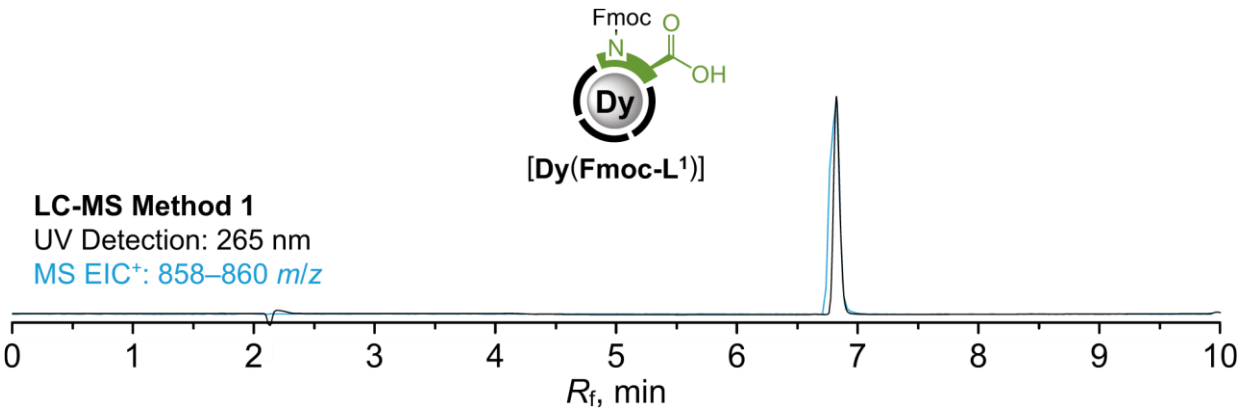

Synthesis and LC-MS chromatogram of building block [Dy(Fmoc-L^1]: In a glass vial (4 mL), **Fmoc-L^1**·2.0TFA·1.3FA (58.0 mg, 58.9 µmol, 1.0 equiv.) was dissolved in H_2O (1 mL) followed by addition of aq. MOPS/NaOH buffer (3.0 M, pH 7.0, 787 µL, 2.36 mmol, 40 equiv.) followed by addition of aq. $DyCl_3$ (100 mM, 700 µL, 70 µmol, 1.2 equiv.) and the resulting solution was stirred at RT for 15 mins. The mixture was then purified by preparative HPLC (C18, H_2O/MeCN gradient with 0.1% TFA additive). Fractions with product were joined and lyophilized to give product as white solid. **Yield:** 42.0 mg (68%; 1 step; based on **Fmoc-L^1**2.0·TFA1.3·FA). **ESI-HRMS:** 881.1928 $[M+Na]^+$ (theor. $[C_{34}H_{40}O_{11}N_5Dy_1Na_1]^+ = 881.1908$). **EA** ($C_{34}H_{40}N_5O_{11}Dy_1$·1.1TFA·3.5$H_2O$, M_R = 1045.7): C 41.6 (41.9); H 4.6 (4.4); N 6.7 (6.4); F 6.0 (6.0); Dy 15.5 (12.5).

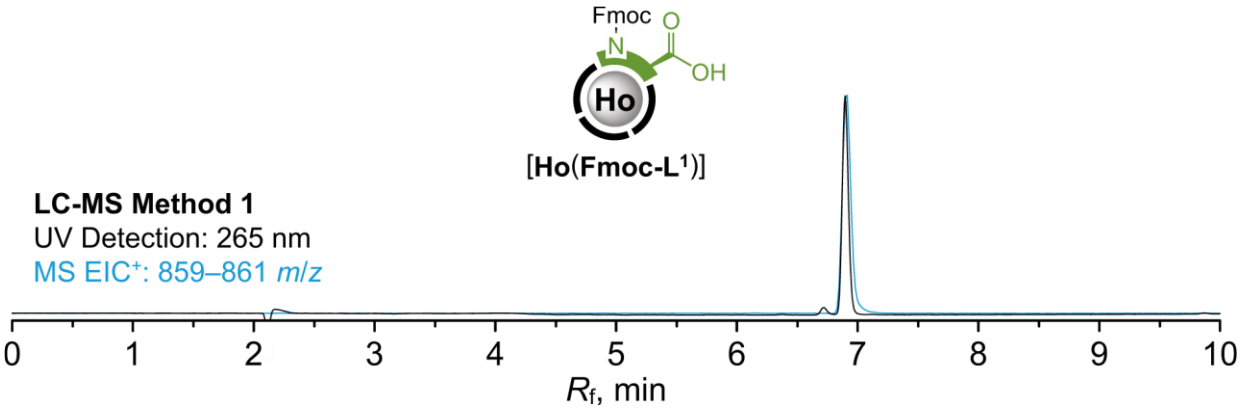

Synthesis and LC-MS chromatogram of building block [Ho(Fmoc-L^1]: In a glass vial (4 mL), **Fmoc-L^1**·2.0TFA·1.3FA (58.0 mg, 58.9 µmol, 1.0 equiv.) was dissolved in H_2O (1 mL) followed by addition of aq. MOPS/NaOH buffer (3.0 M, pH 7.0, 787 µL, 2.36 mmol, 40 equiv.) followed by addition of aq. $HoCl_3$ (100 mM, 700 µL, 70 µmol, 1.2 equiv.) and the resulting solution was stirred at RT for 15 mins. The mixture was then purified by preparative HPLC (C18, H_2O/MeCN gradient with 0.1% TFA additive). Fractions with product were joined and lyophilized to give product as pinkish solid. **Yield:** 38.5 mg (62%; 1 step; based on **Fmoc-L^1**·2.0TFA·1.3FA). **ESI-HRMS:** 860.2111 $[M+H]^+$ (theor. $[C_{34}H_{41}O_{11}N_5Ho_1]^+$ =

860.2100). **EA** ($C_{34}H_{40}N_5O_{11}Ho_1 \cdot 1.1TFA \cdot 3.5H_2O$, M_R = 1048.1): C 41.5 (41.9); H 4.6 (4.5); N 6.7 (6.2); F 6.0 (5.8); Dy 15.7 (13.5).

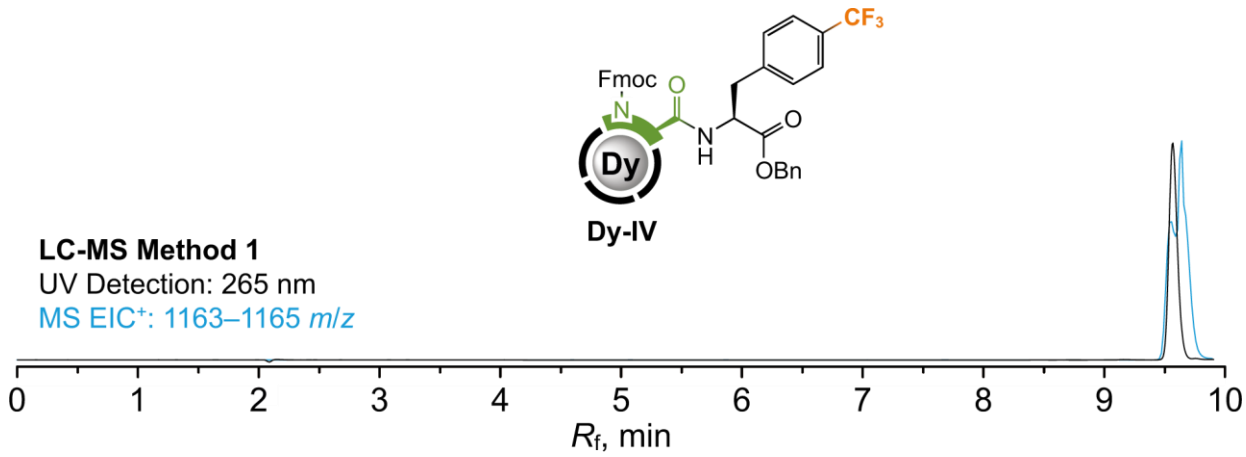

Synthesis and LC-MS chromatogram of intermediate Dy-IV: In a glass vial (4 mL), [**Dy**(**Fmoc-L^1**)] ·1.1TFA·3.5H_2O (15.5 mg, 14.8 µmol, 1.0 equiv.) was dissolved in dry DMSO (460 µL), followed by addition of H-Phe{*p*-CF_3}-OBn (100 mM in dry DMSO, 204 µL, 20.4 µmol, 1.4 equiv.), PyAOP (100 mM in dry DMSO, 850 µL, 85.0 µmol, 5.7 equiv.) and DIPEA (14.6 µL, 84.0 µmol, 5.7 equiv.). The resulting solution was stirred at 80 °C for 5 mins. The mixture was then purified by preparative HPLC (C18, H_2O/MeCN gradient with 0.1% FA additive). Fractions with product were joined and lyophilized to give product as white solid. **Yield:** 13.7 mg (76%; 1 step; based on [**Dy**(**Fmoc-L^1**)] ·1.1TFA·3.5H_2O assuming **Dy-IV**·1.0FA, M_R = 1209). **ESI-HRMS:** 1164.3113 $[M+H]^+$ (theor. $[C_{51}H_{55}O_{12}N_6F_3Dy_1]^+$ = 1164.3116).

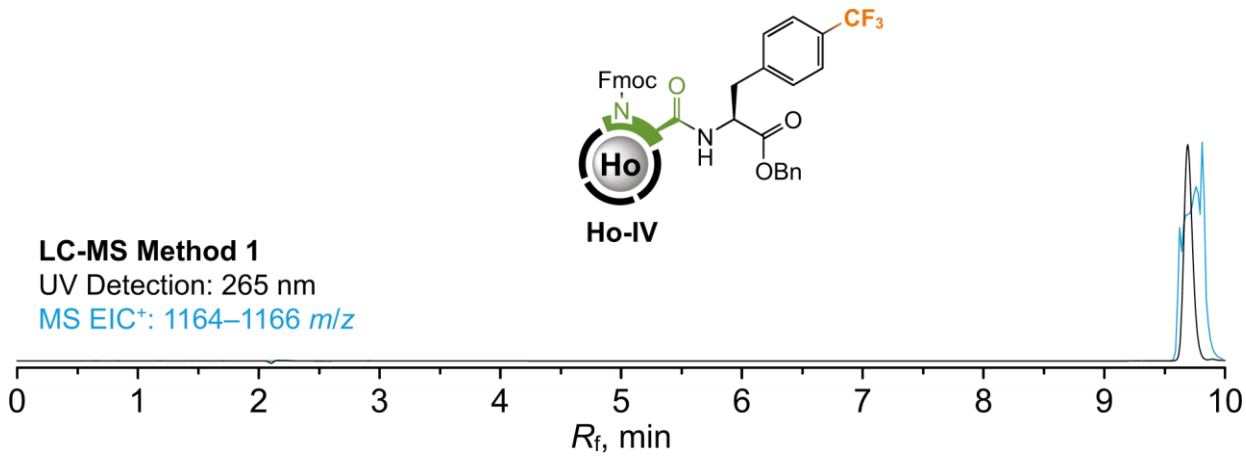

Synthesis and LC-MS chromatogram of intermediate Ho-IV: In a glass vial (4 mL), [**Ho**(**Fmoc-L^1**)]·1.1TFA·3.5H_2O (15.5 mg, 14.8 µmol, 1.0 equiv.) was dissolved in dry DMSO (460 µL), followed by addition of H-Phe{*p*-CF_3}-OBn (100 mM in dry DMSO, 204 µL, 20.4 µmol, 1.4 equiv.), PyAOP (100 mM

in dry DMSO, 850 µL, 85.0 µmol, 5.7 equiv.) and DIPEA (14.6 µL, 84.0 µmol, 5.7 equiv.). The resulting solution was stirred at 80 °C for 5 mins. The mixture was then purified by preparative HPLC (C18, H_2O/MeCN gradient with 0.1% FA additive). Fractions with product were joined and lyophilized to give product as pinkish solid. **Yield:** 10.5 mg (59%; 1 step; based on [**Ho**(**Fmoc-L^1**)] ·1.1TFA·3.5H_2O assuming **Ho-IV**·1.0FA, M_R = 1211). **ESI-HRMS:** 1165.3122 $[M+H]^+$ (theor. $[C_{51}H_{55}O_{12}N_6F_3Ho_1]^+$ = 1165.3128).

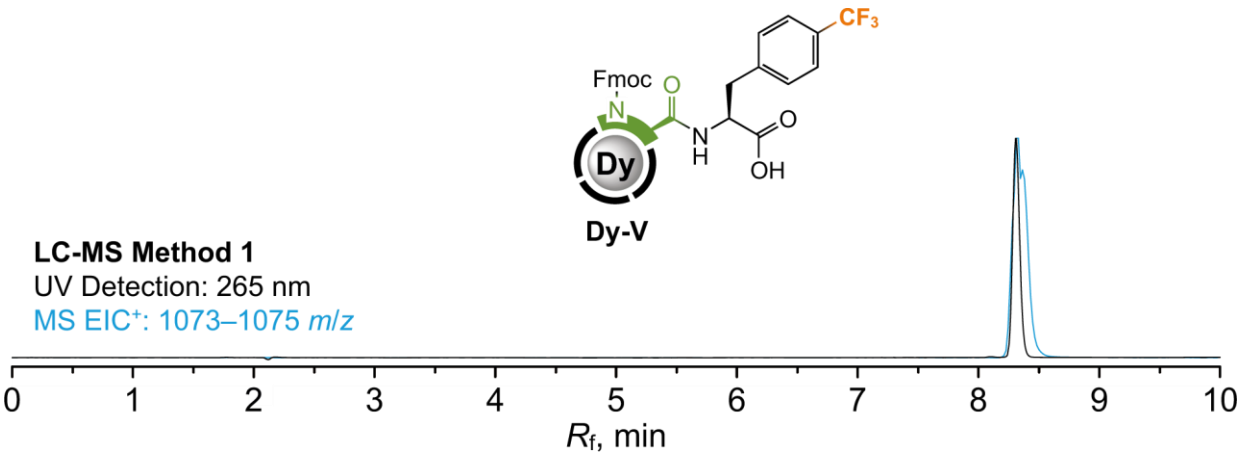

Synthesis and LC-MS chromatogram of intermediate Dy-V: In a pear-shaped glass flask (25 mL), Pd@C (10%, 5 mg) was three-times secured with Ar followed by addition of solution of intermediate **Dy-IV** (12.4 mg, 10.3 µmol assuming **Dy-IV**·1.0FA, 1.0 equiv.) in MeOH (9 mL) through septum. The mixture was then stirred at RT for 30 min with slow bubbling of H_2 (from balloon) through the mixture. Reaction mixture was filtered through syringe microfilter (PTFE) and the filtrate was evaporated to dryness. Residue was purified by preparative HPLC (C18, H_2O/MeCN gradient with 0.1% TFA additive). Fractions with product were joined and lyophilized to give product as white solid. **Yield:** 7.0 mg (58%; 1 step; based on **Dy-IV**·1.0FA assuming **Dy-V**·1.0TFA, M_R = 1186). **ESI-HRMS:** 1074.2655 $[M+H]^+$ (theor. $[C_{44}H_{49}O_{12}N_6F_3Dy_1]^+$ = 1074.2647).

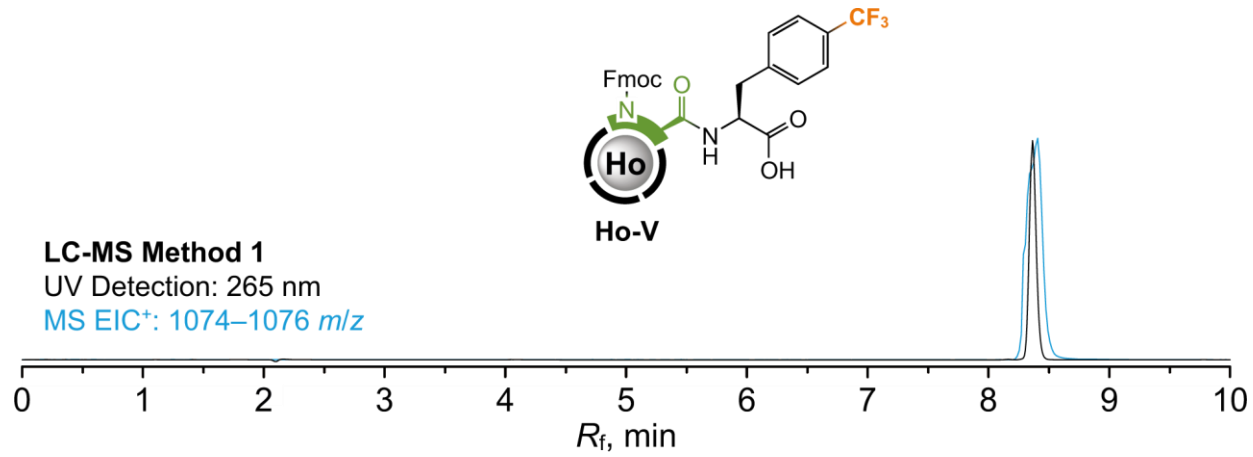

Synthesis and LC-MS chromatogram of intermediate Ho-V: In a pear-shaped glass flask (25 mL), Pd@C (10%, 3 mg) was three-times secured with Ar followed by addition of solution of intermediate **Ho-IV** (10.3 mg, 8.5 µmol assuming **Ho-IV**·1.0FA, 1.0 equiv.) in MeOH (5 mL) through septum. The mixture was then stirred at RT for 30 min with slow bubbling of H_2 (from balloon) through the mixture. Reaction mixture was filtered through syringe microfilter (PTFE) and the filtrate was evaporated to dryness. Residue was purified by preparative HPLC (C18, H_2O/MeCN gradient with 0.1% TFA additive). Fractions with product were joined and lyophilized to give product as pinkish solid. **Yield:** 7.6 mg (75%; 1 step; based on **Ho-IV**·1.0FA assuming **Ho-V**·1.0TFA, M_R = 1189). **ESI-HRMS:** 1075.2663 $[M+H]^+$ (theor. $[C_{44}H_{49}O_{12}N_6F_3Ho_1]^+$ = 1075.2658).

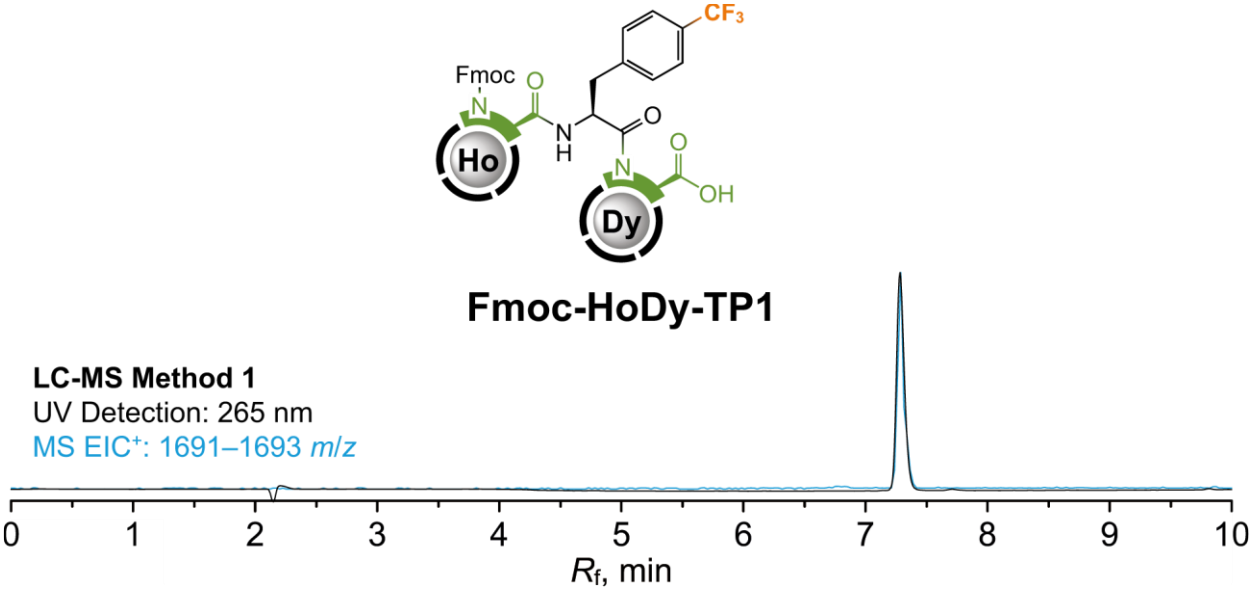

Synthesis and LC-MS chromatogram of intermediate Fmoc-HoDy-TP1: In a glass vial (4 mL), **Ho-V** (7.6 mg, 6.4 µmol assuming **Ho-V**·1.0TFA, 1.0 equiv.) and [**Dy**(**L**^{1})]·1.2TFA·3.0H_2O (6.3 mg, 7.6 µmol, 1.2 equiv.) were dissolved in dry DMSO (550 µL) followed by addition of PyAOP (100 mM in dry DMSO,

64 µL, 6.4 µmol, 1.0 equiv.) and DIPEA (5.7 µL, 32.5 µmol, 5 equiv.). The resulting solution was stirred at RT for 15 mins. The mixture was then purified by preparative HPLC (C18, H_2O/MeCN gradient with 0.1% FA additive). Fractions with product were joined and lyophilized to give product as pinkish solid. **Yield:** 3.6 mg (33%; 1 step; based on **Ho**·1.0TFA assuming **Fmoc-HoDy-TP1** ,M_R = 1692). **ESI-HRMS:** 847.1983 $[M+2H]^{2+}$ (theor. $[C_{63}H_{78}O_{20}N_{11}F_3Ho_1Dy_1]^{2+}$ = 847.1980).

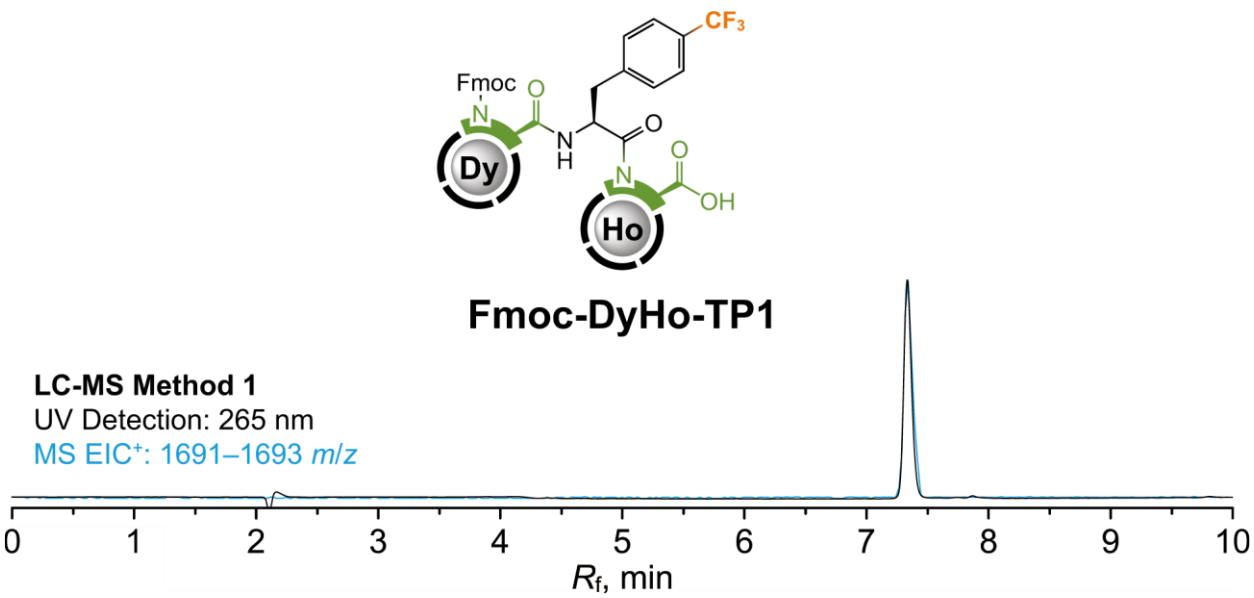

Synthesis and LC-MS chromatogram of intermediate Fmoc-DyHo-TP1: In a glass vial (4 mL), **Dy-V** (7.0 mg, 5.9 µmol assuming **Dy-V**·1.0TFA, 1.0 equiv.) and [**Ho**($\mathbf{L^1}$)] ·1.1TFA·3.0H_2O (6.4 mg, 7.8 µmol, 1.3 equiv.) were dissolved in dry DMSO (550 µL) followed by addition of PyAOP (100 mM in dry DMSO, 86 µL, 8.6 µmol, 1.5 equiv.) and DIPEA (13.6 µL, 78.0 µmol, 13 equiv.). The resulting solution was stirred at RT for 15 mins. The mixture was then purified by preparative HPLC (C18, H_2O/MeCN gradient with 0.1% FA additive). Fractions with product were joined and lyophilized to give product as pinkish solid.**Yield:** 3.6 mg (36%; 1 step; based on **Dy-V**·1.0TFA assuming **Fmoc-DyHo-TP1** ,M_R = 1692). **ESI-HRMS:** 847.1985 $[M+2H]^{2+}$ (theor. $[C_{63}H_{78}O_{20}N_{11}F_3Ho_1Dy_1]^{2+}$ = 847.1980).

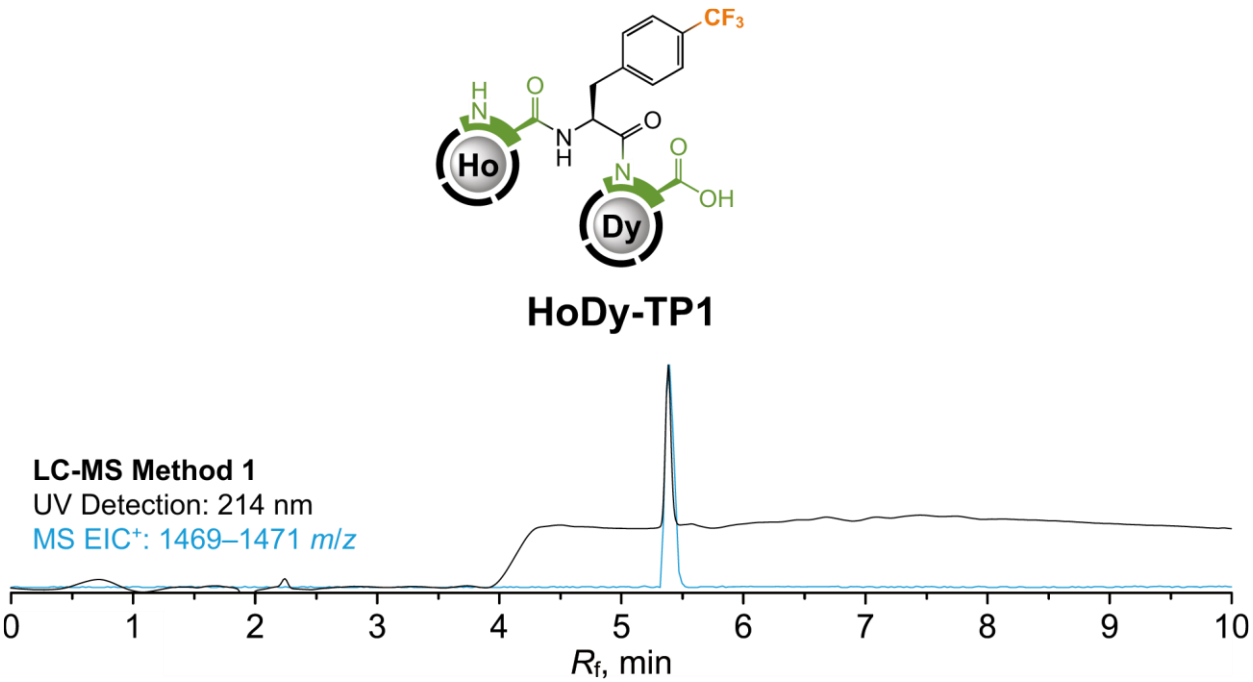

Synthesis and LC-MS chromatogram of HoDy-TP1: In a glass vial (4 mL), **Fmoc-HoDy-TP1** (3.6 mg, 2.1 µmol, 1.0 equiv.) was dissolved in 2% DBU in DMF (213 µL, 29 µmol, 14 equiv.) and the solution was stirred at RT for 5 mins. Reaction was quenched with FA (1.1 µL, 29 µmol, 14 equiv.). The mixture was then purified by preparative HPLC (C18, H_2O/MeCN gradient with 0.1% FA additive). Fractions with product were joined and lyophilized to give product as pinkish solid. **Yield:** 2.8 mg (75%; 1 step; based on **Fmoc-HoDy-TP1**). **NMR (aq. MOPS pH = 7.0, external D_2O): ^{19}F** (470.4 MHz, T = 298.2 K) δ_F –54.75 (CF_3, s). **ESI-HRMS:** 736.1645 $[M+2H]^{2+}$ (theor. $[C_{48}H_{68}O_{18}N_{11}F_3Ho_1Dy_1]^{2+}$ = 736.1640). **EA** ($C_{48}H_{66}N_{11}O_{18}Ho_1Dy_1 \cdot 3.6FA \cdot 6.3H_2O$, M_R = 1750): C 35.4 (35.2); H 5.0 (4.7); N 8.8 (9.0); F 3.3 (3.1).

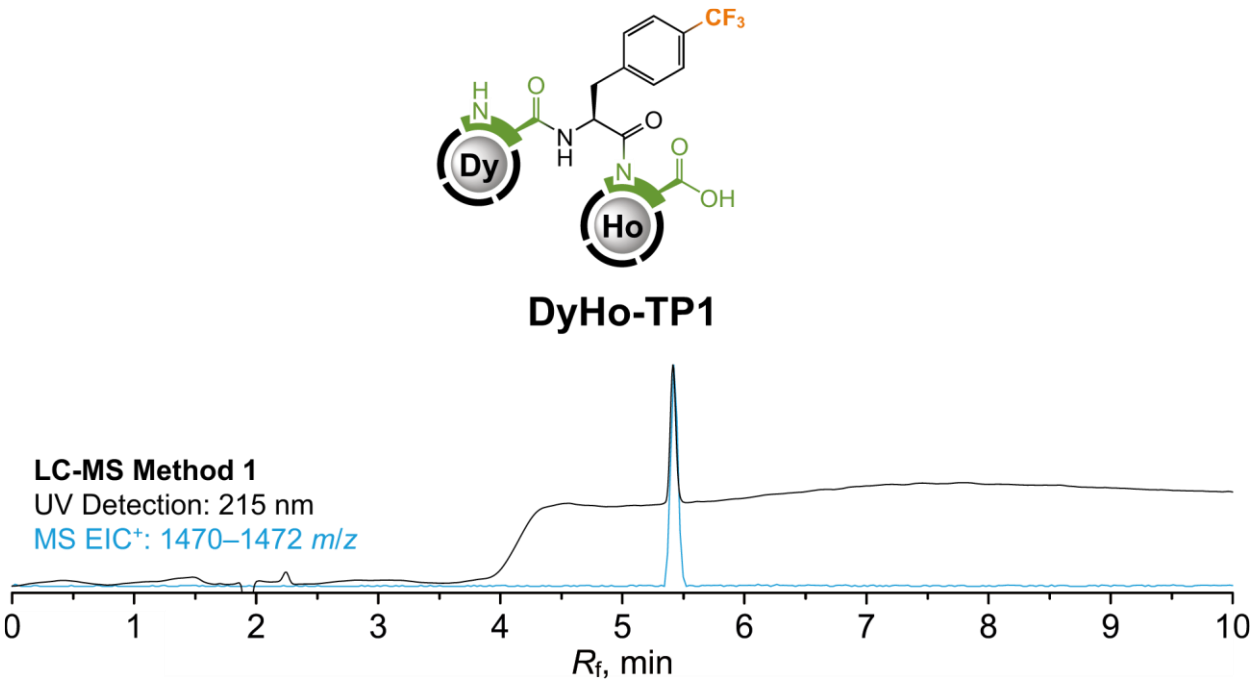

Synthesis and LC-MS chromatogram of DyHo-TP1: In a glass vial (4 mL), **Fmoc-DyHo-TP1** (3.6 mg, 2.1 µmol, 1.0 equiv.) was dissolved in 2% DBU in DMF (213 µL, 29 µmol, 14 equiv.) and the solution was stirred at RT for 5 mins. Reaction was quenched with FA (1.1 µL, 29 µmol, 14 equiv.). The mixture was then purified by preparative HPLC (C18, H_2O/MeCN gradient with 0.1% FA additive). Fractions with product were joined and lyophilized to give product as pinkish solid.**Yield:** 2.2 mg (59%; 1 step; based on **Fmoc-DyHo-TP1** assuming **DyHo-TP1**·3.6FA·6.3H_2O according to **HoDy-TP1** analogy, M_R = 1750). **NMR (aq. MOPS pH = 7.0, external D_2O): ^{19}F** (470.4 MHz, T = 298.2 K) δ_F –62.74 (CF_3, s). **ESI-HRMS:** 736.1645 $[M+2H]^{2+}$ (theor. $[C_{48}H_{68}O_{18}N_{11}F_3Dy_1Ho_1]^{2+}$ = 736.1640).

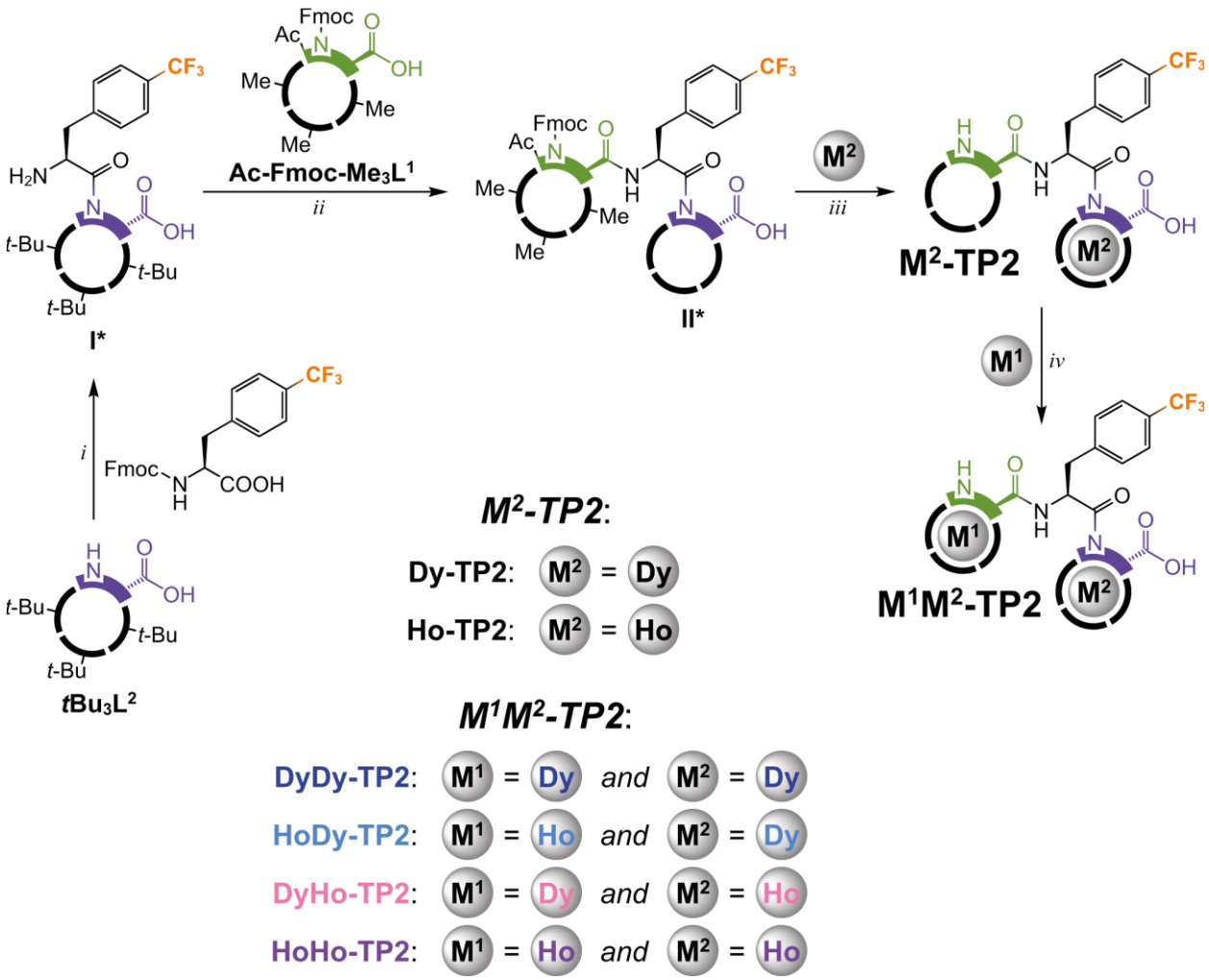

Synthesis of M^1M^2-TP2 tripeptides with Dy^{3+} and Ho^{3+} cations. ***Conditions:*** (*i*) Fmoc-Phe{*p*-CF_3}-OH, PyAOP, DIPEA, DMSO *followed by* DBU, DMF; (*ii*) **Ac-Fmoc-Me_3L^1**, PyAOP, DIPEA, DMSO *followed by* TFA; (*iii*) M^2Cl_3, aq. MOPS/NaOH buffer (pH 7.0) *followed by* LiOH, H_2O, MeOH; (*iv*) M^1Cl_3, aq. MOPS/NaOH buffer (pH 7.0).

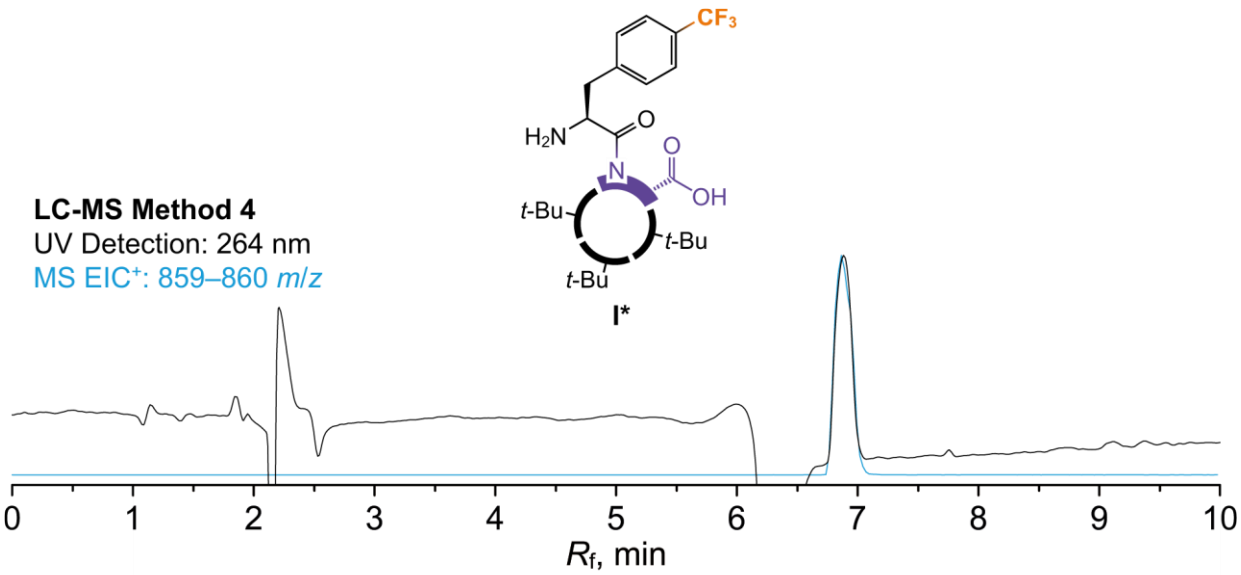

Synthesis and LC-MS chromatogram of intermediate I*: In a glass vial (4 mL), Fmoc-Phe{*p*-CF_3}-OH (9.7 mg, 21.3 µmol, 0.9 equiv.), PyAOP (11.1 mg, 21.3 µmol, 0.9 equiv.) and DIPEA (19 µL, 3106 µmol, 4.7 equiv.) were dissolved in dry DMSO (1.0 mL). After 1 min, ***t*Bu$_3$L^2**·3.0TFA·3.1H_2O (23.6 mg, 22.7 µmol, 1.0 equiv.) was added and solution was stirred at RT for 5 mins. Solution was purified by preparative HPLC (C18, H_2O/MeCN gradient with 0.1% FA additive). Fractions with Fmoc protected product were joined and lyophilized. The resulting white solid was dissolved in dry DMF (1.5 mL) followed by addition of DBU (30 µL, 202 µmol, 8.9 equiv.). After 5 mins, the reaction was quenched with TFA (15 µL, 202 µmol, 8.9 equiv.) and diluted with H_2O (1 mL). Solution was then purified by preparative HPLC (C18, H_2O/MeCN gradient with 0.1% FA additive). Fractions with product were joined and lyophilized to give product as white solid. **Yield:** 17 mg (87%; 2 steps; based on ***t*Bu$_3$L^2**·3.0TFA·3.1H_2O assuming zwitterionic form of **I**, M_R = 859.0). **ESI-HRMS:** 859.4786 $[M+H]^+$ (theor. $[C_{41}H_{66}F_3O_{10}N_6]^+$ = 859.4787).

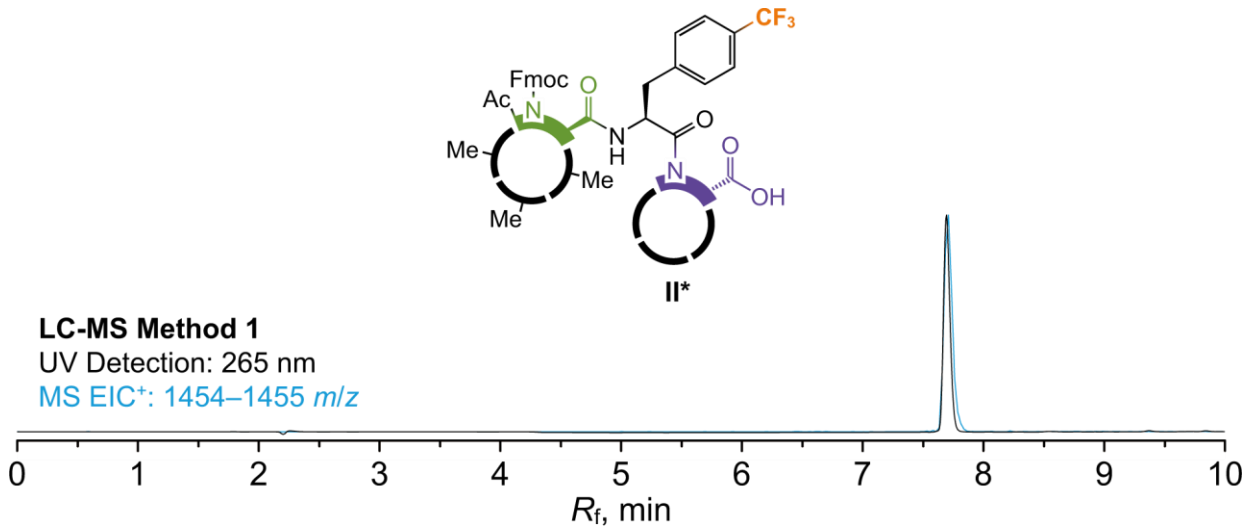

Synthesis and LC-MS chromatogram of intermediate II*: In a glass vial (4 mL), **Ac-Fmoc-Me$_3$L^1**·1.9TFA·1.3H$_2$O (7.4 mg, 7.1 µmol, 1.0 equiv.), PyOAP (3.7 mg, 7.1 µmol, 1.0 equiv.) and DIPEA (6 µL, 35 µmol, 5.0 equiv.) was dissolved in dry DMSO (300 µL). The resulting mixture was stirred at RT for 1 min followed by addition of solution of **I*** (9.0 mg, 10.5 µmol assuming zwitterionic form, 1.5 equiv.) in dry DMSO (100 µL) and the mixture was further stirred at RT for 5 mins. Solution was then purified by preparative HPLC (C18, H$_2$O/MeCN gradient with 0.1% FA additive). Fractions with *tert*-butyl product were joined and lyophilized. The resulting solid was dissolved in TFA (0.7 mL) and the resulting solution was stirred at RT for 16 h. Reaction mixture was evaporated to dryness and twice co-evaporated with MeOH. Residue was purified by preparative HPLC (C18, H$_2$O/MeCN gradient with 0.1% TFA additive). Fractions with product were joined and lyophilized to give product as white solid. **Yield:** 6.3 mg (52%; 2 steps; based on **Ac-Fmoc-Me$_3$L^1**·1.9TFA·1.3H$_2$O assuming **II***·2TFA M_R = 1682). **ESI-HRMS:** 1454.6335 $[M+H]^+$ (theor. $[C_{68}H_{91}F_3O_{21}N_{11}]^+$ = 1454.6338).

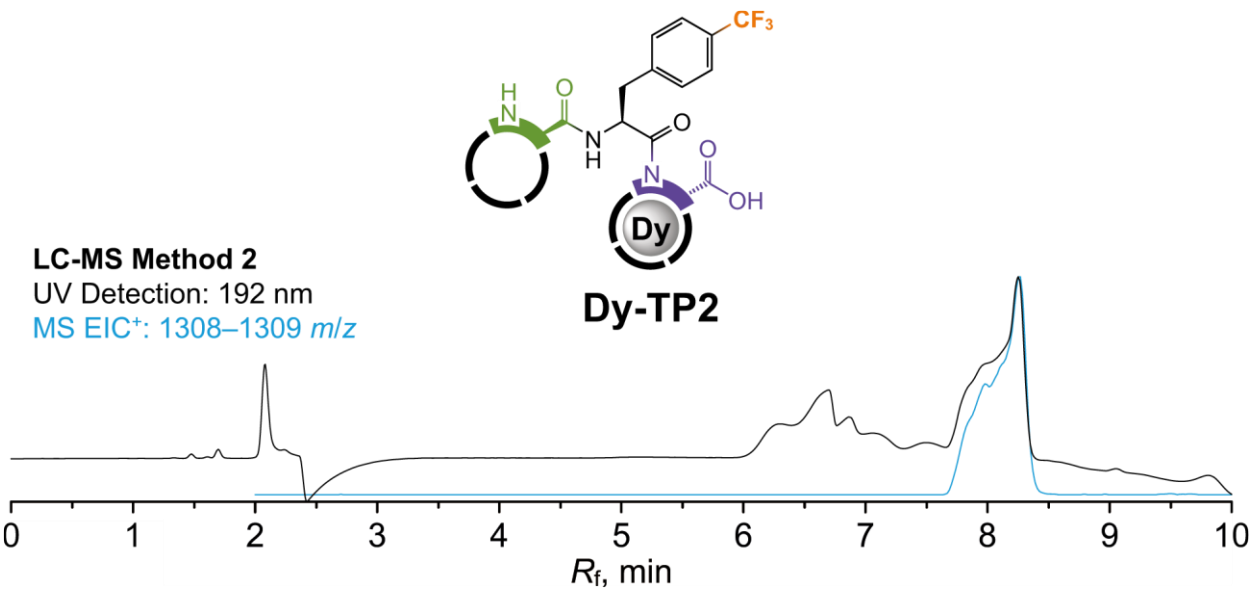

Synthesis and LC-MS chromatogram of intermediate Dy-TP2: In a glass vial (4 mL), **II*** (2.0 mg, 1.2 µmol assuming **II***·2TFA, 1.0 equiv.) was dissolved in aq. MOPS/NaOH buffer (500 mM, pH 7.0, 400 µL, 200 µmol, 170 equiv.) followed by addition of aq. $DyCl_3$ (100 mM, 17 µL, 1.7 µmol, 1.4 equiv.). The resulting solution was stirred at RT for 16 h. The mixture was then purified by preparative HPLC (C18, H_2O/MeCN gradient with 0.1% FA additive). Fractions with product were joined and lyophilized to give product as white solid. The resulting white solid was dissolved in a mixture of MeOH (600 µL) and H_2O (50 µL) followed by addition of aq. LiOH (1 M, 40 µL, 40 µmol, 34 equiv.) and the mixture was stirred at RT for 2 d. Reaction was then quenched by FA (2.0 µL, 40 µmol, 34 equiv.) and the mixture was evaporated to dryness. The residue was purified by preparative HPLC (C18, H_2O/MeCN gradient with 0.1% FA additive). Fractions with product were joined and lyophilized to give product as white solid. **Yield:** 0.7 mg (41%; 2 steps; based on **II***·2TFA assuming **Dy-TP2**·2.5FA ,M_R = 1423). **ESI-HRMS:** 655.2113 $[M+2H]^{2+}$ (theor. $[C_{48}H_{71}O_{18}N_{11}F_3Dy_1]^{2+}$ = 655.2106).

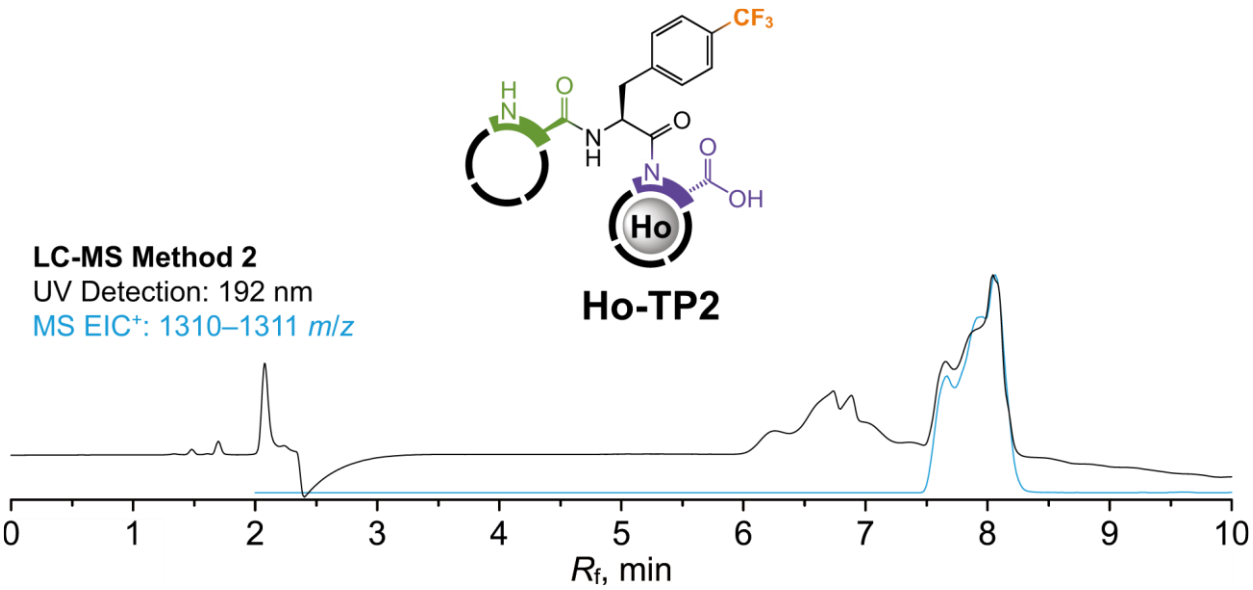

Synthesis and LC-MS chromatogram of intermediate Ho-TP2: In a glass vial (4 mL), **II*** (2.0 mg, 1.2 µmol assuming **II***·2TFA, 1.0 equiv.) was dissolved in aq. MOPS/NaOH buffer (500 mM, pH 7.0, 400 µL, 200 µmol, 170 equiv.) followed by addition of aq. $HoCl_3$ (100 mM, 17 µL, 1.7 µmol, 1.4 equiv.). The resulting solution was stirred at RT for 16 h. The mixture was then purified by preparative HPLC (C18, H_2O/MeCN gradient with 0.1% FA additive). Fractions with product were joined and lyophilized to give product as white solid. The resulting white solid was dissolved in a mixture of MeOH (600 µL) and H_2O (50 µL) followed by addition of aq. LiOH (1 M, 40 µL, 40 µmol, 34 equiv.) and the mixture was stirred at RT fot 2 d. Reaction was then quenched by FA (2.0 µL, 40 µmol, 34 equiv.) and the mixture was evaporated to dryness. The residue was purified by preparative HPLC (C18, H_2O/MeCN gradient with 0.1% FA additive). Fractions with product were joined and lyophilized to give product as white solid. **Yield:** 0.8 mg (47%; 2 steps; based on **II***·2TFA assuming **Ho-TP2**·2.5FA, M_R = 1425). **ESI-HRMS:** 655.7117 $[M+2H]^{2+}$ (theor. $[C_{48}H_{71}O_{18}N_{11}F_3Ho_1]^{2+}$ = 655.7111).

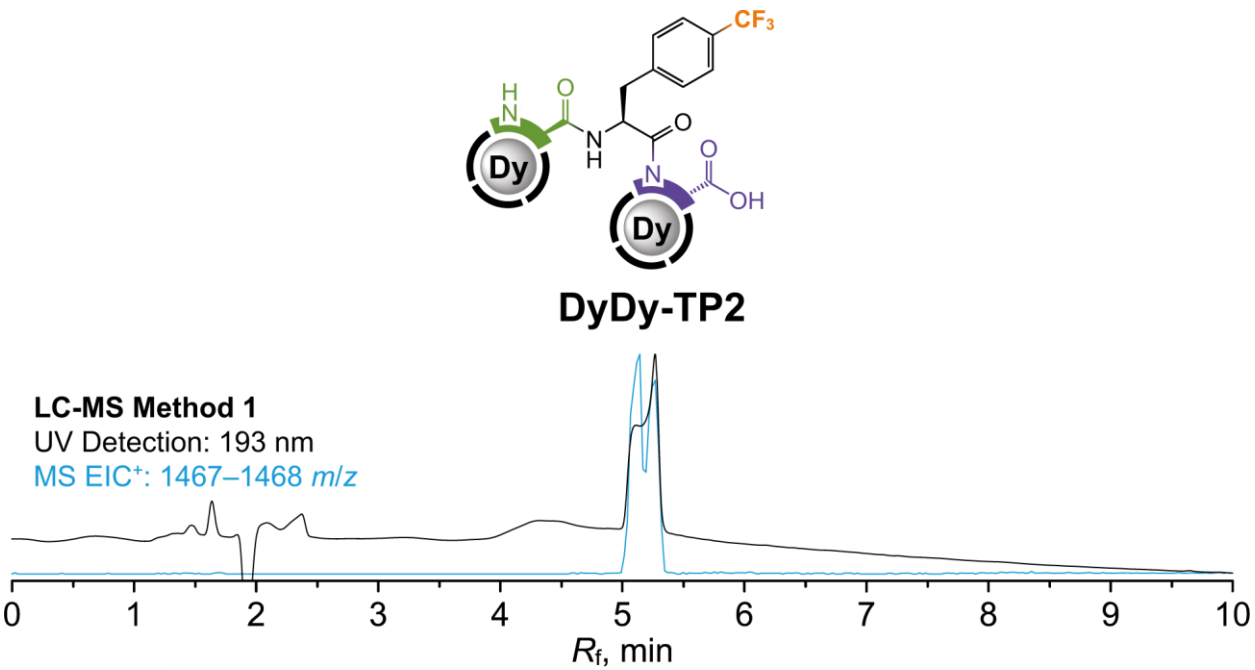

Synthesis and LC-MS chromatogram of DyDy-TP2: In a glass vial (4 mL), **Dy-TP2** (0.3 mg, ~0.2 µmol assuming **Dy-TP2**·2.5FA, 1.0 equiv.) was dissolved in aq. MOPS/NaOH buffer (500 mM, pH 7.0, 500 µL, 250 µmol, ~1200 equiv.) followed by addition of aq. $DyCl_3$ (100 mM, 4 µL, 0.4 µmol, ~1.9 equiv.) and the resulting solution was stirred at RT for 15 mins. The mixture was then purified by preparative HPLC (C18, H_2O/MeCN gradient with 0.1% TFA additive). Fractions with product were joined and lyophilized to give product as white solid. **Yield:** ~0.2 mg. **NMR (aq. MOPS pH = 7.0, external D_2O): ^{19}F** (470.4 MHz, T = 298.2 K) δ_F –90.53 (CF_3, s). **ESI-HRMS:** 735.6636 $[M+2H]^{2+}$ (theor. $[C_{48}H_{68}O_{18}N_{11}F_3Dy_2]^{2+}$ = 735.6634).

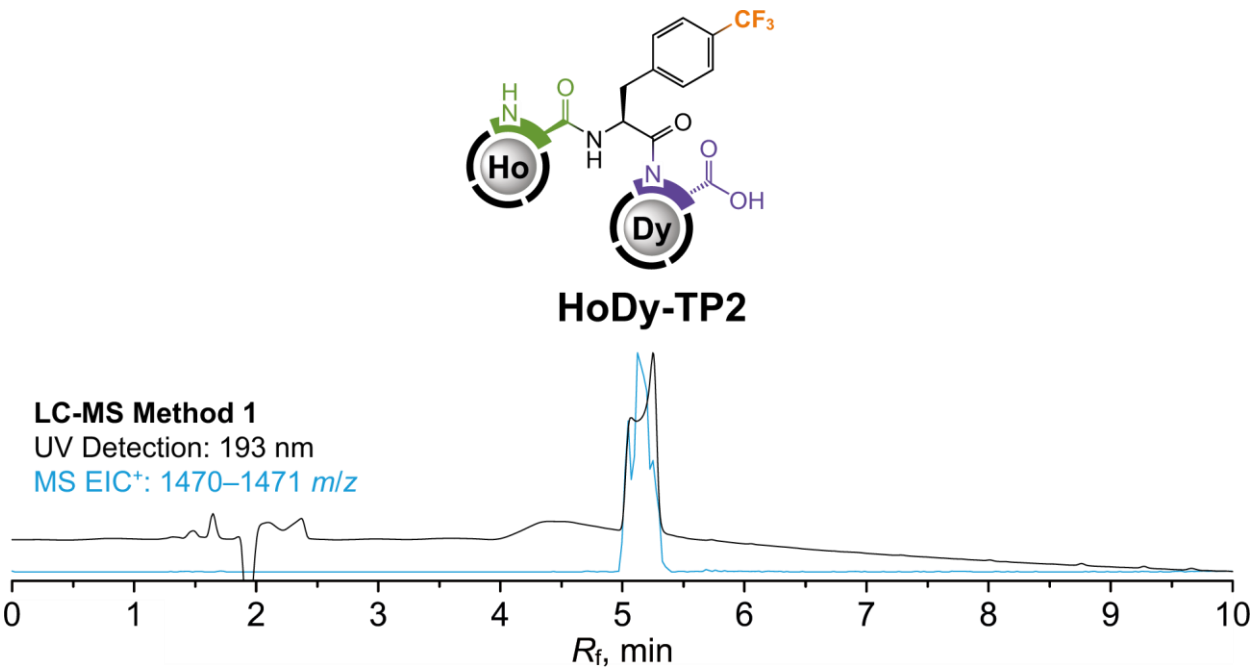

Synthesis and LC-MS chromatogram of HoDy-TP2: In a glass vial (4 mL), **Dy-TP2** (0.3 mg, ~0.2 µmol assuming **Dy-TP2**·2.5FA, 1.0 equiv.) was dissolved in aq. MOPS/NaOH buffer (500 mM, pH 7.0, 500 µL, 250 µmol, ~1200 equiv.) followed by addition of aq. $HoCl_3$ (100 mM, 4 µL, 0.4 µmol, ~1.9 equiv.) and the resulting solution was stirred at RT for 15 mins. The mixture was then purified by preparative HPLC (C18, H_2O/MeCN gradient with 0.1% TFA additive). Fractions with product were joined and lyophilized to give product as white solid. **Yield:** ~0.3 mg. **NMR (aq. MOPS pH = 7.0, external D_2O):** ^{19}**F** (470.4 MHz, T = 298.2 K) δ_F –91.95 (CF_3, s). **ESI-HRMS:** 736.1637 $[M+2H]^{2+}$ (theor. $[C_{48}H_{68}O_{18}N_{11}F_3Ho_1Dy_1]^{2+}$ = 736.1640).

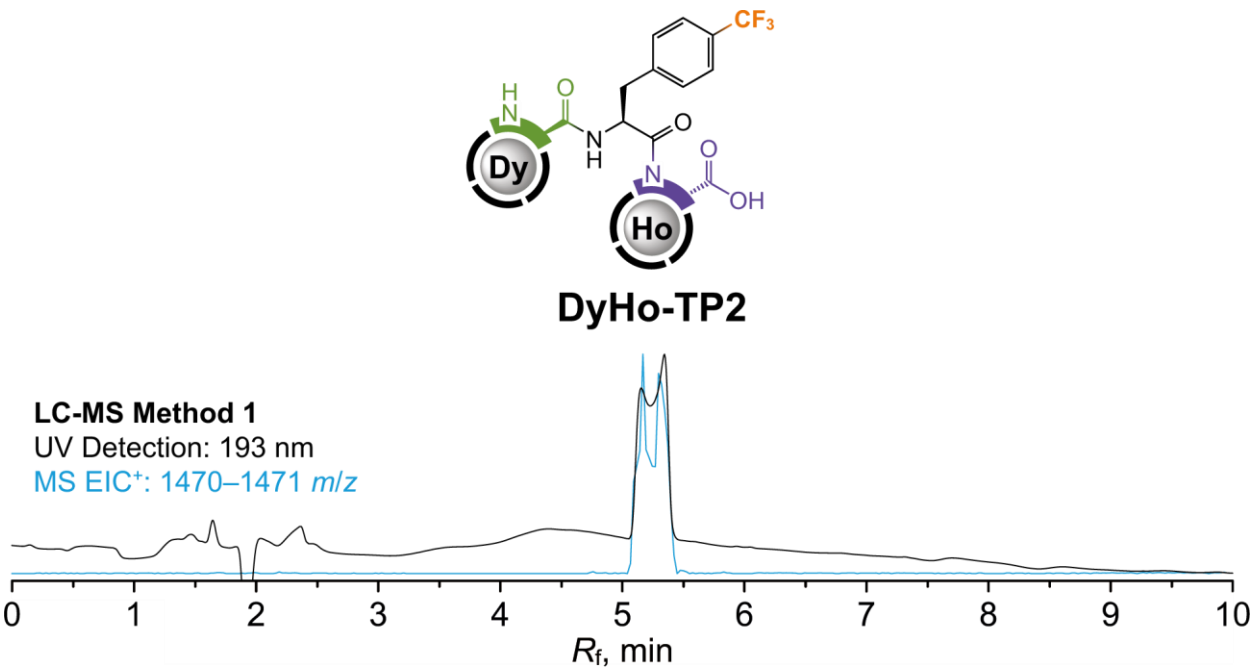

Synthesis and LC-MS chromatogram of DyHo-TP2: In a glass vial (4 mL), **Ho-TP2** (0.4 mg, ~0.3 µmol assuming **Ho-TP2**·2.5FA, 1.0 equiv.) was dissolved in aq. MOPS/NaOH buffer (500 mM, pH 7.0, 500 µL, 250 µmol, ~900 equiv.) followed by addition of aq. $DyCl_3$ (100 mM, 4 µL, 0.4 µmol, ~1.4 equiv.) and the resulting solution was stirred at RT for 15 mins. The mixture was then purified by preparative HPLC (C18, H_2O/MeCN gradient with 0.1% TFA additive). Fractions with product were joined and lyophilized to give product as white solid. **Yield:** ~0.3 mg. **NMR (aq. MOPS pH = 7.0, external D_2O):** ^{19}**F** (470.4 MHz, T = 298.2 K) δ_F –75.75 (CF_3, s). **ESI-HRMS:** 736.1645 $[M+2H]^{2+}$ (theor. $[C_{48}H_{68}O_{18}N_{11}F_3Dy_1Ho_1]^{2+}$ = 736.1640).

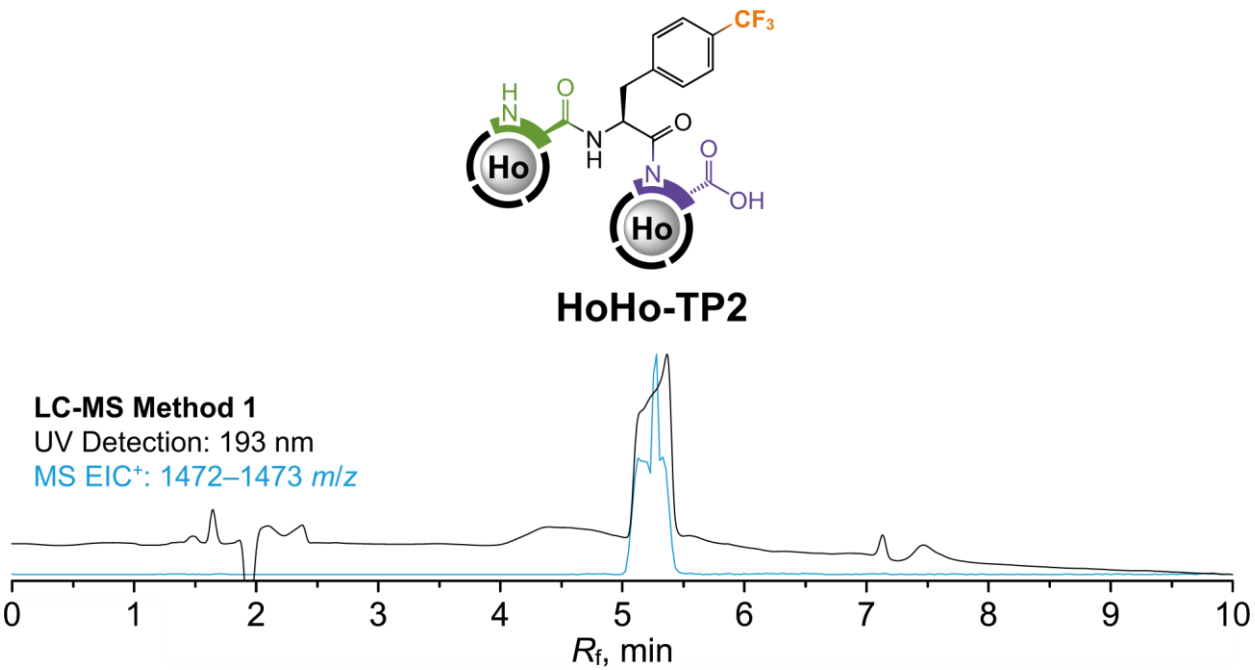

Synthesis and LC-MS chromatogram of HoHo-TP2: In a glass vial (4 mL), **Ho-TP2** (0.4 mg, ~0.3 µmol assuming **Ho-TP2**·2.5FA, 1.0 equiv.) was dissolved in aq. MOPS/NaOH buffer (500 mM, pH 7.0, 500 µL, 250 µmol, ~900 equiv.) followed by addition of aq. $HoCl_3$ (100 mM, 4 µL, 0.4 µmol, ~1.4 equiv.) and the resulting solution was stirred at RT for 15 mins. The mixture was then purified by preparative HPLC (C18, H_2O/MeCN gradient with 0.1% TFA additive). Fractions with product were joined and lyophilized to give product as white solid. **Yield:** ~0.4 mg. **NMR (aq. MOPS pH = 7.0, external D_2O): ^{19}F** (470.4 MHz, T = 298.2 K) δ_F –77.42 (CF_3, s). **ESI-HRMS:** 736.6644 $[M+2H]^{2+}$ (theor. $[C_{48}H_{68}O_{18}N_{11}F_3Ho_2]^{2+}$ = 736.6646).

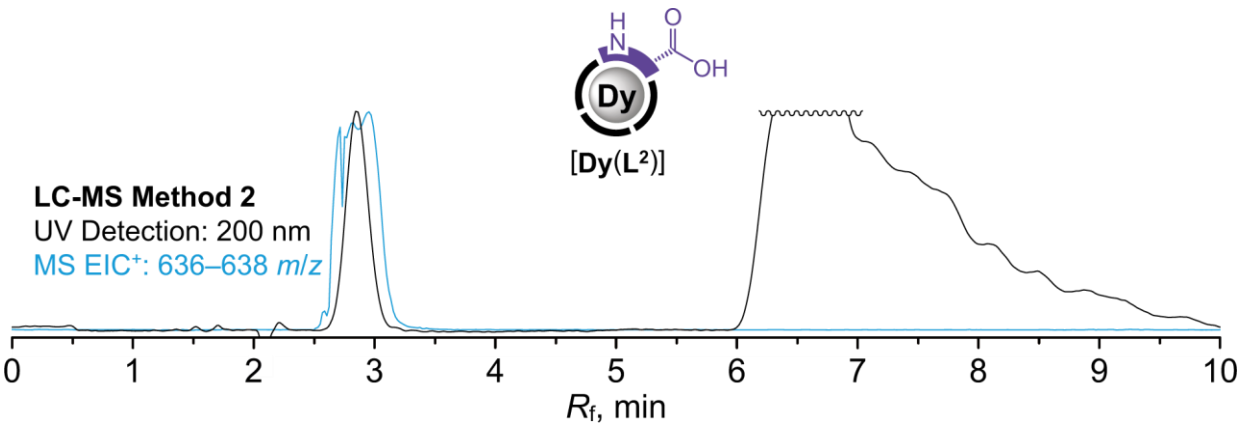

Synthesis and LC-MS chromatogram of building block [Dy(L²)]: In a glass vial (4 mL), **L²**·2.4TFA·2.5H_2O (30.0 mg, 37.8 µmol, 1.0 equiv.) was dissolved in aq. MOPS/NaOH buffer (0.5 M, pH 7.0, 759 µL, 380 µmol, 10 equiv.) followed by addition of aq. $DyCl_3$ (100 mM, 778 µL, 77.8 µmol, 2.1 equiv.) and the resulting solution was stirred at RT for 15 mins. The mixture was then purified by preparative HPLC (C18, H_2O/MeCN gradient with 0.1% TFA additive). Fractions with product were joined and re-purified by preparative HPLC (C18, H_2O/MeCN gradient with 0.1% FA additive) lyophilized to give product as white solid. **Yield:** 15.2 mg (58%; 1 step; based on **L²**·2.4TFA·2.5H_2O). **ESI-HRMS:** 637.1410 $[M+H]^+$ (theor. $[C_{19}H_{31}O_9N_5Dy_1]^+$ = 637.1408). **EA** ($C_{19}H_{30}N_5O_9Dy_1$·0.2TFA·0.7H_2O, M_R = 688.4): C 33.8 (34.4); H 4.9 (5.0); N 10.2 (9.6); F 1.7 (1.6); Dy 23.6 (20.6). ***Preparation of single crystals:*** In a glass vial (4 mL), aq. solution of [**Dy**(**L²**)] (~20 mM, 60 µL, ~1.20 µmol, 1.0 equiv.; filtered through syringe microfilter) was mixed with aq. solution of $HClO_4$ (~1.0 M, 1.22 µL, 1.22 µmol, ~1.0 equiv.) and the resulting solution was briefly vortexed. Then, THF (291 µL), *1,4*-dioxane (100 µL) and H_2O (100 µL) was added, and the resulting mixture was filtered through syringe microfilter to a new glass vial (40 mL). Then *1,4*-dioxane (~100 µL) was slowly added dropwise until opalescence occurred. The mixture was then sealed with a cap and gently heated using heat gun until clear solution was produced. The mixture was then left standing at RT for 1 week, producing single crystals of [**Dy**(**L²**)]·3H_2O suitable for X-Ray analysis.

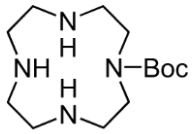

9

Synthesis of intermediate 9: In a round-bottom glass flask (50 mL), cyclen (172 mg, 1.00 mmol, 1.0 equiv.) was dissolved in DCM (10 mL) and tert-butyl (4-nitrophenyl) carbonate (239 mg, 1.00 mmol, 1.0 equiv.) in DCM (10 mL) was added dropwise. Reaction mixture was stirred at RT for 2 h. Mixture was then evaporated to dryness and residue was purified by preparative HPLC (C18, H_2O/MeCN gradient with 0.1% TFA additive). Fractions with product were joined and immediately lyophilized to give product as white solid. **Yield:** 300 mg (57%; 1 step; based on **cyclen**); **NMR (CD$_3$CN): ^{1}H** (400.1 MHz, T = 300 K) δ_H 1.43 (CH_3, s, 9H); 3.01–3.09 (*mc*, m, 4H); 3.12–3.19 (*mc*, m, 4H); 3.24–3.30 (*mc*, m, 4H); 3.42–3.48 (*mc*, m, 4H). **^{13}C{^{1}H}** (100.6 MHz, T = 300 K) δ_C 28.49 (*C*H$_3$, s); 45.14 (*mc*, s); 45.73 (*mc*, s); 48.64 (*mc*, s); 48.91 (*mc*, s); 81.57 (*C*–CH$_3$, s); 156.71 (*C*O, s). **ESI-HRMS:** 273.2288 $[M+H]^+$ (theor. $[C_{13}H_{29}O_2N_4]^+$ = 273.2285). **EA** ($C_{13}H_{28}N_4O_2$·2.1TFA·0.8H_2O, M_R = 526.2)**:** C 38.3 (38.9); H 6.1 (5.2); N 10.7 (10.2); F 22.7 (21.9).

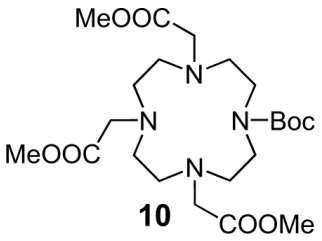

10

Synthesis of intermediate 10: In a glass vial (20 mL), **9**·2.1TFA·0.8H_2O (79 mg, 0.15 mmol, 1.0 equiv.) was dissolved in MeCN (5 mL) followed by addition of K_2CO_3 (76 mg, 0.55 mmol, 3.8 equiv.) and methyl bromoacetate (52 µL, 0.55 mmol, 3.8 equiv.). The resulting suspension was stirred at RT for 16 h. Mixture was then filtered through syringe microfilter (PTFE) and the filtrate was evaporated to dryness. Residue was purified by preparative HPLC (C18, H_2O/MeCN gradient with 0.1% TFA additive). Fractions with product were joined and immediately lyophilized to give product as white solid. **Yield:** 73 mg (70%; 1 step; based on **9**·2.1TFA·0.8H_2O assuming **10**·2.0TFA, M_R = 716.6). **NMR (CDCl$_3$): ^{1}H** (400.1 MHz, T = 300 K) δ_H 1.44 (CH_3–C, s, 9H); 2.86–3.65 (*mc*, CH_2–CO, m, 16H+2H); 3.70 (CH_3–O, s, 3H); 3.72 (CH_3–O, s, 6H); 3.85 (CH_2–CO, bs, 4H). **^{13}C{^{1}H}** (100.6 MHz, T = 300 K) δ_C 28.50 (*C*H$_3$–C, s); 46.64 (*mc*, s); 50.09 (*mc*, s); 52.46–56.11 (*mc*, *C*H$_2$–CO, *C*H$_3$–O, m); 81.87 (*C*–CH$_3$, s); 156.99 (*C*O–N, s); 170.30 (*C*O–O, s); 171.89 (*C*O–O, s).

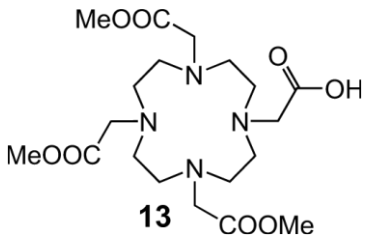

13

One-pot synthesis of intermediate 13: In a glass vial (20 mL), **10** (73 mg, 102 µmol assuming **10**·2.0TFA, 1.0 equiv.) was dissolved in TFA (3 mL, 39.2 mmol, 385 equiv.) and the resulting solution was stirred at RT for 2 h. Mixture was evaporated to dryness and twice co-evaporated with MeOH. Residue was purified by preparative HPLC (C18, H_2O/MeCN gradient with 0.1% TFA additive). Fractions with intermediate **11** were joined and immediately lyophilized. The resulting solid was dissolved in MeCN (5 mL) followed by addition of K_2CO_3 (40 mg, 291 µmol, 2.9 equiv.) and tert-butyl bromoacetate (21 mg, 107 µmol, 1.05 equiv.). The resulting suspension was stirred at RT for 2 h. Mixture was then filtered through syringe microfilter (PTFE) and the filtrate was evaporated to dryness. Residue containing intermediate **12** was dissolved in TFA (3 mL, 39.2 mmol, 385 equiv.) and the resulting solution was stirred at RT for 16 h. Mixture was evaporated to dryness and twice co-evaporated with MeOH. Residue was purified by preparative HPLC (C18, H_2O/MeCN gradient with 0.1% TFA additive). Fractions with product were joined and immediately lyophilized to give product as white solid. **Yield:** 27.2 mg (40%; 3 steps; based on **10**·2.0TFA assuming **13**·2.0TFA, M_R = 674.5). **NMR ($CDCl_3$): ^{1}H** (400.1 MHz, T = 300 K) δ_H 2.95–3.19 (*mc*, m, 8H); 3.24–3.45 (*mc*, m, 8H); 3.56–3.73 (C*H*$_2$–CO, C*H*$_3$–O, m, 4H+6H); 3.79 (C*H*$_3$–O, s, 3H); 3.97 (C*H*$_2$–CO, bs, 4H). **^{13}C{^{1}H}** (100.6 MHz, T = 300 K) δ_C 49.65 (*mc*, s); 49.83 (*mc*, s); 52.16 (*mc*, s); 52.37 (*mc*, s); 52.86–55.81 (*mc*, *C*H$_2$–CO, *C*H$_3$–O, m); 168.81 (*C*O, s); 169.49 (*C*O–O, s); 172.20 (*C*O–O, s). **ESI-HRMS:** 447.2445 $[M+H]^+$ (theor. $[C_{19}H_{35}O_8N_4]^+$ = 447.2449).

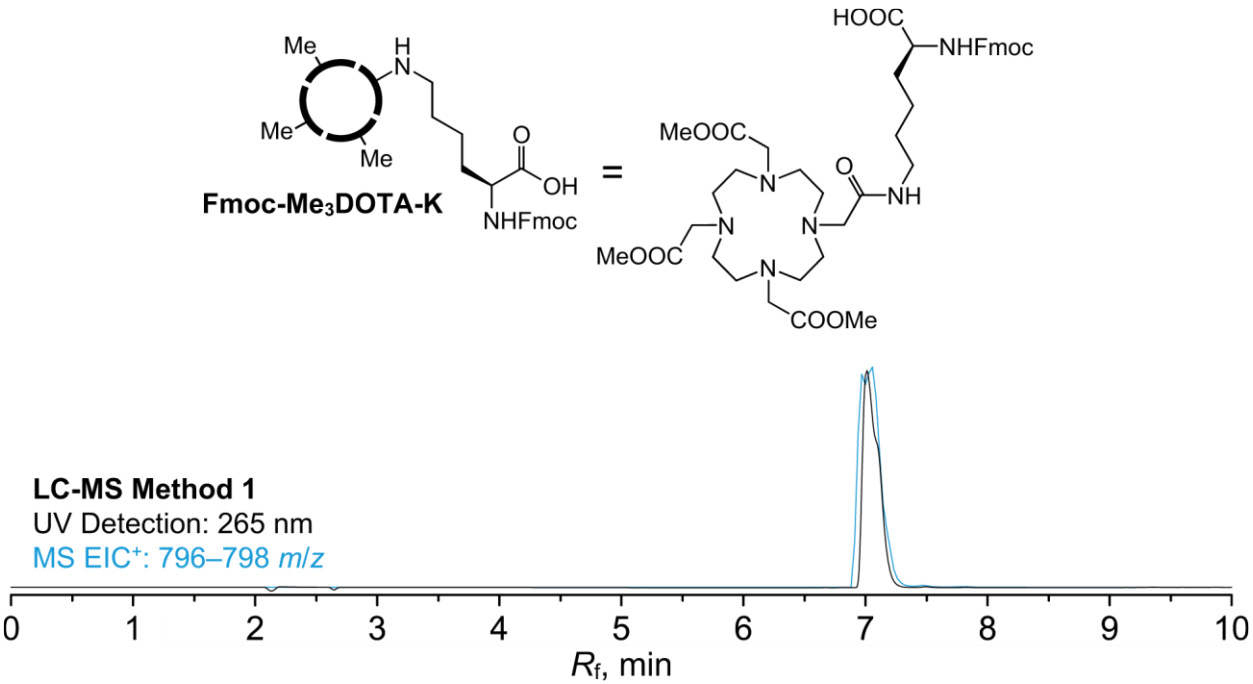

Synthesis and LC-MS chromatogram of building block Fmoc-Me$_3$DOTA-K: In a glass vial (4 mL), **10** (22 mg, 32.6 µmol assuming **10**·2.0TFA, 1.0 equiv.), PyAOP (17 mg, 32.6 µmol, 1.0 equiv.) and DIPEA (29 µL, 166 µmol 5.1 ,equiv.) were dissolved in dry DMSO (620 µL). After 1 min of stirring, Fmoc-lysine-OH (16 mg, 32.6 µmol, 1.0 equiv.) was added and the resulting solution was stirred at RT for 5 mins. Mixture was then purified by preparative HPLC (C18, H_2O/MeCN gradient with 0.1% TFA additive). Fractions with product were joined and immediately lyophilized to give product as white solid. **Yield:** 11.1 mg (33%; 1 step; based on **10**·2.0TFA). **ESI-HRMS:** 797.4083 $[M+H]^+$ (theor. $[C_{40}H_{57}O_{11}N_6]^+$ = 797.4080). **EA** ($C_{40}H_{56}N_6O_{11}$·1.8TFA·1.3H_2O, M_R = 1025.5)**:** C 51.1 (51.8); H 5.9 (5.4); N 8.2 (7.4); F 10.0 (9.2).

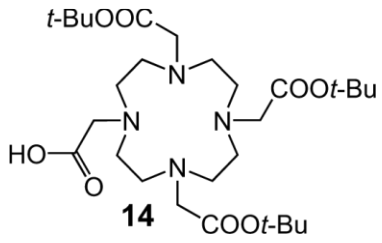

Synthesis of intermediate 14: In a pear-shaped glass flask (50 mL), **tBu$_3$DO3A**·HBr (242 mg, 0.41 mmol, 1.0 equiv.), methyl bromoacetate (65 mg, 0.43 mmol, 1.05 equiv.) and K_2CO_3 (112 mg, 0.81 mmol, 2.0 equiv.) were mixed in 16 mL of MeCN. The mixture was stirred at RT for 20 h, followed by addition of H_2O (12 mL) and aq. LiOH (1.0 M, 2.03 mL, 2.03 mmol, 5.0 equiv.). The mixture was further stirred at RT

for 18 h and then it was neutralized by TFA. Mixture was evaporated to dryness and the residue was purified by preparative HPLC (C18, H_2O/MeCN gradient with 0.1% TFA additive). Fractions with product were joined and lyophilized to give product as white solid. **Yield:** 225 mg (62%; 1 step; based on **tBu$_3$DO3A**·HBr). **NMR (CD$_3$CN): ^{1}H** (400.1 MHz, T = 300 K) δ_H 1.45 (CH_3, s, 18H); 1.53 (CH_3, s, 9H); 3.03 (*mc*, bs, 8H); 3.32 (*mc*, bs, 4H); 3.36 (*mc*, bs, 4H); 3.55 (CH_2–CO, s, 4H); 3.90 (CH_2–CO, s, 2H); 4.05 (CH_2–CO, s, 2H). **^{13}C{^{1}H}** (100.6 MHz, T = 300 K) δ_C 28.35 (*C*H$_3$, s); 28.38 (*C*H$_3$, s); 49.54 (*mc*, s); 49.78 (*mc*, s); 52.26 (2 × s); 54.90 (*C*H$_2$–CO, s); 55.73 (*C*H$_2$–CO, s); 55.83 (*C*H$_2$–CO, s); 83.35 (*C*–CH$_3$, s); 85.24 (*C*–CH$_3$, s); 168.78–171.14 (*C*O, m). **ESI-HRMS:** 573.3854 $[M+H]^+$ (theor. $[C_{28}H_{53}O_8N_4]^+$ = 573.3858). **EA** ($C_{28}H_{52}N_4O_8$·2.6TFA·1.1H_2O, M_R = 888.9): C 44.9 (45.1); H 6.4 (6.2); N 6.3 (6.1); F 16.7 (16.4).

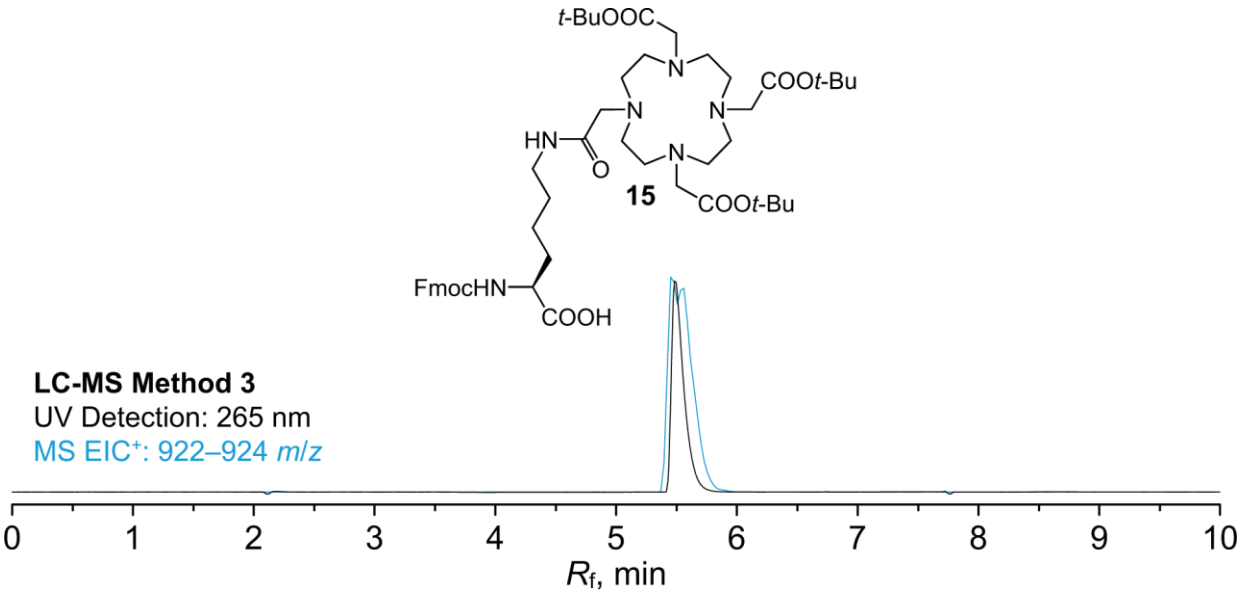

Synthesis and LC-MS chromatogram of intermediate 15: In a glass vial (4 mL), **14**·2.6TFA·1.1H_2O (66 mg, 74.3 µmol, 1.0 equiv.), PyAOP (39 mg, 71.0 µmol, 0.95 equiv.) and DIPEA (66 µL, 376 µmol, 5.1 equiv.) were dissolved in dry DMSO (1.4 mL). After 1 min of stirring, Fmoc-lysine-OH (37 mg, 75.1 µmol, 1.0 equiv.) was added and the resulting solution was stirred at RT for 5 mins. Mixture was then purified by preparative HPLC (C18, H_2O/MeCN gradient with 0.1% TFA additive). Fractions with product were joined and lyophilized to give product as white solid. **Yield:** 42.5 mg (50%; 1 step; based on **14**·2.6TFA·1.1H_2O assuming **15**·2.0TFA, M_R = 1151 .(**ESI-HRMS:** 923.5488 $[M+H]^+$ (theor. $[C_{49}H_{75}O_{11}N_6]^+$ = 923.5488).

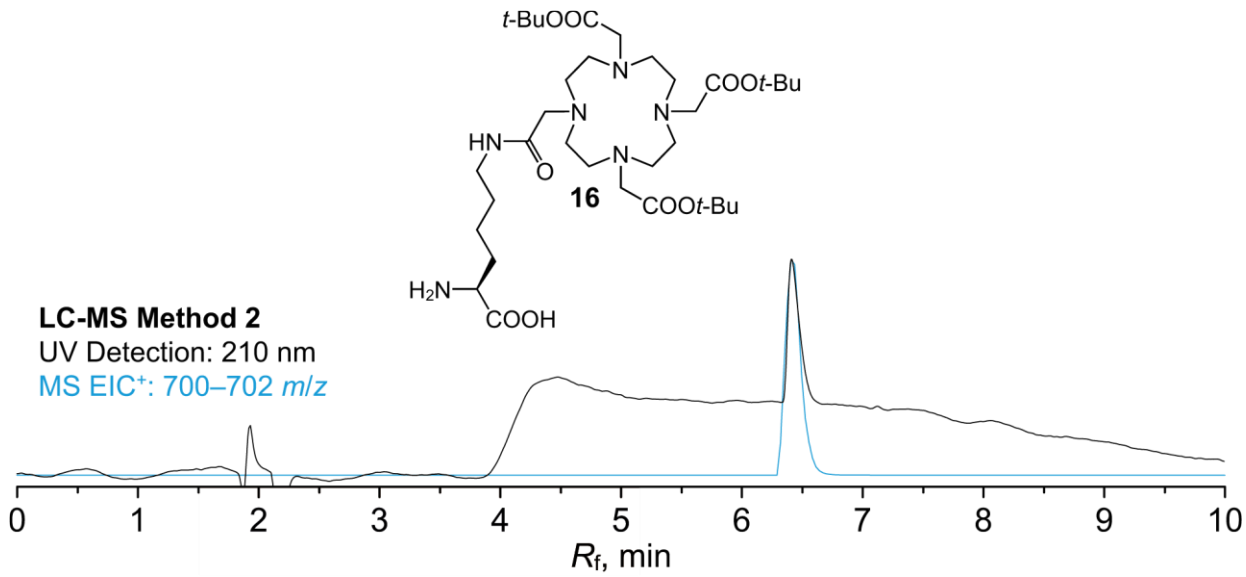

Synthesis and LC-MS chromatogram of intermediate 16: In a glass vial (4 mL), **15** (36.3 mg, 31.5 µmol assuming **15**·2.0TFA, 1.0 equiv.) was dissolved in DMF (2.5 mL) followed by addition of DBU (55 µL, 368 µmol, 11.7 equiv.). After 5 mins, the reaction was quenched with TFA (28 µL, 366 µmol, 11.7 equiv.) and diluted with H_2O (1 mL). Mixture was then purified by preparative HPLC (C18, H_2O/MeCN gradient with 0.1% TFA additive). Fractions with product were joined and lyophilized to give product as white solid. **Yield:** 22.4 mg (69%; 1 step; based on **15**.2·0TFA). **ESI-HRMS:** 701.4805 $[M+H]^+$ (theor. $[C_{34}H_{65}O_9N_6]^+$ = 701.4808). **EA** ($C_{34}H_{64}N_6O_9$·2.5TFA·2.3H_2O, M_R = 1027.3): C 45.6 (44.9); H 7.0 (6.2); N 8.2 (7.7); F 13.9 (13.3).

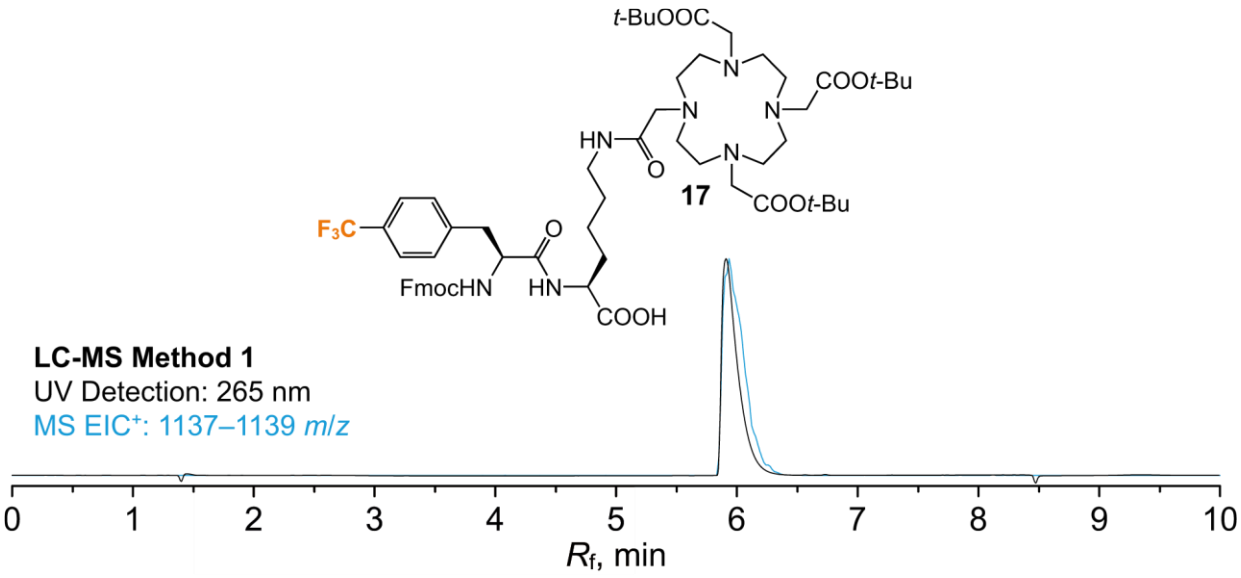

Synthesis and LC-MS chromatogram of intermediate 17: In a glass vial (4 mL), Fmoc-Phe{*p*-CF_3}-OH (100 mM in dry DMSO, 221 µL, 22.1 µmol, 1.0 equiv.), PyAOP (100 mM in dry DMSO, 221 µL, 22.1 µmol, 1.0 equiv.) and DIPEA (100 mM in dry DMSO, 221 µL, 22.1 µmol, 1.0 equiv.) were mixed. After 1 min, **16** (100 mM in dry DMSO, 221 µL, 22.1 µmol, 1.0 equiv.) was added and the mixture was stirred at RT for 5 mins. Mixture was then purified by preparative HPLC (C18, H_2O/MeCN gradient with 0.1% TFA additive). Fractions with product were joined and lyophilized to give product as white solid. **Yield:** 20.0 mg 66%; 1 step; based on **16**·2.5TFA·2.3H_2O assuming **17**·2.0TFA, M_R = 1367) **ESI-HRMS:** 1138.6048 $[M+H]^+$ (theor. $[C_{59}H_{83}O_{12}N_7F_3]^+$ = 1138.6046).

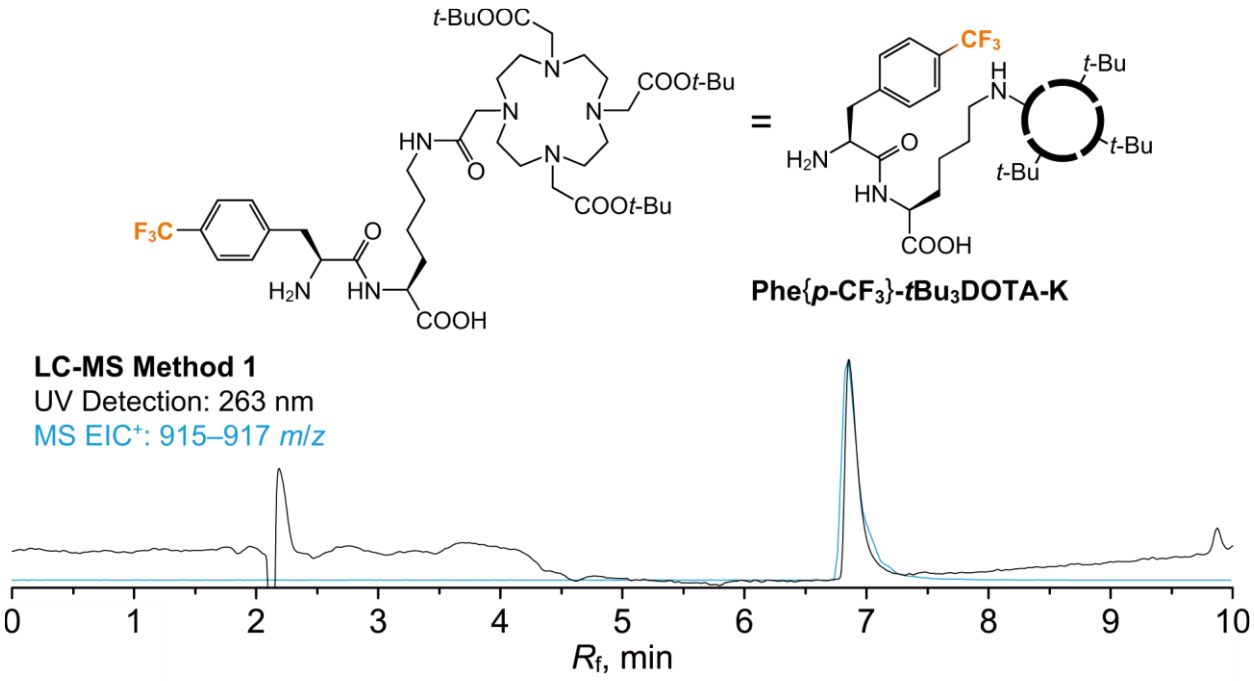

Synthesis and LC-MS chromatogram of building block Phe{*p*-CF$_3$}-*t*Bu$_3$DOTA-K: In a glass vial (4 mL), **17** (19 mg, 13.9 µmol assuming **19**·2.0TFA, 1.0 equiv.) was dissolved in DMF (1.4 mL) followed by addition of DBU (27 µL, 181 µmol, 13.0 equiv.). After 5 mins, the reaction was quenched with TFA (14 µL, 183 µmol, 13.1 equiv.) and diluted with H_2O (1 mL). Mixture was then purified by preparative HPLC (C18, H_2O/MeCN gradient with 0.1% TFA additive). Fractions with product were joined and lyophilized to give product as white solid. **Yield:** 11 mg (66%; 1 step; based on **19**·2.0TFA assuming **Phe{*p*-CF$_3$}-*t*Bu$_3$DOTA-K**·2.5TFA, $M_R = 1201$). **ESI-HRMS:** 916.5364 $[M+H]^+$ (theor. $[C_{44}H_{73}O_{10}N_7F_3]^+ = 916.5366$).

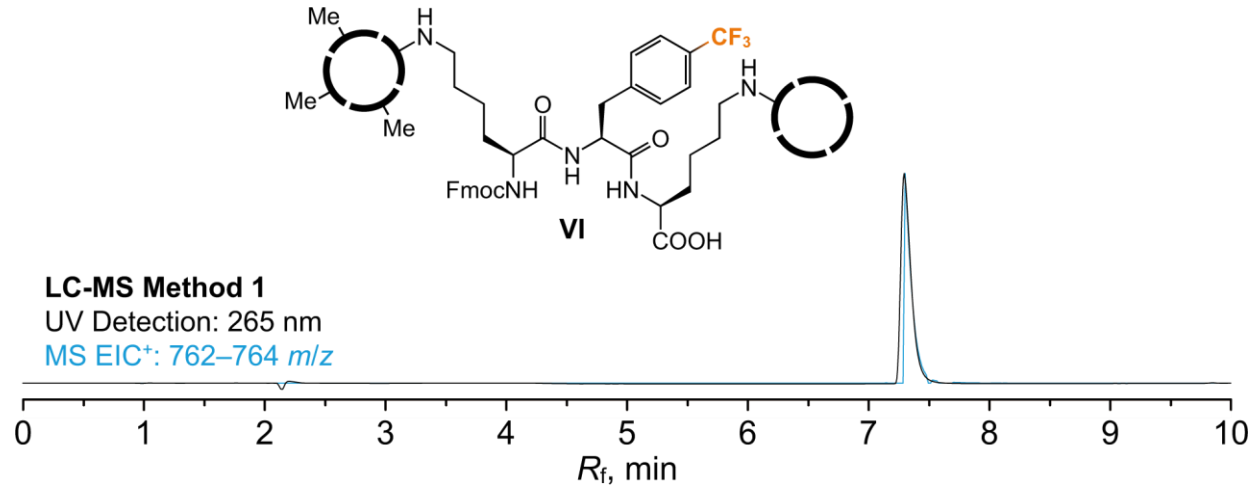

Synthesis and LC-MS chromatogram of intermediate VI: In a glass vial (4 mL), **Fmoc-Me$_3$DOTA-K**·1.8TFA·1.3H_2O **(**10 mg, 9.8 µmol, 1.3 equiv.) was dissolved in dry DMSO **(**650 µL) followed by

addition of PyAOP (100 mM in dry DMSO, 95 µL, 9.5 µmol, 1.3 equiv.) and DIPEA (17 µL, 97 µmol, 13 equiv.). After 1 min, **Phe{*p*-CF$_3$}-*t*Bu$_3$DOTA-K** (9.1 mg, 7.6 µmol assuming **Phe{*p*-CF$_3$}-*t*Bu$_3$DOTA-K**·2.5TFA, 1.0 equiv.) was added and the mixture was stirred at RT for 5 mins. Mixture was then purified by preparative HPLC (C18, H$_2$O/MeCN gradient with 0.1% TFA additive). Fractions with *tert*-butyl protected product were joined and lyophilized. The resulting white solid was dissolved in TFA (3 mL). The resulting solution was stirred at RT for 24 h. Mixture was evaporated to dryness and the residue was purified by preparative HPLC (C18, H$_2$O/MeCN gradient with 0.1% TFA additive). Fractions with product were joined and lyophilized to give product as white solid. **Yield:** 6.6 mg (44%; 2 steps; based on **Phe{*p*-CF$_3$}-*t*Bu$_3$DOTA-K**·2.5TFA assuming **VI**·4.0TFA, M_R = 1983 .(**ESI-HRMS:** 763.8729 $[M+2H]^{2+}$ (theor. $[C_{72}H_{104}O_{20}N_{13}F_3]^{2+}$ = 763.8731).

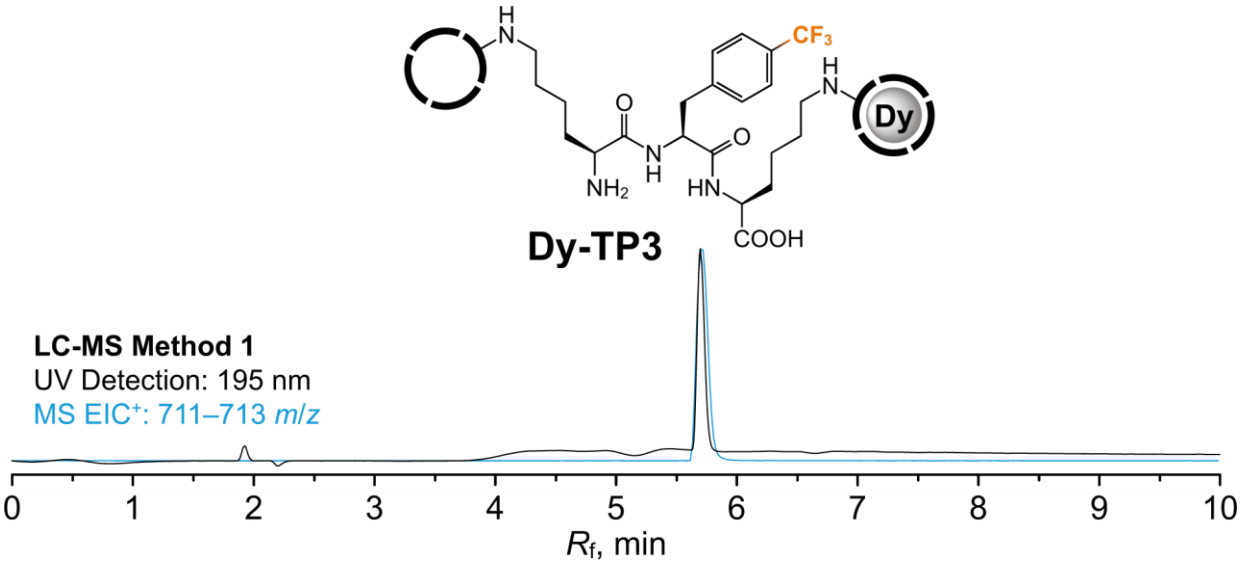

Synthesis and LC-MS chromatogram of intermediate Dy-TP3: In a glass vial (4 mL), **VI** (3.3 mg, 1.7 µmol assuming **VI**·4.0TFA) was dissolved in aq. MOPS/NaOH buffer (500 mM, pH 7.0, 500 µL, 250 µmol, 150 equiv.) followed by addition of aq. DyCl$_3$ (100 mM, 19 µL, 1.9 µmol, 1.1 equiv.) and the resulting solution was stirred at RT for 15 mins. The mixture was then purified by preparative HPLC (C18, H$_2$O/MeCN gradient with 0.1% TFA additive). Fractions with Fmoc/methyl ester protected product were joined and lyophilized. The resulting white solid was dissolved in MeOH (460 µL) and H$_2$O (40 µL) followed by addition of aq. LiOH (1.0 M, 42 µL, 42 µmol, 25 equiv.) and the mixture was stirred at RT for 24 h. Reaction was then quenched by FA (16 µL, 42 µmol, 25 equiv.) and the mixture was evaporated to dryness. The residue was purified by preparative HPLC (C18, H$_2$O/MeCN gradient with 0.1% FA additive). Fractions with product were joined and lyophilized to give product as white solid. **Yield:** 2.0 mg (78%; 2 steps; based on **VI**·4.0TFA assuming **Dy-TP3**·2.5FA, M_R = 1537. (**ESI-HRMS:** 712.2681 $[M+2H]^{2+}$ (theor. $[C_{54}H_{85}O_{18}N_{13}F_3Dy_1]^{2+}$ = 712.2684).

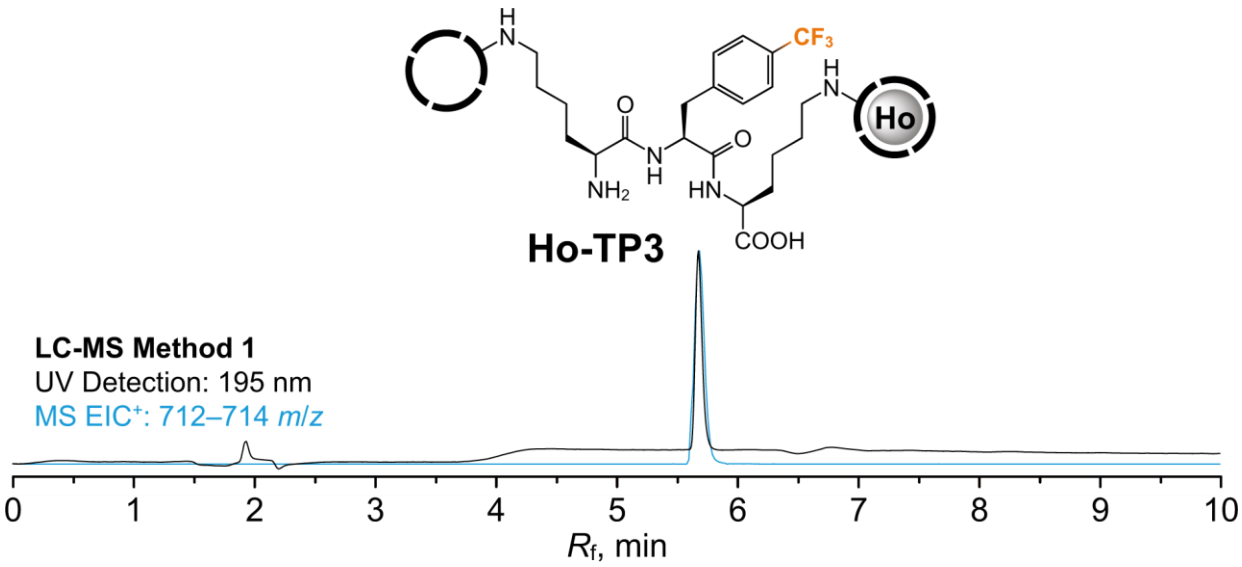

Synthesis and LC-MS chromatogram of intermediate Ho-TP3: In a glass vial (4 mL), **VI** (3.3 mg, 1.7 µmol assuming **VI**·4.0TFA) was dissolved in aq. MOPS/NaOH buffer (500 mM, pH 7.0, 500 µL, 250 µmol, 150 equiv.) followed by addition of aq. $HoCl_3$ (100 mM, 19 µL, 1.9 µmol, 1.1 equiv.) and the resulting solution was stirred at RT for 15 mins. The mixture was then purified by preparative HPLC (C18, H_2O/MeCN gradient with 0.1% TFA additive). Fractions with Fmoc/methyl ester protected product were joined and lyophilized. The resulting white solid was dissolved in MeOH (460 µL) and H_2O (40 µL) followed by addition of aq. LiOH (1.0 M, 42 µL, 42 µmol, 25 equiv.) and the mixture was stirred at RT for 24 h. Reaction was then quenched by FA (16 µL, 42 µmol, 25 equiv.) and the mixture was evaporated to dryness. The residue was purified by preparative HPLC (C18, H_2O/MeCN gradient with 0.1% FA additive). Fractions with product were joined and lyophilized to give product as pinkish solid. **Yield:** 2.0 mg (78%; 2 steps; based on **VI**·4.0TFA assuming **Ho-TP3**·2.5FA, M_R = 1539). **ESI-HRMS:** 712.7693 $[M+2H]^{2+}$ (theor. $[C_{54}H_{85}O_{18}N_{13}F_3Ho_1]^{2+}$ = 712.7690).

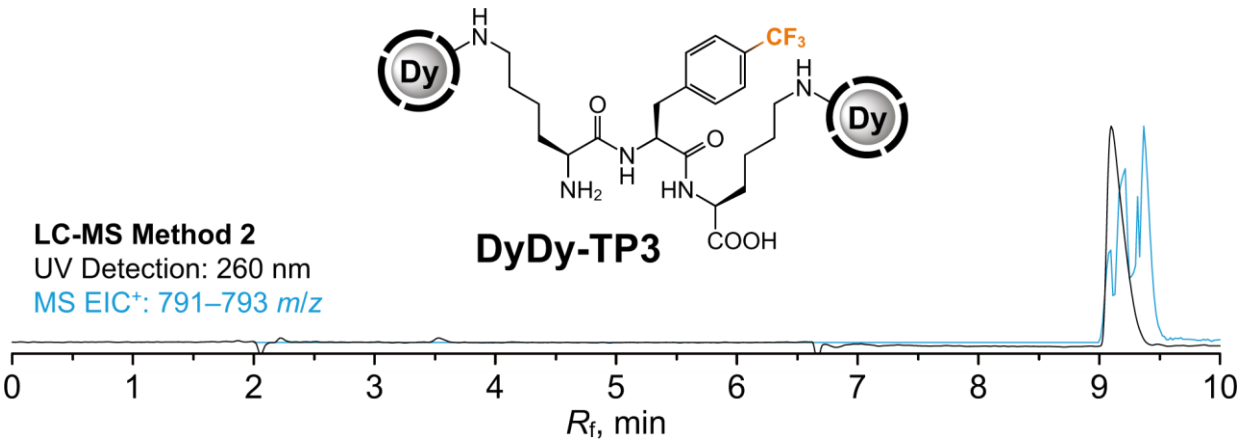

Synthesis and LC-MS chromatogram of DyDy-TP3: In a glass vial (4 mL), **Dy-TP3** (1.0 mg, 0.6 µmol assuming **Dy-TP3**·2.5FA, 1.0 equiv.) was dissolved in aq. MOPS/NaOH buffer (500 mM, pH 7.0, 500 µL, 250 µmol, 420 equiv.) followed by addition of aq. $DyCl_3$ (100 mM, 7 µL, 0.7 µmol, 1.1 equiv.) and the resulting solution was stirred at RT for 16 h. The mixture was then purified by preparative HPLC (C18, H_2O/MeCN gradient with 0.1% FA additive). Fractions with product were joined and lyophilized to give product as white solid. **Yield:** 0.7 mg (66%; 1 step; based on **Dy-TP3**·2.5FA assuming **DyDy-TP3**·1.0FA, M_R = 1627). **NMR (aq. MOPS pH = 7.0, external D_2O): ^{19}F** (470.4 MHz, T = 298.2 K) δ_F –62.71 (CF_3, m). **ESI-HRMS:** 792.7215 $[M+2H]^{2+}$ (theor. $[C_{54}H_{82}O_{18}N_{13}F_3Dy_2]^{2+}$ = 792.7213).

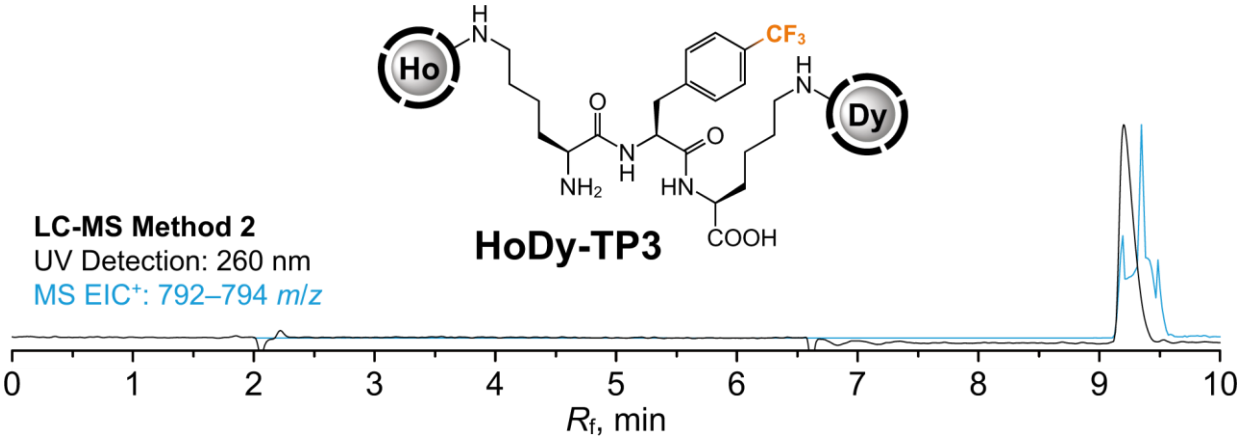

Synthesis and LC-MS chromatogram of HoDy-TP3: In a glass vial (4 mL), **Dy-TP3** (1.0 mg, 0.6 µmol assuming **Dy-TP3**·2.5FA, 1.0 equiv.) was dissolved in aq. MOPS/NaOH buffer (500 mM, pH 7.0, 500 µL, 250 µmol, 420 equiv.) followed by addition of aq. $HoCl_3$ (100 mM, 7 µL, 0.7 µmol, 1.1 equiv.) and the resulting solution was stirred at RT for 16 h. The mixture was then purified by preparative HPLC (C18, H_2O/MeCN gradient with 0.1% FA additive). Fractions with product were joined and lyophilized to give product as pinkish solid. **Yield:** 1.0 mg (94%; 1 step; based on **Dy-TP3**·2.5FA assuming **HoDy-TP3**·1.0FA

M_R = 1630). **NMR (aq. MOPS pH = 7.0, external D_2O): ^{19}F** (470.4 MHz, T = 298.2 K) δ_F –62.79 (CF_3, m). **ESI-HRMS:** 793.2217 $[M+2H]^{2+}$ (theor. $[C_{54}H_{82}O_{18}N_{13}F_3Ho_1Dy_1]^{2+}$ = 793.2218).

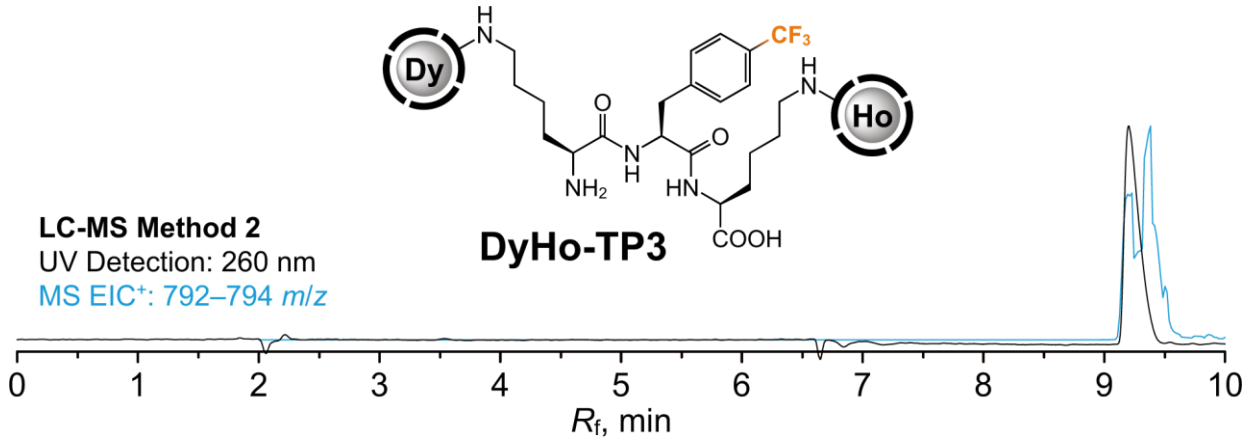

Synthesis and LC-MS chromatogram of DyHo-TP3: In a glass vial (4 mL), **Ho-TP3** (1.0 mg, 0.6 µmol assuming **Ho-TP3**·2.5FA, 1.0 equiv.) was dissolved in aq. MOPS/NaOH buffer (500 mM, pH 7.0, 500 µL, 250 µmol, 420 equiv.) followed by addition of aq. $DyCl_3$ (100 mM, 7 µL, 0.7 µmol, 1.1 equiv.) and the resulting solution was stirred at RT for 16 h. The mixture was then purified by preparative HPLC (C18, H_2O/MeCN gradient with 0.1% FA additive). Fractions with product were joined and lyophilized to give product as pinkish solid. **Yield:** 0.8 mg (76%; 1 step; based on **Ho-TP3**·2.5FA assuming **DyHo-TP3**·1.0FA M_R = 1630). **NMR (aq. MOPS pH = 7.0, external D_2O): ^{19}F** (470.4 MHz, T = 298.2 K) δ_F –62.77 (CF_3, m). **ESI-HRMS:** 793.2222 $[M+2H]^{2+}$ (theor. $[C_{54}H_{82}O_{18}N_{13}F_3Dy_1Ho_1]^{2+}$ = 793.2218).

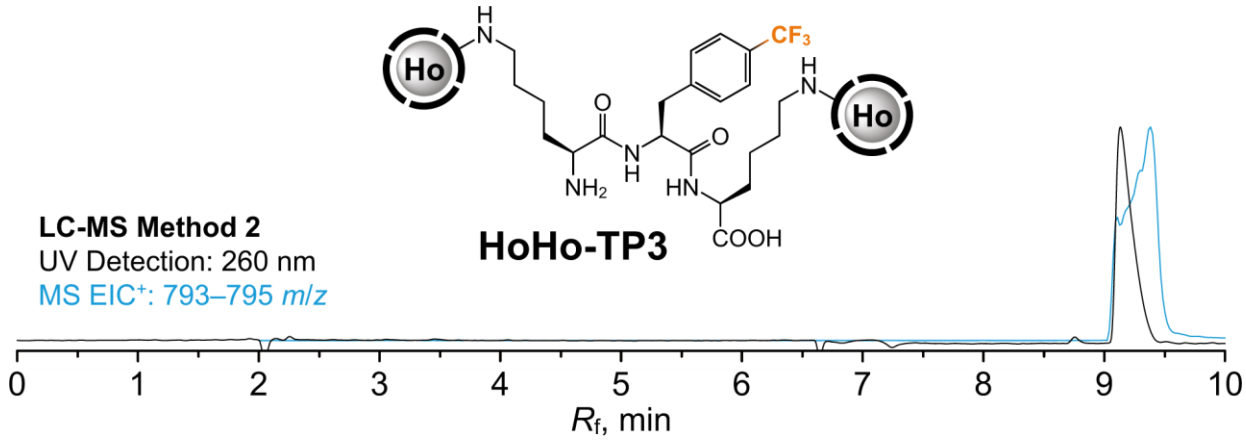

Synthesis and LC-MS chromatogram of HoHo-TP3: In a glass vial (4 mL), **Ho-TP3** (1.0 mg, 0.6 µmol assuming **Ho-TP3**·2.5FA, 1.0 equiv.) was dissolved in aq. MOPS/NaOH buffer (500 mM, pH 7.0, 500 µL, 250 µmol, 420 equiv.) followed by addition of aq. $HoCl_3$ (100 mM, 7 µL, 0.7 µmol, 1.1 equiv.) and the

resulting solution was stirred at RT for 16 h. The mixture was then purified by preparative HPLC (C18, H_2O/MeCN gradient with 0.1% FA additive). Fractions with product were joined and lyophilized to give product as pinkish solid. **Yield:** 1.0 mg (94%; 1 step; based on **Ho-TP3**·2.5FA assuming **HoHo-TP3**·1.0FA M_R = 1632). **NMR (aq. MOPS pH = 7.0, external D_2O): ^{19}F** (470.4 MHz, T = 298.2 K) δ_F –62.72 (CF_3, m). **ESI-HRMS:** 793.7226 $[M+2H]^{2+}$ (theor. $[C_{54}H_{82}O_{18}N_{13}F_3Ho_2]^{2+}$ = 793.7224).

5.2 PET/MRI

Radiolabeling experiments: A solution containing $^{18}F^-$ produced on a cyclotron was absorbed on the QMA column (Sep-Pak, Waters) in either a CO_3^- or OTf^- cycle. Preconditioning of the column to the CO_3^- cycle was done by washing the QMA column with $NaHCO_3$ (0.5 M, 10 mL) followed by washing with H_2O (20 mL) and blowing with air (20 mL). Elution of $^{18}F^-$ from CO_3^- preconditioned column was done by solution of $TBAHCO_3$ or K222 in a mixture of H_2O and MeCN. A volume containing the desired activity was transferred to a 4 ml glass vial with a stirring bar preheated to 120 °C and a stream of argon was introduced. The aqueous solution was evaporated for 5 minutes, and 300 µl of dry MeCN was introduced and evaporated again for 2 minutes. This step was performed twice. Preconditioning of the column to the OTf^- cycle was done by washing the QMA column with KOTf (0.48 M, 10 mL) followed by washing with H_2O (10 mL), air (10 mL) and blowing dry with argon for 20 minutes. Elution of $^{18}F^-$ from OTf^- preconditioned column was done by solution of TBAOTf in dry methanol. The precursor for radiolabeling was introduced in DMSO or MeCN or in mixture of DMSO and MeCN. For elimination of the residual $^{18}F^-$ from the reaction mixture, an alumina SPE Cartridge (Sep-Pak light) was used. After that, the reaction mixture was analyzed on a HPLC equipped with a gamma and UV detector, a YMC-Triart analytical column (5 µm, 120 Å, 150 × 4.6 mm) with a C18 precolumn and equilibrated with isocratic aqueous 3% MeOH in the case of **[Gd(^{18}FL^1)]** preparation or isocratic aqueous 3% MeOH, 10 mM ammonium formate, and 0.005% formic acid in water in the case of **[Gd(^{18}FL^2)].** Analyses were performed at flow rate of 1 mL min^{-1}.

PET/MRI Imaging: Phantom and *in vivo* MR imaging were acquired on a 7 T preclinical MR scanner (Bruker Clinscan, Bruker BioSpin, Ettlingen, Germany) using an 86-mm diameter ^1H transceiver volume coil (Bruker), provided with a small-animal PET insert developed in cooperation with Bruker. For *in vivo* imaging, healthy female C57BL/6 mice (Charles River) were kept under anesthesia using 1.5 % isoflurane in pure oxygen. A cocktail of radioactive **[Gd(^{18}FL^1)]** and nonradioactive **[Gd(FL^1)]** dissolved in saline solution was prepared for each mouse and administered at the beginning of the PET scan as bolus via a catheter placed in a tail vein, to an average final dose of 0.116 ± 0.006 mmol/Kg body weight, corresponding to 0.885 ± 0.074 MBq (n = 3). *In vivo* experiments were conducted according to the German federal regulations regarding use and care of experimental animals and were approved by the local authorities (Regierungspräsidium Tübingen).

MRI sequences: Phantoms of 0.1-0.5 mM **[Gd(FL^1)]**, **[Gd(FL^2)]** and Magnevist (Bayer) dissolved in 50 mM Tris buffer were prepared in 0.3 mL tubes. T_1-weighted MR images of phantoms were acquired using a 2D T_1-FLASH sequence with the following parameters: TE 4 ms, TR 100 ms, flip angle 50°, field of view 50x50 mm^3, 10 slices, slice thickness 1 mm, matrix size 192x192, resolution 0.260x0.260x1 mm^3. T_1 maps were acquired using a standard 2D RARE VTR sequence with 15 TRs: 50, 100, 200, 300, 400, 500, 600,

700, 800, 900, 1000, 1500, 2500, 3000 ms. Other parameters: TE 8 ms, field of view 50x50 mm, 2 slices, slice thickness 1 mm, matrix size 192x192, resolution 0.260x0.260x1 mm^3. T_2-weighted MR images were acquired using a 2D T_2-TurboRARE sequence with the following parameters: TE 28 ms, TR 1800 ms, flip angle 90°, field of view 50x50 mm^3, 20 slices, slice thickness 1 mm, matrix size 256x192, resolution 0.195x0.260x1 mm^3. T_2 maps were acquired using a standard 2D MSME sequence with 60 TEs ranging from 8 to 480 ms. Other parameters: TR 3000 ms, field of view 50x50 mm^3, 5 slices, slice thickness 1 mm, matrix size 192x192, resolution 0.260x0.260x1 mm^3.

For *in vivo* imaging, 30 pre- and 100 post-contrast T_1-weighted images were acquired using a 3D FLASH protocol with the following parameters: TE 2.2 ms, TR 17.5 ms, flip angle 10°, field of view 64x32x21 mm^3, matrix size 231x102x21, resolution 0.277x0.314x1 mm^3, image acquisition time 37.5 s, 130 repetitions.

PET Imaging: For phantom experiments, **[Gd(^{18}FL^1)]** was diluted in **[Gd(FL^1)]** dissolved in PBS to a final concentration of 0.49 mM, corresponding to 0.49 MBq. Phantoms containing 0.048-0.49 mM **[Gd(^{18}FL^1)]** (0.29-0.49 MBq) were prepared in 0.3 mL tubes and placed in the PET/MR scanner. A 600 second single frame PET scan was acquired simultaneously with MR the images. For *in vivo* imaging, a 3750 second scan was started after the acquisition of the first 30 MR images after injection of the radiolabelled contrast agent.

The PET data were saved as list-mode files and reconstructed using an ordered-subsets expectation maximization 2D (OSEM-2D) algorithm written in-house. *In vivo* datasets were reconstructed into 100 frames (37.5 s each) in order to temporally match the MR scans. Decay correction was applied during reconstruction.

Image analysis: PET and MRI images were co-registered using Inveon Acquisition Workplace (Siemens Healthcare).

[Gd(FL^1)] Cytotoxicity: Cytotoxicity of **[Gd(FL^1)]** was evaluated using a MTS assay (Promega, Madison, WI, USA). MC-38 cells (Kerafast) were cultured in T175 flasks with DMEM supplemented with 10% FCS, 1% penicillin/streptomycin, L-glutamine, sodium pyruvate, and 15 mM HEPES in a humidified incubator (5% CO_2, 37°C). For experiments, cells were trypsinized, counted with Trypan Blue and seeded at a density of 2000 cells/well in 96-well plates. After 24 h, cells were incubated for 2 h with 1-10 μM **[Gd(FL^1)]** or Magnevist, then the MTS reagent mix was added. After further incubation at 37°C for 2 or 4 h, absorbance at 490 nm was measured. Cytotoxicity was determined as the metabolic inhibition rate by comparing the absorbance of treated cells to control cells, expressed as %. Experiments were run in triplicate, the results are reported as mean inhibition rate ± SEM.

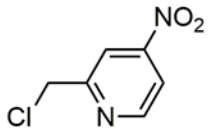

1

Synthesis of *2*-(chloromethyl)-*4*-nitropyridine (1): In a 250 mL round bottom glass flask, *2*-methyl-*4*-nitropyridine *N*-oxide (5.15 g, 33.4 mmol, 1.0 equiv.) was dissolved in DCM (200 mL). Solution of TFAA (14mL, 101 mmol, 3.0 equiv.) in DCM (35 mL) was added dropwise and the resulting suspension was stirred for 96 h at RT. Saturated aqueous solution of K_2CO_3 (40 mL) was added in four portions over period of 1 h and reaction mixture was stirred until bubbling stopped. Water phase was extracted with DCM (2 × 200 mL) and solvent was evaporated on rotary evaporator. The residue was purified by preparative HPLC (C18, H_2O/MeCN gradient with 0.1% FA additive). Fractions with product were joined and lyophilized. The resulting white solid was dissolved in DCM (340 mL) followed by addition of DMF (46 µL, 0.60 mmol, 0.02 eqiv.) and $SOCl_2$ (5.5 mL, 75.1 mmol, 2.25 equiv.) dropwise. After 6 hours of stirring at RT the reaction mixture was put on ice bath and was quenched by careful addition of saturated aqueous solution of $NaHCO_3$ (200 mL). Phases were separated, and the water phase was extracted with DCM (200 mL). The organic phase was dried over Na_2SO_4, filtered and liquids were evaporated on a rotary evaporator. The residue was purified by column chromatography (SiO_2, 100% DCM to 10% MeOH in DCM). Fractions containing the product were pooled and evaporated to dryness to yield the product as yellow oil. **Yield:** 2.2 g (38%; 2 steps; based on **2-methyl-4-nitropyridine *N*-oxide**). **NMR (CDCl₃): ^{1}H** (400.1 MHz, T = 300 K) δ_H 4.80 (CH_2–arom, s, 2H); 7.98 (*arom*, dd, $^3J_{HH}$ = 5, $^4J_{HH}$ = 2, 1H); 8.24 (*arom*, d, $^4J_{HH}$ = 2, 1H); 8.87 (*arom*, d, $^3J_{HH}$ = 5, 1H). **^{13}C{^{1}H}** (100.6 MHz, T = 300 K) δ_C 45.8 (*C*H_2–arom, s); 115.6 (*arom*, s); 115.8 (*arom*, s); 151.8 (*arom*, s); 154.8 (*arom*, s); 160.2 (*arom*, s). **EI-HRMS:** 172.0033 $[M]^+$ (theor. $[C_6H_5O_2N_2Cl_1]^+$ = 172.0034).

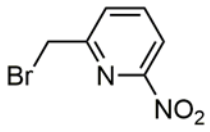

2

Synthesis of *2*-(bromomethyl)-*6*-nitropyridine (2): In a 50 mL pear-shaped glass flask, *2*-methyl-*6*-nitropyridine (224 mg, 1.62 mmol, 1.0 equiv.), NBS (577 mg, 3.24 mmol, 2.0 equiv.) and AIBN (42 mg, 0.26 mmol, 0.16 equiv.) were dissolved in CCl_4 (6 mL). The reaction mixture was heated under reflux for 19 hours.The solvent was evaporated on a rotary evaporator. The residue was purified by preparative HPLC (C18, MeCN/H_2O gradient with 0.1% FA additive). Fractions containing the product were pooled

and DCM was added until separation of phases occurred. The organic phase was separated and washed with saturated aqueous $NaHCO_3$. The organic phase was concentrated on a rotary evaporator,giving the product as colorless solid. **Yield**: 79 mg (23 %, 1 step, based on **2-methyl-6-nitropyridine**). **NMR** ($CDCl_3$): **^{1}H** (400.1 MHz, T = 300 K) δ_H 4.63 (CH_2–arom, s, 2H); 7.87 (*arom*, dd, $^2J_{HH}$ = 7.6, $^3J_{HH}$ = 0.9, 1H); 8.07 (*arom*, t, $^2J_{HH}$ = 7.8, 1H); 8.19 (*arom*, dd, $^2J_{HH}$ = 8.0, $^3J_{HH}$ = 0.8, 1H). **^{13}C{^{1}H}** (100.6 MHz, T = 300 K) δ_C 31.7 (*C*H_2–arom, s); 117.3 (*arom*, s); 129.3 (*arom*, s); 141.1 (*arom*, s); 156.2 (*arom*, s); 157.5 (*arom*, s). **CI-HRMS**: 216.9605 $[M+H]^+$ (theor. $[C_6H_6O_2Br_1N_2]^+$ = 216.9607).

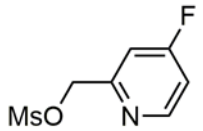

3

Synthesis of (*4*-fluoropyridin-*2*-yl) methyl methanesulfonate (3): In a 50 mL round bottom glass flask, methyl *4*-fluoropicolinate (250 mg, 1.61 mmol, 1.0 equiv.) was dissolved in MeOH (16 mL) and $NaBH_4$ (180 mg, 4.78 mmol, ~3.0 equiv.) was added while stirring. The reaction was stirred for 3 hours at RT, after which H_2O (1 mL) was added. Liquids were evaporated on a rotary evaporator and the residue was suspended in a saturated aqueous solution of K_2CO_3 (25 mL). The water phase was extracted with DCM (2 × 25 mL) and the solvent was evaporated a on rotary evaporator. The residue was dissolved in DCM (11 mL) and Et_3N (280 µL, 2.02 mmol, 1.3 equiv.) was added. The reaction mixture was put on ice bath. After 20 minutes on the ice bath, methanesulfonyl chloride (146 µL, 1.88 mmol, 1.23 equiv.) was added and the reaction mixture was stirred on the ice bath. After 15 minutes the reaction mixture was let warm to RT a was let stirring for 1 hour. The reaction mixture was diluted with DCM (40 mL) and washed with H_2O (2 × 40 mL), brine (40 mL). The organic phase was dried over Na_2SO_4, filtered and liquids were evaporated on a rotary evaporator to yield the product as dark orange oil. **Yield:** 240 mg (77%; 2 steps; based on **methyl *4*-fluoropicolinate**) **NMR** ($CDCl_3$): **^{1}H** (400.1 MHz, T = 300 K) δ_H 3.12 (CH_3, s, 3H); 5.33 (CH_2–arom, s, 2H); 7.04 (*arom.*,ddd, J = 8, 6, 3 Hz 1H); 7.24 (*arom.*, dd, J = 9, 3 Hz, 1H); 8.58 (*arom.*, dd, J = 8, 6 Hz, 1H). **^{13}C{^{1}H}** (100.6 MHz, T = 300 K) δ_C 38.2 (*C*H_3, s); 70.4 (*C*H_2–arom, s); 110.5 (*arom*, d, $^2J_{CF}$ = 18 Hz); 111.7 (*arom*, d, $^2J_{CF}$ = 17 Hz); 152 (*arom*, d, $^3J_{CF}$ = 7 Hz); 157.2 (*arom*, d, $^3J_{CF}$ = 7 Hz); 169.5 (*arom*, d, $^1J_{CF}$ = 265 Hz). **^{19}F{^{1}H}** (376.5 MHz, T = 300.0 K) δ_F –99.3 (s). **CI-HRMS**: 206.0281 $[M+H]^+$ (theor. $[C_7H_9O_3N_1F_1S_1]^+$ = 206.0282).

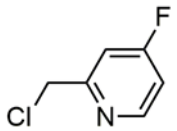

4

Synthesis of *2*-(chloromethyl)-*4*-fluoropyridine (4): In a 50 mL round bottom glass flask, **(*4*-fluoropyridin-*2*-yl)methanol** (227 mg, 1.79 mmol, 1.0 equiv.) was dissolved in DCM (35 mL) and DMF (4 µL, 0.05 mmol, 0.01 equiv.) was added. The reaction mixture was put on ice bath. After 20 minutes on ice bath, thionyl chloride (400 µL, 5.36 mmol, 3.0 equiv.) was added dropwise and reaction mixture was let stir on ice bath. After 15 minutes, the reaction mixture was allowed to let warm to RT. After 1 hour of stirring at RT the reaction mixture was put on ice bath and quenched by careful addition of saturated aqueous solution of $NaHCO_3$ (10 mL). Phases were separated, and the water phase was extracted with DCM (2 × 40 mL). Organic phase was dried over Na_2SO_4, filtered and liquids were evaporated on rotary evaporator to yield the product as colorless oil. **Yield:** 217 mg (83%; 1 step; based on **(*4*-fluoropyridin-*2*-yl)methanol**) **NMR** ($CDCl_3$): **^{1}H** (400.1 MHz, T = 300 K) δ_H 4.69 (CH_2–arom, s, 2H); 7.00 (*arom.*, ddd, J = 8, 6, 2 Hz 1H); 7.24−7.30 (*arom.*, m, 1H); 8.55 (*arom.*, dd, J = 8, 6 Hz H). **^{13}C{^{1}H}** (100.6 MHz, T = 300 K) δ_C 70.8 (*C*H_2–arom, d, $^4J_{CF}$ = 3 Hz); 110.9 (*arom*, d, $^2J_{CF}$ = 18 Hz); 111.2 (*arom*, d, $^2J_{CF}$ = 17 Hz); 151.8 (*arom*, d, $^3J_{CF}$ = 7 Hz); 160.0 (*arom*, d, $^3J_{CF}$ = 7 Hz); 169.4 (*arom*, d, $^1J_{CF}$ = 263 Hz). **^{19}F{^{1}H}** (376.5 MHz, T = 300.0 K) δ_F –100.9 (s). **ESI-MS**: 146.0 $[M+H]^+$(theor. $[C_6H_6N_1F_1Cl_1]^+$ = 146.0).

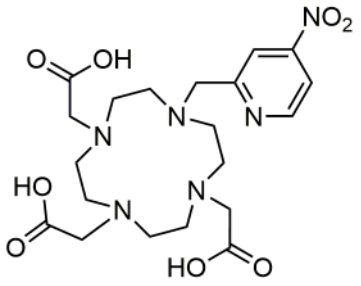

NO_2L^1

Synthesis of ligand NO_2L^1: Solution of **1** (168 mg, 0.97 mmol, 1.1 equiv.) was added to a solution of *t*-BuDO3A·HBr (527 mg, 0.89 mmol, 1.0 equiv.) in MeCN (18 mL) followed by addition of dried K_2CO_3 (489 mg, 3.54 mmol, 4.0 equiv.) and the resulting suspension was stirred for 24 hours at RT. The solids were filtered off and the filtrate was concentrated on rotary evaporator. Resulting oil was purified on preparative HPLC (C18, H_2O/MeCN gradient with 0.1% FA additive). Fractions containing pure product in the form of *tert*-butyl ester were pooled, evaporated to dryness, and several times co-evaporated with

MeOH to remove MeCN. The residue was dissolved in neat TFA (6 mL) and stirred for 16 h at RT. Volatiles were removed on a rotary evaporator and the residue was purified on preparative HPLC (C18, H_2O/MeCN gradient with 0.1% TFA additive). Fractions with product were joined and lyophilized to give a product in the form of TFA salt as a yellowish solid. **Yield**: 342 mg (56 %, 2 steps, based on ***t*-BuDO3A**·HBr). **NMR** (D_2O): **^{1}H** (600.1 MHz, T = 323 K) δ_H 3.09–3.70 (*mc*, CH_2–COOH, m, 22H); 4.35 (CH_2–arom, bs, 2H); 8.14 (*arom*, dd, 1H, $^3J_{HH}$ = 6 Hz, $^4J_{HH}$ = 2 Hz); 8.40 (*arom*, d, 1H, $^3J_{HH}$ = 2 Hz); 8.87 (*arom*, d, 1H, $^3J_{HH}$ = 6Hz). **^{13}C{^{1}H}** (150.9 MHz, T = 323 K) δ_C 49.7 (*mc*, s); 50.6 (*mc*, s); 51.0 (*mc*, s); 54.7 (*mc*, s); 55.8 (*C*H_2–COOH, s); 57.8 (*C*H_2–arom, s); 117.4 (*arom*, s); 118.6 (*arom*, s); 152.0 (*arom*, s); 155.8 (*arom*, s); 173.0 (*C*O, s); 175.5 (*C*O, s). **ESI-HRMS**: 483.2195 $[M+H]^+$ (theor. $[C_{20}H_{31}N_6O_8]^+$ = 483.2198). **EA** ($C_{20}H_{30}N_6O_8$·1.8TFA·1.0H_2O, M_R = 687.7): C 41.2 (42.0); H 4.7 (5.2); N 12.2 (12.8); F 14.9 (15.9).

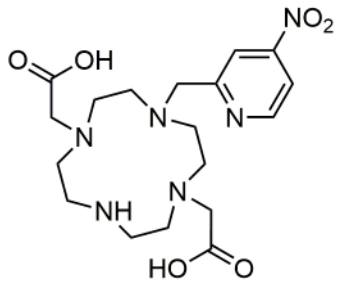

NO_2L^2

Synthesis of ligand NO_2L^2: Solution of **1** (376 mg, 2.18 mmol, 1.0 equiv.) was added to a solution of *t*-BuDO2A (873 mg, 2.18 mmol, 1.0 equiv.) in MeCN (109 mL) followed by the addition of dried K_2CO_3 (301 mg, 2.18 mmol, 1.0 equiv.) and the resulting suspension was stirred for 39 hours at RT. The solids were filtered off and the filtrate was concentrated on a rotary evaporator. Resulting oil was purified on preparative HPLC (C18, H_2O/MeCN gradient with 0.1% TFA additive). Fractions containing pure product in the form of *tert*-butyl ester were pooled, evaporated to dryness, and several times co-evaporated with MeOH to remove MeCN. The residue was dissolved in neat TFA (6 mL) and stirred for 14 h at RT. Volatiles were removed on rotary evaporator and the residue was purified on preparative HPLC (C18, H_2O/MeCN gradient with 0.1% TFA additive). Fractions with product were joined and lyophilized to give product in the form of TFA salt as a yellowish solid. **Yield**: 358 mg (26 %, 2 steps, based on ***t*-BuDO2A**). **NMR** (D_2O): **^{1}H** (600.1 MHz, T = 298.1 K) δ_H 2.88–3.74 (*mc*, CH_2–COOH, m, 20H); 4.91 (CH_2–arom, s, 2H); 8.21 (*arom*, dd, 1H, $^3J_{HH}$ = 5 Hz, $^4J_{HH}$ = 2 Hz); 8.27 (*arom*, dd, 1H, $^3J_{HH}$ = 2 Hz, $^5J_{HH}$ = 1 Hz); 8.85 (*arom*, dd, 1H, $^3J_{HH}$ = 5 Hz, $^5J_{HH}$ = 1 Hz). **^{13}C{^{1}H}** (150.9 MHz, T = 298.1 K) δ_C 43.0 (*mc*, s); 49.1 (*mc*, s); 50.1 (*mc*, s); 52.7 (*mc*, s); 54.5 (*C*H_2–COOH, s); 57.8 (*C*H_2–arom, s); 117.3 (*arom*, s); 118.1 (*arom*, s); 152.5 (*arom*,

s); 153.1 (*arom*, s); 175.0 (*C*O, s). **ESI-HRMS**: 425.2143 $[M+H]^+$ (theor. $[C_{18}H_{29}N_6O_6]^+$ = 425.2143). **EA** ($C_{18}H_{28}N_6O_6 \cdot 1.7TFA \cdot 1.4H_2O$, M_R = 643.5): C 39.9 (39.8); H 5.1 (4.4); N 13.1 (12.4); F 15.1 (14.8).

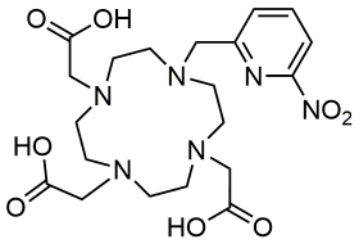

NO_2L^3

Synthesis of ligand NO_2L^3: Solution of **3** (74 mg, 0.34 mmol, 1.1 equiv.) in MeCN (2 mL) was added to a solution of *t*-BuDO3A·HBr (185 mg, 0.31 mmol, 1.0 equiv.) in MeCN (42 mL) followed by addition of dried K_2CO_3 (215 mg, 1.55 mmol, 5 equiv.) and the resulting suspension was stirred for 24 hours at RT. The solids were filtered off and the filtrate was concentrated on a rotary evaporator. Resulting oil was purified on preparative HPLC (C18, H_2O/MeCN gradient with 0.1% FA additive). Fractions containing pure product in the form of *tert*-butyl ester were pooled, evaporated to dryness, and several times co-evaporated with MeOH to remove MeCN. The residue was dissolved in neat TFA (3 mL) and stirred for 16 h at RT. Volatiles were removed on a rotary evaporator and the residue was purified on preparative HPLC (C18, H_2O/MeCN gradient with 0.1% FA additive). Fractions with product were joined and lyophilized to give product in the form of FA salt as a yellowish solid. **Yield**: 50 mg (31 %, 2 steps, based on ***t*-BuDO3A**·HBr). **NMR** (D_2O): **^{1}H** (600.1 MHz, T = 298.1 K) δ_H 2.94–3.18 (*mc*, m, 8H); 3.33–3.51 (*mc*, m, 8H); 3.54 (CH_2–COOH, s, 2H); 3.61–3.82 (CH_2–COOH, m, 4H); 4.05 (CH_2–arom, s, 2H); 8.16 (*arom*, t, 1H, $^3J_{HH}$ = 8 Hz); 8.24–8.33 (*arom*, m, 2H). **^{13}C{^{1}H}** (150.9 MHz, T = 298.1 K) δ_C 48.6 (*mc*, s); 51.1 (*mc*, s); 52.2 (*mc*, s); 54.1 (*C*H$_2$–COOH, s); 56.8 (*C*H$_2$–COOH, s); 58.2 (*C*H$_2$–arom, s); 118.5 (*arom*, s); 132.2 (*arom*, s); 143.6 (*arom*, s); 155.9 (*arom*, s); 157.8 (*arom*, s); 169.9 (*C*O, s); 175.3 (*C*O, s). **ESI-HRMS**: 483.2196 $[M+H]^+$ (theor. $[C_{20}H_{32}N_5O_6]^+$ = 483.2198). **EA** ($C_{20}H_{30}N_6O_8 \cdot 0.8FA$, M_R = 519.3): C 48.1 (47.6); H 6.2 (6.1); N 16.3 (16.2).

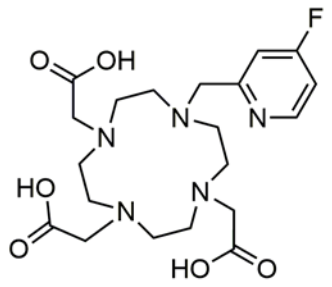

FL^1

Synthesis of ligand FL^1: Solution of **4** (70 mg, 0.48 mmol, 1.02 equiv.) in MeCN (0.7 mL) was added to a solution of *t*-BuDO3A·HBr (281 mg, 0.47 mmol, 1.0 equiv.) in MeCN (9 mL) followed by the addition of dried K_2CO_3 (266 mg, 1.92 mmol, 4 equiv.) and the resulting suspension was stirred for 24 hours at RT. The solids were filtered off and the filtrate was concentrated on a rotary evaporator. Resulting oil was purified on preparative HPLC (C18, H_2O/MeCN gradient with 0.1% FA additive). Fractions containing pure product in the form of *tert*-butyl ester were pooled, evaporated to dryness, and several times co-evaporated with MeOH to remove MeCN. The residue was dissolved in neat TFA (5 mL) and stirred for 16 h at RT. Volatiles were removed on rotary evaporator and the residue was purified on preparative HPLC (C18, H_2O/MeCN gradient with 0.1% TFA additive). Fractions with product were joined and lyophilized to give a product in the form of TFA salt as a white solid. **Yield**: 208 mg (58 %, 2 steps, based on ***t*-BuDO3A**·HBr). **NMR** (D_2O, pH 8): **^{1}H** (600.1 MHz, T = 333 K) δ_H 3.02 (*mc*, m, 4H); 3.13 (*mc*, m, 4H); 3.36 (*mc*, m, 4H); 3.40–3.48 (*mc*, CH_2–COOH, m, 6H); 3.55 (CH_2–COOH, bs, 4H); 3.99 (CH_2–arom, s, 2H); 7.20 (*arom*, ddd, 1H, $^3J_{HF}$ = 8 Hz, $^3J_{HH}$ = 6 Hz, $^4J_{HH}$ = 3 Hz); 7.54 (*arom*, dd, 1H, $^3J_{HF}$ = 10 Hz, $^4J_{HH}$ = 3 Hz); 8.53 (*arom*, dd, 1H, $^4J_{HF}$ = 8 Hz, $^3J_{HH}$ = 6 Hz). **^{13}C{^{1}H}** (150.9 MHz, T = 333 K) δ_C 48.7(*mc*, s); 49.0 (*mc*, s); 51.1 (*mc*, s); 51.9 (*mc*, s); 56.6 (*C*H_2–COOH, s); 56.9 (*C*H_2–COOH, s); 58.3 (*C*H_2–arom, s); 112.2 (*arom*, d, $^2J_{CF}$ = 17 Hz); 113.6 (*arom*, d, $^2J_{CF}$ = 18 Hz); 151.9 (*arom*, d, $^3J_{CF}$ = 8 Hz); 159.3 (*arom*, bs); 169.9 (*arom*, d, $^1J_{CF}$ = 263 Hz); 177.5 (*C*O, s). **^{19}F{^{1}H}** (376.5 MHz, T = 300.0 K) δ_F –99.1 (s). **ESI-HRMS**: 456.2250 $[M+H]^+$ (theor. $[C_{20}H_{31}N_5O_6F_1]^+$ = 456.2253). **EA** ($C_{20}H_{30}F_1N_5O_6$·2.6TFA·0.3H_2O, M_R = 757.3): C 40.0 (39.9); H 4.4 (4.5); N 9.3 (9.1); F 22.1 (22.2).

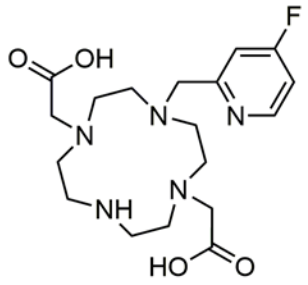

FL²

Synthesis of ligand FL²: Solution of **4** (127 mg, 0.87 mmol, 1.00 equiv.) in MeCN (1 mL) was added to a solution of *t*-BuDO2A (350 mg, 0.87 mmol, 1.0 equiv.) in MeCN (44 mL) followed by the addition of dried K_2CO_3 (121 mg, 0.87 mmol, 1 equiv.) and the resulting suspension was stirred for 24 hours at RT. The solids were filtered off and the filtrate was concentrated on a rotary evaporator. The resulting oil was purified on preparative HPLC (C18, H_2O/MeCN gradient with 0.1% TFA additive). Fractions containing pure product in the form of *tert*-butyl ester were pooled, evaporated to dryness, and several times co-evaporated with MeOH to remove MeCN. The residue was dissolved in neat TFA (5 mL) and stirred for 16 h at RT. Volatiles were removed on a rotary evaporator and the residue was purified on preparative HPLC (C18, H_2O/MeCN gradient with 0.1% TFA additive). Fractions with product were joined and lyophilized to give a product in the form of TFA salt as a white solid. **Yield**: 206 mg (36 %, 2 steps, based on ***t*-BuDO2A**). **NMR** (D_2O): **^{1}H** (500.0 MHz, T = 298.1 K) δ_H 2.96–3.60 (*mc*, CH_2–COOH, m, 20H); 4.70 (CH_2–arom, s, 2H); 7.29 (*arom*, ddd, 1H, $^3J_{HF}$ = 8 Hz, $^3J_{HH}$ = 6 Hz, $^4J_{HH}$ = 3 Hz); 7.34 (*arom*, dd, 1H, $^3J_{HF}$ = 9 Hz, $^4J_{HH}$ = 3 Hz); 8.51 (*arom*, dd, 1H, $^4J_{HF}$ = 8 Hz, $^3J_{HH}$ = 6 Hz). **^{13}C{^{1}H}** (125.7 MHz, T = 298.1 K) δ_C 43.0 (*mc*, s); 49.2 (*mc*, s); 50.0 (*mc*, s); 52.4 (*mc*, s); 54.5 (*C*H_2–COOH, s); 57.8 (*C*H_2–arom, d, $^4J_{CF}$ = 3 Hz); 112.5 (*arom*, d, $^2J_{CF}$ = 19 Hz); 113.5 (*arom*, d, $^2J_{CF}$ = 17 Hz); 152.6 (*arom*, d, $^3J_{CF}$ = 8 Hz); 153.0 (*arom*, d, $^3J_{CF}$ = 8 Hz); 170.3 (*arom*, d, $^1J_{CF}$ = 264 Hz); 174.9 (*C*O, s). **^{19}F{^{1}H}** (376.5 MHz, T = 300.0 K) δ_F –100.1 (s). **ESI-HRMS**: 398.2197 $[M+H]^+$ (theor. $[C_{18}H_{29}N_5O_4F_1]^+$ = 398.2198). **EA** ($C_{18}H_{28}F_1N_5O_4$·2.2TFA·0.9H_2O, M_R = 664.5): C 40.0 (39.9); H 4.4 (4.5); N 9.3 (9.1); F 22.1 (22.2).

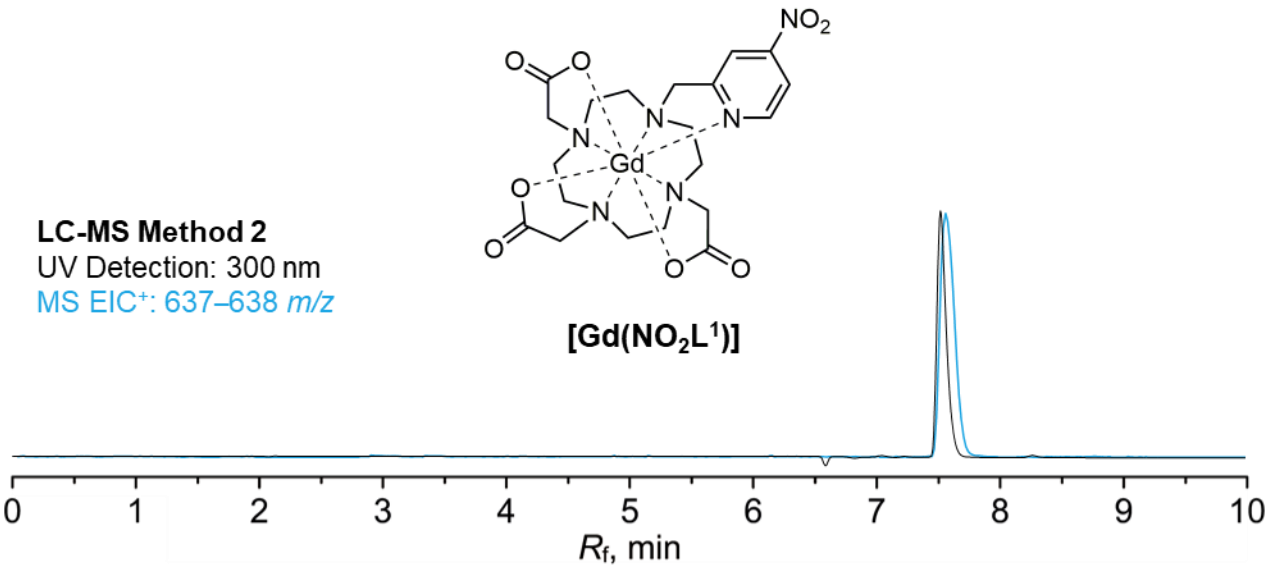

Synthesis and LC-MS chromatogram of [Gd(NO_2L^1)]: In a glass vial (25 mL), **NO_2L^1**·1.8TFA·1.0H_2O (138 mg, 0.20 mmol, 1.0 equiv.) was dissolved in aq. MOPS/NaOH buffer (3M, pH 7.0, 2 mL, 6 mmol, 30 equiv.) followed by the addition of aq. $GdCl_3$ (100 mM, 2.1 mL, 0.21 mmol, 1.05 equiv.) and the resulting solution was stirred at RT for 15 mins. The mixture was then purified by preparative HPLC (C18, H_2O/MeCN gradient with 0.1% FA additive). Fractions with product were joined and lyophilized to give product as a white solid with yellow tint. **Yield:** 111 mg (81%, 1 step, based on **NO_2L^1**·1.8TFA·1.0H_2O). **ESI-HRMS**: 638.1203 $[M+H]^+$ (theor. $[C_{20}H_{28}N_6O_8Gd]^+$ = 638.1204). **EA** ($C_{20}H_{27}N_6O_8Gd$·2.5H_2O, M_R = 687.0): C 35.0 (35.4); H 4.7 (4.4); N 12.2 (11.9); Gd 22.9 (19.4).

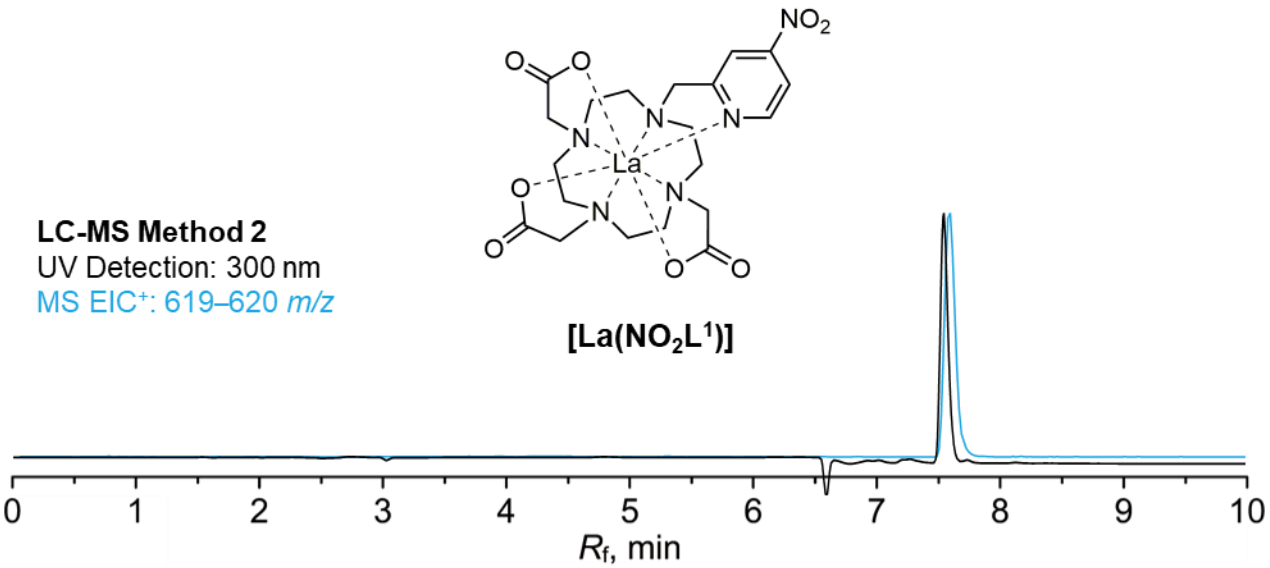

Synthesis and LC-MS chromatogram of [La(NO_2L^1)]: In a glass vial (4 mL), **NO_2L^1**·0.8TFA·0.2FA (10 mg, 17.2 µmol, 1.0 equiv.) was dissolved in aq. MOPS/NaOH buffer (0.5M, pH 7.0, 1032 µL, 516 µmol, 30 equiv.) followed by the addition of aq. $LaCl_3$ (100 mM, 206 µL, 20.6 µmol, 1.2 equiv.) and the resulting solution was stirred at RT for 1 hour. The mixture was then purified by preparative HPLC (C18, H_2O/MeCN gradient with 0.1% FA additive). Fractions with product were joined and lyophilized to give product as a white solid with yellow tint. **Yield:** 12 mg (93 %, 1 step, based on **L^1**·0.8TFA·0.2FA). **ESI-HRMS**: 619.1025 $[M+H]^+$ (theor. $[C_{20}H_{28}N_6O_8La]^+$ = 619.1027). **EA** ($C_{20}H_{27}N_6O_8La$·2.0H_2O·2.0FA, M_R = 746.5): C 35.4 (34.4); H 4.7 (4.2); N 11.3 (11.2); La 18.6 (18.4).

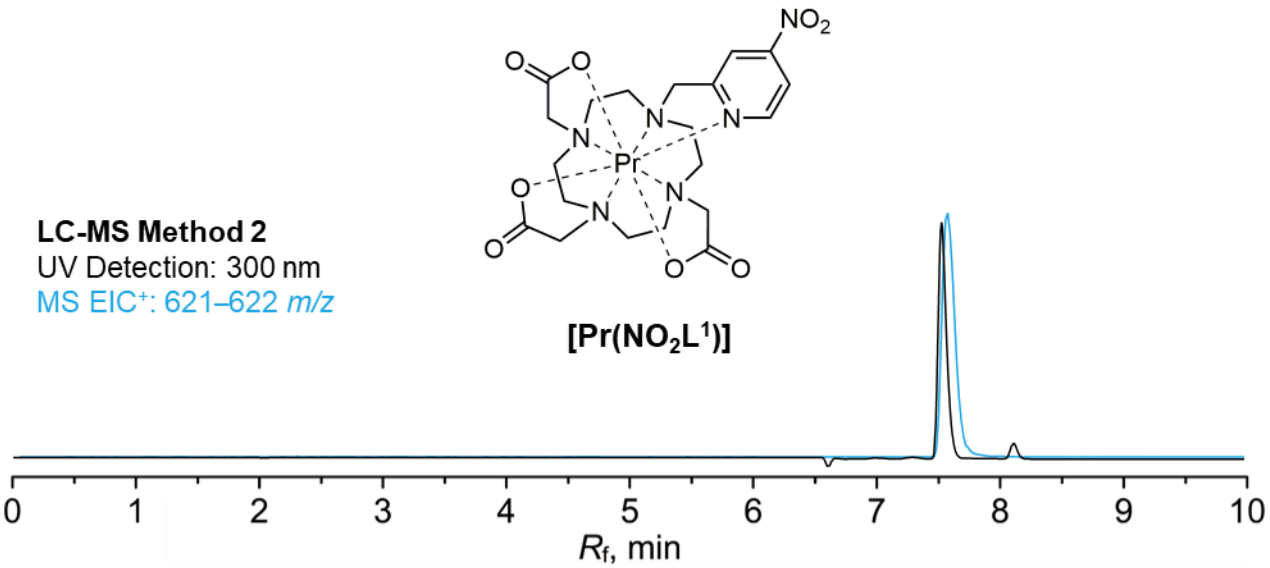

Synthesis and LC-MS chromatogram of [Pr(NO_2L^1)]: In a glass vial (4 mL), **NO_2L^1**·0.8TFA·0.2FA (10 mg, 17.2 µmol, 1.0 equiv.) was dissolved in aq. MOPS/NaOH buffer (0.5M, pH 7.0, 1032 µL, 516 µmol, 30 equiv.) followed by the addition of aq. $PrCl_3$ (100 mM, 206 µL, 20.6 µmol, 1.2 equiv.) and the resulting solution was stirred at RT for 1 hour. The mixture was then purified by preparative HPLC (C18, H_2O/MeCN gradient with 0.1% FA additive). Fractions with product were joined and lyophilized to give product as a white solid with green tint. **Yield:** 10 mg (87 %, 1 step, based on **NO_2L^1**·0.8TFA·0.2FA). **ESI-HRMS**: 643.0860 $[M+Na]^+$ (theor. $[C_{20}H_{27}N_6O_8Na_1Pr_1]^+$ = 643.0859). **EA** ($C_{20}H_{27}N_6O_8Pr_1$·2.0H_2O·0.3FA, M_R = 670.2): C 36.4 (34.8); H 4.8 (4.5); N 12.5 (12.6); Pr 21.0 (19.3).

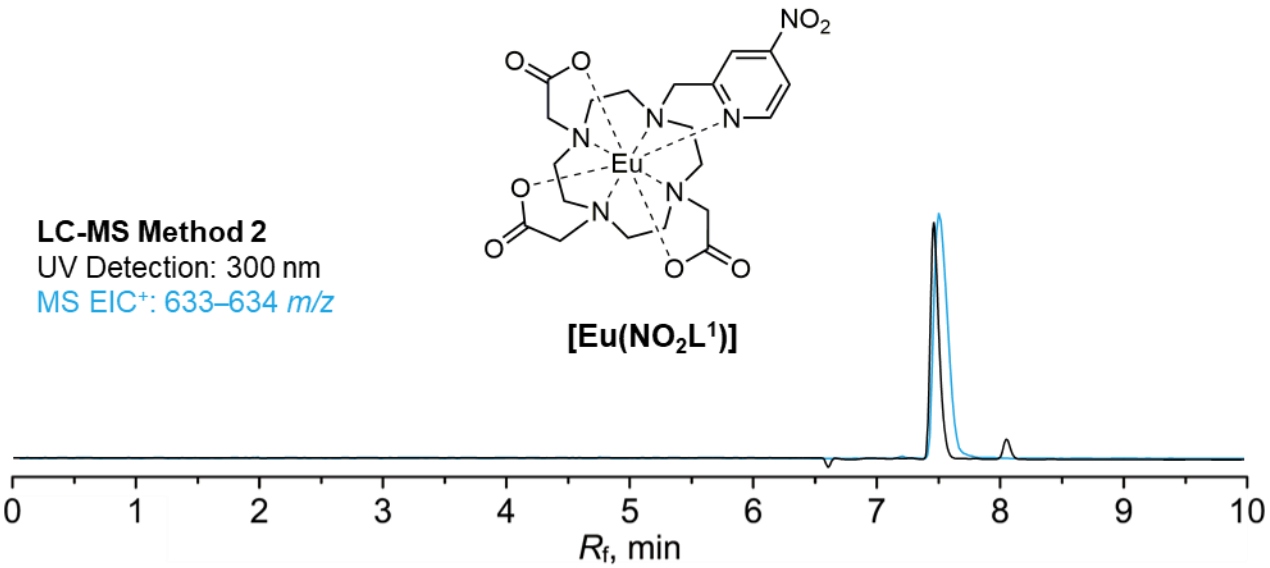

Synthesis and LC-MS chromatogram of [Eu(NO_2L^1)]: In a glass vial (4 mL), $\mathbf{L^1}$·0.8TFA·0.2FA (10 mg, 17.2 µmol, 1.0 equiv.) was dissolved in aq. MOPS/NaOH buffer (0.5M, pH 7.0, 1032 µL, 516 µmol, 30 equiv.) followed by the addition of aq. $EuCl_3$ (100 mM, 206 µL, 20.6 µmol, 1.2 equiv.) and the resulting solution was stirred at RT for 1 hour. The mixture was then purified by preparative HPLC (C18, H_2O/MeCN gradient with 0.1% FA additive). Fractions with product were joined and lyophilized to give product as a white solid with yellow tint. **Yield:** 9.5 mg (77 %, 1 step, based on $\mathbf{L^1}$·0.8TFA·0.2FA). **ESI-HRMS**: 633.1171 $[M+H]^+$ (theor. $[C_{20}H_{28}N_6O_8Eu_1]^+ = 633.1175$). **EA** ($C_{20}H_{27}N_6O_8Eu_1$·2.7$H_2O$·0.9FA, $M_R = 721.5$): C 34.8 (34.6); H 4.8 (4.5); N 11.6 (11.9); Eu 21.1 (20.4).

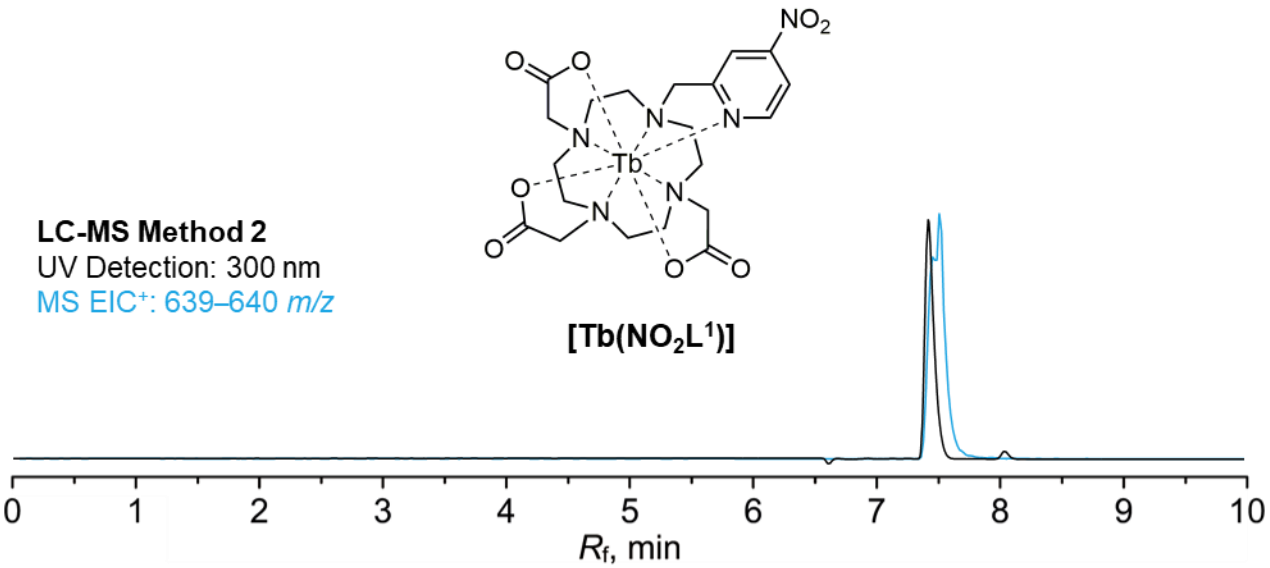

Synthesis and LC-MS chromatogram of [Tb(NO_2L^1)]: In a glass vial (4 mL), **NO_2L^1**·0.8TFA·0.2FA (10 mg, 17.2 µmol, 1.0 equiv.) was dissolved in aq. MOPS/NaOH buffer (0.5M, pH 7.0, 1032 µL, 516 µmol, 30 equiv.) followed by the addition of aq. $TbCl_3$ (100 mM, 206 µL, 20.6 µmol, 1.2 equiv.) and the resulting solution was stirred at RT for 1 hour. The mixture was then purified by preparative HPLC (C18, H_2O/MeCN gradient with 0.1% FA additive). Fractions with product were joined and lyophilized to give product as a white solid with yellow tint. **Yield:** 10 mg (78 %, 1 step, based on **NO_2L^1**·0.8TFA·0.2FA). **ESI-HRMS**: 661.1037 $[M+Na]^+$ (theor. $[C_{20}H_{27}N_6O_8Na_1Tb_1]^+$ = 661.1036). **EA** ($C_{20}H_{27}N_6O_8Tb_1$·2.2H_2O·1.4FA, M_R = 742.5): C 34.6 (34.5); H 4.6 (4.5); N 11.3 (11.4); Tb 21.4 (22.1).

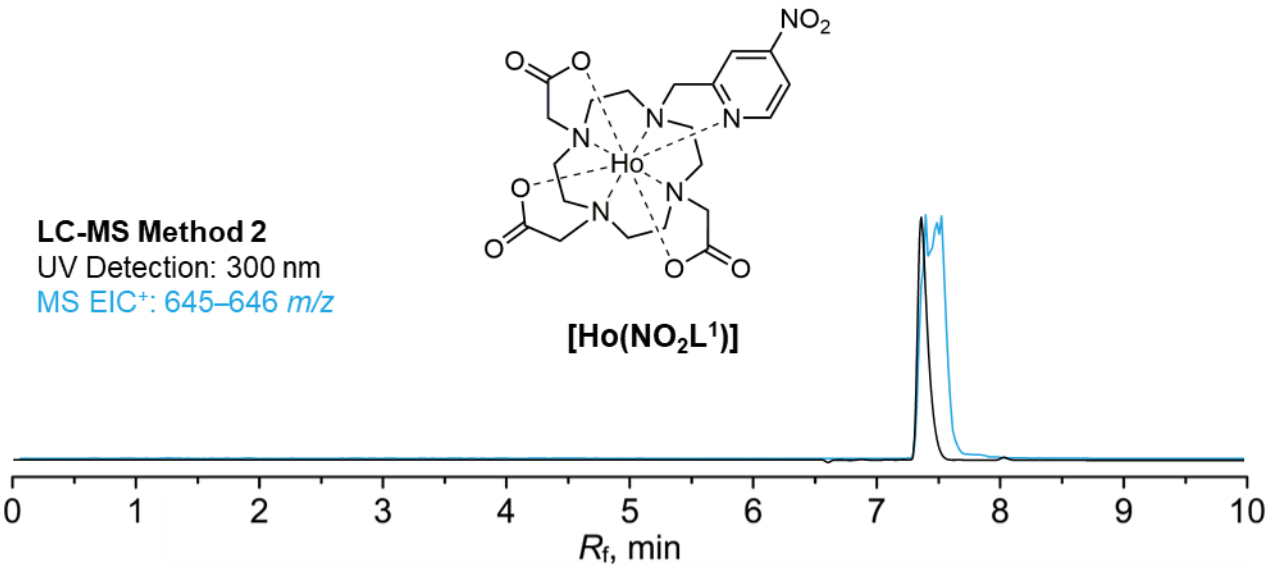

Synthesis and LC-MS chromatogram of [Ho(NO_2L^1)]: In a glass vial (4 mL), **NO_2L^1**·0.8TFA·0.2FA (10 mg, 17.2 µmol, 1.0 equiv.) was dissolved in aq. MOPS/NaOH buffer (0.5M, pH 7.0, 1032 µL, 516 µmol, 30 equiv.) followed by the addition of aq. $HoCl_3$ (100 mM, 206 µL, 20.6 µmol, 1.2 equiv.) and the resulting solution was stirred at RT for 1 hour. The mixture was then purified by preparative HPLC (C18, H_2O/MeCN gradient with 0.1% FA additive). Fractions with product were joined and lyophilized to give product as a pinkish solid. **Yield:** 11 mg (85 %, 1 step, based on **NO_2L^1**·0.8TFA·0.2FA). **ESI-HRMS**: 667.1087 $[M+Na]^+$ (theor. $[C_{20}H_{27}N_6O_8Na_1Ho_1]^+$ = 667.1086). **EA** ($C_{20}H_{27}N_6O_8Ho_1$·1.2H_2O·1.9FA, M_R = 753.5): C 34.9 (34.3); H 4.4 (3.8); N 11.2 (11.8); Ho 21.9 (22.2).

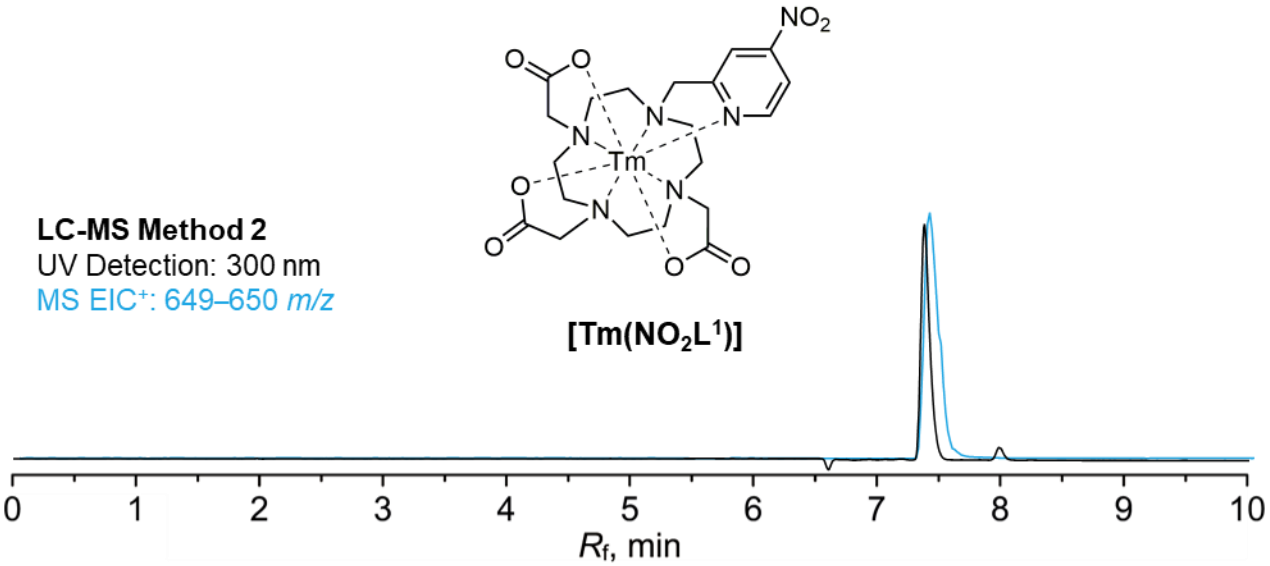

Synthesis and LC-MS chromatogram of [Tm(NO_2L^1)]: In a glass vial (4 mL), NO_2L^1·0.8TFA·0.2FA (10 mg, 17.2 µmol, 1.0 equiv.) was dissolved in aq. MOPS/NaOH buffer (0.5M, pH 7.0, 1032 µL, 516 µmol, 30 equiv.) followed by the addition of aq. $TmCl_3$ (100 mM, 206 µL, 20.6 µmol, 1.2 equiv.) and the resulting solution was stirred at RT for 1 hour. The mixture was then purified by preparative HPLC (C18, H_2O/MeCN gradient with 0.1% FA additive). Fractions with product were joined and lyophilized to give product as a white solid with yellow tint. **Yield:** 9.4 mg (73 %, 1 step, based on NO_2L^1·0.8TFA·0.2FA). **ESI-HRMS**: 671.1123 $[M+Na]^+$ (theor. $[C_{20}H_{27}N_6O_8Na_1Tm_1]^+$ = 671.1125). **EA** ($C_{20}H_{27}N_6O_8Tm_1$·1.8H_2O·1.4FA, M_R = 745.3): C 34.5 (34.2); H 4.5 (4.2); N 11.3 (11.6); Tm 22.7 (22.9).

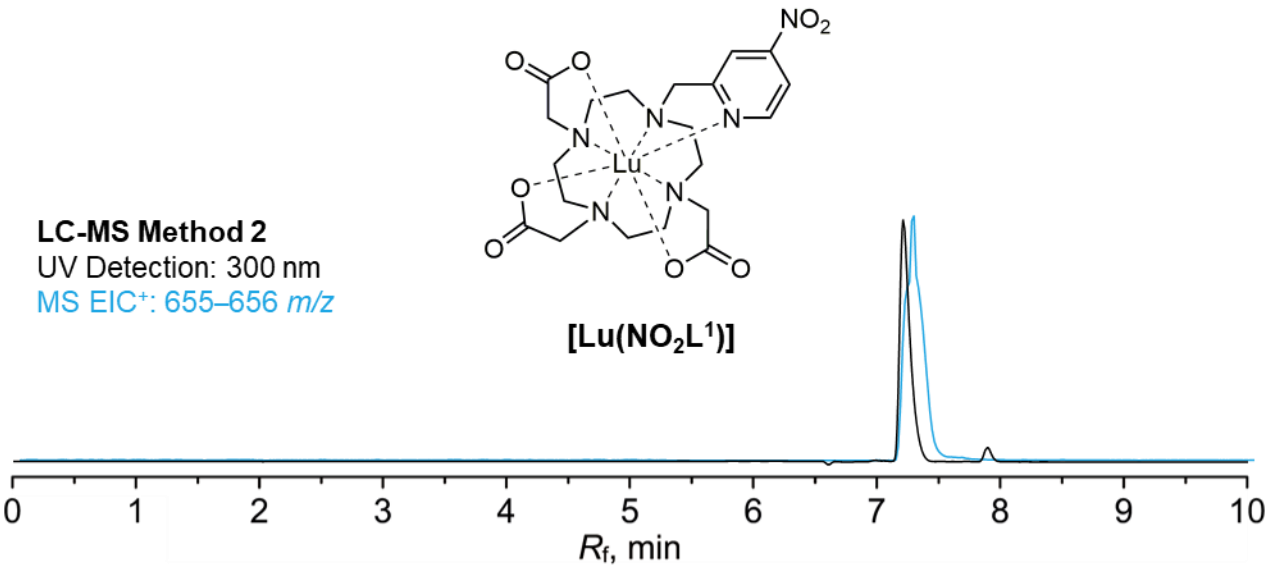

Synthesis and LC-MS chromatogram of [Lu(NO_2L^1)]: In a glass vial (4 mL), **NO_2L^1**·0.8TFA·0.2FA (10 mg, 17.2 µmol, 1.0 equiv.) was dissolved in aq. MOPS/NaOH buffer (0.5M, pH 7.0, 1032 µL, 516 µmol, 30 equiv.) followed by the addition of aq. $LuCl_3$ (100 mM, 206 µL, 20.6 µmol, 1.2 equiv.) and the resulting solution was stirred at RT for 1 hour. The mixture was then purified by preparative HPLC (C18, H_2O/MeCN gradient with 0.1% FA additive). Fractions with product were joined and lyophilized to give product as a white solid with yellow tint. **Yield:** 10 mg (77 %, 1 step, based on **NO_2L^1**·0.8TFA·0.2FA). **ESI-HRMS**: 677.1188 $[M+Na]^+$ (theor. $[C_{20}H_{27}N_6O_8Na_1Lu_1]^+$ = 677.1190). **EA** ($C_{20}H_{27}N_6O_8Lu_1$·1.5H_2O·1.5FA, M_R = 750.5): C 34.4 (34.2); H 4.4 (4.2); N 11.2 (11.4); Lu 23.3 (23.5).

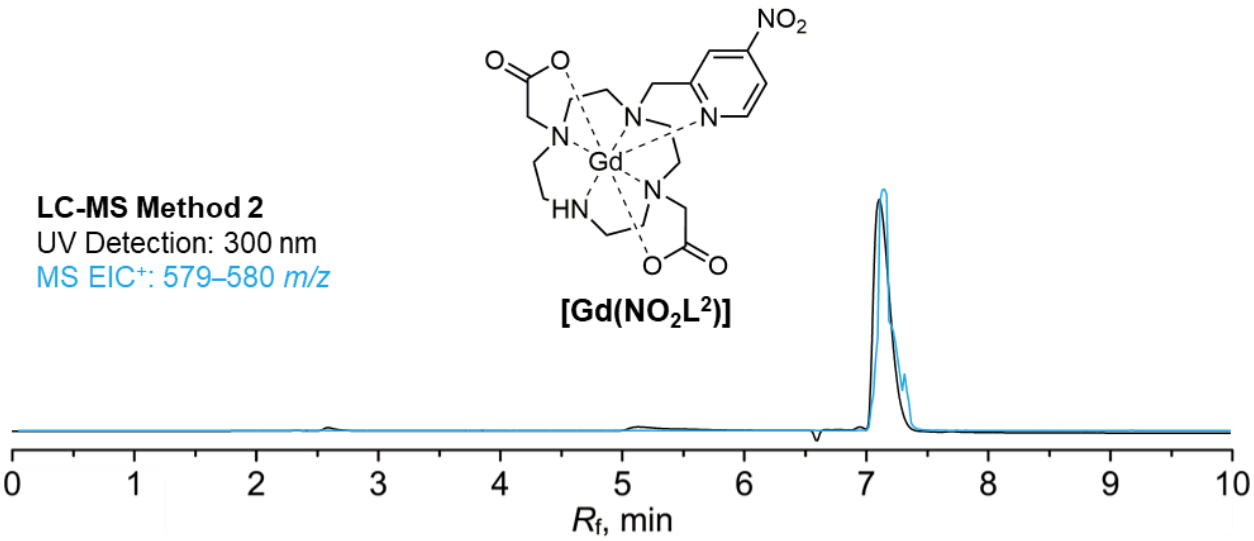

Synthesis and LC-MS chromatogram of [Gd(NO_2L^2)]: In a glass vial (25 mL), **NO_2L^2**·1.7TFA·1.4H_2O (129 mg, 0.20 mmol, 1.0 equiv.) was dissolved in aq. MOPS/NaOH buffer (3M, pH 7.0, 2. mL, 8.02 mmol, 40 equiv.) followed by the addition of aq. $GdCl_3$ (100 mM, 2.2 mL, 0.22 mmol, 1.1 equiv.) and the resulting solution was stirred at RT for 1 hour. The mixture was then purified by preparative HPLC (C18, H_2O/MeCN gradient with 0.1% FA additive). Fractions with product were joined and lyophilized to give a product as a solid with a yellow tint. **Yield:** 92 mg (64 %, 1 step, based on **NO_2L^2**·1.7TFA·1.4H_2O). **ESI-HRMS**: 580.1152 $[M+H]^+$ (theor. $[C_{18}H_{26}N_6O_6Gd_1]^+$ = 580.1149). **EA** ($C_{18}H_{26}N_6O_6Gd_1$·3FA, M_R = 717.8): C 35.1 (34.9); H 4.5 (4.1); N 11.7 (12.1); Gd 21.9 (19.9).

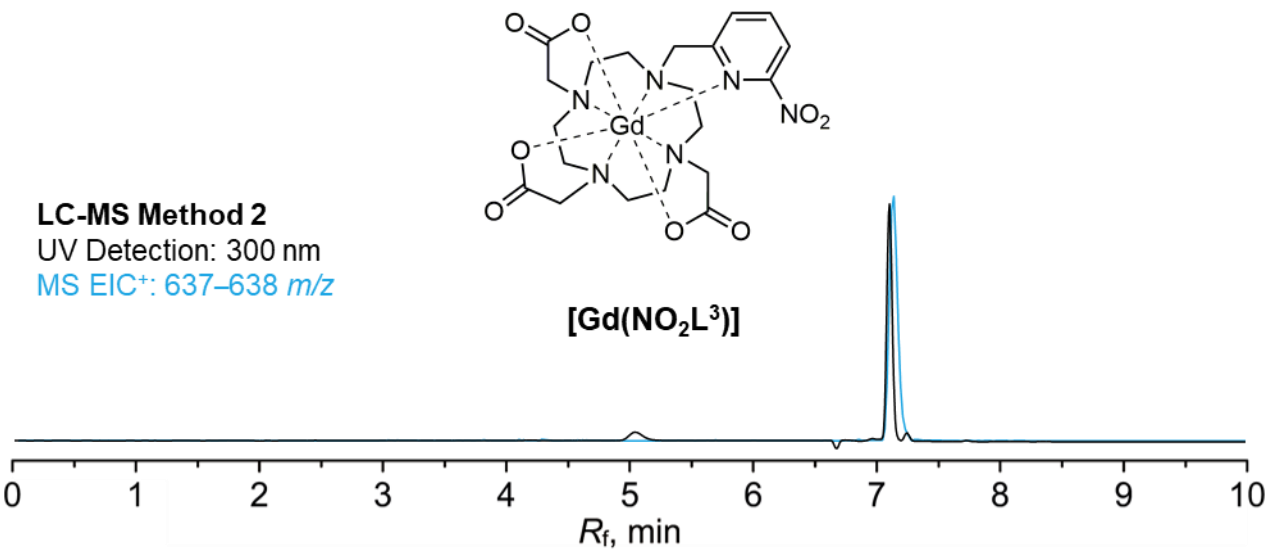

Synthesis and LC-MS chromatogram of [Gd(NO_2L^3)]: In a glass vial (4 mL), **NO_2L^3**·0.8FA (37.4 mg, 71.5 µmol, 1.0 equiv.) was dissolved in aq. MOPS/NaOH buffer (3M, pH 7.0, 0.95 mL, 2.85 mmol, 40 equiv.) followed by the addition of aq. $GdCl_3$ (100 mM, 0.78 mL, 78 µmol, 1.1 equiv.) and the resulting solution was stirred at RT for 1 hour. The mixture was then purified by preparative HPLC (C18, H_2O/MeCN gradient with 0.1% FA additive). Fractions with product were joined and lyophilized to give product as a solid with yellow tint. **Yield:** 33 mg (62 %, 1 step, based on **NO_2L^3**·0.8FA). **ESI-HRMS**: 638.1201 $[M+H]^+$ (theor. $[C_{20}H_{28}N_6O_8Gd]^+$ = 638.1204). **EA** ($C_{20}H_{27}N_6O_8Gd$·2.1FA·1.4H_2O, M_R = 758.6): C 35.0 (34.9); H 4.5 (4.4); N 11.1 (11.2); Gd 20.7 (20.8).

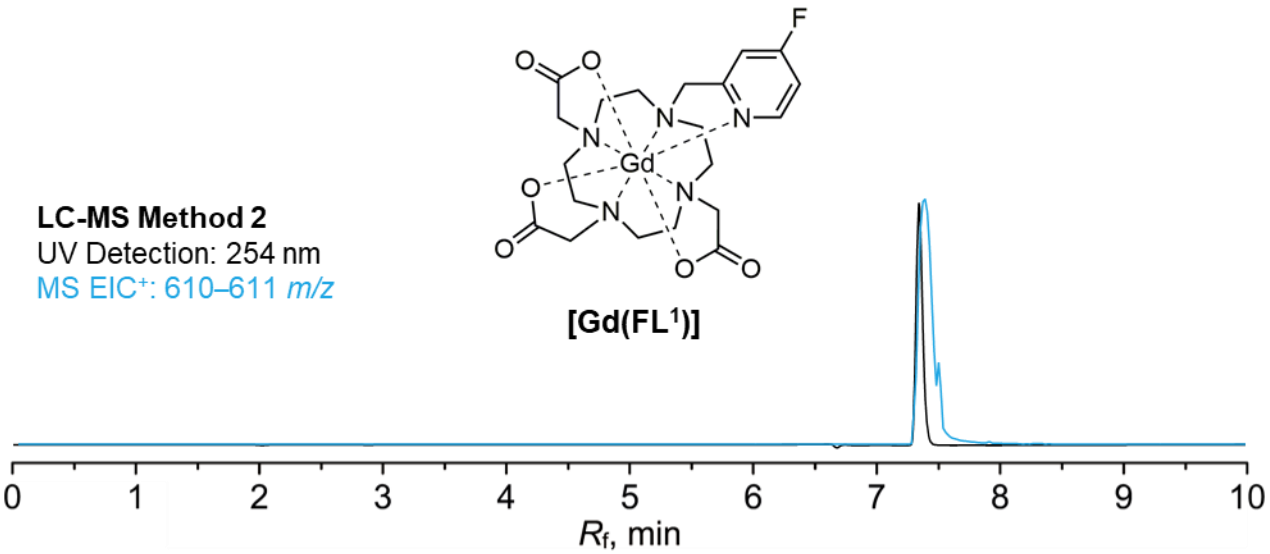

Synthesis and LC-MS chromatogram of [Gd(FL^1)]: In a glass vial (25 mL), **FL^1**·2.6TFA·0.3H_2O (156 mg, 0.21 mmol, 1.0 equiv.) was dissolved in aq. MOPS/NaOH buffer (3M, pH 7.0, 1.9 mL, 5.8 mmol, 28 equiv.) followed by the addition of aq. $GdCl_3$ (100 mM, 2.16 mL, 0.22 mmol, 1.05 equiv.) and the resulting solution was stirred at RT for 15 mins. The mixture was then purified by preparative HPLC (C18, H_2O/MeCN gradient with 0.1% FA additive). Fractions with product were joined and lyophilized to give product as a white solid. **Yield:** 82 mg (59 %, 1 step, based on **FL^1**·2.6TFA·0.3H_2O). **ESI-HRMS**: 611.1275 $[M+H]^+$ (theor. $[C_{20}H_{28}N_5O_6Gd_1F_1]^+$ = 611.1259). **EA** ($C_{20}H_{27}N_5O_6Gd_1F_1$·2.5$H_2O$, M_R = 654.7): C 36.7 (36.2); H 4.9 (5.0); N 10.7 (10.5); Gd 24.0 (19.8); F 2.9 (2.8).

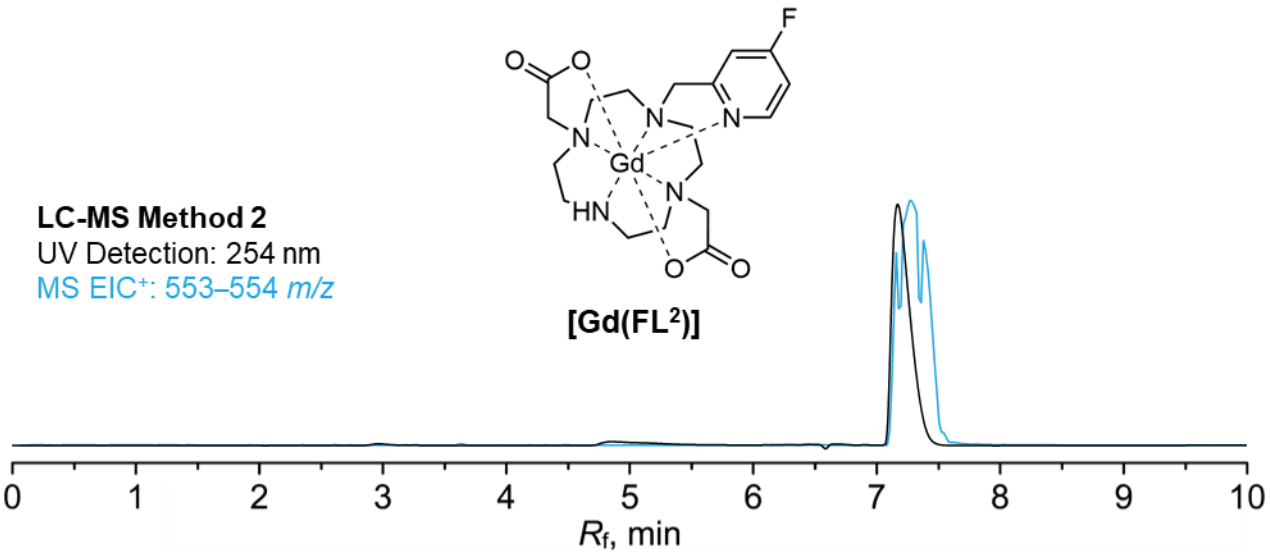

Synthesis and LC-MS chromatogram of [Gd(FL^2)]: In a glass vial (25 mL), **FL^2**·2.2TFA·0.9H_2O (152 mg, 0.22 mmol, 1.0 equiv.) was dissolved in aq. MOPS/NaOH buffer (3M, pH 7.0, 1.64 mL, 4.9 mmol, 21 equiv.) followed by the addition of aq. $GdCl_3$ (100 mM, 2.34 mL, 0.23 mmol, 1.05 equiv.) and the resulting solution was stirred at RT for 15 mins. The mixture was then purified by preparative HPLC (C18, H_2O/MeCN gradient with 0.1% FA additive). Fractions with product were joined and lyophilized to give product as a white solid. **Yield:** 116 mg (77 %, 1 step, based on **FL^2**·2.2TFA·0.9H_2O). **ESI-HRMS**: 553.1214 $[M+H]^+$ (theor. $[C_{18}H_{26}N_5O_4Gd_1F_1]^+$ = 553.1204). **EA** ($C_{18}H_{26}N_5O_4Gd_1F_1$·3.1$H_2O$, M_R = 681.2): C 33.9 (34.5); H 4.7 (4.5); N 10.3 (9.9); Gd 23.1 (19.6); F 7.8 (7.4).

6 CITED LITERATURE

(1) Rosenberg, B.; Vancamp, L.; Trosko, J. E.; Mansour, V. H. Platinum Compounds: A New Class of Potent Antitumour Agents. *Nature* **1969**, *222* (5191), 385–386. https://doi.org/10.1038/222385a0.

(2) Wyllie, S.; Cunningham, M. L.; Fairlamb, A. H. Dual Action of Antimonial Drugs on Thiol Redox Metabolism in the Human Pathogen Leishmania Donovani*. *Journal of Biological Chemistry* **2004**, *279* (38), 39925–39932. https://doi.org/10.1074/jbc.M405635200.

(3) Noweski, A.; Roosen, A.; Lebdai, S.; Barret, E.; Emberton, M.; Benzaghou, F.; Apfelbeck, M.; Gaillac, B.; Gratzke, C.; Stief, C.; Azzouzi, A. R. Medium-Term Follow-up of Vascular-Targeted Photodynamic Therapy of Localized Prostate Cancer Using TOOKAD Soluble WST-11 (Phase II Trials). *European Urology Focus* **2019**, *5* (6), 1022–1028. https://doi.org/10.1016/j.euf.2018.04.003.

(4) Hottinger, D. G.; Beebe, D. S.; Kozhimannil, T.; Prielipp, R. C.; Belani, K. G. Sodium Nitroprusside in 2014: A Clinical Concepts Review. *J Anaesthesiol Clin Pharmacol* **2014**, *30* (4), 462–471. https://doi.org/10.4103/0970-9185.142799.

(5) Kim, N.-H.; Oh, M.-K.; Park, H. J.; Kim, I.-S. Auranofin, a Gold(I)-Containing Antirheumatic Compound, Activates Keap1/Nrf2 Signaling via Rac1/INOS Signal and Mitogen-Activated Protein Kinase Activation. *Journal of Pharmacological Sciences* **2010**, *113* (3), 246–254. https://doi.org/10.1254/jphs.09330FP.

(6) Sgouros, G.; Bodei, L.; McDevitt, M. R.; Nedrow, J. R. Radiopharmaceutical Therapy in Cancer: Clinical Advances and Challenges. *Nat Rev Drug Discov* **2020**, *19* (9), 589–608. https://doi.org/10.1038/s41573-020-0073-9.

(7) Grillo-López, A. J. Zevalin: The First Radioimmunotherapy Approved for the Treatment of Lymphoma. *Expert Review of Anticancer Therapy* **2002**, *2* (5), 485–493. https://doi.org/10.1586/14737140.2.5.485.

(8) Kulik, L. M.; Atassi, B.; van Holsbeeck, L.; Souman, T.; Lewandowski, R. J.; Mulcahy, M. F.; Hunter, R. D.; Nemcek Jr., A. A.; Abecassis, M. M.; Haines III, K. G.; Salem, R. Yttrium-90 Microspheres (TheraSphere®) Treatment of Unresectable Hepatocellular Carcinoma: Downstaging to Resection, RFA and Bridge to Transplantation. *Journal of Surgical Oncology* **2006**, *94* (7), 572–586. https://doi.org/10.1002/jso.20609.

(9) Hennrich, U.; Kopka, K. Lutathera®: The First FDA- and EMA-Approved Radiopharmaceutical for Peptide Receptor Radionuclide Therapy. *Pharmaceuticals* **2019**, *12* (3), 114. https://doi.org/10.3390/ph12030114.

(10) Gupta, R.; Hashmi, M. F. Mo99 - Tc99m Generator. In *StatPearls*; StatPearls Publishing: Treasure Island (FL), 2022.

(11) Kane, S. M.; Davis, D. D. Technetium-99m. In *StatPearls*; StatPearls Publishing: Treasure Island (FL), 2022.

(12) Lavender, J. P.; Lowe, J.; Barker, J. R.; Burn, J. I.; Chaudhri, M. A. Gallium 67 Citrate Scanning in Neoplastic and Inflammatory Lesions. *BJR* **1971**, *44* (521), 361–366. https://doi.org/10.1259/0007-1285-44-521-361.

(13) Franz, K. J.; Metzler-Nolte, N. Introduction: Metals in Medicine. *Chem. Rev.* **2019**, *119* (2), 727–729. https://doi.org/10.1021/acs.chemrev.8b00685.

(14) Moeller, T. Periodicity and the Lanthanides and Actinides. *J. Chem. Educ.* **1970**, *47* (6), 417. https://doi.org/10.1021/ed047p417.

(15) Bünzli, J.-C. G. Benefiting from the Unique Properties of Lanthanide Ions. *Acc. Chem. Res.* **2006**, *39* (1), 53–61. https://doi.org/10.1021/ar0400894.

(16) *Rare Earth Coordination Chemistry: Fundamentals and Applications*; Huang, C.-H., Ed.; John Wiley& Sons: Singapore ; Hoboken, NJ, 2010.

(17) Jakupec, M. A.; Unfried, P.; Keppler, B. K. Pharmacological Properties of Cerium Compunds. In *Reviews of Physiology, Biochemistry and Pharmacology*; Reviews of Physiology, Biochemistry and Pharmacology; Springer: Berlin, Heidelberg, 2005; pp 101–111. https://doi.org/10.1007/s10254-004-0024-6.

(18) Krief, A.; Laval, A.-M. Coupling of Organic Halides with Carbonyl Compounds Promoted by SmI2, the Kagan Reagent. *Chem. Rev.* **1999**, *99* (3), 745–778. https://doi.org/10.1021/cr980326e.

(19) Molander, G. A. Application of Lanthanide Reagents in Organic Synthesis. *Chem. Rev.* **1992**, *92* (1), 29–68. https://doi.org/10.1021/cr00009a002.

(20) Pol, A.; Barends, T. R. M.; Dietl, A.; Khadem, A. F.; Eygensteyn, J.; Jetten, M. S. M.; Op den Camp, H. J. M. Rare Earth Metals Are Essential for Methanotrophic Life in Volcanic Mudpots. *Environmental Microbiology* **2014**, *16* (1), 255–264. https://doi.org/10.1111/1462-2920.12249.

(21) Penfield, J. G.; Reilly, R. F. What Nephrologists Need to Know about Gadolinium. *Nat Rev Nephrol* **2007**, *3* (12), 654–668. https://doi.org/10.1038/ncpneph0660.

(22) Tweedle, M. F.; Hagan, J. J.; Kumar, K.; Mantha, S.; Chang, C. A. Reaction of Gadolinium Chelates with Endogenously Available Ions. *Magnetic Resonance Imaging* **1991**, *9* (3), 409–415. https://doi.org/10.1016/0730-725X(91)90429-P.

(23) Bellin, M.-F.; Van Der Molen, A. J. Extracellular Gadolinium-Based Contrast Media: An Overview. *European Journal of Radiology* **2008**, *66* (2), 160–167. https://doi.org/10.1016/j.ejrad.2008.01.023.

(24) Morcos, S. K. Extracellular Gadolinium Contrast Agents: Differences in Stability. *European Journal of Radiology* **2008**, *66* (2), 175–179. https://doi.org/10.1016/j.ejrad.2008.01.025.

(25) Port, M.; Idée, J.-M.; Medina, C.; Robic, C.; Sabatou, M.; Corot, C. Efficiency, Thermodynamic and Kinetic Stability of Marketed Gadolinium Chelates and Their Possible Clinical Consequences: A Critical Review. *Biometals* **2008**, *21* (4), 469–490. https://doi.org/10.1007/s10534-008-9135-x.

(26) Richman, J. E.; Atkins, T. J. Nitrogen Analogs of Crown Ethers. *Journal of the American Chemical Society* **1974**, 3.

(27) Krause, W. *Contrast Agents I: Magnetic Resonance Imaging*; Springer, 2003.

(28) Jagadish, B.; Brickert-Albrecht, G. L.; Nichol, G. S.; Mash, E. A.; Raghunand, N. On the Synthesis of 1,4,7-Tris(Tert-Butoxycarbonylmethyl)-1,4,7,10-Tetraazacyclododecane. *Tetrahedron Letters* **2011**, *52* (17), 2058–2061. https://doi.org/10.1016/j.tetlet.2010.10.074.

(29) Hopper, L. E.; Allen, M. J. Rapid Synthesis of 1,7-Bis(t-Butoxycarbonylmethyl)-1,4,7,10-Tetraazacyclododecane (DO2A-t-Bu Ester). *Tetrahedron Letters* **2014**, *55* (40), 5560–5561. https://doi.org/10.1016/j.tetlet.2014.08.026.

(30) Li, C.; Wong, W.-T. A Simple, Regioselective Synthesis of 1,4-Bis(Tert-Butoxycarbonylmethyl)-Tetraazacyclododecane. *J. Org. Chem.* **2003**, *68* (7), 2956–2959. https://doi.org/10.1021/jo026436+.

(31) Kalender, W. A. X-Ray Computed Tomography. *Phys. Med. Biol.* **2006**, *51* (13), R29–R43. https://doi.org/10.1088/0031-9155/51/13/R03.

(32) Carovac, A.; Smajlovic, F.; Junuzovic, D. Application of Ultrasound in Medicine. *Acta Inform Med* **2011**, *19* (3), 168–171. https://doi.org/10.5455/aim.2011.19.168-171.

(33) Ross, T. L.; Ametamey, S. M. PET Chemistry: An Introduction. In *Basic Sciences of Nuclear Medicine*; Khalil, M. M., Ed.; Springer International Publishing: Cham, 2021; pp 131–176. https://doi.org/10.1007/978-3-030-65245-6_7.

(34) Thompson, C. M.; Gerdes, J. M.; VanBrocklin, H. F. Positron Emission Tomography Studies of Organophosphate Chemical Threats and Oxime Countermeasures. *Neurobiology of Disease* **2020**, *133*, 104455. https://doi.org/10.1016/j.nbd.2019.04.011.

(35) Wahsner, J.; Gale, E. M.; Rodríguez-Rodríguez, A.; Caravan, P. Chemistry of MRI Contrast Agents: Current Challenges and New Frontiers. *Chem. Rev.* **2019**, *119* (2), 957–1057. https://doi.org/10.1021/acs.chemrev.8b00363.

(36) Boros, E.; Packard, A. B. Radioactive Transition Metals for Imaging and Therapy. *Chem. Rev.* **2019**, *119* (2), 870–901. https://doi.org/10.1021/acs.chemrev.8b00281.

(37) Huettel, S. A.; Song, A. W.; McCarthy, G. *Functional Magnetic Resonance Imaging*, 2nd ed.; Sinauer Associates, 2009.

(38) Salsano, M.; Treglia, G. PET Imaging Using Radiolabelled Antibodies: Future Direction in Tumor Diagnosis and Correlate Applications. *RRNM* **2013**, *3*, 9–17. https://doi.org/10.2147/RRNM.S35186.

(39) Kumar, R.; Alavi, A. Clinical Applications of Fluorodeoxyglucose--Positron Emission Tomography in the Management of Malignant Melanoma. *Curr Opin Oncol* **2005**, *17* (2), 154–159. https://doi.org/10.1097/01.cco.0000152626.98124.3a.

(40) Pacák, J.; Točík, Z.; Černý, M. Synthesis of 2-Deoxy-2-Fluoro-D-Glucose. *J. Chem. Soc. D* **1969**, No. 2, 77–77. https://doi.org/10.1039/C29690000077.

(41) Lee, C. S.; Samii, A.; Sossi, V.; Ruth, T. J.; Schulzer, M.; Holden, J. E.; Wudel, J.; Pal, P. K.; De La Fuente-Fernandez, R.; Calne, D. B.; Stoessl, A. J. In Vivo Positron Emission Tomographic Evidence for Compensatory Changes in Presynaptic Dopaminergic Nerve Terminals in Parkinson's Disease. *Annals of Neurology* **2000**, *47* (4), 493–503. https://doi.org/10.1002/1531-8249(200004)47:4<493::AID-ANA13>3.0.CO;2-4.

(42) Künig, G.; Leenders, K. L.; Sanchez-Pernaute, R.; Antonini, A.; Vontobel, P.; Verhagen, A.; Günther, I. Benzodiazepine Receptor Binding in Huntington's Disease: [11C]Flumazenil Uptake Measured Using Positron Emission Tomography. *Annals of Neurology* **2000**, *47* (5), 644–648. https://doi.org/10.1002/1531-8249(200005)47:5<644::AID-ANA13>3.0.CO;2-C.

(43) Volkow, N. D.; Wang, G.-J.; Telang, F.; Fowler, J. S.; Logan, J.; Wong, C.; Ma, J.; Pradhan, K.; Tomasi, D.; Thanos, P. K.; Ferré, S.; Jayne, M. Sleep Deprivation Decreases Binding of [11C]Raclopride to Dopamine D2/D3 Receptors in the Human Brain. *J. Neurosci.* **2008**, *28* (34), 8454–8461. https://doi.org/10.1523/JNEUROSCI.1443-08.2008.

(44) Falk Delgado, A.; Falk Delgado, A. Discrimination between Primary Low-Grade and High-Grade Glioma with 11C-Methionine PET: A Bivariate Diagnostic Test Accuracy Meta-Analysis. *BJR* **2018**, *91* (1082), 20170426. https://doi.org/10.1259/bjr.20170426.

(45) Wang, J.; Li, J.; Li, S.; Hsu, B. Absolute Resting 13N-Ammonia PET Myocardial Blood Flow for Predicting Myocardial Viability and Recovery of Ventricular Function after Coronary Artery Bypass Grafting. *J. Nucl. Cardiol.* **2020**. https://doi.org/10.1007/s12350-020-02388-7.

(46) Coles, J. P.; Fryer, T. D.; Smielewski, P.; Rice, K.; Clark, J. C.; Pickard, J. D.; Menon, D. K. Defining Ischemic Burden after Traumatic Brain Injury Using 15O PET Imaging of Cerebral Physiology. *J Cereb Blood Flow Metab* **2004**, *24* (2), 191–201. https://doi.org/10.1097/01.WCB.0000100045.07481.DE.

(47) Rohren, E. M.; Turkington, T. G.; Coleman, R. E. Clinical Applications of PET in Oncology. *Radiology* **2004**, *231* (2), 305–332. https://doi.org/10.1148/radiol.2312021185.

(48) Conti, M.; Eriksson, L. Physics of Pure and Non-Pure Positron Emitters for PET: A Review and a Discussion. *EJNMMI Physics* **2016**, *3* (1), 8. https://doi.org/10.1186/s40658-016-0144-5.

(49) Maurer, T.; Eiber, M.; Schwaiger, M.; Gschwend, J. E. Current Use of PSMA–PET in Prostate Cancer Management. *Nat Rev Urol* **2016**, *13* (4), 226–235. https://doi.org/10.1038/nrurol.2016.26.

(50) Kumar, K. The Current Status of the Production and Supply of Gallium-68. *Cancer Biotherapy and Radiopharmaceuticals* **2020**, *35* (3), 163–166. https://doi.org/10.1089/cbr.2019.3301.

(51) Hennrich, U.; Benešová, M. [68Ga]Ga-DOTA-TOC: The First FDA-Approved 68Ga-Radiopharmaceutical for PET Imaging. *Pharmaceuticals* **2020**, *13* (3), 38. https://doi.org/10.3390/ph13030038.

(52) Sanli, Y.; Garg, I.; Kandathil, A.; Kendi, T.; Zanetti, M. J. B.; Kuyumcu, S.; Subramaniam, R. M. Neuroendocrine Tumor Diagnosis and Management: 68Ga-DOTATATE PET/CT. *American Journal of Roentgenology* **2018**, *211* (2), 267–277. https://doi.org/10.2214/AJR.18.19881.

(53) Al-Tamimi, M.; Sulong, G. Tumor Brain Detection Through MR Images: A Review of Literature. *Journal of Theoretical and Applied Information Technology* **2014**, *62*.

(54) Holdsworth, S. J.; Bammer, R. Magnetic Resonance Imaging Techniques: FMRI, DWI, and PWI. *Semin Neurol* **2008**, *28* (4), 395–406. https://doi.org/10.1055/s-0028-1083697.

(55) Pagani, E.; Bizzi, A.; Di Salle, F.; De Stefano, N.; Filippi, M. Basic Concepts of Advanced MRI Techniques. *Neurol Sci* **2008**, *29* (S3), 290–295. https://doi.org/10.1007/s10072-008-1001-7.

(56) Baird, A. E.; Warach, S. Magnetic Resonance Imaging of Acute Stroke. *J Cereb Blood Flow Metab* **1998**, *18* (6), 583–609. https://doi.org/10.1097/00004647-199806000-00001.

(57) Biffar, A.; Dietrich, O.; Sourbron, S.; Duerr, H.-R.; Reiser, M. F.; Baur-Melnyk, A. Diffusion and Perfusion Imaging of Bone Marrow. *European Journal of Radiology* **2010**, *76* (3), 323–328. https://doi.org/10.1016/j.ejrad.2010.03.011.

(58) Jones, K. M.; Pollard, A. C.; Pagel, M. D. Clinical Applications of Chemical Exchange Saturation Transfer (CEST) MRI. *Journal of Magnetic Resonance Imaging* **2018**, *47* (1), 11–27. https://doi.org/10.1002/jmri.25838.

(59) Wang, Z. J.; Ohliger, M. A.; Larson, P. E. Z.; Gordon, J. W.; Bok, R. A.; Slater, J.; Villanueva-Meyer, J. E.; Hess, C. P.; Kurhanewicz, J.; Vigneron, D. B. Hyperpolarized 13C MRI: State of the Art and Future Directions. *Radiology* **2019**, *291* (2), 273–284. https://doi.org/10.1148/radiol.2019182391.

(60) Essig, M.; Dinkel, J.; Gutierrez, J. E. Use of Contrast Media in Neuroimaging. *Magn Reson Imaging Clin N Am* **2012**, *20* (4), 633–648. https://doi.org/10.1016/j.mric.2012.08.001.

(61) Ellis, K. J. Human Body Composition: In Vivo Methods. *Physiological Reviews* **2000**, *80* (2), 649–680. https://doi.org/10.1152/physrev.2000.80.2.649.

(62) Jeon, M.; Halbert, M. V.; Stephen, Z. R.; Zhang, M. Iron Oxide Nanoparticles as T1 Contrast Agents for Magnetic Resonance Imaging: Fundamentals, Challenges, Applications, and Prospectives. *Advanced Materials* **2021**, *33* (23), 1906539. https://doi.org/10.1002/adma.201906539.

(63) Angelovski, G.; Tóth, É. Strategies for Sensing Neurotransmitters with Responsive MRI Contrast Agents. *Chem. Soc. Rev.* **2017**, *46* (2), 324–336. https://doi.org/10.1039/C6CS00154H.

(64) Bonnet, C. S. Zn2+ Detection by MRI Using Ln3+-Based Complexes: The Central Role of Coordination Chemistry. *Coordination Chemistry Reviews* **2018**, *369*, 91–104. https://doi.org/10.1016/j.ccr.2018.04.019.

(65) Malikidogo, K. P.; Martin, H.; Bonnet, C. S. From Zn(II) to Cu(II) Detection by MRI Using Metal-Based Probes: Current Progress and Challenges. *Pharmaceuticals* **2020**, *13* (12), 436. https://doi.org/10.3390/ph13120436.

(66) Li, W.; Fraser, S. E.; Meade, T. J. A Calcium-Sensitive Magnetic Resonance Imaging Contrast Agent. *J. Am. Chem. Soc.* **1999**, *121* (6), 1413–1414. https://doi.org/10.1021/ja9837021.

(67) Yu, J.; Martins, A. F.; Preihs, C.; Clavijo Jordan, V.; Chirayil, S.; Zhao, P.; Wu, Y.; Nasr, K.; Kiefer, G. E.; Sherry, A. D. Amplifying the Sensitivity of Zinc(II) Responsive MRI Contrast Agents by Altering Water Exchange Rates. *J. Am. Chem. Soc.* **2015**, *137* (44), 14173–14179. https://doi.org/10.1021/jacs.5b09158.

(68) Lowe, M. P.; Parker, D.; Reany, O.; Aime, S.; Botta, M.; Castellano, G.; Gianolio, E.; Pagliarin, R. PH-Dependent Modulation of Relaxivity and Luminescence in Macrocyclic Gadolinium and Europium Complexes Based on Reversible Intramolecular Sulfonamide Ligation. *J. Am. Chem. Soc.* **2001**, *123* (31), 7601–7609. https://doi.org/10.1021/ja0103647.

(69) Zhang, S.; Wu, K.; Sherry, A. D. A Novel PH-Sensitive MRI Contrast Agent. *Angewandte Chemie International Edition* **1999**, *38* (21), 3192–3194. https://doi.org/10.1002/(SICI)1521-3773(19991102)38:21<3192::AID-ANIE3192>3.0.CO;2-#.

(70) Duimstra, J. A.; Femia, F. J.; Meade, T. J. A Gadolinium Chelate for Detection of β-Glucuronidase: A Self-Immolative Approach. *J. Am. Chem. Soc.* **2005**, *127* (37), 12847–12855. https://doi.org/10.1021/ja042162r.

(71) Lilley, L. M.; Kamper, S.; Caldwell, M.; Chia, Z. K.; Ballweg, D.; Vistain, L.; Krimmel, J.; Mills, T. A.; MacRenaris, K.; Lee, P.; Waters, E. A.; Meade, T. J. Self-Immolative Activation of β-Galactosidase-Responsive Probes for In Vivo MR Imaging in Mouse Models. *Angewandte Chemie International Edition* **2020**, *59* (1), 388–394. https://doi.org/10.1002/anie.201909933.

(72) Tu, C.; Osborne, E. A.; Louie, A. Y. Synthesis and Characterization of a Redox- and Light-Sensitive MRI Contrast Agent. *Tetrahedron* **2009**, *65* (7), 1241–1246. https://doi.org/10.1016/j.tet.2008.12.020.

(73) Iwaki, S.; Hanaoka, K.; Piao, W.; Komatsu, T.; Ueno, T.; Terai, T.; Nagano, T. Development of Hypoxia-Sensitive Gd3+-Based MRI Contrast Agents. *Bioorganic & Medicinal Chemistry Letters* **2012**, *22* (8), 2798–2802. https://doi.org/10.1016/j.bmcl.2012.02.071.

(74) Terreno, E.; Botta, M.; Boniforte, P.; Bracco, C.; Milone, L.; Mondino, B.; Uggeri, F.; Aime, S. A Multinuclear NMR Relaxometry Study of Ternary Adducts Formed between Heptadentate GdIII Chelates and L-Lactate. *Chemistry – A European Journal* **2005**, *11* (19), 5531–5537. https://doi.org/10.1002/chem.200500129.

(75) Wang, G.; Angelovski, G. Highly Potent MRI Contrast Agent Displaying Outstanding Sensitivity to Zinc Ions. *Angewandte Chemie International Edition* **2021**, *60* (11), 5734–5738. https://doi.org/10.1002/anie.202014431.

(76) Henriksen, O. M.; Marner, L.; Law, I. Clinical PET/MR Imaging in Dementia and Neuro-Oncology. *PET Clinics* **2016**, *11* (4), 441–452. https://doi.org/10.1016/j.cpet.2016.05.003.

(77) Nensa, F.; Beiderwellen, K.; Heusch, P.; Wetter, A. Clinical Applications of PET/MRI: Current Status and Future Perspectives. *Diagn Interv Radiol* **2014**, *20* (5), 438–447. https://doi.org/10.5152/dir.2014.14008.

(78) Martin, O.; Schaarschmidt, B. M.; Kirchner, J.; Suntharalingam, S.; Grueneisen, J.; Demircioglu, A.; Heusch, P.; Quick, H. H.; Forsting, M.; Antoch, G.; Herrmann, K.; Umutlu, L. PET/MRI Versus PET/CT for Whole-Body Staging: Results from a Single-Center Observational Study on 1,003 Sequential Examinations. *Journal of Nuclear Medicine* **2020**, *61* (8), 1131–1136. https://doi.org/10.2967/jnumed.119.233940.

(79) Morsing, A.; Hildebrandt, M. G.; Vilstrup, M. H.; Wallenius, S. E.; Gerke, O.; Petersen, H.; Johansen, A.; Andersen, T. L.; Høilund-Carlsen, P. F. Hybrid PET/MRI in Major Cancers: A Scoping Review. *Eur J Nucl Med Mol Imaging* **2019**, *46* (10), 2138–2151. https://doi.org/10.1007/s00259-019-04402-8.

(80) Chan, S.-C.; Yeh, C.-H.; Yen, T.-C.; Ng, S.-H.; Chang, J. T.-C.; Lin, C.-Y.; Yen-Ming, T.; Fan, K.-H.; Huang, B.-S.; Hsu, C.-L.; Chang, K.-P.; Wang, H.-M.; Liao, C.-T. Clinical Utility of Simultaneous Whole-Body 18F-FDG PET/MRI as a Single-Step Imaging Modality in the Staging of Primary Nasopharyngeal Carcinoma. *Eur J Nucl Med Mol Imaging* **2018**, *45* (8), 1297–1308. https://doi.org/10.1007/s00259-018-3986-3.

(81) Catalano, O. A.; Nicolai, E.; Rosen, B. R.; Luongo, A.; Catalano, M.; Iannace, C.; Guimaraes, A.; Vangel, M. G.; Mahmood, U.; Soricelli, A.; Salvatore, M. Comparison of CE-FDG-PET/CT with

CE-FDG-PET/MR in the Evaluation of Osseous Metastases in Breast Cancer Patients. *Br J Cancer* **2015**, *112* (9), 1452–1460. https://doi.org/10.1038/bjc.2015.112.

(82) Eiber, M.; Rauscher, I.; Souvatzoglou, M.; Maurer, T.; Schwaiger, M.; Holzapfel, K.; Beer, A. J. Prospective Head-to-Head Comparison of 11C-Choline-PET/MR and 11C-Choline-PET/CT for Restaging of Biochemical Recurrent Prostate Cancer. *Eur J Nucl Med Mol Imaging* **2017**, *44* (13), 2179–2188. https://doi.org/10.1007/s00259-017-3797-y.

(83) Freitag, M. T.; Radtke, J. P.; Afshar-Oromieh, A.; Roethke, M. C.; Hadaschik, B. A.; Gleave, M.; Bonekamp, D.; Kopka, K.; Eder, M.; Heusser, T.; Kachelriess, M.; Wieczorek, K.; Sachpekidis, C.; Flechsig, P.; Giesel, F.; Hohenfellner, M.; Haberkorn, U.; Schlemmer, H.-P.; Dimitrakopoulou-Strauss, A. Local Recurrence of Prostate Cancer after Radical Prostatectomy Is at Risk to Be Missed in 68Ga-PSMA-11-PET of PET/CT and PET/MRI: Comparison with MpMRI Integrated in Simultaneous PET/MRI. *European Journal of Nuclear Medicine and Molecular Imaging* **2017**, *44* (5), 776–787. https://doi.org/10.1007/s00259-016-3594-z.

(84) *High-field and Hybrid*. https://healthcare-in-europe.com/en/news/healthcare-in-europe.com/en/news/high-field-hybrid.html (accessed 2022-04-23).

(85) Lois, C.; Bezrukov, I.; Schmidt, H.; Schwenzer, N.; Werner, M. K.; Kupferschläger, J.; Beyer, T. Effect of MR Contrast Agents on Quantitative Accuracy of PET in Combined Whole-Body PET/MR Imaging. *Eur J Nucl Med Mol Imaging* **2012**, *39* (11), 1756–1766. https://doi.org/10.1007/s00259-012-2190-0.

(86) Muehe, A. M.; Theruvath, A. J.; Lai, L.; Aghighi, M.; Quon, A.; Holdsworth, S. J.; Wang, J.; Luna-Fineman, S.; Marina, N.; Advani, R.; Rosenberg, J.; Daldrup-Link, H. E. How to Provide Gadolinium-Free PET/MR Cancer Staging of Children and Young Adults in Less than 1 Hour: The Stanford Approach. *Mol Imaging Biol* **2018**, *20* (2), 324–335. https://doi.org/10.1007/s11307-017-1105-7.

(87) Fendler, W. P.; Czernin, J.; Herrmann, K.; Beyer, T. Variations in PET/MRI Operations: Results from an International Survey Among 39 Active Sites. *Journal of Nuclear Medicine* **2016**, *57* (12), 2016–2021. https://doi.org/10.2967/jnumed.116.174169.

(88) Kiani, A.; Esquevin, A.; Lepareur, N.; Bourguet, P.; Jeune, F. L.; Gauvrit, J. Main Applications of Hybrid PET-MRI Contrast Agents: A Review. *Contrast Media & Molecular Imaging* **2016**, *11* (2), 92–98. https://doi.org/10.1002/cmmi.1674.

(89) Kastelik-Hryniewiecka, A.; Jewula, P.; Bakalorz, K.; Kramer-Marek, G.; Kuźnik, N. <p>Targeted PET/MRI Imaging Super Probes: A Critical Review of Opportunities and Challenges</P>. *IJN* **2022**, *16*, 8465–8483. https://doi.org/10.2147/IJN.S336299.

(90) Bonnemain, B. Superparamagnetic Agents in Magnetic Resonance Imaging: Physicochemical Characteristics and Clinical Applications A Review. *Journal of Drug Targeting* **1998**, *6* (3), 167–174. https://doi.org/10.3109/10611869808997890.

(91) Yang, X.; Hong, H.; Grailer, J. J.; Rowland, I. J.; Javadi, A.; Hurley, S. A.; Xiao, Y.; Yang, Y.; Zhang, Y.; Nickles, R. J.; Cai, W.; Steeber, D. A.; Gong, S. CRGD-Functionalized, DOX-Conjugated, and ^{64}Cu-Labeled Superparamagnetic Iron Oxide Nanoparticles for Targeted Anticancer Drug Delivery and PET/MR Imaging. *Biomaterials* **2011**, *32* (17), 4151–4160. https://doi.org/10.1016/j.biomaterials.2011.02.006.

(92) Kim, S.; Chae, M. K.; Yim, M. S.; Jeong, I. H.; Cho, J.; Lee, C.; Ryu, E. K. Hybrid PET/MR Imaging of Tumors Using an Oleanolic Acid-Conjugated Nanoparticle. *Biomaterials* **2013**, *34* (33), 8114–8121. https://doi.org/10.1016/j.biomaterials.2013.07.078.

(93) Jarrett, B. R.; Gustafsson, B.; Kukis, D. L.; Louie, A. Y. Synthesis of ^{64} Cu-Labeled Magnetic Nanoparticles for Multimodal Imaging. *Bioconjugate Chem.* **2008**, *19* (7), 1496–1504. https://doi.org/10.1021/bc800108v.

(94) Yuan, H.; Wilks, M. Q.; Normandin, M. D.; El Fakhri, G.; Kaittanis, C.; Josephson, L. Heat-Induced Radiolabeling and Fluorescence Labeling of Feraheme Nanoparticles for PET/SPECT Imaging and Flow Cytometry. *Nat Protoc* **2018**, *13* (2), 392–412. https://doi.org/10.1038/nprot.2017.133.

(95) Gholami, Y. H.; Yuan, H.; Wilks, M. Q.; Maschmeyer, R.; Normandin, M. D.; Josephson, L.; Fakhri, G. E.; Kuncic, Z. <p>A Radio-Nano-Platform for T1/T2 Dual-Mode PET-MR Imaging</P>. *IJN* **2020**, *15*, 1253–1266. https://doi.org/10.2147/IJN.S241971.

(96) Frullano, L.; Catana, C.; Benner, T.; Sherry, A. D.; Caravan, P. Bimodal MR–PET Agent for Quantitative PH Imaging. *Angewandte Chemie International Edition* **2010**, *49* (13), 2382–2384. https://doi.org/10.1002/anie.201000075.

(97) Uppal, R.; Catana, C.; Ay, I.; Benner, T.; Sorensen, A. G.; Caravan, P. Bimodal Thrombus Imaging: Simultaneous PET/MR Imaging with a Fibrin-Targeted Dual PET/MR Probe—Feasibility Study in Rat Model. *Radiology* **2011**, *258* (3), 812–820. https://doi.org/10.1148/radiol.10100881.

(98) Boswell, C. A.; Sun, X.; Niu, W.; Weisman, G. R.; Wong, E. H.; Rheingold, A. L.; Anderson, C. J. Comparative in Vivo Stability of Copper-64-Labeled Cross-Bridged and Conventional Tetraazamacrocyclic Complexes. *J. Med. Chem.* **2004**, *47* (6), 1465–1474. https://doi.org/10.1021/jm030383m.

(99) Notni, J.; Hermann, P.; Dregely, I.; Wester, H.-J. Convenient Synthesis of 68Ga-Labeled Gadolinium(III) Complexes: Towards Bimodal Responsive Probes for Functional Imaging with

PET/MRI. *Chemistry – A European Journal* **2013**, *19* (38), 12602–12606. https://doi.org/10.1002/chem.201302751.

(100) Kumar, A.; Zhang, S.; Hao, G.; Hassan, G.; Ramezani, S.; Sagiyama, K.; Lo, S.-T.; Takahashi, M.; Sherry, A. D.; Öz, O. K.; Kovacs, Z.; Sun, X. Molecular Platform for Design and Synthesis of Targeted Dual-Modality Imaging Probes. *Bioconjugate Chem.* **2015**, *26* (3), 549–558. https://doi.org/10.1021/acs.bioconjchem.5b00028.

(101) Brandt, M. R.; Vanasschen, C.; Ermert, J.; Coenen, H. H.; Neumaier, B. 52g/55Mn-Labelled CDTA-Based Trimeric Complexes as Novel Bimodal PET/MR Probes with High Relaxivity. *Dalton Trans.* **2019**, *48* (9), 3003–3008. https://doi.org/10.1039/C8DT04996C.

(102) Vanasschen, C.; Brandt, M.; Ermert, J.; H. Coenen, H. Radiolabelling with Isotopic Mixtures of 52g/55 Mn(Ii) as a Straight Route to Stable Manganese Complexes for Bimodal PET/MR Imaging. *Dalton Transactions* **2016**, *45* (4), 1315–1321. https://doi.org/10.1039/C5DT04270D.

(103) Kretschmer, J.; David, T.; Dračínský, M.; Socha, O.; Jirak, D.; Vít, M.; Jurok, R.; Kuchař, M.; Císařová, I.; Polasek, M. Paramagnetic Encoding of Molecules. *Nat Commun* **2022**, *13* (1), 3179. https://doi.org/10.1038/s41467-022-30811-9.

(104) León-Rodriguez, L. M. D.; Kovacs, Z.; Dieckmann, G. R.; Sherry, A. D. Solid-Phase Synthesis of DOTA–Peptides. *Chemistry – A European Journal* **2004**, *10* (5), 1149–1155. https://doi.org/10.1002/chem.200305389.

(105) Boros, E.; Polasek, M.; Zhang, Z.; Caravan, P. Gd(DOTAla): A Single Amino Acid Gd-Complex as a Modular Tool for High Relaxivity MR Contrast Agent Development. *J. Am. Chem. Soc.* **2012**, *134* (48), 19858–19868. https://doi.org/10.1021/ja309187m.

(106) Brückner, K.; Zitterbart, R.; Seitz, O.; Beck, S.; Linscheid, M. W. Solid Phase Synthesis of Short Peptide-Based Multimetal Tags for Biomolecule Labeling. *Bioconjugate Chem.* **2014**, *25* (6), 1069–1077. https://doi.org/10.1021/bc500082k.

(107) Tremblay, M. S.; Sames, D. Synthesis of Luminescent Heterometallic Bis-Lanthanide Complexes via Selective, Sequential Metallation. *Chem. Commun.* **2006**, No. 39, 4116–4118. https://doi.org/10.1039/B607949K.

(108) Sørensen, T. J.; Tropiano, M.; Kenwright, A. M.; Faulkner, S. Triheterometallic Lanthanide Complexes Prepared from Kinetically Inert Lanthanide Building Blocks. *European Journal of Inorganic Chemistry* **2017**, *2017* (15), 2165–2172. https://doi.org/10.1002/ejic.201700027.

(109) Sørensen, T. J.; Tropiano, M.; Blackburn, O. A.; Tilney, J. A.; Kenwright, A. M.; Faulkner, S. Preparation and Study of an f,f,F′,F″ Covalently Linked Tetranuclear Hetero-Trimetallic Complex – a Europium, Terbium, Dysprosium Triad. *Chem. Commun.* **2012**, *49* (8), 783–785. https://doi.org/10.1039/C2CC35931F.

(110) Kreidt, E.; Leis, W.; Seitz, M. Direct Solid-Phase Synthesis of Molecular Heterooligonuclear Lanthanoid-Complexes. *Nature Communications* **2020**, *11* (1), 1346. https://doi.org/10.1038/s41467-020-15199-8.

(111) Dormoy, J.-R. Synthesis of L-3,4-Didehydroproline: Favoured Orientation in the Key-Step Elimination Reaction. *Synthesis* **1982**, *1982* (9), 753–756. https://doi.org/10.1055/s-1982-29931.

(112) Coenen, H. H.; Gee, A. D.; Adam, M.; Antoni, G.; Cutler, C. S.; Fujibayashi, Y.; Jeong, J. M.; Mach, R. H.; Mindt, T. L.; Pike, V. W.; Windhorst, A. D. Open Letter to Journal Editors on: International Consensus Radiochemistry Nomenclature Guidelines. *Ann Nucl Med* **2018**, *32* (3), 236–238. https://doi.org/10.1007/s12149-018-1238-z.

(113) Schlosser, M.; Rausis, T. The Reactivity of 2-Fluoro- and 2-Chloropyridines toward Sodium Ethoxide: Factors Governing the Rates of Nucleophilic (Het)Aromatic Substitutions. *Helvetica Chimica Acta* **2005**, *88* (6), 1240–1249. https://doi.org/10.1002/hlca.200590104.

(114) Dollé, F.; Dolci, L.; Valette, H.; Hinnen, F.; Vaufrey, F.; Guenther, I.; Fuseau, C.; Coulon, C.; Bottlaender, M.; Crouzel, C. Synthesis and Nicotinic Acetylcholine Receptor in Vivo Binding Properties of 2-Fluoro-3-[2(S)-2-Azetidinylmethoxy]Pyridine: A New Positron Emission Tomography Ligand for Nicotinic Receptors. *J. Med. Chem.* **1999**, *42* (12), 2251–2259. https://doi.org/10.1021/jm9910223.

(115) Dolci, L.; Dolle, F.; Jubeau, S.; Vaufrey, F.; Crouzel, C. 2-[18F]Fluoropyridines by No-Carrier-Added Nucleophilic Aromatic Substitution with [18F]FK-K222—a Comparative Study. *Journal of Labelled Compounds and Radiopharmaceuticals* **1999**, *42* (10), 975–985. https://doi.org/10.1002/(SICI)1099-1344(199910)42:10<975::AID-JLCR256>3.0.CO;2-E.

(116) Karramkam, M.; Hinnen, F.; Vaufrey, F.; Dollé, F. 2-, 3- and 4-[18F]Fluoropyridine by No-Carrier-Added Nucleophilic Aromatic Substitution with K[18F]F-K222 – a Comparative Study. *Journal of Labelled Compounds and Radiopharmaceuticals* **2003**, *46* (10), 979–992. https://doi.org/10.1002/jlcr.730.

(117) Wagner, F. M.; Ermert, J.; Coenen, H. H. Three-Step, "One-Pot" Radiosynthesis of 6-Fluoro-3,4-Dihydroxy-l-Phenylalanine by Isotopic Exchange. *J Nucl Med* **2009**, *50* (10), 1724–1729. https://doi.org/10.2967/jnumed.109.063297.

(118) Weiss, P. S.; Ermert, J.; Castillo Meleán, J.; Schäfer, D.; Coenen, H. H. Radiosynthesis of 4-[18 F]Fluoro- l -Tryptophan by Isotopic Exchange on Carbonyl-Activated Precursors. *Bioorganic & Medicinal Chemistry* **2015**, *23* (17), 5856–5869. https://doi.org/10.1016/j.bmc.2015.06.073.

(119) Brugarolas, P.; Freifelder, R.; Cheng, S.-H.; DeJesus, O. Synthesis of Meta-Substituted [18F]3-Fluoro-4-Aminopyridine via Direct Radiofluorination of Pyridine N-Oxides. *Chem. Commun.* **2016**, *52* (44), 7150–7152. https://doi.org/10.1039/C6CC02362B.

(120) Sagara, H.; Inoue, K.; Yaku, H.; Ohsawa, A.; Someya, T.; Yanagisawa, K.; Ohashi, S.; Ishigaki, R.; Wakabayashi, M.; Muramatsu, Y.; Fujii, H. Optimization of Injection Dose in 18F-FDG PET/CT Based on the 2020 National Diagnostic Reference Levels for Nuclear Medicine in Japan. *Ann Nucl Med* **2021**, *35* (11), 1177–1186. https://doi.org/10.1007/s12149-021-01656-x.

(121) Rohrer, M.; Bauer, H.; Mintorovitch, J.; Requardt, M.; Weinmann, H.-J. Comparison of Magnetic Properties of MRI Contrast Media Solutions at Different Magnetic Field Strengths. *Investigative Radiology* **2005**, *40* (11), 715–724. https://doi.org/10.1097/01.rli.0000184756.66360.d3.

(122) Khalifa, F.; Soliman, A.; El-Baz, A.; Abou El-Ghar, M.; El-Diasty, T.; Gimel'farb, G.; Ouseph, R.; Dwyer, A. C. Models and Methods for Analyzing DCE-MRI: A Review. *Medical Physics* **2014**, *41* (12), 124301. https://doi.org/10.1118/1.4898202.

(123) Sheldrick, G. M. SHELXT – Integrated Space-Group and Crystal-Structure Determination. *Acta Cryst A* **2015**, *71* (1), 3–8. https://doi.org/10.1107/S2053273314026370.

(124) Sheldrick, G. M. Crystal Structure Refinement with SHELXL. *Acta Cryst C* **2015**, *71* (1), 3–8. https://doi.org/10.1107/S2053229614024218.